

Contribution to modeling multipactor and corona discharges in high power electromagnetic fields

THÈSE N° 5542 (2012)

PRÉSENTÉE LE 23 NOVEMBRE 2012

À LA FACULTÉ DES SCIENCES ET TECHNIQUES DE L'INGÉNIEUR
LABORATOIRE D'ÉLECTROMAGNÉTISME ET ACOUSTIQUE
PROGRAMME DOCTORAL EN GÉNIE ÉLECTRIQUE

ÉCOLE POLYTECHNIQUE FÉDÉRALE DE LAUSANNE

POUR L'OBTENTION DU GRADE DE DOCTEUR ÈS SCIENCES

PAR

Francisco Edén SOROLLA ROSARIO

acceptée sur proposition du jury:

Prof. A. Rufer, président du jury
Prof. J. R. Mosig, Dr M. Mattes, directeurs de thèse
Dr J. Puech, rapporteur
Prof. F. Rachidi-Haeri, rapporteur
Dr F. Zimmermann, rapporteur



ÉCOLE POLYTECHNIQUE
FÉDÉRALE DE LAUSANNE

Suisse
2012

Ability is what you are capable of doing.
Motivation determines what you do.
Attitude determines how well you do it.

Lou Holtz

To my teachers.

Acknowledgements

First of all to my thesis advisor and co-advisor, Prof. Juan R. Mosig and Dr. Michael Mattes, respectively, for giving me the opportunity to join the *Laboratoire d'Electromagnétisme et Acoustique* (LEMA) during the pursuit of my PhD at EPFL. I am especially grateful to Dr. Mattes for his technical support and for teaching me how to set out the resolution of a problem following Einstein's approach: "simplify as much as possible but no further" in order to fully reduce the difficulty of a problem while keeping the aspects that account for the physical mechanisms that are to be investigated.

I am deeply indebted to Prof. Benito Gimeno, from the University of Valencia, since he was the person who gave me the opportunity to be enrolled in the awesome world of research when I finished my degree and he has always shown his confidence on my possibilities to succeed in the pursuit of my PhD. He also taught me how to make connections with other researchers and to collaborate with other people, contributing to a very positive attitude in the relation with other members of the scientific community. Thank you very much.

I must include here my teacher of Physics in the high school, Pascual Bosque, who taught me the basis to think like a physicist: sometimes finding the answer by discarding the rest of possibilities, based on assumed principles; sometimes proposing *Gedanken experiments*. Although I do not share the general belief that only few people are capable to obtain a scientific degree in the university, he always trusted in my skills and encouraged me to pursue my dreams despite the impasse for getting the financial support.

A big thank you also goes to Prof. Miguel Ángel Sanchís from the University of Valencia who enlarged my vision about the power that Physics has in the understanding and the resolution of problems in the real world, as well as the fact that life is not a race against time but rather a steeplechase. Thank you very much for the ordinary and for the tutorship lessons where we learnt to really think in Physics.

Thank you to David Raboso for his patience and for teaching me modesty to know when to put my hand on the fire as well as for showing me the real world. In the same context, I am very grateful to Holger Karstensen, Joseph Fuchs and Kuno Wettstein, from Huber and Suhner, AG, for his patience and help in the development of the PSM connector.

I also want to thank Prof. Farhad Rachidi for his valuable remarks and his pleasant words about the thesis and my work, as well as to Prof. Anja Skrivervik for her constant interest in the human aspects of the people at LEMA. I am also very grateful to Eulalia Durussel for her invaluable help from the beginning of my arrival in Lausanne, with all the troubles that my situation entailed at that moment. Thanks to Francesco Merli, too, for his invaluable help during my first months to deal with the problem of filling my apartment with some furniture as well as for the numerous days playing football and evenings plenty of laughs. Thanks to Juliane Iten Chaves Simões as well for her efforts showing me the small things that a quotidian life in a city like Lausanne request.

A big thank you to Roberto Torres who sacrificed his time and energies when I arrived in Lausanne for helping me enormously in the quest of an apartment and other logistics that implied the knowledge of a language that was unknown for me. Thank you for teaching me with your tireless attitude that the unconditional kindness exists, arguing with your example against the commonly accepted belief, for the time being, that selfishness is the natural tendency of the human being. I owe a big thank you to Sergio López, too, since he taught me many secrets about life that my naivety was hiding to myself. He also showed me the romanticism that stoicism may imply and he taught me to be more reflective and the importance of following a strategy in life. I

am deeply indebted to the last, but not the least, within this group of scoundrels, Benjamin Fuchs, my Breton friend who taught me many things: from the *good* French to values like patience, assertiveness, modesty, calm, etc.... Thanks go to all of you for being there when I needed you.

A big thank you to Yannis Koufogiannis for the nice evenings sharing thoughts, ski weekends, games, laughs and good moments together. Thank you for listening and for your understanding. A big thank you to Juan Sebastián Gómez, the closest person to my alter ego, since Ontur is very close to Alicante, for your kindness, your solidarity and your courage to conceive the research as an open activity where everybody can contribute and “naide es más que naide”.

Thank you especially to Ruziça Golubovic for her priceless help and support from the beginning of my stay in Lausanne, as well as to Laleh Golestanirad for her continuous kind words and understanding. Thank you, Gabriela Quintero and Maddalena Violetti, for our long conversations about human relationships. A big thank as well to Elena Díaz for contributing to the nice atmosphere at LEMA. Thanks go to all of you, girls, who made the life at LEMA more colorful with your charm.

A big thank you to Txema Tamayo for his coolness, wisdom and friendliness, as well as for his contagious inner peace. I am also deeply grateful to Marc Esquius and Eduardo Carrasco for their human qualities. I would also like to thank Jean François Zurcher for all his technical support at LEMA and for his advices in the world of photography. I am also grateful to David Desscan for his technical help and for the conversations about many different topics that took place late in the evening after work. Thanks go to all my other colleagues: Rafal Glogowski, Nuno Pires, Mohsen Yousefbeiki, Gabriele Rosati, Marco Letizia, Apostolos Sounas, Jovanche Trajkovikj and Baptiste Hornecker.

I am indebted to all my friends outside the lab for their support: the ones that I met in Switzerland (especially Luis García Naranjo and Carmen Fernández) as well as all my friends beyond Helvetia (especially José Antonio Polo and Loli González). A huge thanks to the rest of my friends: Christian, Juanma, Jorge, Josep, Alejandro, Diego, Benoît, Jesús, Martina, Davide, Alex, Caro and Gon, Joaquim and Susana, Diego Quezada (*con “seta”*) and Paula, Iván and Diana, Lucia, Cedric, Jérôme, Martin, Rubén, Julián, Sergio, Samuel, Danjche (partly responsible of this thesis, too), Marjanche and Nikola, ..., and to all those who made me stronger.

Finally, I am grateful to all my family for their support, particularly my brother, my sister, my parents and grandparents, but especially to my grandfather, responsible of this work, too. I ardently believe in the power of *Pygmalion effect*: a spirited sentence enunciated in the right moment may inject the vital motivation into a person to find his path and believe in the achievement of his dreams. The biggest thanks for this thesis are thus due to my grandfather, who injected into my soul, when I was a kid, all the courage needed to pursue my dream of studying the functioning of the Universe by becoming a physicist.

Summary

Multipactor and microwave corona breakdown are two high frequency discharges occurring within microwave components for space applications as well as within particle accelerators. The appearance of these phenomena results in the exponential growth of the electron population triggered by the interaction of the environmental charged particles with the microwave component. The consequence of these discharges is an electron cloud build-up that, for space applications, loads the Radio Frequency (RF) cavities. This entails the increase of the system noise level and the return loss, generating undesirable harmonics and creating a local augmentation of the temperature that may destroy internal components, with the subsequent failure of the mission. Concerning the particle accelerators, the electron cloud induces the deflection and the deformation of the particle beam, reducing its beam-to-beam collision efficiency and causing the malfunctioning of the accelerator.

The lack of a software or a method to predict the multipactor power breakdown threshold of RF components leads the scientific community to deal with high-cost test campaigns. Although the detection of the radiated power produced by the multipactor current was proposed as a breakdown detection method, no absolute levels of radiation were available to compare with measurements and validate this technique to assess the breakdown onset. In this thesis, an analytical expression to quantify the radiated power spectrum produced by a multipactor discharge within a parallel-plate waveguide has been developed.

As there must be a mechanism to limit the growth of the electron population and the radiated power spectrum depends on the number of electrons, the multipactor steady-state is also analyzed in this thesis. As multipactor breakdown is assumed to be detected when the saturation in the amount of electrons has been reached, an analytical expression of the electron population in the steady-state has been proposed in this thesis. This could help to predict the levels of radiation that must be detected when the breakdown occurs, and could be compared with the measurements to establish a rigorous multipactor detection criterion.

Another part of the thesis deals with the development of a globally convergent algorithm to calculate very efficiently a large amount of roots of the cross-product of Bessel functions. This algorithm can be employed in the calculation of the radiated power spectrum produced by a multipactor discharge within a coaxial waveguide using the appropriated Green function, which needs the evaluation of these roots.

Regarding the corona breakdown, this thesis intends to show the critical dependency of the breakdown power threshold on the ionization rate model. The ionization rate is a gas parameter that provides the amount of electrons released per unit time due to the ionization produced in the gas molecules as function of the electric field amplitude. Three models of the ionization rate found in the literature are considered in this thesis and the corona breakdown power thresholds predicted are compared. Noticeable differences between the results obtained with each model have been found in some cases, which are analyzed in this work.

Finally, in line with this thesis, a new high power SMA-like coaxial connector (in mass and size) has been developed. This thesis shows the design of the "Power Sub-miniature" (PSM) connector, which is capable to withstand high input powers without the risk of corona or multipactor breakdown to occur. The PSM has been manufactured and tested showing excellent multipactor withstanding capabilities. This connector is, in fact, able to withstand, at least, up to 1500 W input power for a pulsed signal of 2% duty-cycle in P-band (438 MHz) as well as in L-band (1124 MHz), without showing any trace of multipactor discharge. This implies an improvement of 50% compared to other powerful connectors such as the TNC. Concerning corona breakdown,

the PSM is able to withstand more than 80 W CW without showing any sign of glowing or noticeable discharge, what is a challenge for coaxial connectors of this size at these input powers.

Keywords: Multipactor, radiated power spectrum, Bessel functions, multipactor saturation, corona breakdown, ionization rates, coaxial connectors.

Résumé

Multipactor et l'effet corona microonde sont deux décharges hautes fréquences qui peuvent avoir lieu dans les composants microondes pour des applications spatiales ainsi que dans des accélérateurs de particules. L'apparition de ces phénomènes se traduit par une augmentation exponentielle de la quantité d'électrons déclenchée par l'interaction des particules chargées dans l'environnement avec le dispositif microonde. La conséquence de ces décharges est la formation d'un nuage d'électrons qui, pour des applications spatiales, charge les cavités RF. Cela entraîne une augmentation du niveau de bruit du système et une dégradation du coefficient de réflexion, génère des harmoniques non voulues et crée une augmentation locale de la température qui peut détruire certains composants internes et ainsi conduire à l'échec de la mission. Pour ce qui est des accélérateurs de particules, le nuage d'électrons entraîne une déviation et une déformation du faisceau de particules. Cela réduit l'efficacité de la collision faisceau à faisceau et conduit à un mauvais fonctionnement de l'accélérateur.

Le manque de logiciel ou méthode pour prédire le seuil de rupture de puissance multipactor des composants RF conduit la communauté scientifique à mener des campagnes de tests à coût élevé. Bien que la détection de la puissance rayonnée produite par le courant multipactor fût proposée comme méthode pour détecter la rupture, aucun niveau absolu de rayonnement n'était prédit pour comparer avec des mesures et ainsi valider cette technique pour évaluer le commencement de la rupture. Dans cette thèse, une expression analytique pour quantifier le spectre de puissance rayonné produit par une décharge multipactor dans un guide d'onde à plaques parallèles a été développée.

Comme on sait qu'il doit y avoir un mécanisme pour delimitier la croissance de la population d'électrons et le spectre de puissance rayonnée dépend du nombre d'électrons, l'état d'équilibre multipactor est aussi analysé dans cette thèse. Comme la rupture multipactor est supposée pouvoir être détectée lorsque la saturation en quantité d'électrons a été atteinte, une expression analytique de la population d'électrons dans l'état d'équilibre a été proposée dans cette thèse. Cela pourrait aider à prédire les niveaux de rayonnement qui doivent être détectés quand la rupture se produit, et cela pourrait être comparé avec les mesures pour établir un critère rigoureux de détection du phénomène multipactor.

De plus, un algorithme convergeant globalement a été développé dans cette thèse pour calculer très rapidement un nombre élevé de racines du produit croisé de fonctions de Bessel. Cet algorithme a été proposé pour calculer efficacement le spectre de puissance rayonné produit par une décharge multipactor dans un guide d'onde coaxial en utilisant les fonctions de Green appropriées, ce qui nécessite le calcul de telles racines.

Concernant l'effet corona, cette thèse a aussi pour but de montrer la dépendance critique entre le seuil de rupture de puissance et le modèle du taux d'ionisation. Le taux d'ionisation est un paramètre du gaz qui donne la quantité d'électrons libérée par unité de temps à cause de l'ionisation produite dans les molécules de gaz en fonction de l'amplitude du champ électrique. Trois modèles de taux d'ionisation trouvés dans la littérature sont considérés et les seuils de puissance de l'effet corona ainsi prédits sont comparés. Les différences obtenues, observables dans certains cas, sont discutées dans cette thèse.

Enfin, dans le cadre de cette thèse un nouveau connecteur à haute puissance de type coaxial SMA (en masse et dimensions) a été développé. Cette thèse montre la conception du connecteur "Power Sub-miniature" PSM qui est capable de supporter des puissances en entrée élevées sans risque d'apparition de l'effet corona ou rupture multipactor. Le PSM a été réalisé et testé montrant une excellente capacité de résistance au multipactor.

Ce connecteur est en effet capable de résister à au moins 1500 W de puissance en entrée pour un signal de type impulsion à cycle de 2% en bande P (438 MHz) ainsi qu'en bande L (1124 MHz) sans apparition de décharge multipactor. Cela signifie une amélioration de 50% par rapport aux autres connecteurs de puissance tels que le TNC. Concernant l'effet corona, le PSM est capable de résister à plus de 80 W à émission continue sans produire d'effluve ni de décharge, ce qui est un défi pour des connecteurs coaxiaux de cette taille à de telles puissances d'entrée.

Mots-clés: Multipactor, spectre de puissance rayonnée, fonctions de Bessel, saturation de multipactor, effet corona, taux d'ionisation, connecteur coaxiaux.

Kurzfassung

Multipaktor- und Mikrowellenkoronadurchbruch¹ sind zwei Hochfrequenzentladungen, die sowohl in Mikrowellensystemen für Weltraumanwendungen (z. B. Satellitensystemen) als auch in Teilchenbeschleunigern auftreten können. Beide Phänomene führen zu einem exponentiellen Anstieg von freien Elektronen durch die Wechselwirkung der geladenen Teilchen mit den Bauteilen, wodurch eine Elektronenwolke im Innern der Systeme entstehen kann. Dies führt zu Fehlanpassungen der HF-Komponenten und verstärktem Rauschen, der Anregung von Oberwellen² sowie einem lokalen Temperaturanstieg, der zu deren Beschädigung oder sogar Zerstörung führen kann, was eine gesamte Weltraummission gefährden kann. Bei Teilchenbeschleunigern kann die Elektronenwolke den Teilchenstrahl ablenken und verformen und dadurch die Effizienz von Teilchenkollisionen verringern.

Da Programme und Methoden zur Simulation der Durchbruchleistung, also der Eingangsleistung bis zu welcher keine Multipaktorentladungen auftreten, fehlen, sind oft teure Testkampagnen notwendig. Dabei könnte die von der entstehenden Elektronenwolke abgestrahlte Leistung zu Diagnosezwecken verwendet werden und als Kriterium dienen, um abzuschätzen, ob im Innern einer HF-Komponente Multipaktor auftritt oder nicht. Um diese Detektionsmethode für Multipaktor einsetzen zu können, müssen aber absolute Leistungswerte in Abhängigkeit der vorhandenen Elektronenzahl bekannt sein, um von gemessenen Leistungen Rückschlüsse auf die Elektronenzahl ziehen zu können. Zu diesem Zweck wurde in dieser Dissertation ein Parallelplattenleiter betrachtet, um ein analytisches Modell herzuleiten, das die abgestrahlte Leistung mit der Anzahl der Elektronen verknüpft.

Weil Multipaktor normalerweise im Sättigungsbereich gemessen, d. h. detektiert wird, muß die Elektronenzahl für diesen Bereich bekannt sein, um die bei Messungen erwarteten Leistungen vorhersagen zu können. Dazu wurde in dieser Arbeit ein analytischer Ausdruck für die Elektronenzahl im Sättigungsbereich hergeleitet, der zusammen mit dem Modell für die abgestrahlte Leistung als Basis für die Entwicklung einer rigorosen Meßvorschrift dienen könnte, um zu entscheiden, ob Multipaktor während einer Testkampagne auftritt.

In diesem Rahmen wurde ferner ein effizienter Algorithmus entwickelt, mit dem eine große Anzahl von Nullstellen der charakteristischen Gleichung für koaxiale Hohlleiter, welche dessen Moden bestimmt, berechnet werden kann. Die Moden wiederum sind notwendig, um die Greensche Funktion des koaxialen Hohlleiters zu berechnen, welche ihrerseits zur Berechnung der abgestrahlten Leistung der Elektronenwolke verwendet werden kann.

Mit Bezug auf Koronadurchbruch versucht diese Arbeit die starke Abhängigkeit der simulierten Durchbruchleistung von den Ionisierungsmodellen aufzuzeigen. Die Ionisierungsrate ist ein Gasparameter, welcher die Anzahl der durch Ionisierung freigesetzten Elektronen pro Zeiteinheit in Abhängigkeit der elektrischen Feldstärke angibt. Drei verschiedene Modelle wurden betrachtet, die vorhergesagten Durchbruchleistungen verglichen und die auftretenden Unterschiede diskutiert.

Schließlich und im Einklang mit dieser Dissertation wurde ein neuartiger koaxialer Steckverbinder vom Typ SMA³ entwickelt. Dieser neue Verbinder, Power-SMA (PSM) genannt, kann sehr hohe Leistungen übertragen,

¹ *engl.* microwave corona breakdown

² *engl.* harmonics

³ *engl.* SubMiniature version A

ohne daß Multipaktor- oder Koronaentladungen auftreten. Messungen ergaben eine Übertragungsleistung von mindestens 1500 W gepulst (2% Einschaltdauer⁴) im P-Band (438 MHz) und L-Band (1184 MHz) sowie 80 W CW. Dies entspricht einer Verbesserung von 50% gegenüber vergleichbaren Steckverbindern wie z. B. dem TNC, was eine echte Herausforderung für Verbinder dieser Größe bei derartigen Eingangsleistungen darstellt.

Schlagwörter: Multipaktor, Strahlungsleistungsdichte, Bessel Funktionen, Multipaktorsättigung, Korona-durchbruch, Ionisierungsraten, koaxiale Steckverbinder.

⁴engl. duty-cycle

Contents

1	Introduction	1
1.1	Framework	1
1.1.1	Space weather and applications	2
1.1.2	Accelerators	3
1.2	Corona overview	5
1.3	Multipactor overview	6
1.4	Thesis scope	6
1.5	Thesis outline	7
1.6	Original contributions	9
1.7	Acknowledgments	9
2	Multipactor breakdown	11
2.1	Introduction	11
2.2	Classical multipactor resonance conditions	11
2.3	Positive relative impact velocity condition	22
2.4	Stability condition	26
2.5	Returning condition	30
2.6	Multipactor susceptibility chart	35
2.7	Summary	40
3	Radiation of a multipactor discharge	41
3.1	Introduction	41
3.2	Theory	42
3.2.1	Uniform current model	43
3.2.2	Point current model	48
3.3	Results	55
3.4	Summary	59
4	Roots of the cross-product of Bessel functions	63
4.1	Introduction	63
4.2	Theory	64
4.2.1	Roots of $TM_{0,s}$ modes	65
4.2.2	Roots of $TM_{\nu,s}$ modes	68
4.2.3	Roots of $TE_{\nu,s}$ modes	70
4.3	Main results	72
4.4	Summary	77

5	Multipactor saturation	81
5.1	Introduction	81
5.2	Multipactor breakdown with space charge effects	82
5.2.1	Equations of motion of the electron sheet	83
5.2.2	Stability of the multipactor discharge	85
5.3	Mechanisms of saturation	92
5.3.1	Impact energy limit mechanism	94
5.3.2	Returning limit mechanism	95
5.4	Range of validity of the saturation mechanisms	101
5.5	Summary	104
6	Corona breakdown	107
6.1	Transport theory of charged particles in gases	107
6.2	Corona breakdown	111
6.3	Ionization rate models	115
6.3.1	Woo's model	115
6.3.2	Lupan's model	116
6.3.3	Mayhan's model	116
6.3.4	Comparison of the ionization rates	117
6.4	Numerical solution of the corona equation	119
6.5	Results	120
6.5.1	Corona discharge in a parallel-plate waveguide	121
6.5.2	Corona discharge in a rectangular waveguide	124
6.5.3	Corona discharge in a circular waveguide	128
6.5.4	Corona discharge in a coaxial waveguide	136
6.5.5	Corona discharge in a rectangular cavity	142
6.5.6	Corona discharge of a monopole antenna	145
6.6	Summary	158
7	Power Sub-miniature connector	161
7.1	Motivation	161
7.1.1	Coaxial connector parameters	162
7.1.2	Coaxial connector series	162
7.1.3	Space applications	164
7.2	Guidelines	166
7.2.1	Multipactor guidelines	166
7.2.2	Corona guidelines	168
7.2.3	Outgassing and venting	170
7.3	PSM design	171
7.4	High power analysis	172
7.4.1	Multipactor analysis	172
7.4.2	Corona analysis	173
7.5	Test results	173
7.5.1	Low power performance	176

7.5.2	High power performance	176
7.5.3	Multipactor tests	176
7.5.4	Corona tests	178
7.6	Discrepancies	181
7.7	Summary	182
8	Outlook and future work	185
A	Returning limit analysis	187
A.1	Returning limit equation	187
A.1.1	Zero initial velocity	188
A.1.2	Non-zero initial velocity	190
B	Input power of a monopole antenna	195
C	Equations of motion of multipactor with space charge effects	197
	Bibliography	201

Introduction

Contents

1.1 Framework	1
1.1.1 Space weather and applications	2
1.1.2 Accelerators	3
1.2 Corona overview	5
1.3 Multipactor overview	6
1.4 Thesis scope	6
1.5 Thesis outline	7
1.6 Original contributions	9
1.7 Acknowledgments	9

1.1 Framework

The current trend in the market of microwave devices for space telecommunication systems is the fabrication of devices working at higher frequencies and with higher input powers without limiting any of their features and still working properly. This is due to the market demand of increasing the amount of information that telecommunication satellites have to be able to handle within a framework where the welfare of the society has become more and more dependent on the communications through different services that they can provide: GPS, GSM, meteorology, exploratory space missions, tele-assisted surgery, etc....

At the same time, the need of reducing costs for launching satellites increasingly forces the weight of the devices inside them to be reduced. To do so, the inner dimensions of the waveguides are reduced, what enables the functioning at higher operating frequencies. This yields an increase of the electromagnetic field strength inside them, what greatly increases the risk of multipactor and corona discharges to occur with the danger of destroying a part of or the complete telecommunication system.

On the other hand, the casuistry of multipactor breakdown also involves the malfunctioning of particle accelerators. The radiation produced by the highly accelerated charged particles induces the photo-electron emission at the boundaries of the beam pipe where the beam particles travel through. The appearance of an electron cloud within the beam pipe perturbs the beam and reduces the beam-to-beam collision efficiency drastically, provoking the malfunctioning of the particle accelerator.

1.1.1 Space weather and applications

The space weather is a very hostile environment for telecommunication satellites: energetic charged particles with energies in the MeV range are commonly encountered throughout the Earth magnetosphere, in interplanetary space and in the magnetospheres of other planets, like Mercury. The origin of these particles is provided by manifold sources like the energetic solar eruptions (likewise called solar bursts or coronal mass ejections); the Galactic Cosmic Rays (GCR), whose origin is not completely understood yet; and the secondary radiation produced by the interaction of these particles with materials of the spacecraft, among others [ECSS 2000].

It is interesting to remark that the same agent responsible of trapping these particles around the Earth, which affects the functioning of the satellites, protects life on the planet from this harsh environment. Indeed, the Earth magnetic field deflects the charged particles coming from the solar wind or from the above-mentioned sources and they remain trapped along the magnetic field lines preventing hazardous radiation on the planet surface. This effect is known as geomagnetic shielding, and creates a region of the atmosphere called magnetosphere, which is like a hemisphere on the sun side, with a boundary at approximately 10-12 Earth-radii ($R_E = 6370$ km). On the anti-sunward direction, it is cylindrical with approximately $40R_E$ in diameter. Due to the solar wind, the magnetosphere extends over several hundred R_E on the night side of the Earth, forming a magnetic tail. The lower part of the magnetosphere is called plasmasphere, where the trapped radiation is mainly confined, forming the Van Allen belts (see Fig. 1.1).

The radiation belts, likewise called Van Allen belts, consist of energetic electrons and ions that are magnetically trapped moving back and forth along the Earth magnetic field lines. They are mainly electrons of up to a few MeV energy and protons of up to several hundreds MeV energy. Nevertheless, though the magnetosphere contains these particles far from the surface, they can easily reach polar regions and high altitudes such as the geostationary orbit. Therefore, many orbits are affected by this radiation, and the interaction of the charged particles with the devices at the payload of the satellites can result in a blackout between the spacecraft and the base station on the Earth, what can provoke the loss of the spacecraft or the failure of a complete mission.

The electrons that are responsible for the malfunctioning of some components on the satellites come also from the surface of conductors within the microwave devices when the electric field is very strong so as to make the electrons overcome the potential barrier by the tunneling effect. This process is named field emission [Fowler 1928, Woode 1989], and though it predicts the need of very strong electric fields to allow the release of the electrons, irregularities, oxide or dirt contaminants on the surface can induce electron emission at appreciably lower field strengths.

In any case, the space weather is not only hazardous for telecommunications satellites, but also for on-ground applications in power grids like high voltage transmission lines, telephone networks, oil and gas pipelines, railways and undersea communication cables. The appearance of geomagnetically induced currents is provoked by the intense magnetic field variations in the magnetosphere occurring when a solar storm arises, which induces large electric fields and currents over large areas of Earth's surface. The interconnecting networks act as giant antennas that channel the induced currents from the ground, and provoke the failure of many systems in few minutes.

The most well-known example is the one that occurred in Quebec in 1989, where a geomagnetic storm provoked that the power grid in the region experienced 15 failures only during the first 30 seconds, and the result was a province-wide blackout. And that storm was less intense than others experienced by the Earth before [IEEE 2012].

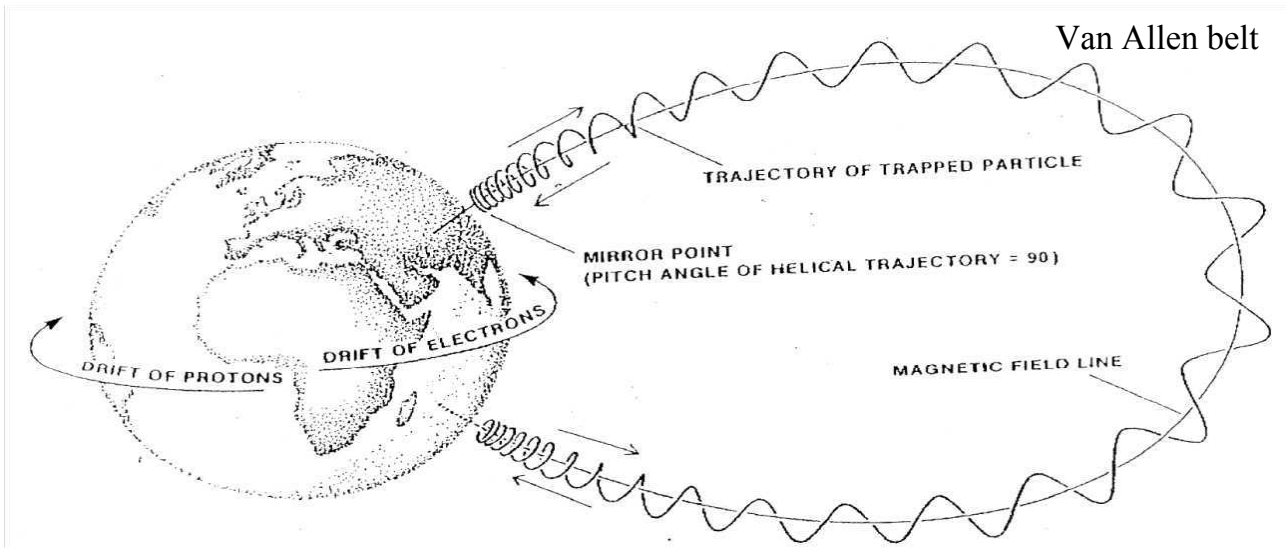


Figure 1.1: Sketch of the magnetosphere and of the geomagnetic shielding produced by the Van Allen belts. Extracted from [ECSS 2000].

1.1.2 Accelerators

The multipactor effect is not only important for space applications, but in particle accelerators as well [Ohmi 1995, Izawa 1995, Kravchuk 1999, Ohmi 2000, Rummolo 2001, Harkay 2003, Furman 2003, Cimino 2004, Abe 2006, Gusarova 2009] like, for instance, in the Large Hadron Collider (LHC) in CERN. Nevertheless, the mechanism of multipactor breakdown in particle accelerators is different to space applications. Beam-induced multipactor was firstly observed as a pressure rise at the Intersecting Storage Ring (ISR) of CERN in 1977. Even earlier observations were reported from a small proton storage ring at Novosibirsk. In 1989, a positron-beam instability at the Photon Factory (PF) in the High Energy Accelerator Research Organization (KEK), located in Japan, was attributed to the presence of an electron cloud.

A combination of processes leads to an electron-cloud build-up in the vacuum chamber of the LHC. Each passing bunch, formed by protons, radiates in the X-rays spectrum, generating a number of primary electrons on the boundaries of the beam pipe by the photoelectric effect. These electrons are accelerated by the beam field and upon impact on the boundaries of the vacuum chamber generate secondary electrons. If the energy of the electrons is sufficiently high the number of electrons after the impact becomes larger, and the number of electrons grows exponentially if there is a certain synchronicity between the motion of the electrons and the bunch passage periodicity. The electron growth stops when the electron density roughly equals the neutralization density, where the attractive force from the beam is, on average, balanced by the space-charge field of the electron cloud. A uniformly distributed electron cloud all inside the beam pipe can be responsible for bunch instabilities. Multi-bunch instabilities were first observed at the PF in KEK and are already widely investigated by means of computer simulations: if a bunch is sent through and offset with respect to the other bunches, it will perturb the electron-cloud distribution and the next bunch will receive an additional deflection caused by this perturbation, causing the malfunctioning of the accelerator. The electron cloud can also act similar to a short-range wake field and drive a single bunch instability.

Observations at the PF included an increased vertical beam size, coupled bunch oscillations, a low threshold current, a broad distributions of sidebands, and the inefficiency of a clearing gap. The main concern for the LHC

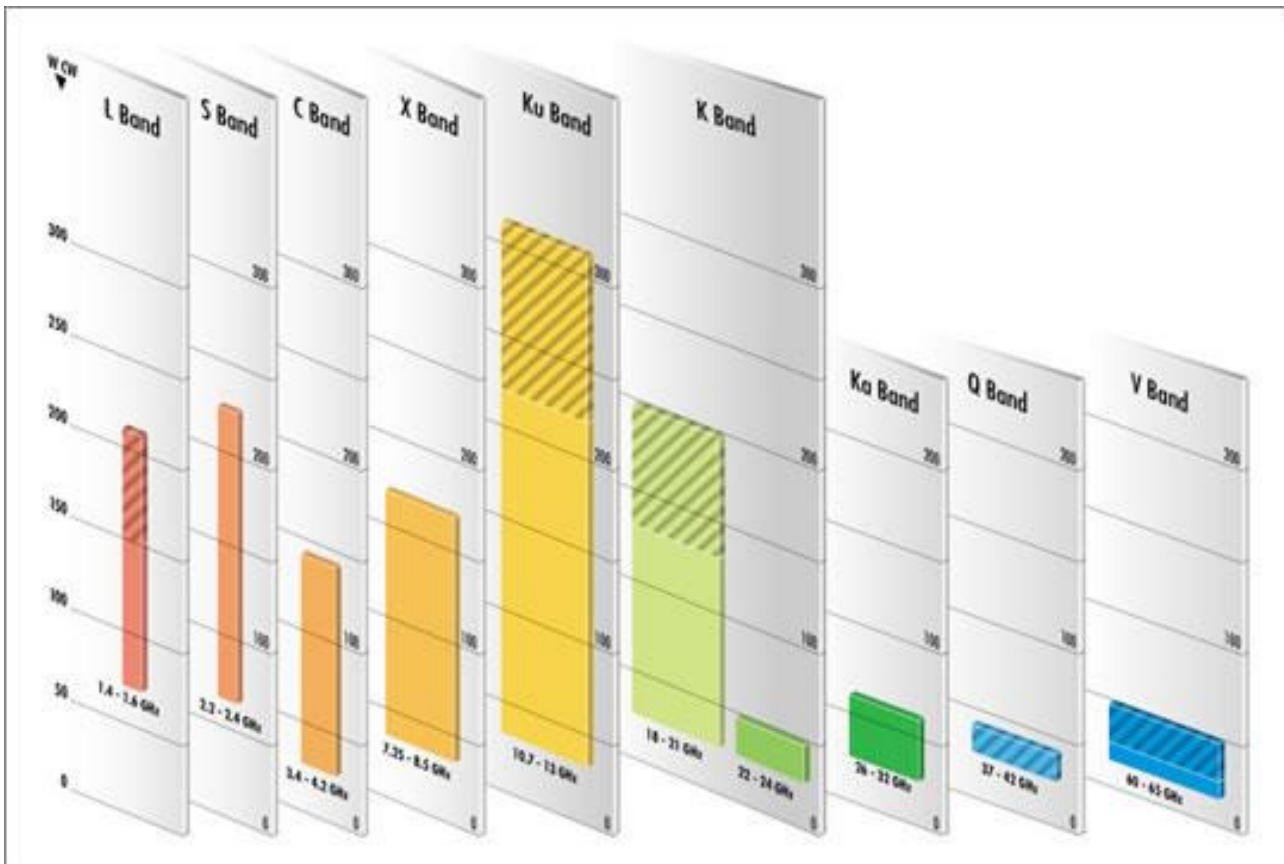


Figure 1.2: Scheme depicting the delivery working powers of the currently available Traveling Wave Tubes (TWT's) at different frequency bands¹.

¹Extracted from <http://www.thales-electron-devices.de/about.php?lang=en>

is the heat load on the cold vacuum chamber inside the super-conducting magnets, for which only limited cooling capacity is available. Since 1998, electron-cloud effects are seen with the LHC beam in the Super Proton Synchrotron (SPS), which has allowed the development of a suite of dedicated electron-cloud diagnostics and numerous beam studies. Electron-cloud effects have also been seen in the lower-energy Proton-Synchrotron (PS) and even in the PS-to-SPS transfer line.

Nevertheless, there is an important difference between the satellite (space) and the accelerator community: while in some particle accelerators the occurrence of multipactor, though being harmful, can be accepted and damaged components be exchanged for space applications the appearance of multipactor can result in a blackout between the spacecraft and the base station on the Earth, which can jeopardize the complete mission. Concerning the particular case of the LHC arc beam screens, the components exchange is practically impossible or not easy, but in space applications there is no way for doing it.

1.2 Corona overview

Corona discharge exhibits the lowest breakdown power threshold under medium-pressure-range conditions, which comprises the Ionosphere (60 to 800 km height). Although corona seems not to be a potential danger in satellite applications because the operating condition of a satellite is at very low pressures (much higher altitudes), the Telemetry, Tracking and Control system (TTC) is sometimes switched on during the launch of the satellite to check some parameters like the velocity or the position of the spacecraft. This phase of the launch is important to guarantee the success of the manoeuvre and it occurs in fact when the rocket traverses the upper part of the atmosphere, which corresponds to the Ionosphere (100 to 1000 km height) [ECSS 2000]. The presence of a big amount of electrons and the presence of a non-negligible pressure makes very high the risk of corona breakdown in the microwave range. In the case of reentry vehicles or during the exploration of planets and their moons, the presence of the planetary atmosphere implies the risk of corona breakdown, too.

The consequences of a corona discharge for antennas are the decrease of the transmitted signal intensity, the change in the input impedance and the radiation pattern, the modification of the pulse shape and noise modulation of the signal. Besides the increase of the return loss, the harmful effects of corona breakdown for filter-based waveguide technology and for coaxial connectors include a dramatic temperature rise due to the ohmic losses produced in the plasma that is formed, provoking the partial or total destruction of the onboard components.

The corona breakdown, also called gas discharge, is produced due to a locally rapid increase of the electron population because of the ionization of gas molecules trapped within gaps inside microwave devices. This discharge is produced when the RF field accelerates the environmental electrons and they impact against the gas molecules with enough energy as to ionize them, releasing new electrons. The electron growth within the gaps renders the gas conductive, loading the cavity formed by the gap and cutting off the signal transmission. In order to avoid the corona onset for in-orbit conditions, appropriated venting holes must ensure the evacuation of the remaining gas trapped during on-ground manufacturing and assembly of the microwave devices.

The mean free-path of a particle within a gas becomes longer as the gas pressure decreases, since the average number of collisions with the particles performing the gas also decreases. As mentioned before, corona breakdown is produced under medium-pressure conditions when the mean free-path of the electrons in the gas is not large enough as to permit the electrons to reach the walls of the devices. If the pressure is too low and the latter occurs, multipactor breakdown can arise by the release of secondary electrons on the boundaries of the microwave components. Nevertheless, both discharges can coexist at some pressure when the mean free-path

is of the order of the air gaps [Höhn 1997].

1.3 Multipactor overview

Multipactor is a vacuum Radio-Frequency (RF) discharge that can occur within the microwave components of telecommunication satellites [de Lara 2006] as well as in particle accelerator structures [Lyneis 1977] whose occurrence implies the possible failure of the system. The harsh space weather provides a large amount of free electrons in the satellite's environment that can penetrate into the high electric field region of microwave components as, for instance, within the gaps existing between cable-connector transitions, male-female interfaces or within waveguide-based components.

Unlike the corona breakdown, multipactor only occurs under ultra-high vacuum conditions (pressure $< 10^{-5}$ mBar). The effect of multipactor is the loading of the RF cavities, increasing the system noise level and the return loss, generating undesirable harmonics [Udiljak 2003] and creating a local augmentation of the temperature that may severely damage or destroy internal components, what would be fatal for the space mission. The multipactor breakdown also reduces the signal-to-noise ratio due to the absorption of the electromagnetic energy by the electrons, which are accelerated by the electromagnetic field. It has also been reported that a multipactor discharge may trigger the corona breakdown by a dramatic temperature rise and the subsequent increase of pressure due to a fast outgassing process [Woode 1989].

Accelerated by the microwave field, the electrons can collide with the walls of the components and, if the impact energy is high enough, release other electrons, called secondary electrons [Vaughan 1989]. The averaged number of released electrons per impacting one is called the secondary-electron-yield (SEY), which is characteristic of each material, and determines the multipactor power threshold. If the flight time of an electron launched from the initial plate traveling to the opposite one is an odd number of half periods of the RF signal, the secondary electrons released will see exactly the same conditions in reverse. If the resonant condition between the motion of the electrons and the RF signal is maintained and the SEY is higher than one when colliding with the plates, an electron avalanche builds up and multipactor breakdown arises.

The multipactor phenomenon is a research topic which is becoming important as the technical specifications of the satellites demand higher input powers into the waveguides that are commonly used for the devices on board of the satellites, as well as smaller dimensions to reduce the weight of the satellites launched into space. Furthermore, the need of reducing the dimensions of the microwave devices is due to the trend of using higher frequencies (see Fig. 1.2), in order to ensure that only the fundamental mode of the waveguide propagates, avoiding the appearance of higher order modes. The increase of the input power, as well as the decrease of the dimensions of the waveguides make the appearance of multipactor more likely to occur due to the increase of the electromagnetic energy density inside the devices.

However, finding a general solution to avoid the problem of multipactor discharge for any case, any geometry or any device is still nowadays a challenge. There is neither a unique nor a definitive model to predict the multipactor breakdown power threshold and a generally accepted criterion for the experimental detection of the multipactor onset does not exist yet.

1.4 Thesis scope

The lack of fully-tested softwares or models to assess the occurrence of multipactor and/or corona discharges results in high-cost test campaigns as well as long design periods to fabricate devices able to cope with power

handling capabilities demanded by the market. This is the reason for the increasing interest from the satellite industry to invest in the research area of multipactor and corona breakdown.

The lack of a unique criterion to assess the multipactor breakdown onset experimentally makes difficult the evaluation of high power withstanding capabilities of microwave devices. A multipactor discharge is known to radiate at higher frequencies than the one of the signal carrier. Measurements of the radiated power spectrum of the electron cloud, using the third harmonic detection technique [Udiljak 2007] (or other harmonics) [Sorolla 2008], can be compared with the predicted radiated power spectrum of a multipactor discharge following the proposed study. The comparison could establish, indeed, a unique criterion to assess the multipactor onset unambiguously.

The first part of this thesis intends to bring some insights analyzing the radiated power spectrum produced by a multipactor current and the steady-state or saturation stage of the discharge, since the electron population growth must reach a limit. The study of the multipactor radiation and of the saturation level of electron population are destined to help in the establishment of a criterion to assess experimentally the multipactor occurrence unambiguously. An algorithm to calculate a large number of roots of the cross-product of Bessel functions and of their derivatives is also developed in this thesis in order to speed up the calculation of the radiated power spectrum produced by a multipactor current within coaxial waveguides.

Concerning the corona breakdown it must be mentioned that there is not a unique model of ionization that could explain satisfactorily the experimental measurements. Another goal of this thesis is the analysis of the three mostly cited ionization models comparing the measurements of the corona breakdown power threshold presented in the literature with the results obtained with the numerical solution of the corona equation predicted. For this, a code that solves the corona equation is developed in this thesis using the Finite Elements method. It is shown that some models of ionization agree well with the measurements at certain pressures, but no satisfactory model has been found in the literature that could predict accurately the measurements of the corona power threshold in the whole pressure range.

Finally, within the framework of the thesis, the analysis of all these problems resulted in the design, manufacturing and experimental testing of a new SMA-like coaxial connector, capable of withstanding much higher input powers than similar devices of previous generations. The conception of this Power Sub-Miniature (PSM) connector has been developed during this thesis, giving rise to the appearance of a new coaxial connector whose power-handling capabilities are similar to the ones of a TNC, but with a considerable mass and size reduction.

1.5 Thesis outline

It is always useful to start the analysis of multipactor with the parallel-plate geometry, where the electric field of the fundamental mode, Transverse Electromagnetic (TEM) mode, is constant along the space between the plates. This fact simplifies enormously the study of the multipactor discharge since, in this case, the motion of an electron can be calculated analytically. The study of multipactor under the parallel-plate approximation can be useful for some devices when one of the dimensions is much larger than the others; for example, within rectangular waveguides, where the height is much smaller than the width, or within the irises of corrugated filters where the electric field is homogeneous far from the borders.

In the manufacturing process of more complex devices like in coaxial connectors, small gaps may appear due to mechanical tolerances like, for instance, in the male-female interface or in the cable-entry of the connector. If the gaps are small enough, the electric field profile is quite homogeneous and the multipactor withstanding capabilities of the device can also be studied applying the parallel-plate model. The analysis of

the multipactor discharge for parallel-plate geometries is studied in Chapter 2, which will be useful to understand the analysis of small gaps where the electric field can be approximated by a homogeneous profile in the development of the design of the PSM.

In Chapter 3 a simple and novel model to evaluate analytically the radiated power spectrum of a multipactor discharge within a parallel-plate waveguide is presented. In a first approach, the discharge is modeled as a uniform electric current radiating inside an infinite parallel-plate waveguide region, the far electric and magnetic fields are calculated and analytical integration of the Poynting vector associated to the radiated fields for each harmonic of the current is found. The results are compared with the ones obtained when using the general frequency domain Green function of the problem applying the image series approach, showing an excellent agreement between the results obtained with both methods.

In order to detect the presence of multipactor some experimental methods have been proposed in the literature, like the third harmonic detection technique [Udijak 2003], which proposes the search of the third harmonic of the radiated power spectrum of the electron cloud current to witness the presence of the discharge. As it will be shown in Chapter 3, the intensity of the radiated power spectrum depends on the number of electrons involved in the discharge, and the detection is supposed to take place when the saturation is reached. Therefore, the saturation stage of multipactor is considered of interest since it can guide towards a criterion to assess the breakdown onset. In Chapter 5 the equations of motion of the electron cloud formed by the discharge are calculated taking into account the space charge effects. The saturation is identified by the interaction of the electron cloud with its image charge through the plates. The stability of the electron population growth is analyzed and two mechanisms of saturation to explain the steady-state multipactor for voltages near above the threshold onset are identified. It will be shown that the impact energy in the collision against the metal plates decreases during the electron population growth due to the attraction of the electron sheet by the image through the initial plate. When this growth remains stable till the impact energy reaches the first cross-over point the electron surface density tends to a constant value. When the stability is broken before reaching the first cross-over point the surface charge density oscillates chaotically bounded within a certain range. In this case, an expression to calculate the maximum electron surface charge density is found whose predictions agree with the simulations when the voltage is not too high.

In Chapter 4 a very efficient globally convergent algorithm to calculate the roots of the cross-product of Bessel functions and of their derivatives is developed. The numerical calculation of these roots is needed when finding the radiated power spectrum of a multipactor discharge within a coaxial line, therefore a robust algorithm to find these roots will accelerate noticeably the evaluation of the radiated power produced by a multipactor current for coaxial geometries.

The comparison of three ionization rate models found in the literature will be analyzed in Chapter 6 in the light of the simulations of the corona breakdown power threshold obtained for different microwave devices. Initially, the corona withstanding capabilities of a parallel-plate waveguide are studied; later on, the rectangular, circular and coaxial waveguides are analyzed with the Finite Elements code developed; and finally, the corona breakdown power of a rectangular cavity and a monopole antenna are presented. The simulations have been obtained in every case with the three different ionization models, showing noticeable discrepancies between them, due to the highly nonlinear character of the corona equation.

Finally, within the framework of the ESA contract No. 20967/07/NL/GLC “High power SMA connector”, Chapter 7 shows the steps followed in the development of the PSM connector, which has potential applications in space telecom missions because of their light weight, small size and high power withstanding capabilities. The analysis of multipactor and corona breakdown of the connector will be presented together with the steps followed during the design of the PSM for the optimization of its microwave breakdown withstanding capabil-

ities. The experimental values of the corona and multipactor power threshold will be shown and its comparison with the predictions will be analyzed. The result was the manufacturing of a coaxial connector approximately 50% lighter than the TNC but with similar high power withstanding capabilities.

1.6 Original contributions

The primary original contributions developed in this thesis are summarized in what follows.

- **Chapter 2, Section 2.5**, together with the analysis depicted in **Appendix A** show the general conditions under which the returning of an electron to the initial plate for multipactor breakdown within a parallel-plate waveguide is produced.
- **Chapter 3** shows an analytical formula to predict the radiated power spectrum produced by a multipactor discharge within a parallel-plate waveguide for the “effective electron” model, i.e., without taking into account space charge effects.
- **Chapter 4** describes a globally convergent algorithm that calculates a large number of roots of the cross-product of Bessel functions and of their derivatives. This algorithm can accelerate noticeably the calculation of the radiated power spectrum produced by a multipactor discharge within a coaxial waveguide.
- **Chapter 5** solves the equations of motion of a multipactor electron cloud in a parallel-plate waveguide for the mono-energetic model (Sombrin’s model) taking into account space charge effects. For the first time, multipactor steady-state is predicted by the analytical equations of motion of the electron cloud by its interaction with the image charge through the plates. The mechanisms of multipactor saturation are described and an analytical expression for the maximum surface charge density for one of the mechanisms is presented.
- **Chapter 6** the comparison of the corona power threshold obtained with different ionization rate models is shown. The corona breakdown is solved with an in-house Finite Elements code, showing noticeable discrepancies between the results obtained with the different ionization models and comparing the predictions with measurements when it was possible.

Chapter 7 shows the steps followed in the design of a new high power SMA-like coaxial connector, the Power Sub-miniature (PSM) connector. The PSM has been manufactured and tested, exhibiting excellent high power withstanding capabilities and with similar dimensions as the SMA connector.

1.7 Acknowledgments

The author wishes to acknowledge European Space Agency for partial support of this thesis developed within the framework of the ESA contract No. 20967/07/NL/GLC “High power SMA connector”.

The author also wishes to acknowledge the Swiss National Science Foundation for partial support of this thesis developed under the SNSF contract No. 200021_129661 “Modeling microwave-electron interaction in the LHC beam pipe”.

Multipactor breakdown

Contents

2.1	Introduction	11
2.2	Classical multipactor resonance conditions	11
2.3	Positive relative impact velocity condition	22
2.4	Stability condition	26
2.5	Returning condition	30
2.6	Multipactor susceptibility chart	35
2.7	Summary	40

2.1 Introduction

The first studies about electrical discharges at high frequencies and low pressures were made by Camille and Henri Gutton (father and son) and published in 1928 [Gutton 1928]. However, the origin of the name multipactor dates back to the first works made by Philo Taylor Farnsworth where the author developed a discharge tube to reproduce images taking advantage of the produced electronic avalanche leading to the advent of the future television [Farnsworth 1934]. Nowadays the opposite is searched, that is to say, to avoid the avalanche to prevent the harmful consequences that the discharge creates in the electromagnetic devices on board of space satellites.

In this chapter the multipactor susceptibility chart for the classical resonance theory is going to be calculated for a parallel-plate waveguide at a given frequency, f , gap distance between plates, d , and applied voltage, V_{RF} . To do so we need to study the conditions under which multipactor can occur. Basically, we will see that two conditions must be satisfied: the resonant condition that predicts the synchronization between the motion of the electrons and the phase change of the RF field, and the impact energy against the plates being able to release a bigger number of electrons than originally, named secondary electrons.

2.2 Classical multipactor resonance conditions

The Multipactor phenomenon can be described as an electron avalanche whose electrons resonate with the electromagnetic field propagating through the waveguide. To describe the process in the parallel-plate waveguide we can imagine an initial electron leaving one of the plates with initial velocity v_0 . This may occur, for instance, due to the impact of some electron -coming from the outer space that may traverse one of the walls of the waveguide- against the considered plate releasing a primary electron. The electron coming from the outer space traversing the walls of the device can be considered as a primary electron as well.

When the primary electron is accelerated towards the opposite plate by the electric field, one or more secondary electrons may be released if the primary electron reaches the opposite plate with a kinetic energy above a threshold value called first cross-over point, which will be described later. The released secondary electrons can act later as primary electrons, too, being potentially able to release other secondary electrons on the plate that the primary electron left. This will only happen if the electric field has different polarity, but the same value, with respect to the one it had when the primary electrons left the plate, just in the instant when the secondary electrons are released. If this occurs, a self-sustained process is maintained and every secondary electron is released just when the electric field inverts its polarity, producing an exponential growth of the electron population causing the multipactor discharge. In Fig. 2.1 the motion of the electrons that leads to the multipactor onset is shown for a special case where the amount of electrons released by secondary emission is exactly two per impacting electron. Note that, as the electron has negative charge, the first electron accelerates towards the opposite plate when the electric field is negative. There is a short period of time in the beginning of the motion for which the electric field is positive, but the initial velocity of the electron makes the continuous traveling towards the top plate possible. The electron collides against the plate and two other electrons are released by the impact that travel, in turn, towards the initial plate with the same initial velocity as the first electron. Both secondary electrons impact against the bottom plate and four secondary electrons are released, and so on. Observe that the phase of the electric field when the secondary electrons are released is exactly π -shifted with respect to the previous collision.

It must be mentioned that other kind of resonances can occur like, for instance, let us imagine many primary electrons returning to the initial plate entailing usually a low impact energy with the subsequent decrease of the electron population. If the remaining electrons impact against the opposite plate with such an energy that the SEY compensates the decrease of the electron population of the first impact, multipactor can also occur when the product of both SEY is larger than unity. Moreover, the polarity of the electric field when the remaining electrons after the first impact reach the opposite plate must be the same in reverse as when the primary electrons were launched [Kishek 2012], like in the classical multipactor resonance. Another type of resonance occurs when the two-way transit time of the electrons, traveling between the plates, is an integer number of RF periods, not necessarily implying the same time for the primary electron to reach the opposite plate as for the secondary traveling in the opposite direction to reach the initial one. The most general case of resonance in case that their flight times are different is named complex modes [Buyanova 2006] where two particular cases were studied previously [Gilardini 1992, Kryazhev 2002] named hybrid and polyphase resonances. The rigorous study of these kind of resonances would extend enormously the discussion of the different conditions that may lead to a multipactor discharge, which is out of the scope of this chapter, but it must be remarked that the discrepancies between simulations and measurements that have been observed along the multipactor analysis development have been explained by the presence of the complex modes, as it will be commented at the end of this chapter.

In order to study the classical multipactor resonance for parallel-plate geometries we firstly assume that only the fundamental mode of the waveguide is going to be excited (TEM). Secondly, we assume the motion of the electron to be in one dimension, that is to say, we neglect the magnetic field and consider the motion of the electron along the z axis which crosses perpendicularly both plates, separated by a distance d . The voltage applied between the plates, V_{RF} , leads to an electric field which is constant along the z -axis and equal the voltage divided by the distance, d , (see Fig. 2.2).

We are going to assume that the time between the instant when the primary electron impacts against one plate and the instant when the secondary electrons are released can be neglected. This can be justified taking into account that the real time in the releasing process is around five orders of magnitude smaller than the period of the RF signal. Nevertheless, the growth of the electron population in the waveguides produced by multipactor

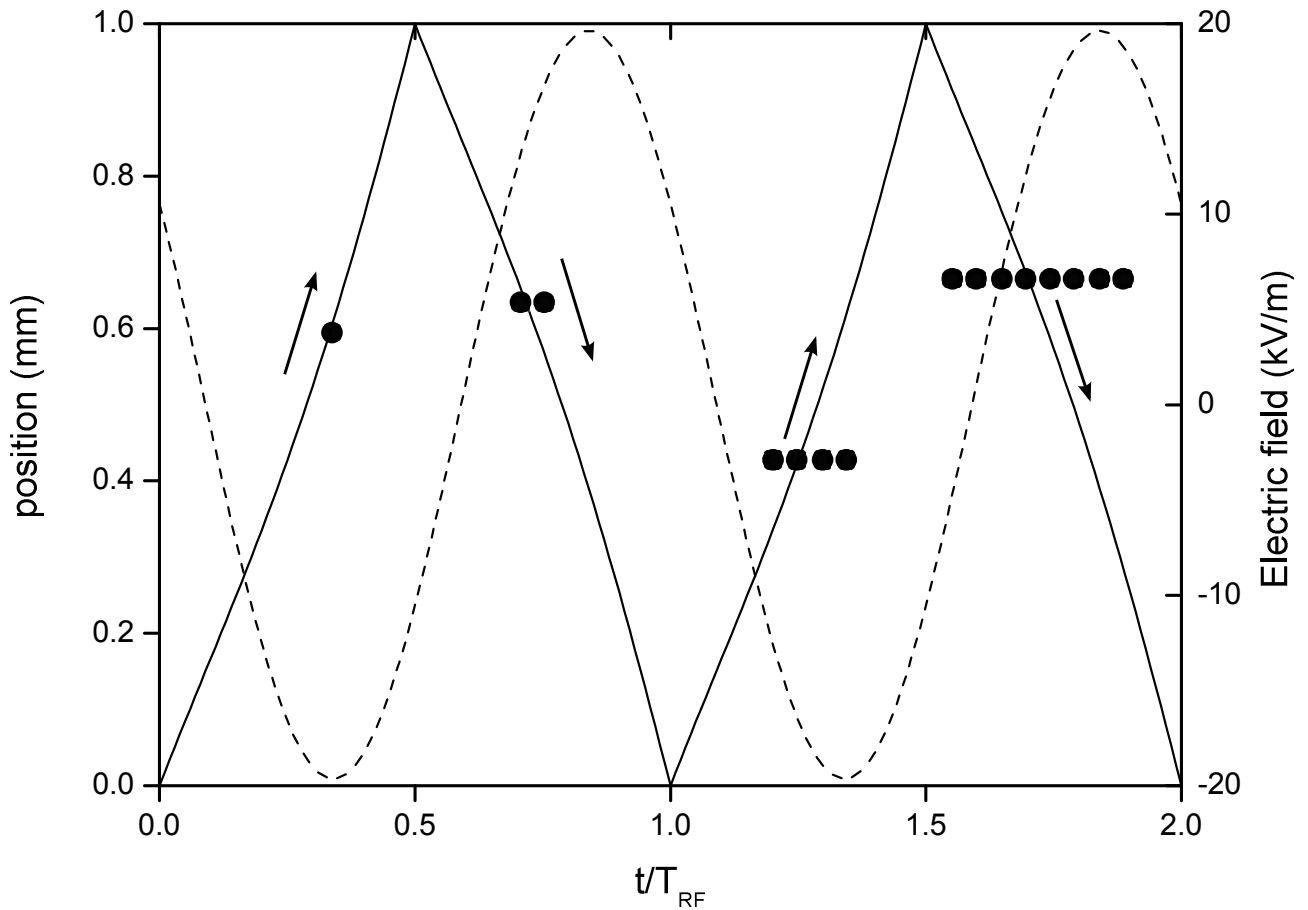


Figure 2.1: Example of the upcoming multipactor discharge for a parallel-plate waveguide represented by the position of the electron (solid) and the electric field (dashed) vs. the time normalized to the RF period of the signal. The initial velocity is $v_0 \simeq 1.73 \cdot 10^6$ m/s and the voltage $V_{RF} = 19.64$ V. The phase of the electric field when the electron leaves the initial plate is $\alpha = 1.00388$ rad.

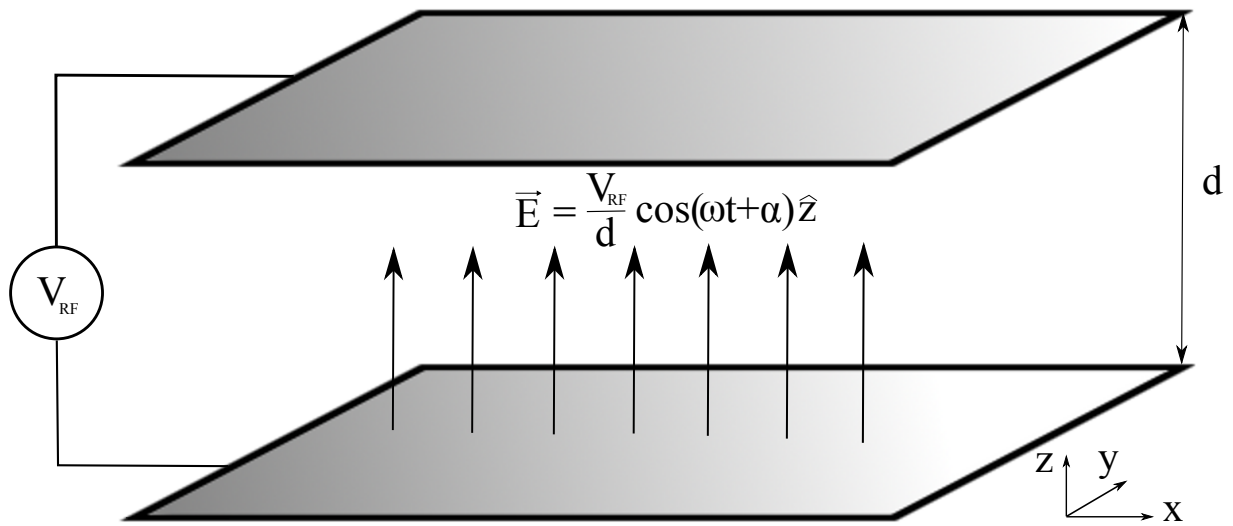


Figure 2.2: The electric field of the fundamental mode of an unbounded parallel-plate waveguide is uniform across the gap between the plates.

is noticeable in a few periods what justifies this approximation. To guarantee the existence of the resonance condition along time, the stability of the resonance is going to be analyzed later in order to see whether a small delay in the transit from the instant when the primary electron impacts against the plate and the one when the secondaries are released, affects the resonance condition or not. However, we will leave this point for the end.

If we neglect the presence of the magnetic field and we write the electric field as $\mathbf{E} = \frac{V_{RF}}{d} \cos(\omega t) \hat{\mathbf{z}}$ in the region between plates, where $\omega = 2\pi f$ is the angular frequency of the RF field, we can write the Lorentz equation to find the acceleration that the particle is subject to as follows:

$$m_e \mathbf{a} = -e \mathbf{E}$$

where m_e and $-e$ are the mass and the charge of the electron, respectively. The equation of motion of the electron along the z-axis is, thus:

$$\mathbf{a} = \frac{-e V_{RF}}{m_e d} \cos(\omega t) \hat{\mathbf{z}}. \quad (2.1)$$

In order to find the dependency of the velocity, v_z , and the position of the electron, $z'(t)$, on time within the parallel-plate waveguide we must set the initial conditions. If we call t_α the instant when the electron leaves the plate on the bottom, placed at $z' = 0$, ωt_α is the phase of the electric field at that instant. If we assume that the electron leaves the bottom plate with velocity v_0 the following initial conditions apply:

$$\begin{aligned} \alpha &= \omega t_\alpha \\ \dot{z}'(t_\alpha) &\equiv v_z(t_\alpha) = v_0 \\ z'(t_\alpha) &\equiv z'_0 = 0 \end{aligned}$$

where α represents the phase of the electric field when the electron leaves the initial plate towards the opposite. Thus, velocity and position can be written as follows:

$$v_z(t) = v_0 + \frac{e V_{RF}}{m_e \omega d} (\sin \alpha - \sin \omega t), \quad (2.2a)$$

$$z'(t) = \frac{v_0}{\omega} (\omega t - \alpha) + \frac{e V_{RF}}{m_e \omega^2 d} (\cos \omega t - \cos \alpha + (\omega t - \alpha) \sin \alpha). \quad (2.2b)$$

As it will be explained later, it is natural to refer to the velocity of an electron by its corresponding kinetic energy, usually defined in eV (electron-volt). An electron-volt is the electron charge times one Joule ($1 \text{ eV} = 1.6 \cdot 10^{-19} \text{ J}$). Therefore, the relation between “velocity” (energy) in eV and velocity in (m/s) is the following:

$$v [\text{eV}] = \frac{1}{2e} m_e v^2 [\text{m/s}].$$

Equations of motion (2.2a) and (2.2b) represent the position and velocity of a single electron with respect to time. Therefore, the study that follows to know whether multipactor may occur is based on what has been called the “effective electron” model, where the equation of motion of a single electron does not take into account the effect of the charge of the rest of electrons within the parallel-plate waveguide on it. The space charge effects will be considered in Chapter 5, where a more realistic equation of motion for the electrons will be found by taking into account the influence of the charge density of the electron cloud on its motion.

As it was explained in the introduction, one of the conditions that must apply for multipactor to occur is the synchronicity between the motion of the electrons and the phase evolution of the RF field in the waveguide. For the classical resonance theory the electrons leaving the initial plate have to arrive to the opposite one just

when the RF field has the same value but opposite sign with respect to the one when they abandoned the first plate. This guarantees that all the secondary electrons are released with the same initial conditions from any plate and the electron avalanche is developed.

To express mathematically this resonance condition we set the instant t_i of the impact against the opposite plate to be such that the following expression is satisfied:

$$\omega t_i = \alpha + N\pi, \quad (2.3)$$

where N is an integer number that represents the number of half-cycles passed since the electron leaves the initial plate till it reaches the opposite plate, and it is named order of multipactor. In Fig. 2.3 several examples for the trajectories of an electron for different orders of multipactor are shown starting from t_α . Note that N is an odd integer for the phase of the electric field when the electron reaches the opposite plate to be $N\pi$ -shifted with respect to that one when the electron left the plate. Note also that the total time for the electron to reach the opposite plate and return to the initial one is N times the RF period of the signal.

If we apply the resonant condition to (2.2b) setting d as the position of the electron at the instant of impact, then we get

$$d = \frac{N\pi v_0}{\omega} + \frac{eV_{RF}}{m_e\omega^2 d} [N\pi \sin \alpha - 2 \cos \alpha]. \quad (2.4)$$

Thus, we can isolate the phase of resonance as function of the frequency, distance and RF voltage applying the property

$$a \sin x + b \cos x = \sqrt{a^2 + b^2} \sin(x + \lambda)$$

where

$$\lambda = \arctan\left(\frac{b}{a}\right) + \begin{cases} 0 & \text{if } a \geq 0, \\ \pi & \text{if } a < 0. \end{cases}$$

Therefore, the phase of resonance can be considered as function of v_0 and V_{RF} , and be written as follows:

$$\alpha_{res}^{(1)}(v_0, V_{RF}) = -\lambda + \arcsin\left\{\frac{m_e\omega d}{eV_{RF}R}(\omega d - N\pi v_0)\right\} \quad (2.6a)$$

$$\alpha_{res}^{(2)}(v_0, V_{RF}) = (\pi - \lambda) - \arcsin\left\{\frac{m_e\omega d}{eV_{RF}R}(\omega d - N\pi v_0)\right\} \quad (2.6b)$$

where $R = \sqrt{(N\pi)^2 + 4}$ and $\lambda = -\arctan\left(\frac{2}{N\pi}\right)$.

The two solutions correspond to the first branch $\left(\left[\alpha_{res}^{(1)} + \lambda\right] \in [-\pi/2, \pi/2]\right)$ and the second branch $\left(\left[\alpha_{res}^{(2)} + \lambda\right] \in [\pi/2, 3\pi/2]\right)$ of the arcsin function, respectively. It must be remarked that the condition applied to find these phases only represents part of the actual resonance condition since two cases may arise that do not represent the condition that we are searching. Namely, in Fig. 2.4 the motion of an electron is shown for two different phases of resonance that, although they predict impact against the opposite plate at $t_i = \frac{\alpha + \pi}{\omega}$, they imply impacts against the opposite or the initial plate prior to the expected instant. Therefore, the study of the electron returning to the initial plate or impacting against the opposite plate prior to the requested instant will be studied later.

For the moment, let us assume that these two cases will arise under exceptional conditions and let us study the second condition for multipactor to occur: The impact energy of the electron against the opposite plate must be high enough as to release some electrons in the collision (secondary electrons). It is known that every

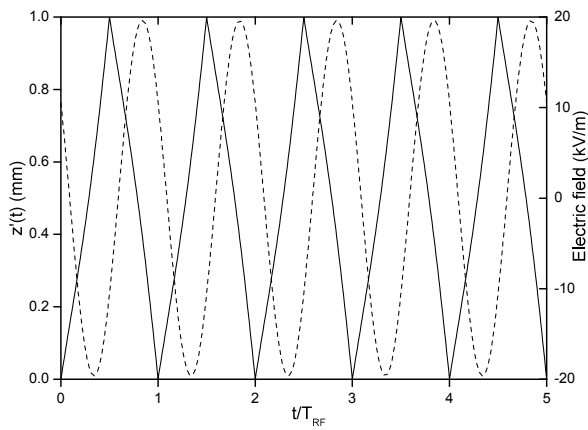
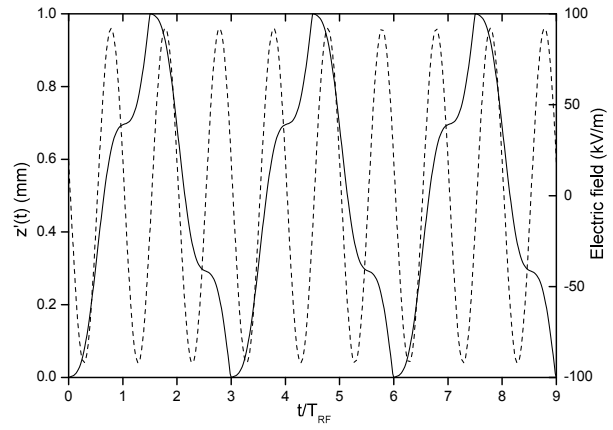
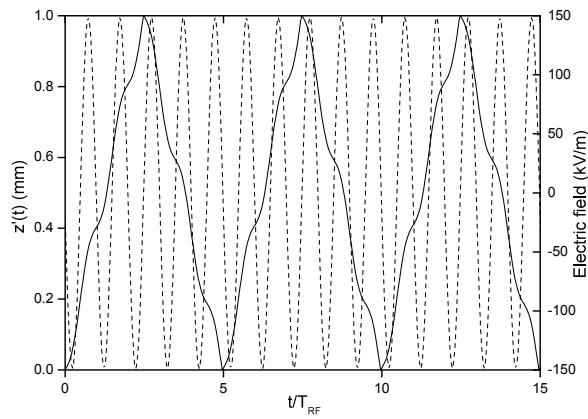
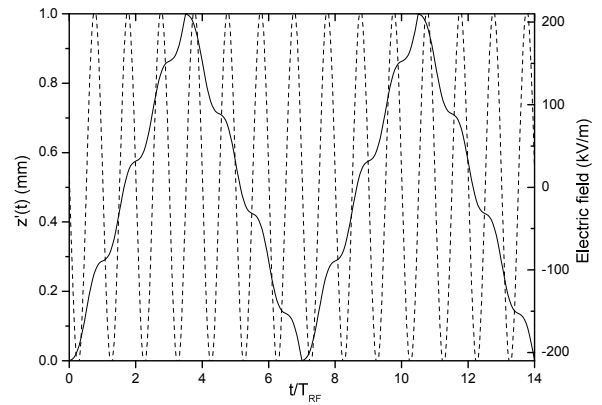
(a) $N = 1, f = 1$ GHz.(b) $N = 3, f = 2$ GHz.(c) $N = 5, f = 4$ GHz.(d) $N = 7, f = 5$ GHz.

Figure 2.3: Position of the electron (solid line) and electric field (dashed line) vs. time over RF period in a parallel-plate waveguide ($d = 1$ mm).

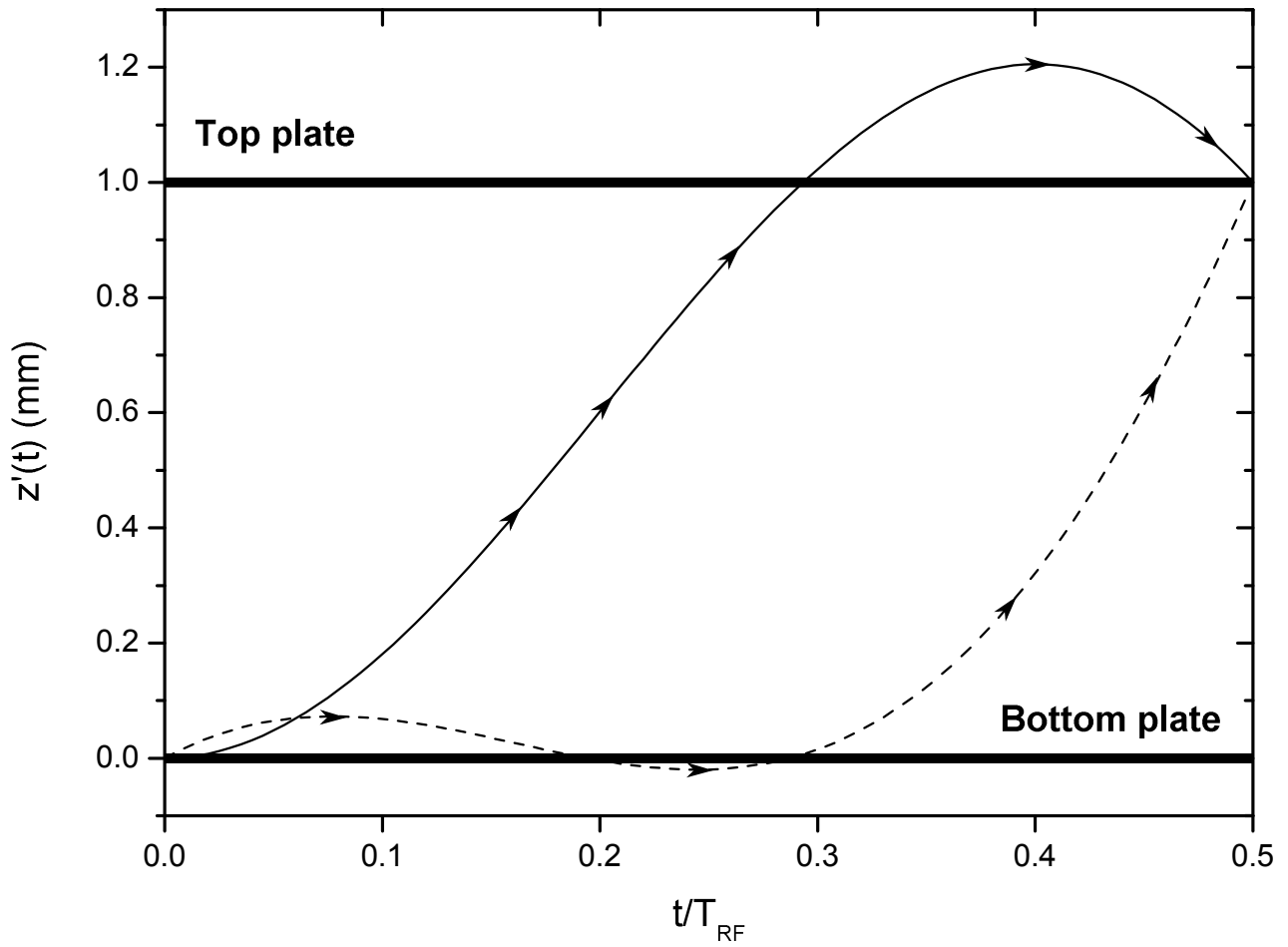


Figure 2.4: Theoretical trajectory of an electron for $d = 1$ mm and $f = 0.5$ GHz if the plates did not exist. The solid line is obtained with $v_0 = 0$ eV and $V_{RF} = 60$ V, ($\alpha = 3.45429$ rad) and the dashed line with $v_0 = 3$ eV and $V_{RF} = 55$ V, ($\alpha = 0.55963$ rad).

material, regardless whether it is dielectric or metal, presents a secondary electron yield (SEY) that defines the mean number of emitted secondary electrons per primary impacting electron as function of the impact energy and the impact angle with respect to the surface normal at the impact point.

There exist two interesting points associated to the SEY curve corresponding to the beginning and the end of the range of energies for which the secondary electron yield is above the unity. These points are respectively named first and second cross-over point, E_1 and E_2 . The SEY curve presents an universal shape for every material although the measurements at very high energies seem to differ from this shape [Dekker 1957]. Measuring both cross-over points, the maximum SEY and the impact energy of the primary electrons for which the yield is maximum, allows us to describe the secondary electron emission properties of any material. Other attempts to describe the secondary emission properties at higher energies have been made where more parameters are needed [Furman 2003]. In any case, the low energy range is the most interesting region of the SEY since the multipactor breakdown threshold occurs at the low impact energy region of the SEY and this is the critical value that limits the maximum input power that the microwave device can withstand ensuring no risk of multipactor discharge. The SEY curve of a sample of Gold has been obtained with the measurements of the SEY parameters and is represented in Fig. 2.5 using Vaughan's development [Vaughan 1989]. The author establishes the dependency of the SEY curve on the angle of incidence via an empirical factor, k_s , which stands for the smoothness of the surface of the material and that ranges from 0 to 2. A value of $k_s = 1.5$ has been chosen in the presented plot of the SEY curve for the sample of Gold.

It must be mentioned that the SEY curve is found by fitting the experimental values like the first and second cross-over points together with the impact energy for which the SEY is maximum and its value, in three regions of the spectrum of the collision energy ensuring the continuity of the function at the interface of the different zones. However, the semi-empirical approach presented in [Vaughan 1989] does not ensure the continuity of the first derivative of the secondary electron yield function at the bounds of all the regions. This is the reason why the SEY curve for the normal impact angle shown in Fig. 2.5 exhibits a non-differentiable point

Thus, the electron avalanche may occur, together with the resonant condition, if the impact energy of the electrons belong to the interval between the points E_1 and E_2 . The cross-over points are often expressed in eV, this is the reason why the velocity is usually represented by the corresponding kinetic energy of an electron as it was explained before.

Therefore, the second condition to be considered is the electron impact energy together with the resonance condition (2.3) to know whether multipactor can occur. Let us name v_1 the velocity associated to the first cross-over point of a material subject to the impact of electrons and v_i the impact velocity of the electron on the metal plates. We can insert the resonance condition and v_i into (2.2a) to write:

$$v_i = v_0 + \frac{2eV_{RF}}{m_e\omega d} \sin \left\{ \alpha_{res}^{(a)}(v_0, V_{RF}) \right\}, \quad (a) = 1, 2. \quad (2.7)$$

As the values of the initial velocity, v_0 , are typically smaller than the impact velocity, v_i , we can avoid cases as the one represented by the solid line in Fig. 2.4 restricting the search of the phases of resonance to the interval $\alpha_{res}^{(a)} \in [0, \pi]$ in order to ensure that $\sin \alpha_{res}^{(a)} > 0$ and therefore, $v_i > v_0$, in (2.7).

Inserting (2.6) into (2.7) we obtain:

$$v_i = v_0 + 2v_\omega \sin \left(\arcsin \left[\frac{(\omega d - N\pi v_0)}{v_\omega R} \right] - \lambda \right) \quad (2.8a)$$

$$v_i = v_0 + 2v_\omega \sin \left((\pi - \lambda) - \arcsin \left[\frac{(\omega d - N\pi v_0)}{v_\omega R} \right] \right) \quad (2.8b)$$

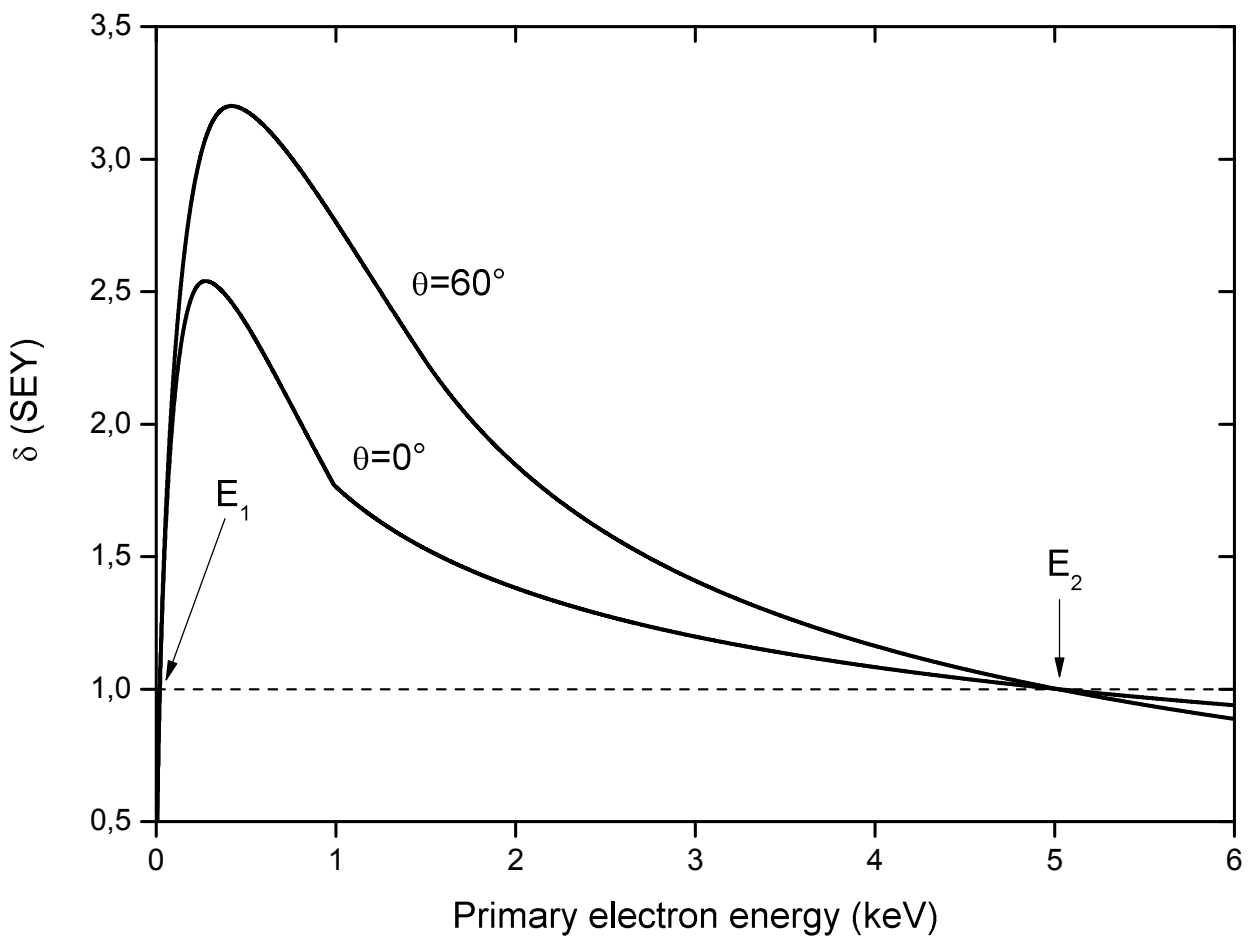


Figure 2.5: SEY curve obtained for two different angles of incidence. The parameters of the curve are $E_1 = 20$ eV, $E_2 = 5016$ eV, $E_{max} = 275$ eV, $\delta_{max} = 2.54$.

for $\alpha_{res}^{(1)}$ and $\alpha_{res}^{(2)}$, respectively, where

$$v_\omega \equiv \frac{eV_{RF}}{m_e\omega d}. \quad (2.9)$$

If we use the trigonometric relations

$$\begin{aligned} \sin(\eta \pm \mu) &= \sin \eta \cos \mu \pm \cos \eta \sin \mu \\ \cos(\arcsin x) &= \sqrt{1 - x^2} \end{aligned}$$

the expressions (2.8) boil down to

$$(v_i - v_0) = 2v_\omega \Delta^\pm \quad (2.10)$$

where \pm corresponds to $\alpha_{res}^{(1)}$, respectively, and

$$\Delta^\pm = \left[\frac{(\omega d - N\pi v_0)}{v_\omega R} \cos \lambda \pm |\sin \lambda| \sqrt{1 - \left(\frac{(\omega d - N\pi v_0)}{v_\omega R} \right)^2} \right],$$

where it has been used $\sin \lambda < 0$, since $\lambda \in [-\pi/2, 0]$.

Although (2.10) may be used for general purposes, we are mainly interested in cases where the initial velocity is smaller than the impact velocity. Therefore, taking into account that $v_\omega > 0$ and $\cos \lambda > 0$, we can find the phase of resonance that must be applying depending on the sign of Δ^\pm in order to ensure that the LHS of (2.10) is positive. Let us rewrite (2.10) as follows:

$$\frac{R}{2}(v_i - v_0) - (\omega d - N\pi v_0) \cos \lambda = \pm |\sin \lambda| \sqrt{(v_\omega R)^2 - (\omega d - N\pi v_0)^2}. \quad (2.11)$$

Besides the sign \pm the RHS is strictly positive, therefore, the phase of resonance corresponds to $\alpha_{res}^{(1)}$ when the LHS is positive and to $\alpha_{res}^{(2)}$ when it is negative. The condition to know which phase of resonance applies can be further developed considering the trigonometric properties:

$$\begin{aligned} \cos(\arctan x) &= \frac{1}{\sqrt{1 + x^2}}, \quad x \in [0, \infty) \\ \sin(\arctan x) &= \frac{x}{\sqrt{1 + x^2}}, \quad x \in [0, \infty) \end{aligned}$$

which allows us to write $\cos \lambda = \frac{N\pi}{R}$ and $\sin \lambda = \frac{-2}{R}$. Finding the value of ωd that defines the change of sign of (2.11) allows us to define the phase of resonance according to the sign of Δ^\pm :

$$\begin{cases} \alpha_{res}^{(1)} & \text{if } 0 \leq (fd) \leq v_N \\ \alpha_{res}^{(2)} & \text{if } (fd) \geq v_N \end{cases} \quad (2.12a)$$

$$(2.12b)$$

where

$$v_N = \frac{R^2 v_i + D^2 v_0}{4\pi^2 N}.$$

and $D = \sqrt{(N\pi)^2 - 4}$.

Coming back to (2.10) we can isolate V_{RF} and write the multipactor breakdown voltage as function of the order of multipactor, N , the initial velocity, v_0 , the impact velocity, v_i , and the frequency-gap product fd :

$$\begin{aligned} V_{RF}(v_0; v_i, \omega d, N) &= \\ &= \frac{m_e \omega d}{2e} \sqrt{\frac{R^2}{4}(v_i - v_0)^2 + (\omega d - N\pi v_0)^2 - N\pi(v_i - v_0)(\omega d - N\pi v_0)} \end{aligned} \quad (2.13)$$

provided that the factor inside the square root is positive, what implies that the phase of resonance is real-valued. To ensure this, the absolute value of the argument of arcsin in (2.6) must be lower than one, what is equivalent to write:

$$\left\{ \begin{array}{ll} 0 \leq \frac{(\omega d - N\pi v_0)}{v_\omega R} \leq 1 & \text{if } (fd) \geq \frac{N}{2}v_0 \\ 0 \geq \frac{(\omega d - N\pi v_0)}{v_\omega R} \geq -1 & \text{if } (fd) \leq \frac{N}{2}v_0. \end{array} \right.$$

These two inequalities define the values of the RF voltage, V_{RF} , for which the phase of resonance is real-valued as function of the fd product. It can be proved that both conditions are equivalent to the following one:

$$V_{RF} \geq \frac{m_e \omega d |\omega d - N\pi v_0|}{eR}. \quad (2.14)$$

2.3 Positive relative impact velocity condition

If we call $(v_i - v_0)$ relative impact velocity, we must ensure that this quantity is positive in order to avoid the consideration of an impact against the top plate at the instant provided by the resonance condition (2.3) entailing a negative velocity. This would imply an impact like the one represented by the solid line in Fig. 2.4 or a collision energy lower than v_0 , which, in practice, is lower than the first cross-over point [Semenov 2005], and none of these cases is of our interest for the study of multipactor. This condition is equivalent to impose that $\sin \alpha_{res}^{(a)} > 0$ (see (2.8)), what can be rewritten as follows:

$$\begin{aligned} \alpha_{res}^{(1)} : \quad & 0 \leq \arcsin \left\{ \frac{m_e \omega d}{eV_{RF}R} (\omega d - N\pi v_0) \right\} - \lambda \leq \frac{\pi}{2} \\ \alpha_{res}^{(2)} : \quad & \frac{\pi}{2} \leq (\pi - \lambda) - \arcsin \left\{ \frac{m_e \omega d}{eV_{RF}R} (\omega d - N\pi v_0) \right\} \leq \pi. \end{aligned}$$

In order to find the RF voltage that satisfies the conditions above, we have to recall (2.12) and be careful with the phase of resonance that applies depending on the value of the frequency-gap product taking into account that $v_N > N/2 \cdot v_0$. It can be proved that the above conditions are equivalent to

$$V_{RF} \geq \frac{m_e \omega d |\omega d - N\pi v_0|}{2e} \quad \text{if } (fd) \leq \frac{N}{2}v_0, \quad (2.15a)$$

$$V_{RF} \geq \frac{m_e \omega d (\omega d - N\pi v_0)}{eN\pi} \quad \text{if } v_N \geq (fd) \geq \frac{N}{2}v_0, \quad (2.15b)$$

$$\frac{m_e \omega d (\omega d - N\pi v_0)}{2e} \geq V_{RF} \geq \frac{m_e \omega d (\omega d - N\pi v_0)}{eN\pi} \quad \text{if } (fd) \geq v_N. \quad (2.15c)$$

To plot the multipactor breakdown curves taking into account the restriction that the relative velocity at the instant of impact must be positive, the calculation of the boundaries of the fd product is needed. Inserting (2.13) into (2.15), the values of the frequency-gap product for which the phase of resonance does not imply neither an impact against the opposite plate prior to the expected one, nor an impact energy lower than the initial one, can be expressed as follows:

$$0 \leq fd \leq \frac{N}{4}(v_i + v_0) \quad (2.16a)$$

$$\tilde{v}_N \leq fd \quad (2.16b)$$

where

$$\tilde{v}_N = \frac{N \left(R^2 v_i + (D^2 - 8) v_0 \right)}{4D^2}.$$

Fig. 2.6 shows the gap in the fd product for which the multipactor breakdown curves at each impact energy does not respect that the relative velocity at impact time must be positive, represented by the dashed region, which becomes larger as the impact energy increases. Considering the results obtained in (2.14) together with (2.15), and given the initial and impact velocities and the order of multipactor, the domain of validity for the RF voltage can be plotted vs. the frequency-gap product as in Fig. 2.7. The white region represents the values of V_{RF} and fd for which the phase of resonance is not real-valued, in contrast with the dashed and gray zones, which show the areas where the sinus of the phase of resonance is positive or negative, respectively. The gray zone represents the area where the electron may impact against the top plate prior to the instant expected according to the resonance condition (as presented by the solid line in Fig. 2.4); and the dashed area represents the region where this cannot occur, which is of our interest. Note the absence of restriction in the value of the RF voltage to ensure that the electron will not impact against the opposite plate prior to the time predicted by (2.3) at $fd = N/2 \cdot v_0$, splitting the domain into two parts according to this value of the fd product. On the other hand, the region where the electron can overcome the opposite plate before expected according to (2.3) is bigger in the low fd product region as this is more likely to occur when the distance between the plates (or the frequency) decreases. On the opposite corner of the plot there is another region that predicts a negative sinus for the phase of resonance at high values of the fd product and RF voltages due to the periodic character of the arcsinus function around zero established by the condition $fd = N/2 \cdot v_0$. The plot has been done for a fixed impact energy, $v_i = 30$ eV, since the domain of validity changes with it, and the multipactor breakdown voltage predicted by (2.13) has also been represented in Fig. 2.7. Note how the gap in the multipactor breakdown curve is produced due to the violation of the condition that guarantees that the impact against the opposite plate is produced with positive relative velocity. The gap for order of multipactor $N = 3$ is much smaller than for $N = 1$ because the range of phases of resonance that imply that the electron impacts against the opposite plate before the expected instant according to the resonance condition, is narrower. Therefore, the restriction of positive relative velocity at impact time is more difficult to be violated for higher orders of multipactor.

Usually, the chosen value of the initial velocity to reproduce the multipactor susceptibility chart is small, between 0eV and 10eV, within the energy range where the number of secondary electrons is maximum [Schreiber 2002]. Nevertheless, the tail in the energy spectrum of the secondary electrons shows that few electrons with high initial velocity, till 50 eV in some cases, are present, too [Furman 2003]. In Fig. 2.8 the curves of the multipactor breakdown voltage for different values of v_i have been represented for $v_0 = 1$ eV, where the plots without and with restriction, regarding the positive relative velocity at impact time, show no-

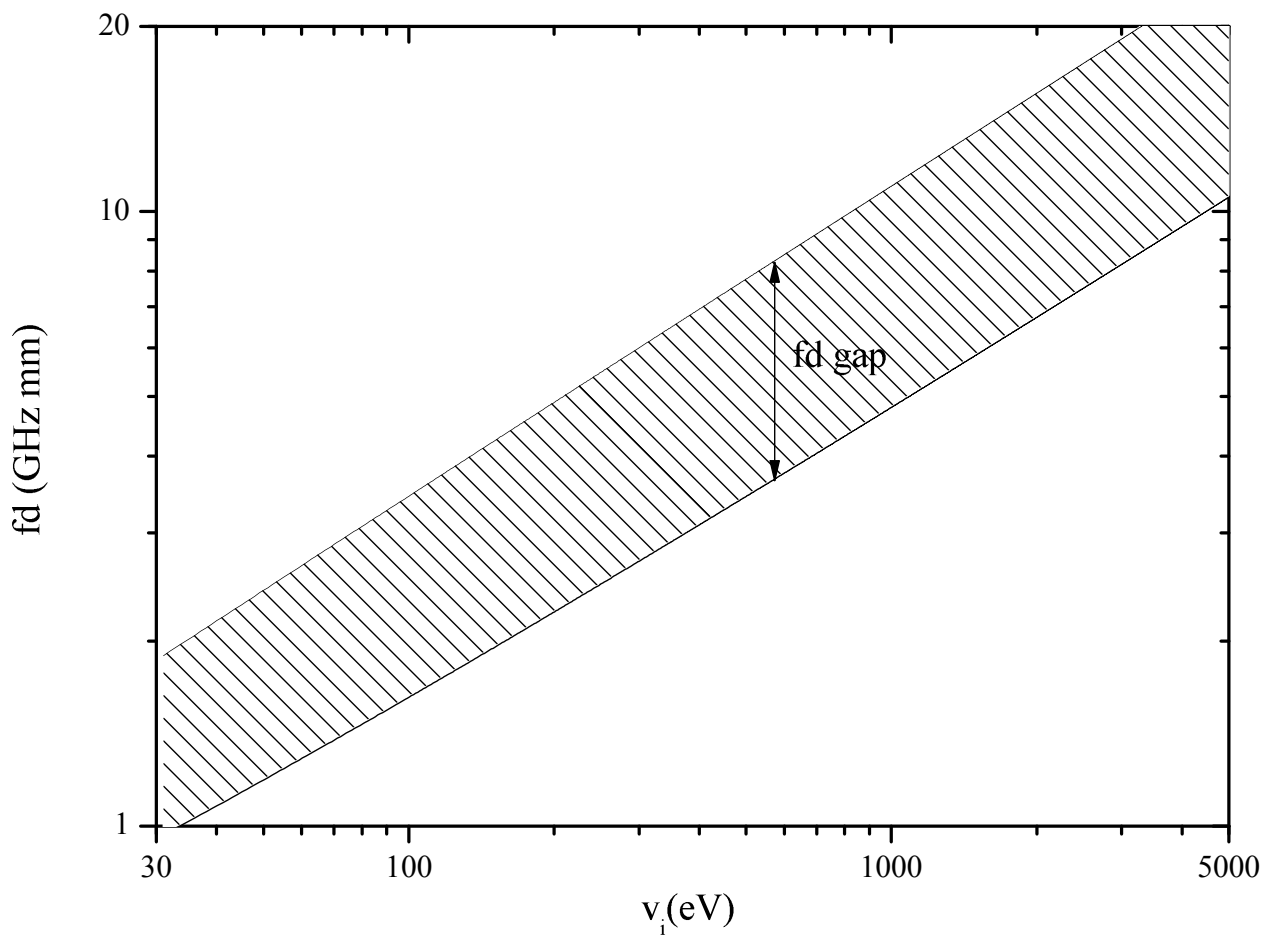
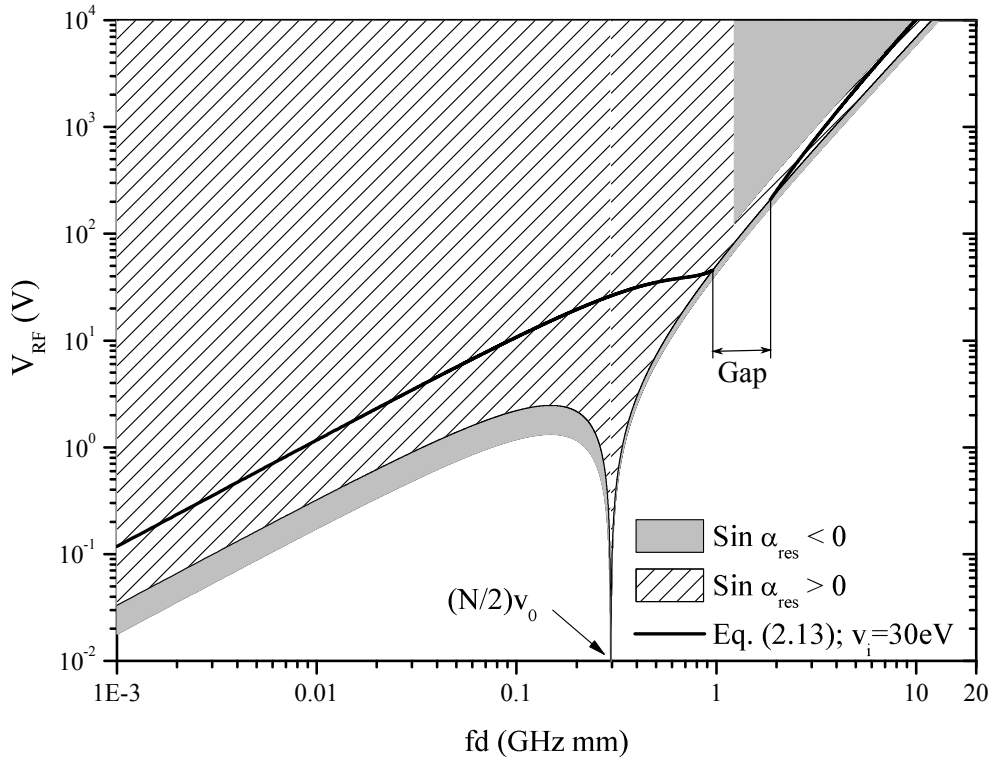
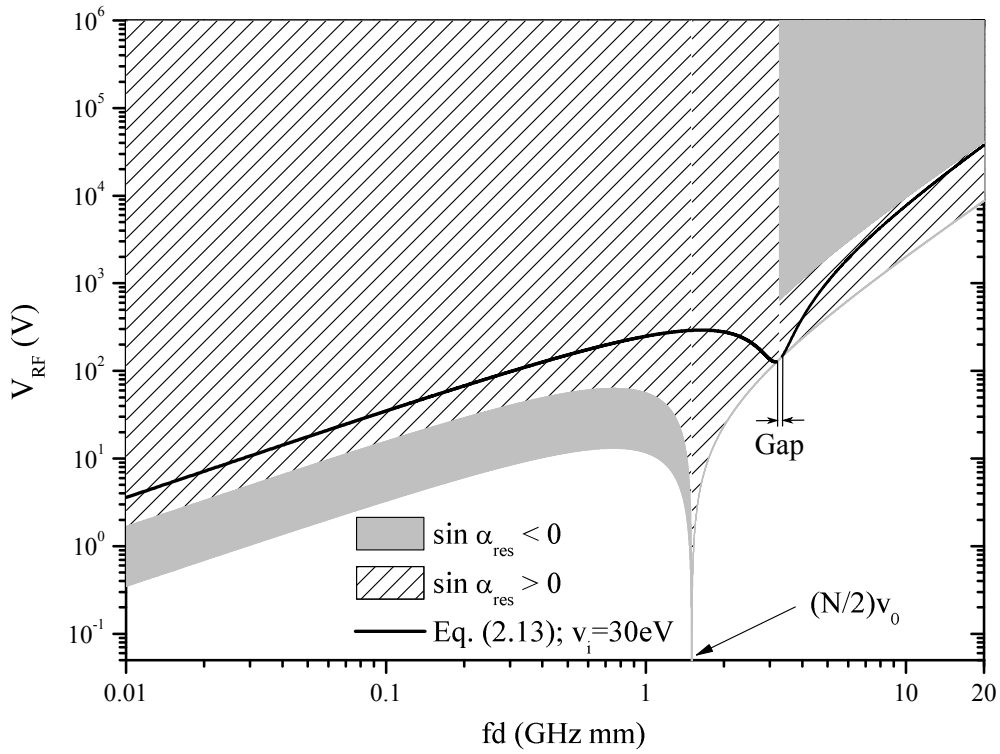


Figure 2.6: Gap of the fd product vs. the impact velocity v_i in the multipactor susceptibility chart produced by the constraint of positive relative velocity at impact time; $v_0 = 1$ eV.



(a) $N = 1, v_0 = 1$ eV.



(b) $N = 3, v_0 = 2.85$ eV.

Figure 2.7: Domain of validity for α_{res} without taking into account the restriction of the returning to the initial plate before reaching the opposite one; $v_i = 30$ eV.

ticeably differences for order of multipactor $N = 1$, and slight differences for $N > 1$, as it was commented before regarding the gaps in Fig. 2.7.

Regarding Fig. 2.8a it must be mentioned that, above $1 \text{ GHz} \cdot \text{mm}$, the multipactor voltage threshold is found in curves associated to different values of v_i for different values of the fd product, crossing each other. This implies that the multipactor threshold is not always defined by the curve obtained for the lowest value of v_i , i.e., the first cross-over point of the SEY curve of the material that the plates are made of. Furthermore, this effect is more visible as the order of multipactor increases. Only in the region of low fd products the multipactor voltage threshold can be identified with the curve obtained with the lowest v_i possible. This connects with the fact that, as Fig. 2.8b shows, the gap in the fd product seems to decrease as the impact energy increases (in this case it is more visible for order of multipactor one) whereas Fig. 2.6 showed that this gap grows as the impact energy increases. The perception of the decrease of the gap is due to the fact that the curves for different impact energies cross each other. Therefore, the gap for $N = 1$ and $v_i = 100 \text{ eV}$ in Fig. 2.8b seems to be smaller than for lower v_i , but actually the apparent small gap is produced between the curves for $v_i = 100 \text{ eV}$ and $v_i = 30 \text{ eV}$. The gap for $N = 3$ and $N = 5$ is less visible in Fig. 2.8b because the distance between $N/4 \cdot (v_i + v_0)$ and \tilde{v}_N , expressed by (2.16), becomes shorter as the order of multipactor increases. At the end, the overall effect of considering the constraint of positive relative velocity at impact time is that the envelope of the multipactor threshold in the susceptibility chart is modified.

2.4 Stability condition

Another property that must be verified regarding the resonance is its stability. Let us imagine that the motion of the electron starts near a certain phase of the RF signal for which the resonance condition applies. To consider a self-sustained resonance, the difference between the impact and launch phase (between ωt_i and α) must converge to the quantity predicted by (2.3) with increasing time. If this does not occur, the motion is to be said unstable, since the synchronicity between the electron's motion and the time change of the RF signal breaks as time advances. The multipactor discharge onset can only be explained by a stable resonant motion, because the probability of considering an electron starting to travel from one plate to the opposite at the exact phase of resonance α_{res} is negligible. Therefore, only for values of the initial phase that imply the convergence to α_{res} can guarantee the permanence of the resonance along time and, thus, the multipactor breakdown onset.

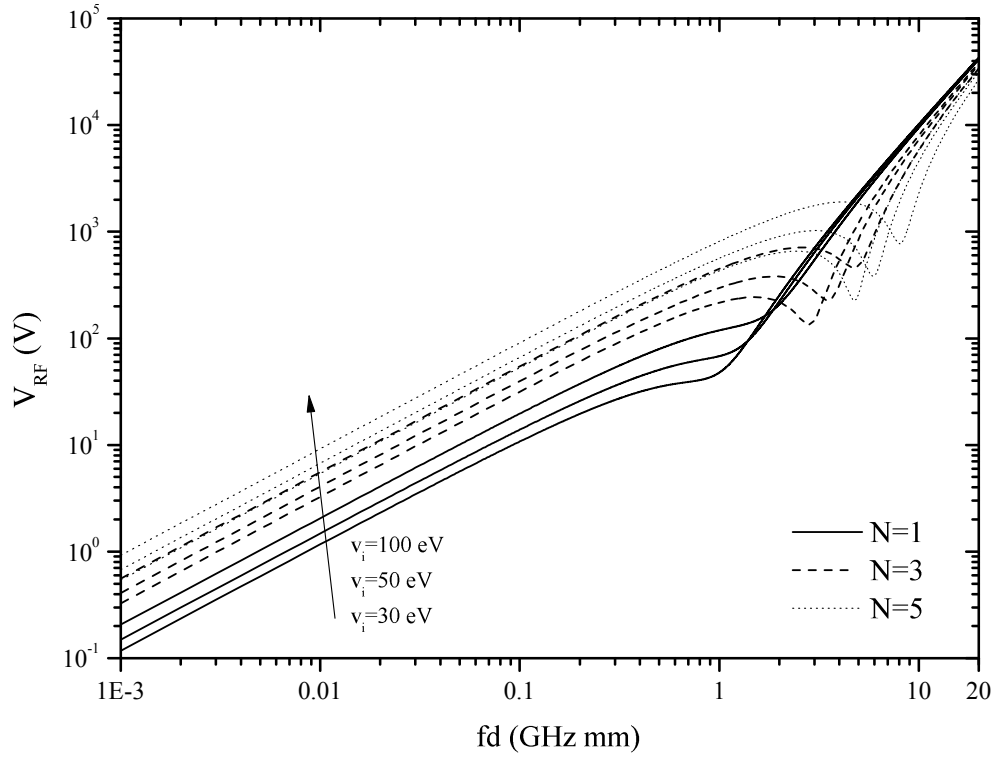
In order to assess whether the resonance is stable or not, we can make use of the stability study presented in [Riyopoulos 1995], very similar to the general theory of stability of Lyapunov exponents described in [Lyapunov 1992]. The relation between launch and impact phase, ϕ_n and ϕ_{n+1} , respectively, can be defined by an implicit function using the equation of position of the electron (2.2b) setting $z' = d$

$$F(\phi_{n+1}, \phi_n; v_0, f, d, V_{RF}) \equiv d - \frac{v_0(\phi_{n+1} - \phi_n)}{2\pi f} + \frac{eV_{RF}}{m_e 4\pi^2 f^2 d} (\cos \phi_{n+1} - \cos \phi_n + (\phi_{n+1} - \phi_n) \sin \phi_n), \quad (2.17)$$

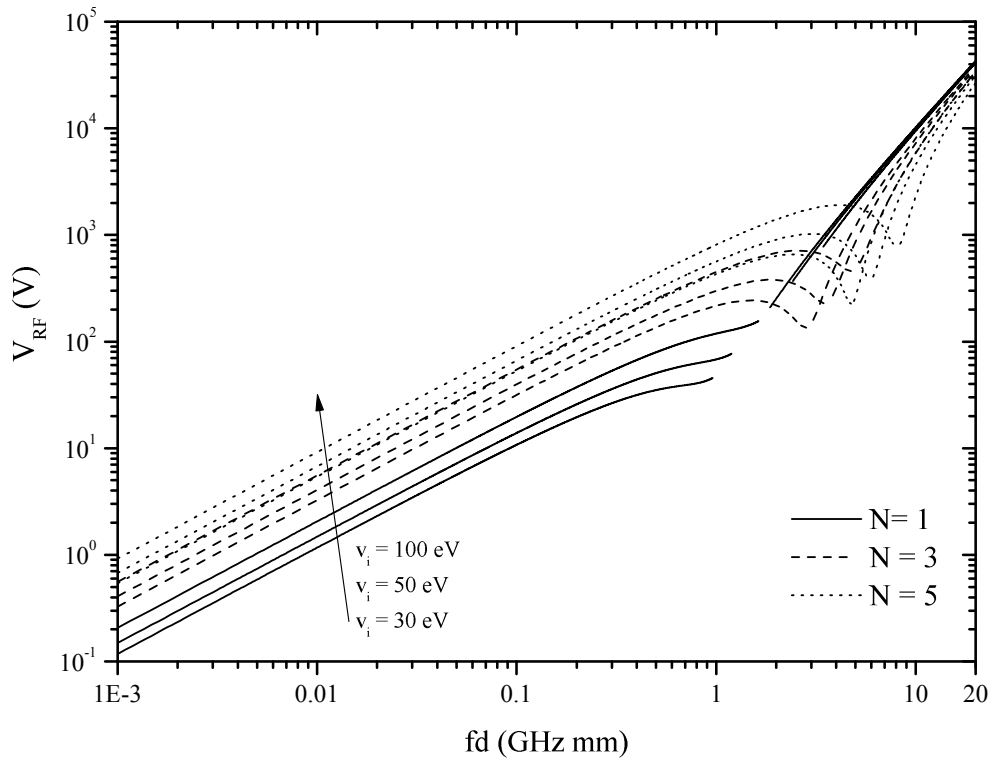
what allows us to define the impact phase, ϕ_{n+1} , as a function of the launch phase, ϕ_n

$$\phi_{n+1} = \tilde{f}(\phi_n; v_0, f, d, V_{RF}). \quad (2.18)$$

We can develop (2.18) into a Taylor series up to the first order around α_{res} , which is the fixed phase of reso-



(a) No restriction.



(b) Restriction $\sin \alpha > 0$.

Figure 2.8: Multipactor breakdown voltage vs. fd obtained with (2.13). The initial velocity is $v_0 = 1$ eV.

nance, obtaining:

$$\phi_{n+1} \simeq \tilde{f}(\alpha_{res}; v_0, f, d, V_{RF}) + \left. \frac{\partial \tilde{f}}{\partial \phi_n} \right|_{\alpha_{res}} (\phi_n - \alpha_{res}).$$

As α_{res} is periodic, the expression $\alpha_{res} + N\pi = \tilde{f}(\alpha_{res}; v_0, f, d, V_{RF})$ is satisfied. If we subtract the first term from the RHS using the last expression and taking $mod(N\pi)$, we get

$$\phi_{n+1} - \alpha_{res} \simeq \left. \frac{\partial \tilde{f}}{\partial \phi_n} \right|_{\alpha_{res}} (\phi_n - \alpha_{res}).$$

Therefore, the partial derivative of the function \tilde{f} with respect to the launch phase, ϕ_n , is named stability factor, G , since it gives the deviation between the initial and final phases with respect to the fixed phase of resonance, α_{res} , as it is shown next

$$\phi_{n+1} - \alpha_{res} \simeq G(\phi_n - \alpha_{res}) \rightarrow G = \frac{\phi_{n+1} - \alpha_{res}}{\phi_n - \alpha_{res}}.$$

As the function \tilde{f} defines an implicit relation between the launch and impact phases the stability factor can be calculated using (2.17)

$$G \equiv \left. \frac{\partial F / \partial \phi_n}{\partial F / \partial \phi_{n+1}} \right|_{\phi_n = \alpha_{res}; \phi_{n+1} = \alpha_{res} + N\pi}. \quad (2.19)$$

When the absolute value of the stability factor is below unity the distance between the consecutive launch phases and the fixed phase of resonance decreases, yielding a stable resonant motion; the opposite case occurs if the absolute value of G lies above unity. Therefore, the stability factor assesses whether the synchronicity of the motion with the RF field is guaranteed forever ($|G| < 1$) or whether, on the contrary, the impact phase differs from the one fixed by the resonant condition more and more after each impact ($|G| > 1$):

$$\begin{aligned} |G| < 1 & \quad (\text{Stable resonance}) \\ |G| > 1 & \quad (\text{Unstable resonance}) \end{aligned}$$

Substituting ϕ_n and ϕ_{n+1} by α_s and $\alpha_s + N\pi$, respectively, in (2.17) and this into (2.19) applying the stable resonance inequality, the condition of the stability factor being below unity can be rewritten as

$$\left| v_0 - \frac{eV_{RF}}{m_e 2\pi f d} N\pi \cos \alpha_s \right| < \left| v_0 + \frac{2eV_{RF}}{m_e 2\pi f d} \sin \alpha_s \right|$$

where α_s stands for stable phase of resonance. The values of α_s that satisfy this inequality represent the initial phases that, impact after impact, will converge to the fixed phase of resonance α_{res} . This inequality can be rewritten as follows

$$|V_\omega - N\pi \cos \alpha_s| < |V_\omega + 2 \sin \alpha_s|$$

where it has been defined the variable

$$V_\omega = \frac{v_0}{v_\omega} = \frac{v_0 m_e 2\pi f d}{eV_{RF}}. \quad (2.20)$$

The variable V_ω represents the normalized initial velocity with respect to the microwave velocity, v_ω .

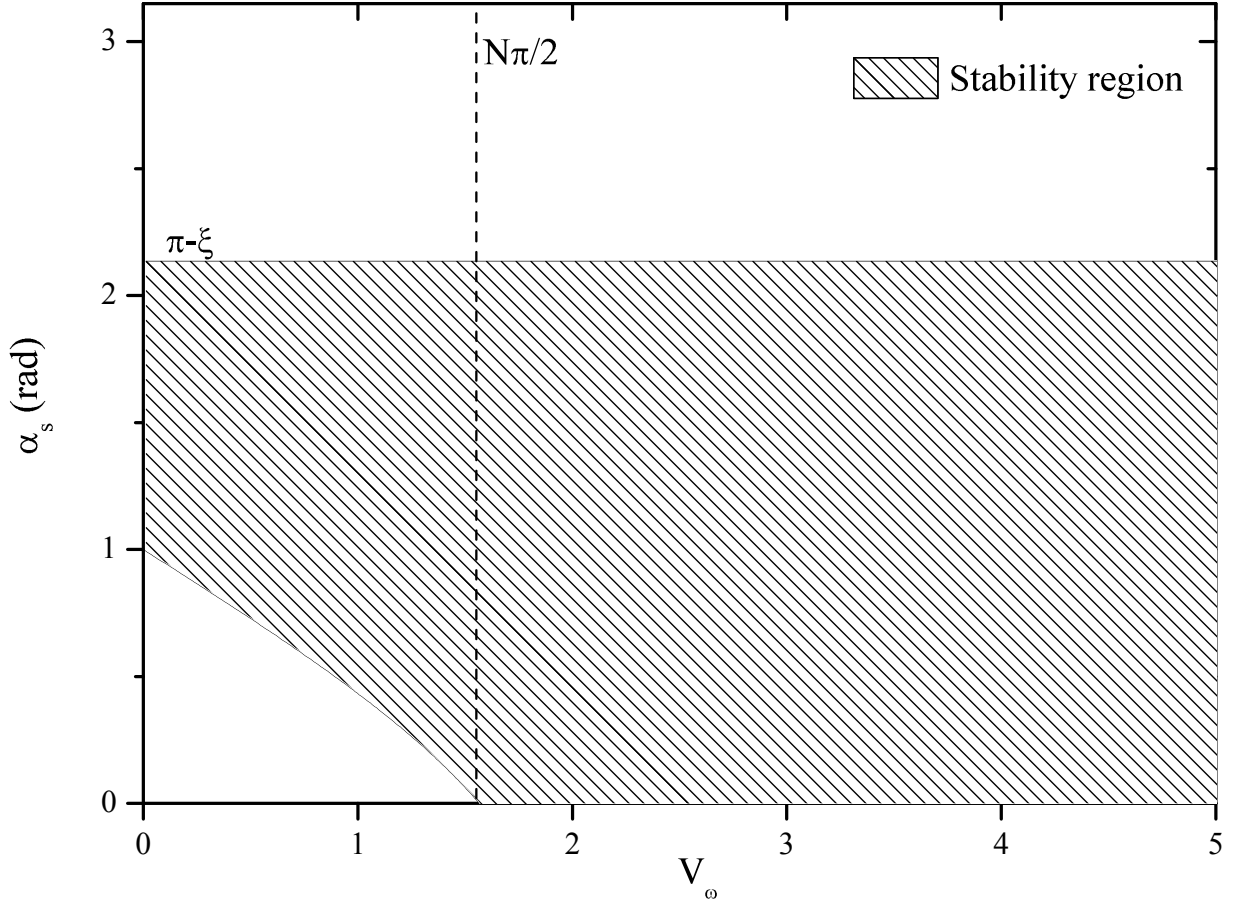


Figure 2.9: Domain of stability provided by (2.21) for $N = 1$.

Taking into account the restriction of positive velocity together with the stability condition, the valid range of the phase of resonance to plot the multipactor susceptibility chart can be written as

$$\left\{ \begin{array}{l} \xi - \arcsin\left(\frac{2V_\omega}{R}\right) < \alpha_s < \pi - \xi \quad \text{if } V_\omega \leq \frac{N\pi}{2} \\ 0 < \alpha_s < \pi - \xi \quad \text{if } V_\omega \geq \frac{N\pi}{2} \end{array} \right\} \quad (2.21a)$$

$$\left\{ \begin{array}{l} \xi - \arcsin\left(\frac{2V_\omega}{R}\right) < \alpha_s < \pi - \xi \quad \text{if } V_\omega \leq \frac{N\pi}{2} \\ 0 < \alpha_s < \pi - \xi \quad \text{if } V_\omega \geq \frac{N\pi}{2} \end{array} \right\} \quad (2.21b)$$

where $\xi = \arctan\left(\frac{N\pi}{2}\right)$.

The domain of stability for order of multipactor $N = 1$ is represented by the dashed area in Fig. 2.9, where it has been represented within the region defined by the positive relative velocity at impact time, i.e., $\alpha \in [0, \pi]$. The origin of the restrictions reproduced in the multipactor susceptibility chart in Fig. 2.10 with respect to the one shown in Fig. 2.8 is twofold. The stability constraint eliminates the very low values of the fd product, but the other extreme is also interrupted by the condition of positive relative velocity at impact time.

Regarding the analysis of the stability, if we substitute (2.13) into (2.20) it can be proved that V_ω is always smaller than $N\pi/2$ for the typical values of v_0 . Therefore, the first condition (2.21a) for the stability restriction

applies for any value of the frequency-gap product. As (2.12a) predicts, for $fd < v_N$ the phase of resonance is $\alpha_{res}^{(1)}$, and it can be proved that the value of this phase obtained by (2.6a) lies below the range defined by the stability condition, (2.21a), when the fd product is too small. Above a certain value of the frequency-gap product the phase of resonance, $\alpha_{res}^{(1)}$, lies within the range of validity imposed by the stability condition until the restriction of the positive relative velocity applies. Later, there is a gap in the value of the fd product defined by (2.16) and, since $\tilde{v}_N > v_N$, the phase of resonance outside the prohibited region delimited by the positive relative velocity condition is defined by $\alpha_{res}^{(2)}$. However, all the values of the phase of resonance yielded by (2.6b) lie above the range that guarantees the stability. This implies that the maximum value of the fd product defining the region where multipactor of order N occurs is $fd = N/4 \cdot (v_i + v_0)$. Beyond this point, the expression (2.13) predicts values of the multipactor voltage threshold that cross the predictions obtained for bigger values of v_i within the first part of the curves, when $fd < \tilde{v}_N$.

Therefore, the right side of the envelope for each order N is delimited by the condition of positive relative velocity at impact time. The left side boundary of each region is provided, however, by the stability condition, and the bottom and top boundaries are provided by the first and second cross-over point, respectively. The multipactor susceptibility chart is shown in Fig. 2.10 for an initial velocity of $v_0 = 1$ eV, where the boundaries come closer to each other as the order of multipactor grows, what results in the narrowing of the zones where the discharge occurs as the order increases, almost depicting a single line for high orders of resonance.

2.5 Returning condition

It has not been checked yet that the multipactor susceptibility chart yields with values of the RF voltage and the fd product for which the electron does not return to the initial plate before arriving to the opposite one. The goal of this section is, analogously to the analysis of the stability condition, to find the values of the launch phase ensuring that the electron does not return to the initial plate. As it will be shown later, the solution that is going to be found gives us the maximum launch phase that induces the return of the electron to the initial plate, what implies that for smaller values the return also occurs. Beyond the maximum launch phase that is to be found, the electron will reach the opposite plate without colliding with the initial one. The limiting case corresponds to the return of the electron to the initial plate with zero velocity, which is the condition that we are going to consider in order to find that maximum. The returning limit has already been analyzed in the literature and some analytical approximations to the launch phase that makes the electron to return to the initial plate with zero velocity have been given for very small values of the initial velocity [Semenov 2005].

Therefore, we have to solve the following system of equations to calculate the launch phase that makes the RF field pull back the electron to the initial plate such that it reaches the origin with zero velocity and positive acceleration (see Fig. 2.11):

$$\left\{ \begin{array}{l} z' = 0 \\ \dot{z}' = 0 \end{array} \right\} \quad (2.22a)$$

$$\left\{ \begin{array}{l} \dot{z}' = 0 \end{array} \right\} \quad (2.22b)$$

$$\left\{ \begin{array}{l} \ddot{z}' > 0 \end{array} \right\} \quad (2.22c)$$

Here we only present the results, the detailed analysis of this system of equations is described in the Appendix A, whose solution is found at the end by searching the roots of a single function (A.17). The solution of that function provides the returning initial phase, α_R , which is the launch phase that induces the impact of the electron against the initial plate with zero velocity. The impact against the initial plate is produced at

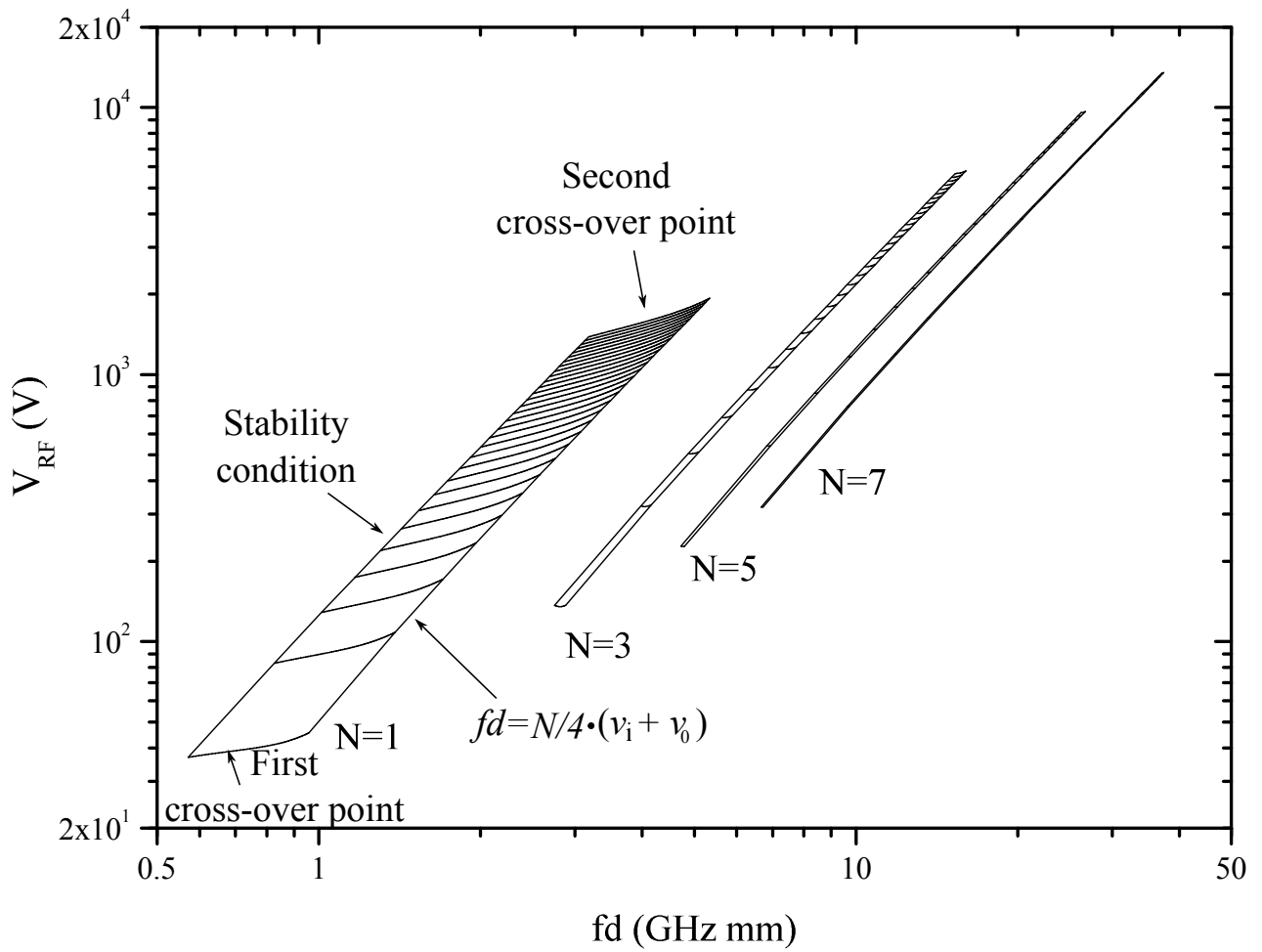


Figure 2.10: Multipactor susceptibility chart taking into account $\sin \alpha > 0$ and the stability condition. The parameters are $v_0 = 1$ eV, $E_1 = 30$ eV, $E_2 = 1200$ eV.

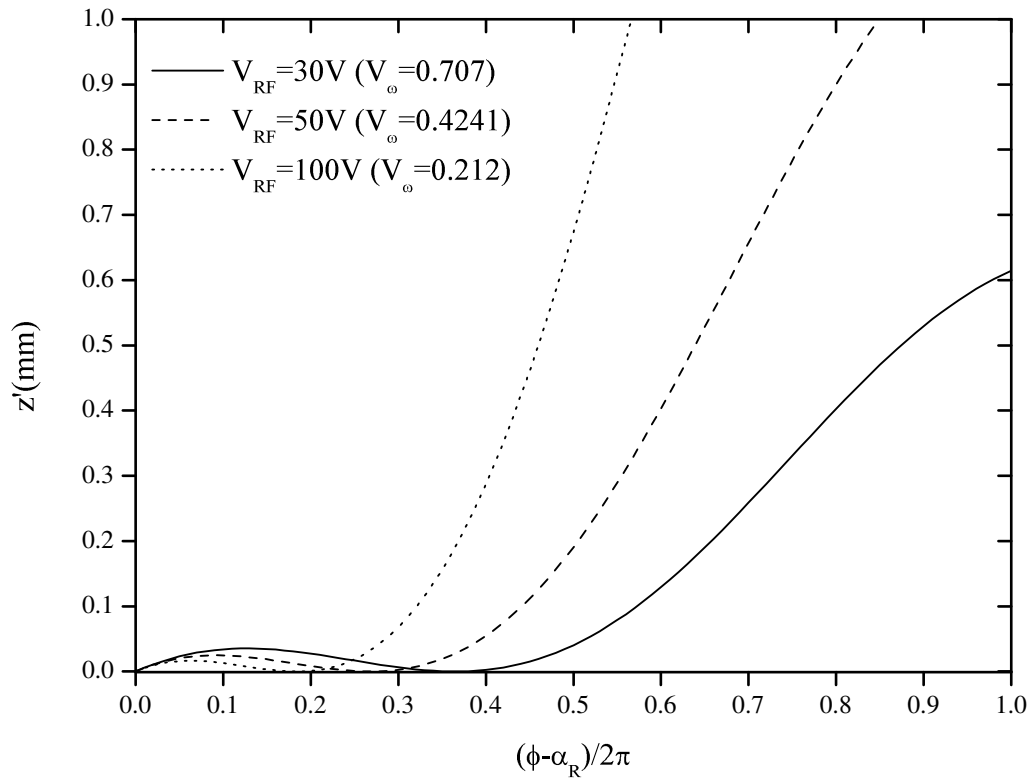


Figure 2.11: Example of returning for $fd = 1 \text{ GHz} \cdot \text{mm}$ and $v_0 = 1 \text{ eV}$. Note that the origin is represented at zero for all the launch phases whose values are $\alpha_R = 0.0258557 \text{ rad}$ (solid), $\alpha_R = 0.438889 \text{ rad}$ (dashed) and $\alpha_R = 0.796789 \text{ rad}$ (dotted).

the returning impact phase, ϕ_R , which can be calculated from the returning initial phase as it is shown in the Appendix A. The results are presented in Fig. 2.12, where the returning initial and impact phases are plotted as function of V_ω . The gray zone represents the values of the launch phase that guarantee the non-returning of the electron to the initial plate. The thin solid line represents the solution of (A.17) for the first branch defined by $(\alpha_R \in [-\frac{\pi}{2}, \frac{\pi}{2}])$, which defines the values of the launch phase, $\alpha_R^{(1)}$, for which the electron will impact against the initial plate with zero velocity at the impact phase, $\phi_R^{(1)}$, defined by the dashed line. For values of the initial phase above $\alpha_R^{(1)}$ the electron cannot return, since they define the maximum launch phase able to induce the impact of the electron against the initial plate as mentioned before.

However, there is a second branch solution of (A.17) for $(\alpha_R \in [\frac{\pi}{2}, \frac{3\pi}{2}])$, what results in the returning initial phase $\alpha_R^{(2)}$ represented by the thick solid line in Fig. 2.12. The electrons launched at the initial phase represented by that line will collide against the initial plate at the returning impact phase $\phi_R^{(2)}$, represented by the dashed-dotted line, provided that they do not collide previously with the opposite plate. For values of the initial phase above $\alpha_R^{(2)}$ the electrons that will not impact against the opposite plate will collide against the initial one with negative velocity. As the initial phase increases exceeding the limit imposed by $\alpha_R^{(2)}$, the electrons will collide with the initial plate increasing the absolute value of the negative velocity at the impact.

Since the transit time from the beginning of the motion to the impact against the initial plate is represented by the difference between $(\phi_R^{(1)} - \alpha_R^{(1)})$, from Fig. 2.12 it can be inferred that the electron cannot reach the opposite plate before colliding with the initial one satisfying the resonance condition (2.3). Even in the limit for values of $V_\omega \gtrsim 1.1$ the difference of phases yields π , but it is still insufficient to allow the electron to impact against the opposite plate satisfying the resonance condition. Furthermore, for values of $V_\omega > 1.1$, the returning launch phase predicted by the solution of (2.22) lies below 0 rad, and we have already seen that for the classical multipactor resonance condition the initial phase must be greater than zero to ensure that the velocity is positive when colliding against the opposite plate. Therefore, we do not have to worry for the possibility that the study of the returning limit could neglect the possibility of a classical multipactor resonance because the solution provided by the returning limit is incompatible with the classical resonance condition.

We can see how the distance between the dashed-dotted and the thick solid lines in Fig. 2.12 is bigger than the distance between the thin dashed and solid ones, therefore, the transit time from launch to impact is much larger for the second branch solution of (A.17) than for the first one. This occurs because the values of the initial phase belonging to the second branch induce a much higher acceleration in the beginning of the motion of the electron, what pushes the electron further away from the birth plate. This implies that the electron needs more time to return to the initial plate than when the initial phase lies within the first branch. However, the solution of the second branch has not been taken into account when plotting the multipactor susceptibility chart because the phases of resonance that belong to the second branch violate the positive relative velocity condition at collision time on the opposite plate.

Note how in Fig. 2.12 the predicted maximum launch phase to induce the collision of the electron against the initial plate decreases as the normalized initial velocity V_ω augments. To understand this, observe that in Fig. 2.11 the electron stays longer within the region between the plates prior to the returning, as the value of V_ω increases. As the initial velocity increases V_ω does likewise, thus the RF field needs more time to accelerate the electron such that it returns to the initial plate. This is only possible when the launch phase, α_R , decreases below zero, explaining why α_R decreases when V_ω grows. As V_ω represents the relative initial velocity, v_0 , with respect to the microwave velocity, v_ω , it is natural expecting that above a certain value of V_ω the initial

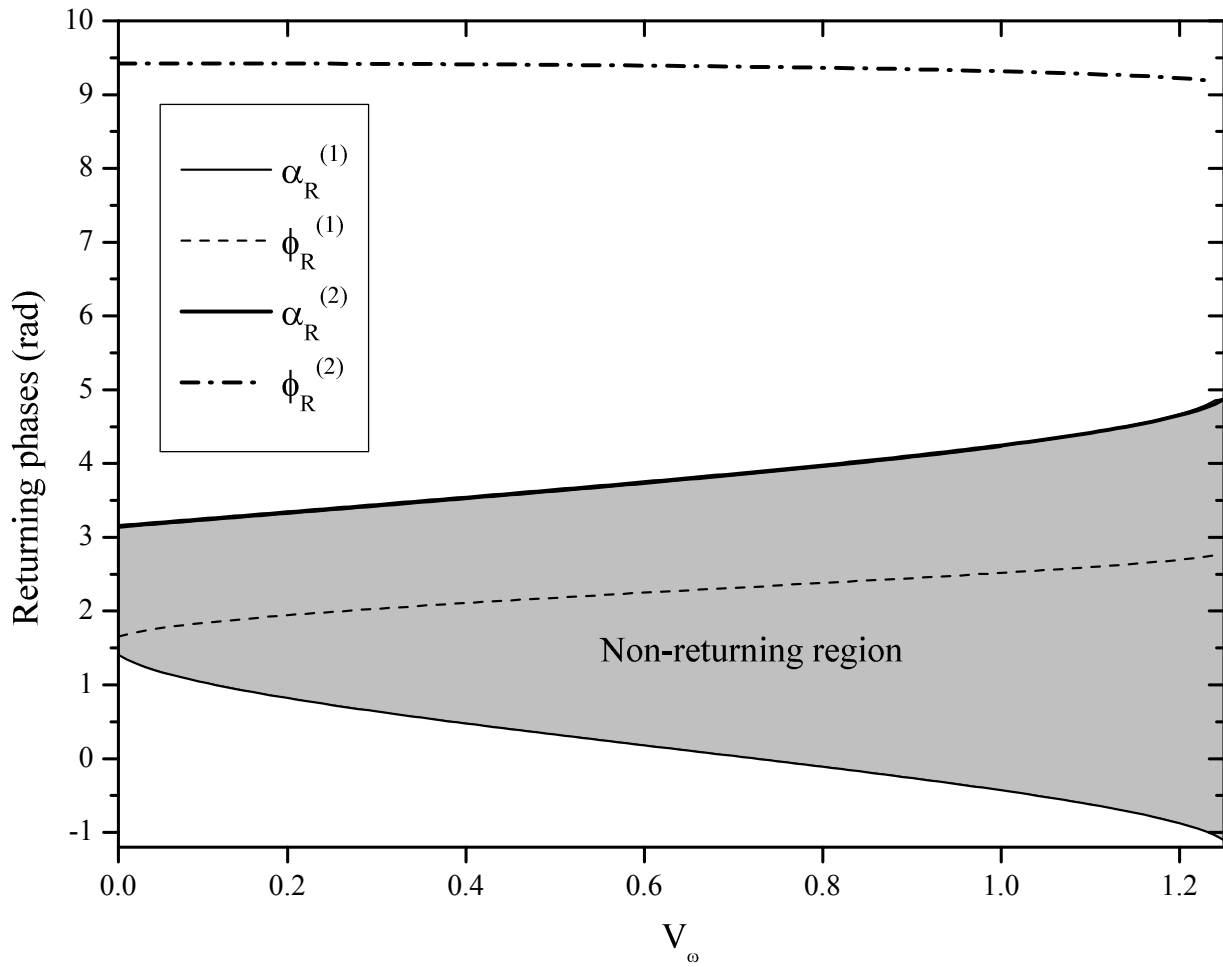


Figure 2.12: Solution of the returning limit. The variables $\alpha_R^{(1)}$ and $\alpha_R^{(2)}$ are the two initial phases for which the electron will impact against the initial plate with zero velocity at the impact phases $\phi_R^{(1)}$ and $\phi_R^{(2)}$, respectively.

velocity will be so high (or the field strength so low) that the force of the RF field will not be able to make the electron return to the initial plate for any initial phase. In the Appendix A this limit has been found to be located around $V_{\omega}^{max} \approx 1.26$.

The differences between the multipactor susceptibility chart taking into account the stability and the returning limit conditions can be seen in Fig. 2.13a. The dashed lines represent the multipactor onset region including unstable phases of resonance but limited to the returning condition. This means that the dashed lines show the regions for which the motion of the electron satisfies the resonance condition and the impact energy above the first cross-over point ensuring that the electron does not return to the initial plate before reaching the opposite one. Nevertheless, this case includes values of the phase of resonance that may lead to unstable resonant motions. On the contrary, the solid line represents the values of the RF voltage and the fd product for which the resonance is stable but it is not guaranteed that the electron does not return to the initial plate before reaching the opposite one.

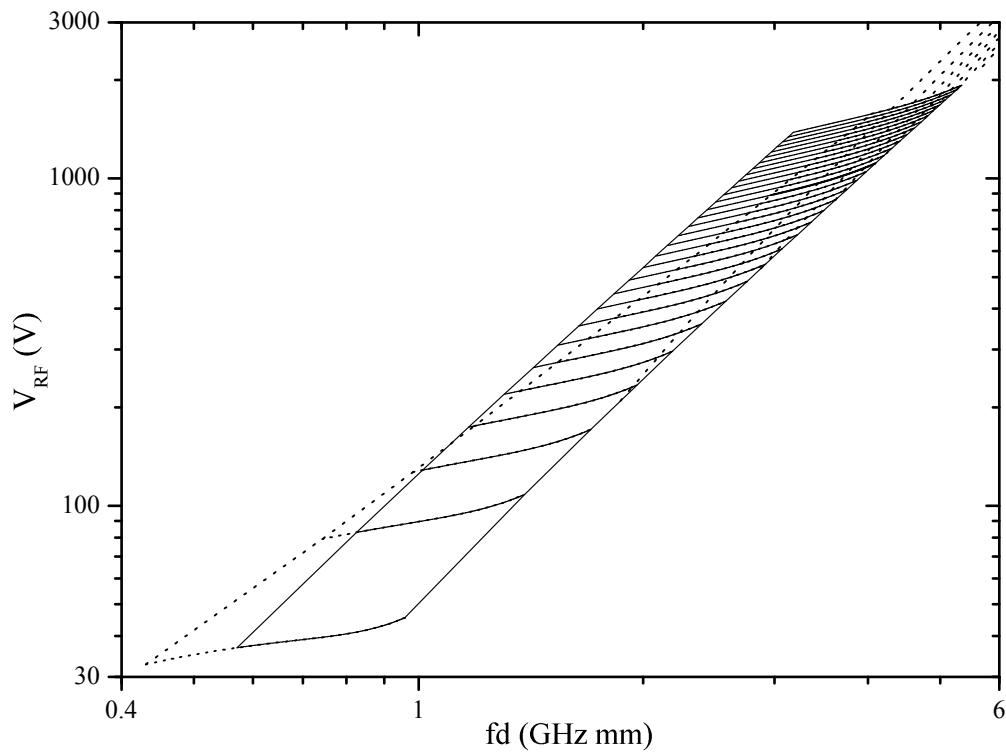
It is interesting to note that the returning condition is less restrictive for low voltages than for high ones. This can be understood if we remark that, for low voltages, V_{ω} is larger than in the high voltage region. Therefore, it is more likely to occur the return of the electron to the birth plate when the voltage applied is low because the range of values of the launch phase that provoke the return of the electron to the birth plate enlarges as V_{ω} increases (see Fig. 2.12). The restriction of the returning limit predicts a smaller region for the multipactor occurrence in the high-voltage region, however, it only modifies the left boundary of the multipactor chart (see Fig. 2.13). On the right boundary of the envelope, the positive relative impact velocity condition until $fd = N/4 \cdot (v_i + v_0)$ provides the vertical limit of the multipactor chart. Interestingly, the returning limit does not seem to delimit the roof of the multipactor chart, as depicted by the dashed lines in Fig. 2.13a, though they imply unstable phases of resonance. This was already pointed out in [Shemelin 1986], and it has been verified that the values of the phase of resonance corresponding to the dashed lines above the upper limit, fixed by the stability condition, lie within the non-returning area depicted in Fig. 2.12, what shows a clear difference in the analysis of the returning limit done in other studies like in [Udiljak 2007].

2.6 Multipactor susceptibility chart

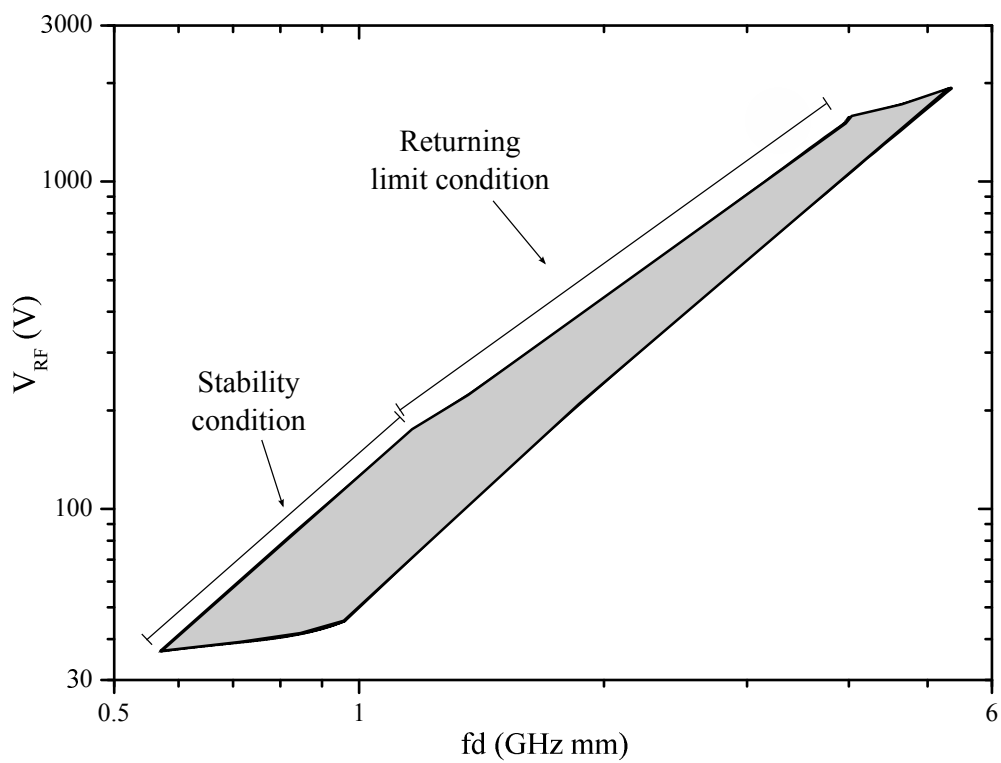
The envelope of the multipactor susceptibility chart considering the restrictions imposed by the returning limit and the stability conditions represented in Fig. 2.13a is plotted in Fig. 2.13b. Comparing both figures it can be seen that the envelope is mainly the same, except on the left side, which differs from the left boundary provided by the stability condition shown in Fig. 2.13a. Indeed, the upper region of the left boundary of the envelope narrows the multipactor susceptibility chart beyond the stability condition due to the returning limit restriction.

For higher orders of multipactor the returning limit does not impose any restriction to the envelope of the multipactor susceptibility chart beyond the constraint provided by the stability condition (see Fig. 2.14a). The multipactor voltage breakdown increases with the order of multipactor thus the variable V_{ω} decreases. We should recall the fact that the amount of initial phases that lead the electron to return to the initial plate is less restrictive as V_{ω} decreases. Therefore, for high orders of multipactor the returning limit is less important than the stability condition in the envelope of the multipactor susceptibility chart.

To finish, it must be remarked that some parts of the multipactor curves taking into account the returning limit (dashed lines) with high impact velocity, v_i , lie below the curves obtained with lower values of v_i , as it has already been mentioned regarding Fig. 2.8, because the lines corresponding to different values of the collision energy cross each other.

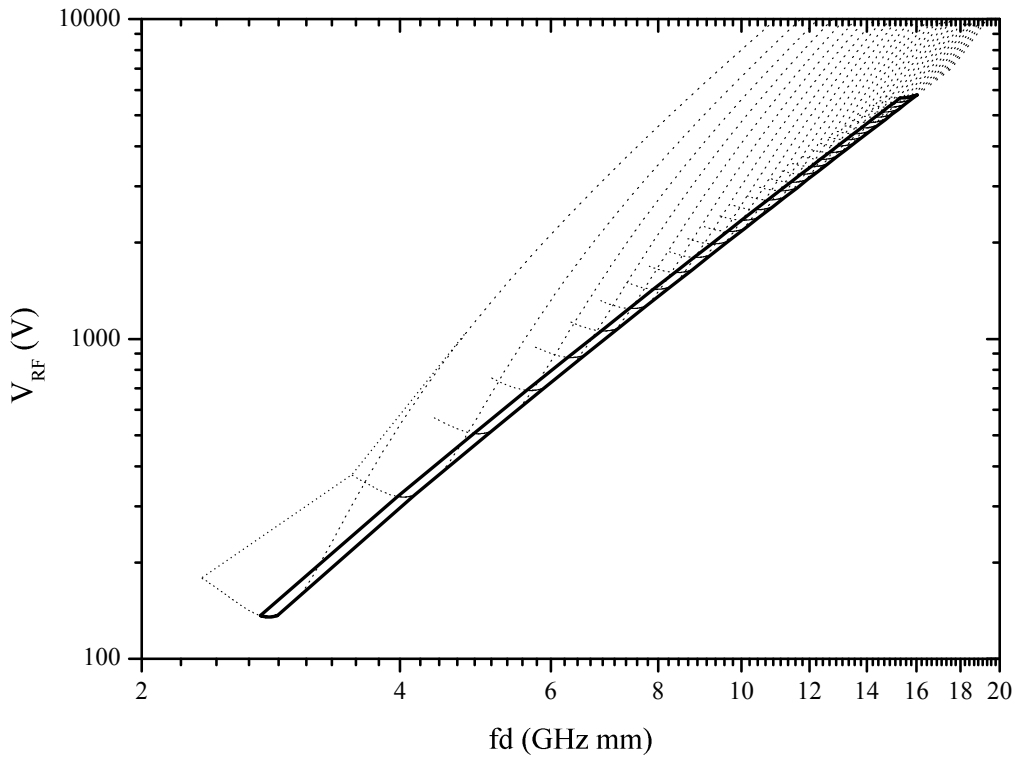


(a) Multipactor susceptibility chart delimited by the stability condition (solid line) and the returning limit condition (dashed line).

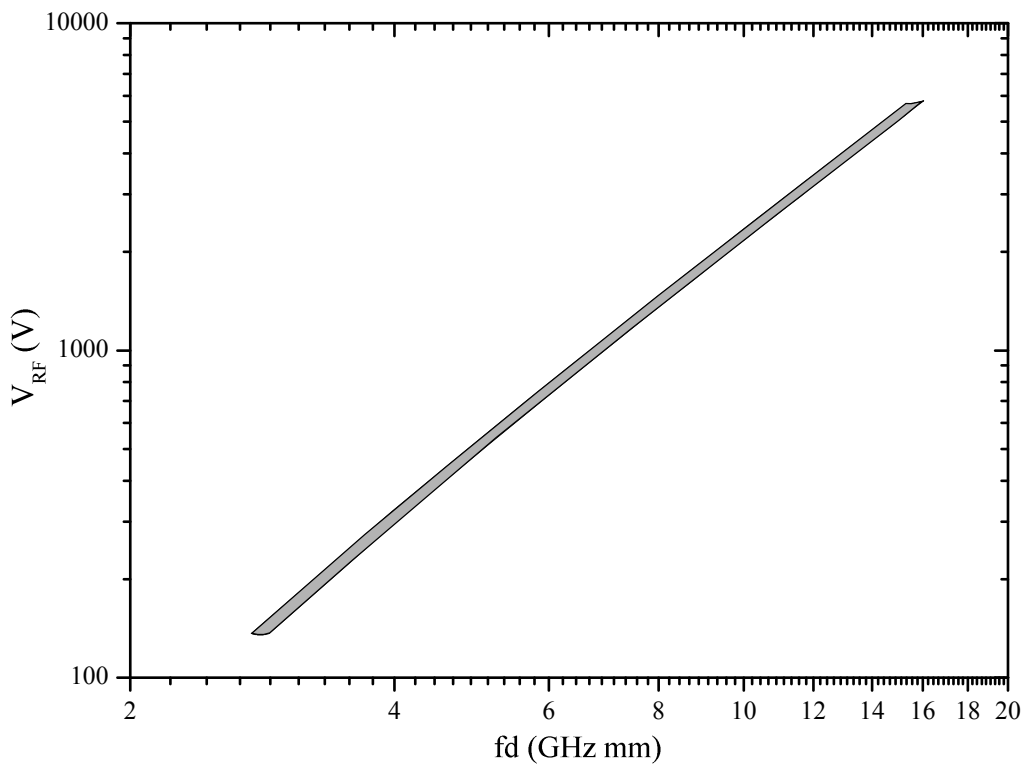


(b) Multipactor susceptibility chart delimited by the envelope of the most restrictive among the stability and the returning limit conditions.

Figure 2.13: Multipactor susceptibility chart for $N = 1$ for $v_0 = 1$ eV, $E_1 = 30$ eV, $E_2 = 1200$ eV.



(a) Multipactor susceptibility chart delimited by the stability condition (solid line) and the returning limit condition (dashed line).



(b) Multipactor susceptibility chart delimited by the envelope of the most restrictive among the stability and the returning limit conditions.

Figure 2.14: Multipactor susceptibility chart for $N = 3$ using the same parameters as for Fig. 2.13.

The predicted multipactor breakdown voltage threshold depends on the initial velocity of the secondary electrons, which usually ranges from 0 to 10 eV, as it can be observed in Fig. 2.15, where the analytical multipactor susceptibility chart is represented for two illustrating values of the initial velocity. Note how the band for $N = 5$ obtained with $v_0 = 5$ eV (dashed line) overlaps the band for $N = 7$ obtained with $v_0 = 1$ eV (solid line). Therefore, it is shown that the initial velocity represents a crucial parameter in the understanding of the experimental measurements of the multipactor breakdown threshold, however, the initial velocity distribution of the secondary electrons follows a Maxwellian distribution [Semenov 2001, Coves 2008] and no fixed velocity can be assumed to calculate accurately the multipactor susceptibility chart.

It is interesting to observe that the multipactor breakdown threshold does not necessarily decrease as the initial velocity of the electrons increases, as a too much simplified approach to the problem could infer, because the electrons need less energy to reach the first cross-over point for high initial velocities. This simplistic model would overlook the fact that not only the required energy to guarantee the secondary emission is requested for the discharge to arise, the resonance together with the stability condition also fix the boundaries of the multipactor zones.

The experimental measurements of the multipactor power threshold on a silver-plated parallel-plate waveguide carried out at ESA-ESTEC and extracted from [Woode 1989] have been included in the plot for comparison with the predictions. The first cross-over point of the SEY curve of silver is $E_1 = 30$ eV. The agreement of the measurements with the predictions is quite good for the first order of multipactor if we consider the first three experimental values. Nevertheless, as the frequency-gap product increases different types of resonances might appear like the hybrid and polyphase modes, which have been proposed to better explain some experimental points obtained between the bands of different orders of multipactor [Gilarini 1992, Kryazhev 2002, Buyanova 2006, Udiljak 2007]. But the spread in the initial velocity of the secondary electrons shows already the possibility of finding experimental points between the bands for different orders of multipactor when the initial velocity is varied. Moreover, taking into account that the right-side boundaries of the multipactor zones are defined by $fd = N/4 \cdot (v_i + v_0)$, if we consider zero initial velocity, the multipactor susceptibility chart could also fit more experimental points.

Finally, the flow chart showing the procedure to assess the breakdown onset and to represent the susceptibility zones plotted in Fig. 2.15 is outlined next. We are going to enumerate the steps to follow in order to know whether multipactor of order N occurs within a parallel-plate waveguide assuming a fixed value for the initial velocity of the electrons. The impact velocity corresponding to the first and second cross-over point of the material considered is named v_1 and v_2 , respectively, and must be known to plot the multipactor susceptibility regions.

1. Fix the values of v_1 and v_2 according to the SEY properties of the material that the plates are made of.
2. Fix the order of multipactor, N , and the initial velocity, v_0 , that will be used.
3. Choose a value of the fd product.
4. Find the phase of resonance, α_{res} , that must apply, according to the value of fd :
 - If $fd < v_N$, the phase of resonance is $\alpha_{res} = \alpha_{res}^{(1)}$.
 - If $fd > v_N$, the phase of resonance is $\alpha_{res} = \alpha_{res}^{(2)}$.
5. Choose a value of the applied voltage between the plates, V_{RF} .

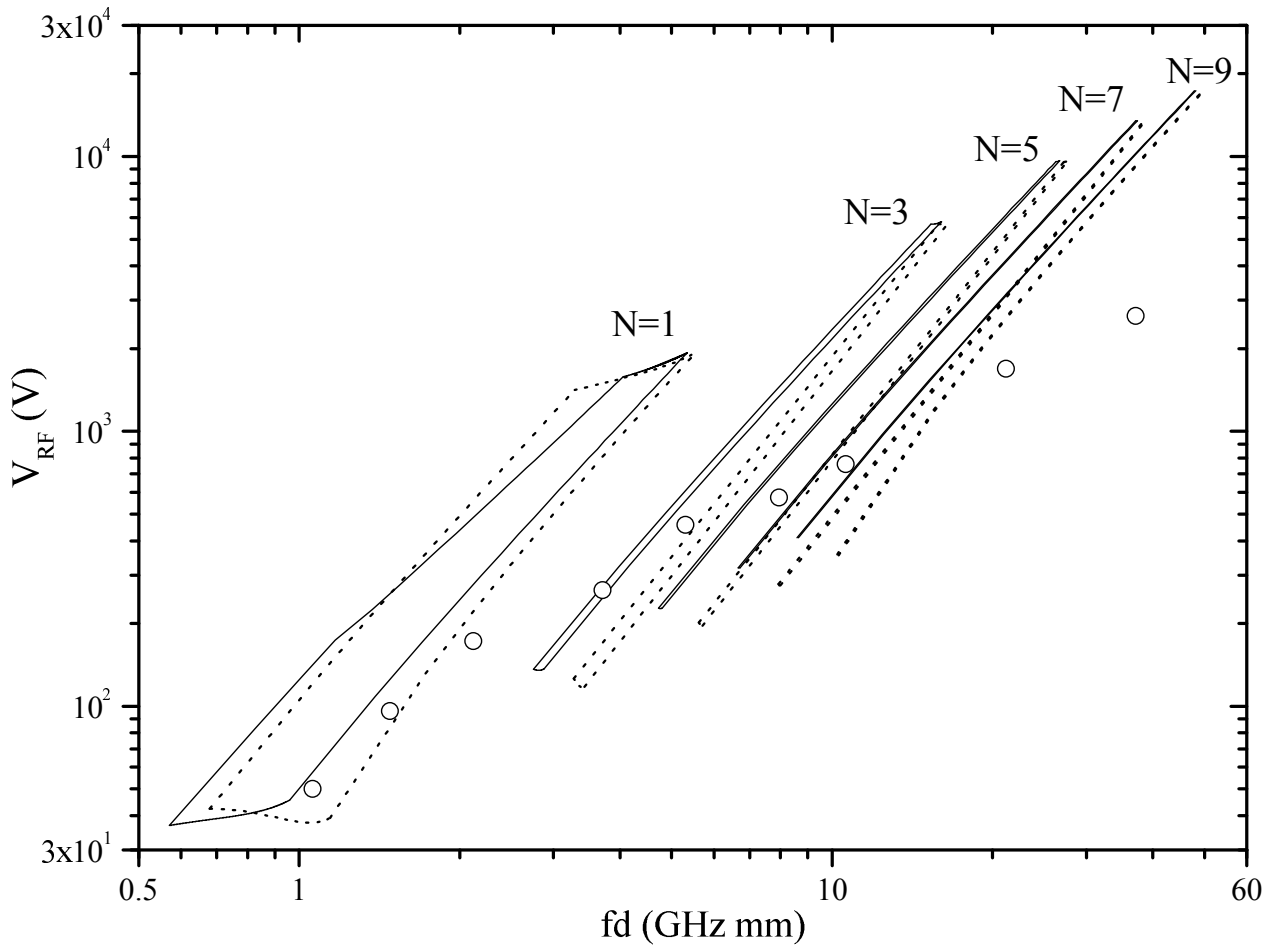


Figure 2.15: Multipactor susceptibility chart for $N = 1, 3, 5, 7, 9$ obtained with $v_0 = 1 \text{ eV}$ (solid) and $v_0 = 5 \text{ eV}$ (dashed) together with measurements (circles) obtained for a material whose first cross-over point is $E_1 = 30 \text{ eV}$.

6. To ensure that the phase of resonance is real-valued, (2.14) must be satisfied.
7. To ensure that the relative impact velocity is positive, (2.16a) must be satisfied.
8. To ensure the stability of the resonant motion of the electron, the inequality (2.21a) must be satisfied for the α_{res} obtained according to the value of the fd product.
9. To ensure the non-returning of the electron to the initial plate, the phase of resonance must satisfy $\pi > \alpha_{res} > \alpha_R^{(1)}$, where $\alpha_R^{(1)}$ is plotted in Fig. 2.12.
10. If everything above is satisfied, calculate the value of the impact velocity (2.7):
 - If $v_i < v_1$ or $v_i > v_2$, multipactor does not occur.
 - If $v_1 < v_i < v_2$, multipactor occurs.

2.7 Summary

In this chapter, we have presented the steps to follow in order to plot the multipactor susceptibility chart for a parallel-plate waveguide. This allows the study and design of new devices, where the parallel-plate approximation can be done, ensuring their optimal performance regarding the multipactor withstanding capabilities avoiding the risk of multipactor breakdown. Although the presence of hybrid modes allow a better fit of the predicted multipactor breakdown threshold to the experimental measurements, the classical resonance provides a satisfactory explanation of the multipactor breakdown voltage threshold. The plot of the multipactor susceptibility chart represents a useful tool in the study and design of corrugated filters or of more complex devices where small gaps might appear as a result of mechanical tolerances produced during the manufacturing process, like in coaxial connectors.

A slightly different interpretation of the boundaries of the multipactor susceptibility chart has been explained based on the restrictions imposed by the positive relative velocity at the impact time together with the stability and returning limit conditions. The value of the initial velocity has been proved to be crucial in the prediction of the multipactor breakdown threshold, showing a satisfactory agreement between the measurements and the predicted multipactor susceptibility chart for two different values of the initial velocity.

The multipactor breakdown threshold can also be studied tracking the motion of electrons subject to the electromagnetic field and calculating the collision energy and the corresponding SEY when impacting against the plates. The calculation of the SEY along the simulation time allows the calculation of the susceptibility chart and the plot of the breakdown voltage vs. the fd product by showing the amount of released secondary electrons at the end of the simulation. This analysis has shown to be useful for multi-carrier signals or for highly inhomogeneous distributions of the electromagnetic field, however, this process is, by far, computationally more expensive than the plot of the susceptibility chart in the way as presented in this chapter.

Radiation of a multipactor discharge

Contents

3.1	Introduction	41
3.2	Theory	42
3.2.1	Uniform current model	43
3.2.2	Point current model	48
3.3	Results	55
3.4	Summary	59

3.1 Introduction

The analysis of the radiated power produced by a multipactor current is very important from a practical point of view, because the noise created by the discharge is employed to experimentally detect the occurrence of the phenomenon (as the third-harmonic detection technique) [Udiljak 2003]. This method proposes the search of the third harmonic of the radiated power spectrum of the current produced by the electron cloud to witness the presence of the breakdown, since the first harmonic of the multipactor current is assumed to be obscured by the signal. The intensity of the radiated power spectrum depends on the number of electrons involved in the discharge [Sorolla 2008], and as multipactor steady-state is supposed to occur very quickly, the detection is assumed to take place when the saturation is reached.

The problem of saturation is analyzed in Chapter 5, but there is another ingredient that must be added to the analysis of the multipactor discharge in order to establish a criterion to assess its occurrence. In this chapter we are going to analyze the problem of the radiation of a multipactor discharge within a parallel-plate waveguide applying the “effective electron” or “single electron” model as in Chapter 2. In order to describe the multipactor current, the considered equations of motion do not take into account neither space charge effects, as presented in 2.2, nor the presence of the magnetic field. Then, the current of the electron cloud produced by the discharge will be assumed to move perpendicular to the plates, denoted as z -direction. The current produced by the electron cloud will be decomposed into harmonics and the electromagnetic field of each harmonic will be calculated finding the electromagnetic potentials. Once the electromagnetic fields are known, the radiated power of each harmonic will be found by evaluating the Poynting vector integrated across an imaginary surface far enough from the source, yielding the radiated power spectrum of the multipactor discharge.

The prediction of the radiated power spectrum together with an estimation of the saturation levels, and the comparison with measurements, should allow to define a criterion to assess the breakdown onset. This is the reason why the analysis of the radiated power spectrum produced by a multipactor current is important, since it will bring new insights towards the joint development of a multipactor onset criterion.

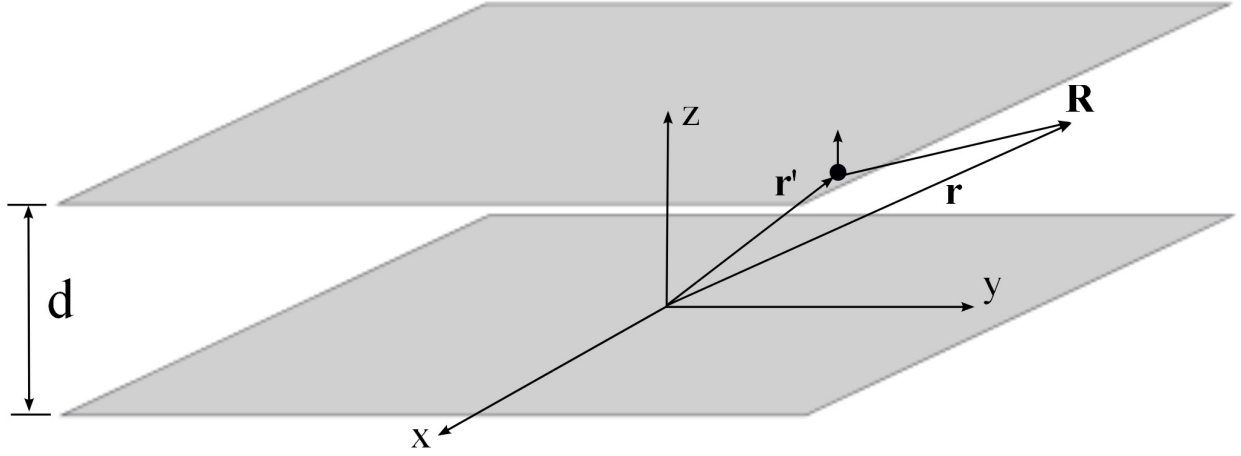


Figure 3.1: Electron moving between the parallel-plates.

3.2 Theory

If we consider the origin of coordinates at the bottom plate (see Fig. 3.1), we can describe the velocity of the electron by a piecewise function using (2.2a) as follows:

$$v_z(t) = \begin{cases} v_0 + v_\omega (\sin \alpha - \sin \omega t), & t \in \left(t_\alpha, t_\alpha + N \frac{T}{2} \right] \\ -v_0 - v_\omega (\sin \alpha + \sin \omega t), & t \in \left(t_\alpha + N \frac{T}{2}, t_\alpha + NT \right] \end{cases} \quad (3.1a)$$

$$(3.1b)$$

where N is the order of multipactor, $v_\omega = \frac{eV_{RF}}{m_e \omega d}$, T is the period of the microwave signal and $t_\alpha = \alpha/\omega$ is the instant when the electron leaves the bottom plate, since the time origin has been referred to the microwave signal. The variables α and $\omega = 2\pi f$ are the phase of the RF field when the electron leaves the birth plate and the angular frequency of the signal, respectively.

Note that this function is a periodic signal of period NT , thus the microwave frequency is given by f and the frequency of the signal represented by the velocity function is f/N . In Fig. 3.2 an example of velocity function for order of multipactor $N = 7$ is plotted, where the vertical axis shows the velocity of an electron driven by a harmonic electric field and the horizontal axis shows the time normalized to the RF period. Note how the velocity changes sharply from positive to negative values and later from negative to positive, what indicates the occurrence of the impact against the top and bottom plates, respectively. This cycle defines the period of the signal that represents the multipactor current.

By calling \mathbf{r}' and \mathbf{r} the electron's position vector and the observation point vector, respectively (see Fig. 3.1), we can define the current density generated by an electron moving with velocity v_z within the parallel-plate waveguide as:

$$\mathbf{J} = -ev_z(t)\delta(x - x')\delta(y - y')\delta(z - z'(t))\hat{z} = I_z\delta(x - x')\delta(y - y')\hat{z}, \quad (3.2)$$

where \hat{z} is the unit vector in the z direction. Note that the current has been calculated for a single electron, following the approach of the "effective electron" model. If we assume a homogeneous distribution of electrons

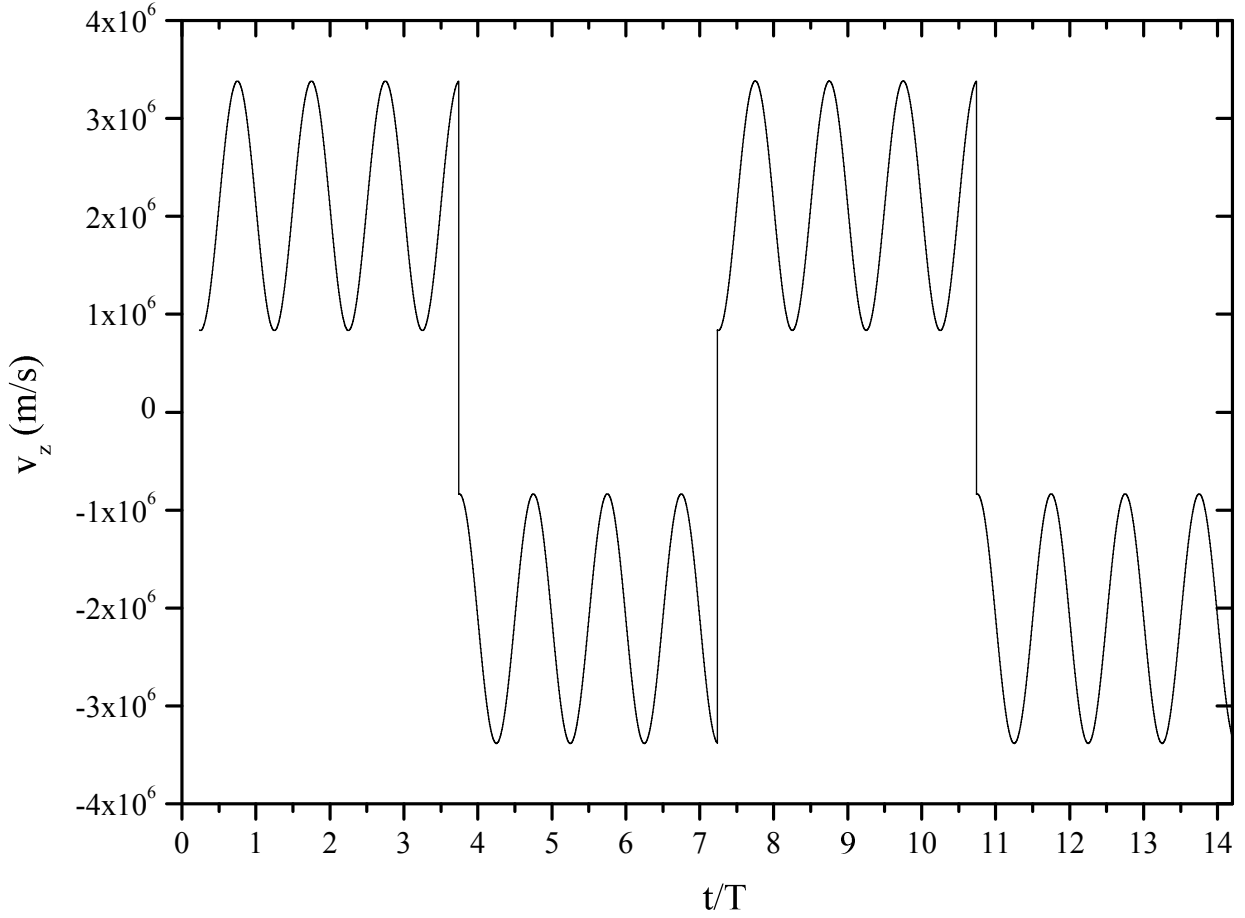


Figure 3.2: Example of the velocity function of an electron under multipactor regime for $N = 7$.

across the space between the plates that do not interact with each other, the total current defined by the electron cloud for the “effective electron” model in z -direction is defined by

$$I_z [z'(t)] = -ev_z(t)\delta(z - z'(t)). \quad (3.3)$$

3.2.1 Uniform current model

Taking into account that the distance between the plates is usually much smaller than the observation distance, we can calculate the space-averaged current associated to each electron defining an equivalent current as

$$I_{eq} \equiv \langle I_z [z'(t)] \rangle = \frac{-e}{d} \int_0^d v_z(t)\delta(z - z'(t))dz = \frac{-e}{d}v_z(t). \quad (3.4)$$

Once the equivalent current, which will be used to calculate the radiated power spectrum, has been defined, we can take advantage of the periodicity of the velocity function to develop it into a Fourier series. We can,

therefore, obtain the harmonics of the equivalent current that will be used later, approximating the velocity by

$$v_z(t) \approx \frac{1}{2}a_0 + \sum_{m=1}^{\infty} \{a_m \cos(\omega_m t) + b_m \sin(\omega_m t)\}, \quad (3.5)$$

where the angular frequency of the m -th harmonic is defined by $\omega_m = \frac{m}{N}\omega$.

The coefficients a_m and b_m are given by the integrals

$$\begin{cases} a_m = \frac{2}{NT} \int_{t_\alpha}^{t_\alpha+NT} v_z(t) \cos(\omega_m t) dt, & m = 0, 1, 2, \dots \\ b_m = \frac{2}{NT} \int_{t_\alpha}^{t_\alpha+NT} v_z(t) \sin(\omega_m t) dt, & m = 1, 2, \dots \end{cases} \quad (3.6a)$$

$$\quad (3.6b)$$

Then, substituting (3.1) into (3.6) we can find the coefficients

$$\begin{cases} a_m = \frac{2 [(-1)^m - 1] (v_0 + v_\omega \sin \alpha) \sin(m\alpha/N)}{m\pi} \\ b_m = -v_\omega \delta_{m,N} + \frac{2 [(-1)^m - 1] (v_0 + v_\omega \sin \alpha) \cos(m\alpha/N)}{m\pi} \end{cases} \quad (3.7a)$$

$$\quad (3.7b)$$

where $\delta_{m,N}$ is the Kronecker delta.

As the velocity defined in (3.1) is an odd function, only the odd harmonics do not vanish, as it can be seen by substituting the index m by any even number in (3.7), which sets null the numerator of the fractions. Moreover, since the order of multipactor for the classical resonance conditions is also an odd number, the Kronecker delta yields a null value and the coefficient b_m vanishes for every even harmonic, too.

We can make use of an alternative expression for the Fourier series defined in (3.5) as follows:

$$v_z(t) \approx \sum_{m=1}^{\infty} c_m \cos(\omega_m t - \delta_m), \quad (3.8)$$

where the new coefficients are related to a_m and b_m by the expressions

$$\begin{cases} c_m = \sqrt{a_m^2 + b_m^2} \\ \delta_m = \arctan\left(\frac{b_m}{a_m}\right). \end{cases} \quad (3.9a)$$

$$\quad (3.9b)$$

Thus, we can rewrite the equivalent current as follows:

$$I_{eq} = -\frac{e}{2d} \sum_{\substack{m=-\infty \\ (m \text{ odd})}}^{+\infty} c_m e^{j(\omega_m t - \delta_m)} = \sum_{\substack{m=1 \\ (m \text{ odd})}}^{+\infty} \left(-\frac{e}{d} c_m \cos(\omega_m t - \delta_m) \right) \quad (3.10)$$

which allows us to define a complex current $\tilde{I}_m \equiv -\frac{e}{d} c_m e^{j(\omega_m t - \delta_m)}$ for which the m -th harmonic is defined as

$$i_m = -\frac{e}{d} c_m e^{-j\delta_m}. \quad (3.11)$$

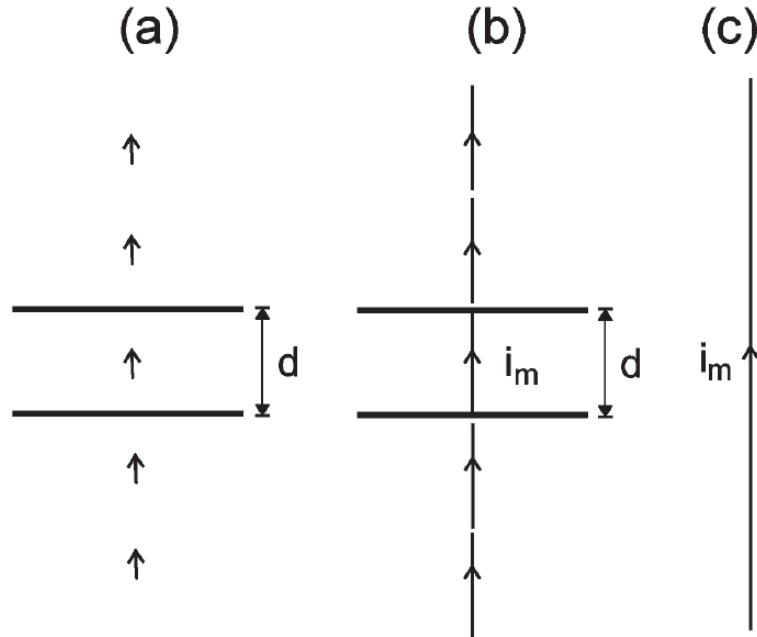


Figure 3.3: Description of the multipactor current. (a) Sketch of the set of images for a point current between two parallel-plates. (b) Sketch of the set of images for the equivalent uniform current within the parallel-plate region. (c) Equivalent multipactor current in the parallel-plate waveguide is equivalent to an infinitely long uniform wire current.

Once the current associated to each harmonic is found, the vector potential can be calculated by finding the Green function of the Helmholtz equation for the vector potential within a parallel-plate region and integrating with the equivalent current. For an unbounded parallel-plate waveguide, the image theory provides a very easy solution for representing the Green function. It is known that the image of a negative point charge in front of an infinitely long metal plate is the same charge with opposite sign, placed on the other side of the plate at the same distance [Panofsky 1955]. Therefore, the current source and the image currents are oriented in the same direction. Taking into account the presence of both plates and the superposition principle, it can be proved that the set of images can be represented by the sketch shown in Fig. 3.3 (a). If we consider the space-averaged equivalent current of multipactor, the image theory defines a set of images that has been depicted in Fig. 3.3 (b). At the end, the problem has become the calculation of the radiation of a limitless uniform vertical current i_m radiating into the free-space sketched in Fig. 3.3 (c).

Therefore, we need to calculate the electromagnetic fields radiated by a uniform time-harmonic current oscillating with frequency f_m , as shown in Fig. 3.3 (c). For simplicity, the cylindrical coordinates system will be used to calculate the radiated fields. We will use the scalar and vector potentials formulation for the time-harmonic fields in free-space, which is based on the calculation of both the electric scalar ϕ and the magnetic vector potential \mathbf{A} , satisfying the Lorenz gauge [Balanis 1989]. Since the current i_m is oriented along the z -axis, it can be proved that the only non-zero component of the vector potential is the z component, denoted

as A_{z_m} , which satisfies the Helmholtz differential equation

$$\nabla^2 A_{z_m} + k_m^2 A_{z_m} = -\mu_0 i_m \quad (3.12)$$

where μ_0 is the magnetic permeability of free-space and $k_m = m(k/N)$, with $k = \omega/c$.

In order to find the vector potential from the Helmholtz equation we can apply the convolution of the free-space Green function with the current i_m ,

$$A_{z_m}(\mathbf{r}) = \mu_0 \int_{-\infty}^{\infty} i_m g_m^{(0)}(\mathbf{r}, \mathbf{r}') dz' \quad (3.13)$$

where the free-space Green function $g_m^{(0)}(\mathbf{r}, \mathbf{r}')$ is defined as

$$g_m^{(0)}(\mathbf{r}, \mathbf{r}') = \frac{e^{-jk_m R}}{4\pi R}. \quad (3.14)$$

The variable R is the magnitude of the vector \mathbf{R} , which defines the relative position of the observation point, \mathbf{r} , with respect to the source point, \mathbf{r}' , i.e., $\left(R = \sqrt{(\rho - \rho')^2 + (z - z')^2}\right)$ (see Fig. 3.4).

Therefore, the expression of the vector potential can be found in cylindrical coordinates as follows:

$$A_{z_m}(\mathbf{r}) = \frac{\mu_0}{4\pi} i_m \int_{-\infty}^{\infty} \frac{\exp\left\{-jk_m \sqrt{\rho^2 + (z - z')^2}\right\}}{\sqrt{\rho^2 + (z - z')^2}} dz' \quad (3.15)$$

where $\rho' = 0$ has been substituted in the expression of the free-space Green function. The result of the integral can be proved to be

$$A_{z_m}(\rho) = \mu_0 i_m \left(\frac{H_0^{(2)}(k_m \rho)}{4j} \right) \quad (3.16)$$

where $H_0^{(2)}$ is the zeroth-order Hankel function of the second kind. In fact the term between brackets represents the free-space 2D Green function, since the dependence of the vector potential on the z -coordinate has disappeared by the symmetry of the structure. Once the scalar potential is known, the electric scalar potential can be found using the Lorenz gauge, resulting in

$$\phi_m = j \frac{c}{k_m} \nabla \cdot (A_{z_m} \hat{z}) = j \frac{c}{k_m} \frac{\partial A_{z_m}}{\partial z} = 0. \quad (3.17)$$

The electromagnetic fields can be calculated using the electromagnetic potentials as follows:

$$\begin{cases} \mathbf{E} = -\nabla\phi - \frac{\partial \tilde{\mathbf{A}}}{\partial t} \\ \mathbf{H} = (1/\mu_0) \nabla \times \tilde{\mathbf{A}}. \end{cases} \quad (3.18a)$$

$$(3.18b)$$

where $\tilde{\mathbf{A}} = \mathbf{A}e^{j\omega_m t}$.

In order to calculate the far-field expressions of the electromagnetic fields the approximation of the Hankel function for large values of the argument is applied:

$$H_0^{(2)}(x) \approx \sqrt{\frac{2}{\pi x}} e^{-j(x-\pi/4)},$$

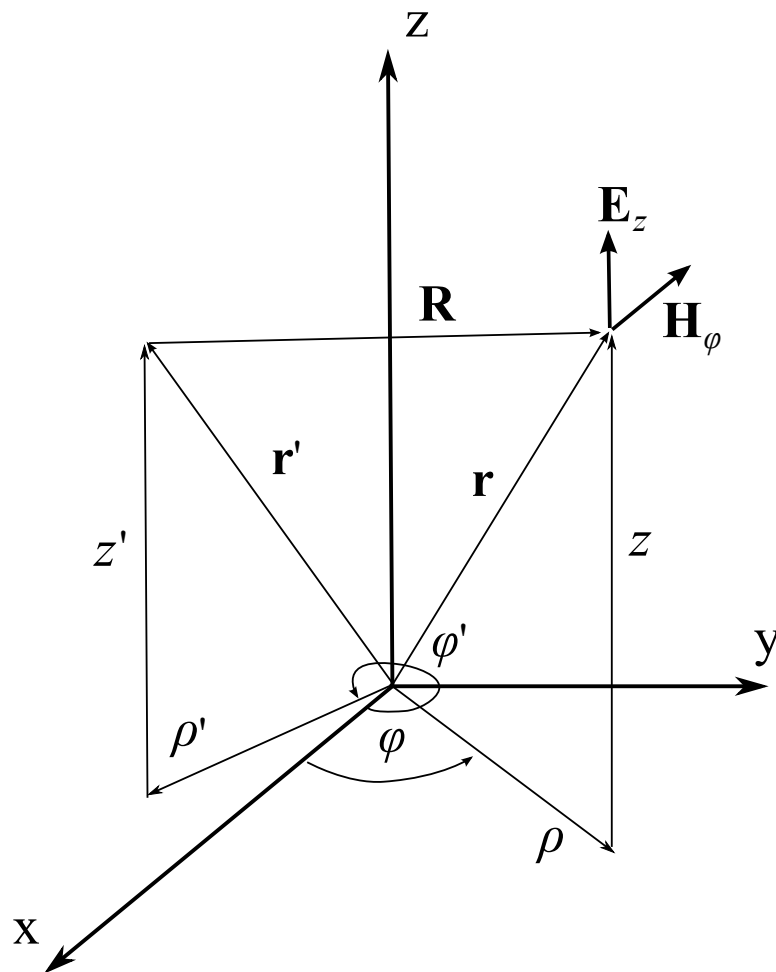


Figure 3.4: Radiated electromagnetic field and the cylindrical system of coordinates used in the calculation of the radiated fields.

which can be substituted into (3.16) and (3.18) to obtain

$$\begin{cases} \mathbf{E}_m^{rad} = -j\omega_m A_{z_m} \hat{z} \approx -\mu_0 \omega_m i_m \sqrt{\frac{1}{8\pi k_m \rho}} e^{-j(k_m \rho - \pi/4)} \hat{z} \\ \mathbf{H}_m^{rad} = \frac{1}{\mu_0} \nabla \times (A_{z_m} \hat{z}) \approx \left(\frac{-j}{2\rho^{3/2}} + \frac{k_m}{\rho^{1/2}} \right) i_m \sqrt{\frac{1}{8\pi k_m}} e^{-j(k_m \rho - \pi/4)} \hat{\phi}. \end{cases} \quad (3.19a)$$

$$\quad (3.19b)$$

The first term within the brackets in the expression of the magnetic field will be neglected, since it will not contribute to the radiated power as the product with the electric field will decay faster than the differential surface element, which is proportional to ρ . The configuration of the far fields of the considered problem is shown in Fig. 3.4. Note that the electric and magnetic fields are supposed to be far enough from the current source to be considered as the radiated electromagnetic fields.

With the values of the far fields, the radiated power can be calculated by integrating the Poynting vector on the surface of an imaginary cylinder of radius L surrounding the uniform current (see Fig. 3.5). Since the electromagnetic fields are time-harmonic signals, the time-averaged Poynting vector associated to the electromagnetic fields (3.19) for each harmonic of the current can be written

$$P_m^{rad} = \frac{1}{2} \int_{\varphi=0}^{\varphi=2\pi} \rho d\varphi \int_{z=0}^{z=d} \text{Re} \left[\mathbf{E}_m^{rad} \times \left(\mathbf{H}_m^{rad} \right)^* \right] dz \quad (3.20)$$

for $\rho = L$, where $*$ denotes the complex conjugate.

Therefore, the time-averaged power radiated by a single electron moving in resonance with the RF field within the parallel-plate waveguide is given by

$$P_m^{rad} = \frac{\mu_0 \omega_m}{16\pi} |i_m|^2 \int_{\varphi=0}^{\varphi=2\pi} L d\varphi \int_{z=0}^{z=d} \frac{dz}{L} = 10^{-7} \pi^2 \frac{m}{N} f d |i_m|^2, \quad (3.21)$$

where the value for the free-space permeability $\mu_0 = 4\pi \cdot 10^{-7} \text{ V} \cdot \text{s}/(\text{A} \cdot \text{m})$ has been used.

Taking into account (3.6), (3.9) and (3.11) the value of $|i_m|^2$ can be expressed as function of the variables used in Chapter 2 in order to rewrite the analytical formula for the radiated power of the multipactor discharge in a more useful way

$$P_m^{rad} = 10^{-7} \pi^2 \frac{m}{N} \frac{f}{d} e^2 \left[\left(\frac{x}{m\pi} \right)^2 + \left(v_\omega + \frac{4x \cos(m\alpha/N)}{m\pi} \right) v_\omega \delta_{m,N} \right] \quad (3.22)$$

where the variable $x = (v_0 + v_\omega \sin \alpha)$ has been defined.

3.2.2 Point current model

In order to validate the expression of the radiated power spectrum for a multipactor discharge (3.22), we are going to calculate the radiated power spectrum of the same problem applying the image method to the infinitesimal current produced by the electron moving between the plates driven by the microwave field.

To do so let us recall (3.3) and let us apply the property of the Dirac delta distribution

$$\delta [h(t)] = \sum_{p=1}^M \frac{\delta(t - t_p)}{|\dot{h}(t_p)|}, \quad |\dot{h}(t_p)| \neq 0, \quad (3.23)$$

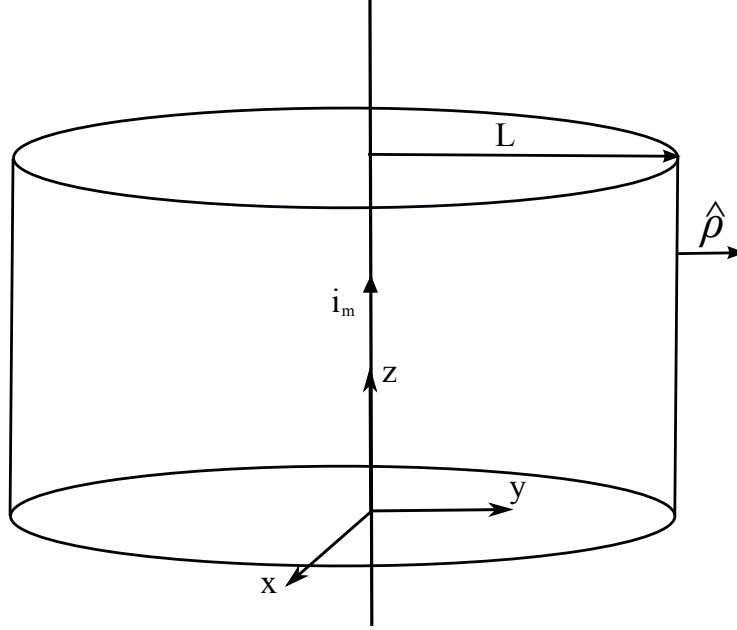


Figure 3.5: Imaginary cylinder surrounding the uniform current. The radial component of the Poynting vector is integrated on the side walls of the cylinder.

where $h(t) = z - z'(t)$ and M is the number of roots of this function, t_p representing the value of the root. The time derivative of that function is represented by $\dot{h}(t) = v_z(t)$, which is evaluated at the instant t_p . Thus, the rigorous form of the multipactor current is

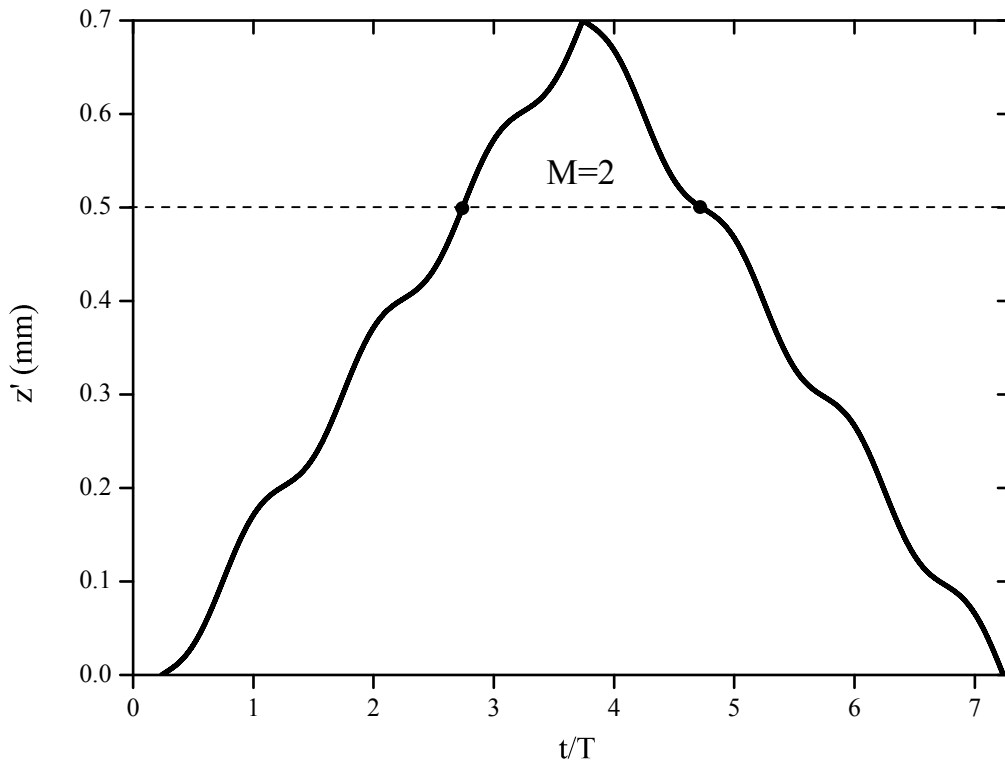
$$I_z [z'(t)] = -e v_z(t) \sum_{p=1}^M \frac{\delta(t - t_p)}{|v_z(t_p)|} = -e \sum_{p=1}^M \frac{v_z(t_p)}{|v_z(t_p)|} \delta(t - t_p) \quad (3.24)$$

where the dependency on the z -coordinate has been transferred to the knowledge of the instant t_p when the electron is placed at the position z' . In general, the amount of roots, M , for the classical resonance condition (2.3) is two for any order of multipactor, N , as it can be clearly seen in Fig. 3.6a.

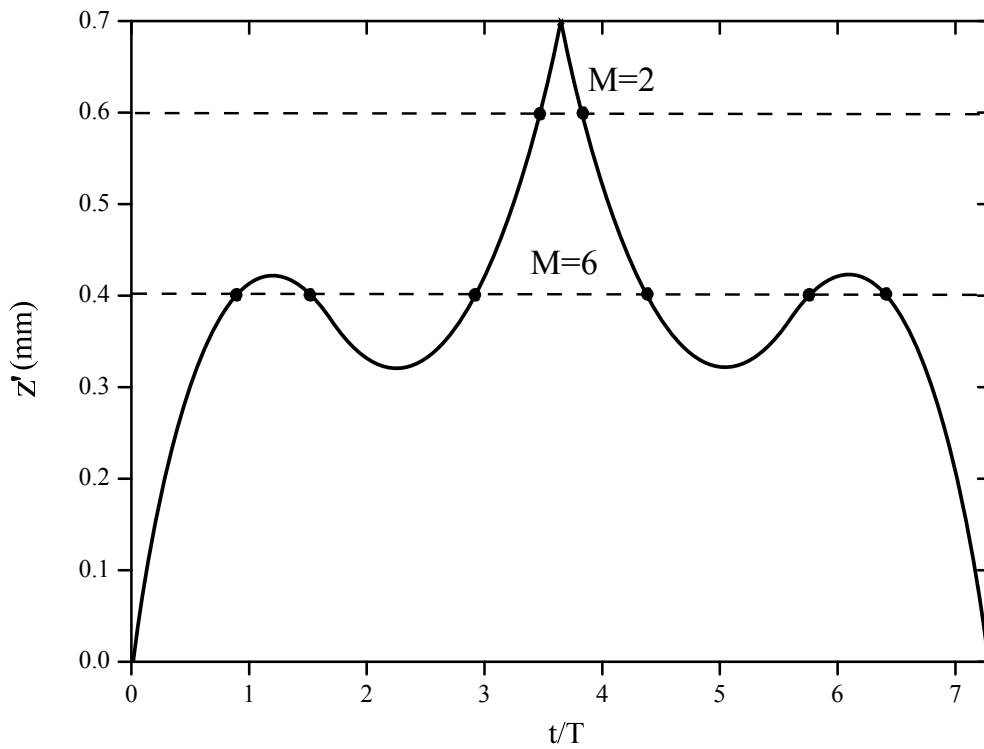
Nevertheless, there might be some cases for which the number of roots is bigger than two if the electron reduces its velocity below zero and it passes by the same point three times during its flight from the bottom to the top plate. As the classical resonance predicts the same transit time from the top plate to the bottom one, the same occurs when traveling in the opposite direction, as it has been depicted in Fig. 3.6b, where the number of roots at $z = 0.4$ mm is $M = 6$. This must be taken into account when using (3.24), since the amount of roots that must be calculated depends, in general, on the position of the electron between the plates.

As (3.24) is non-zero when $t = t_p$, the coefficients of the Fourier series of the point current read as follows:

$$\begin{cases} \tilde{a}_m(z) = \frac{2}{T} \sum_{p=1}^M \text{sgn} [v_z(t_p)] \cos(\omega_m t_p), m \in \mathbb{N}^0 & (3.25a) \\ \tilde{b}_m(z) = \frac{2}{T} \sum_{p=1}^M \text{sgn} [v_z(t_p)] \sin(\omega_m t_p), m \in \mathbb{N}^+ & (3.25b) \end{cases}$$



(a) In this case there exist only two roots ($M = 2$) at any position.



(b) In this case there are more than two roots within a certain range of positions.

Figure 3.6: Roots of the function $g(t)$ within a period of the velocity signal for $d = 7$ mm and $N = 7$.

where the coefficients of the Fourier series depend implicitly on the z coordinate via the instant t_p . Using the alternative definition of the Fourier series, the point current can be represented as

$$I_z(z) \approx -e \sum_{m=1}^{\infty} \tilde{c}_m(z) \cos(\omega_m t - \tilde{\delta}_m(z)), \quad (3.26)$$

where the new coefficients \tilde{c}_m and $\tilde{\delta}_m$ depend now on the position of the electron. Some examples of the Fourier coefficients vs. the position of the electron within the plates are shown in Fig. 3.7 for different orders of multipactor.

In this case the complex current is defined as $\tilde{I}_m(z) \equiv -e\tilde{c}_m(z)e^{j(\omega_m t - \tilde{\delta}_m(z))}$ for which the m -th harmonic is now defined as

$$i_m(z) = -e\tilde{c}_m(z)e^{j\tilde{\delta}_m(z)}. \quad (3.27)$$

The representation of the current provided by (3.26) at different values of the z coordinate is shown in Fig. 3.8 calculated with 100, 1000 and 10000 harmonics. Note that the current is negative in the first part of the plot since the electron's charge is negative and the electron travels from the bottom to the top plate in the positive direction of the z -axis. The positive current represents the travel back of the electron from the top to the bottom plate. The current actually represents the motion of the electron vs. time at different positions. Indeed, note that the negative current evaluated at $z = 0.75$ mm becomes positive prior to currents evaluated at other positions, since the electron passes by that point before arriving to the subsequent positions on its way back to the bottom plate. It is worth-while remarking that the vertical scale of the plot increases by an order of magnitude as the number of harmonics used to represent the point current is augmented by the same factor.

In this case, as the direction of the currents is along the z -axis, the non-null component of the vector potential is the z component as well. Substituting the harmonic current (3.27) into (3.13) with the corresponding Green function the vector potential for the point current can be calculated as

$$A_{z_m}(\rho, z) = -e\mu_0 \left\{ \int_0^d \tilde{c}_m(z') e^{j\tilde{\delta}_m(z')} g_m(\mathbf{r}; \mathbf{r}') dz' \right\} \quad (3.28)$$

where the Green function of the point current within the parallel-plates in this case is calculated applying the image method for a point current, thus, becoming a series of free-space Green function applied at the position of the image currents. Thus, the Green function of the vector potential can be expressed as [Hanson 2002]

$$g_m(\mathbf{r}; \mathbf{r}') = \sum_{s=-\infty}^{+\infty} g_m^{(0)}(\mathbf{r}; \mathbf{r}'_s) = \frac{1}{4\pi} \sum_{s=-\infty}^{+\infty} \left(\frac{e^{-jk_m R_s^+}}{R_s^+} + \frac{e^{-jk_m R_s^-}}{R_s^-} \right) \equiv g_m(\mathbf{r}; z') \quad (3.29)$$

where $R_s^\pm = \sqrt{\rho^2 + (z \mp z' - 2sd)^2}$, with z and z' the vertical coordinate of the observation and the source point, respectively, in the cylindrical coordinates system, and where the radial coordinate of the electron has been arbitrarily taken to be $\rho' = 0$.

The magnetic field can be calculated using the expression (3.18b) and (3.29), what results in

$$\mathbf{H}_m = H_{\varphi_m} \hat{\varphi} = -\frac{1}{\mu_0} \frac{\partial A_{z_m}}{\partial \rho} \hat{\varphi} = e\hat{\varphi} \int_0^d \frac{\partial g_m(\mathbf{r}; z')}{\partial \rho} \tilde{c}_m(z') e^{j\tilde{\delta}_m(z')} dz'. \quad (3.30)$$

In order to calculate the electric field we need to calculate the electric scalar potential from the Lorenz gauge, obtaining

$$\phi_m = \frac{j}{\omega_m \mu_0 \epsilon_0} \nabla \cdot A_{z_m} \hat{z}, \quad (3.31)$$

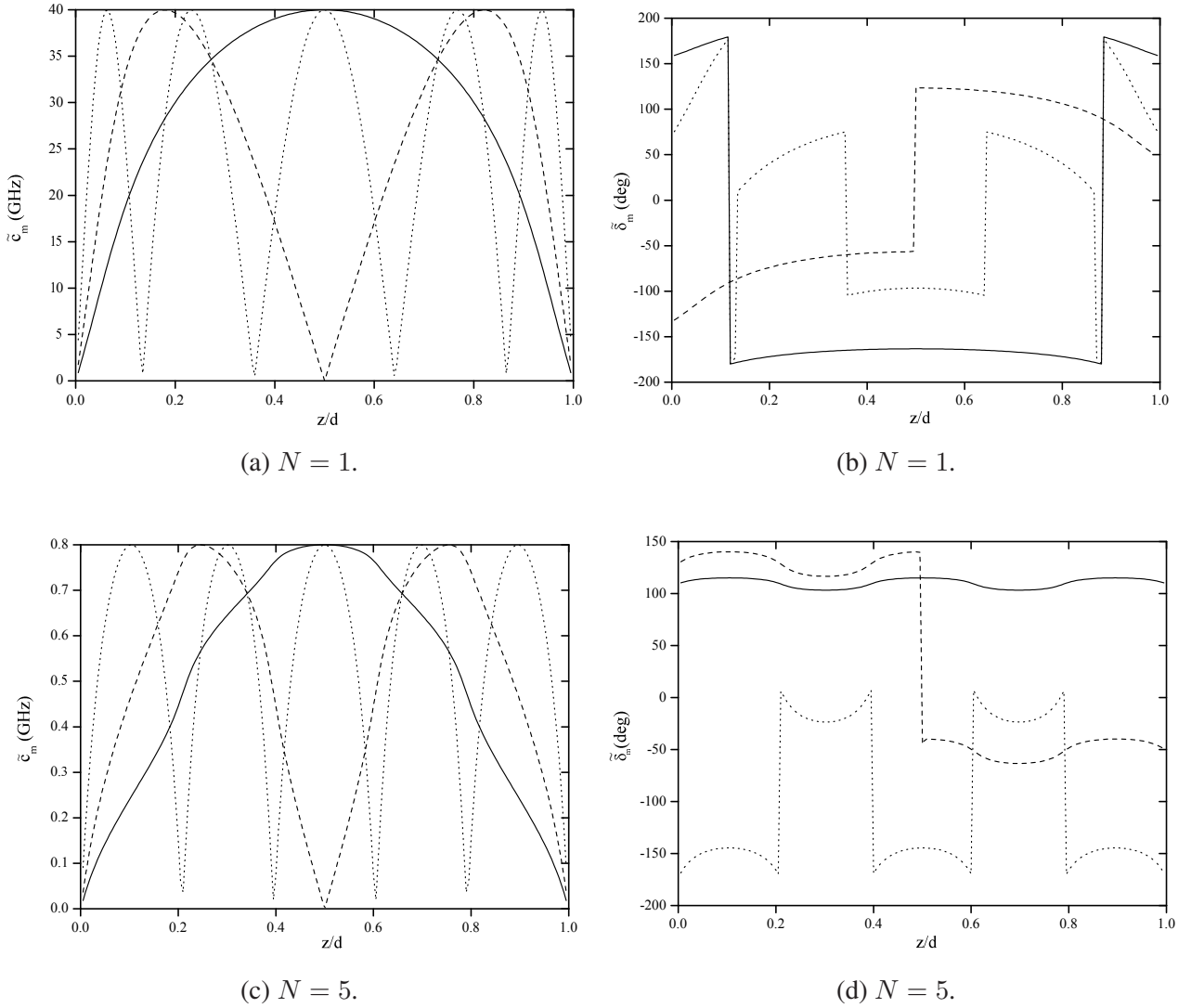


Figure 3.7: Fourier coefficients of the current (3.24) for the harmonics $m = 1$ (solid), $m = 2$ (dashed), $m = 5$ (dotted). The parameters for $N = 1$ are: $f = 10$ GHz, $d = 0.1$ mm, $v_0 = 2$ eV, $V_{RF} = 60$ V and $\alpha_{res} = 68.16$ deg. For $N = 5$: $f = 1$ GHz, $d = 15.65$ mm, $v_0 = 3.68$ eV, $V_{RF} = 412.34$ V and $\alpha_{res} = 97.15$ deg.

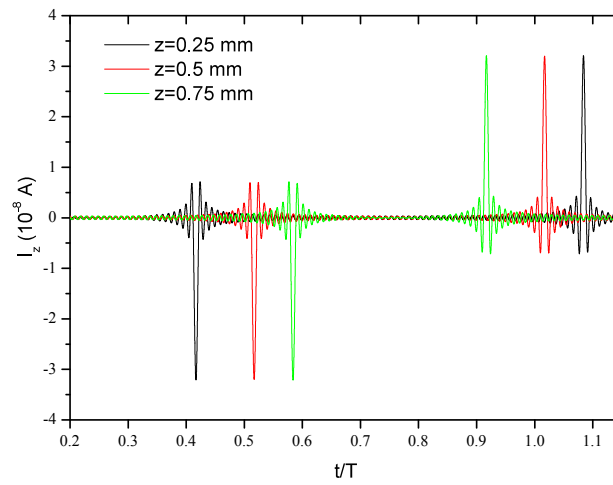
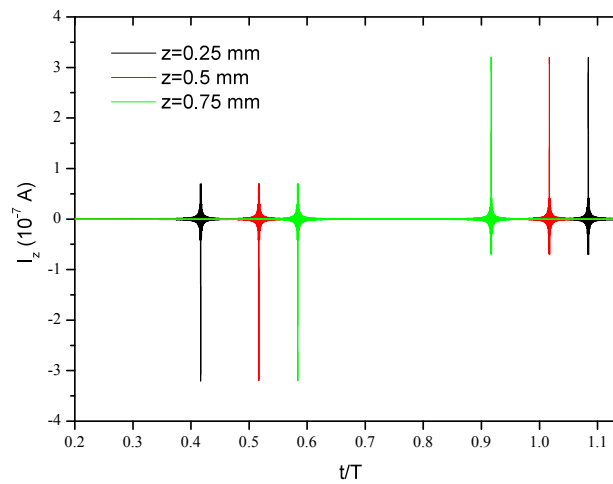
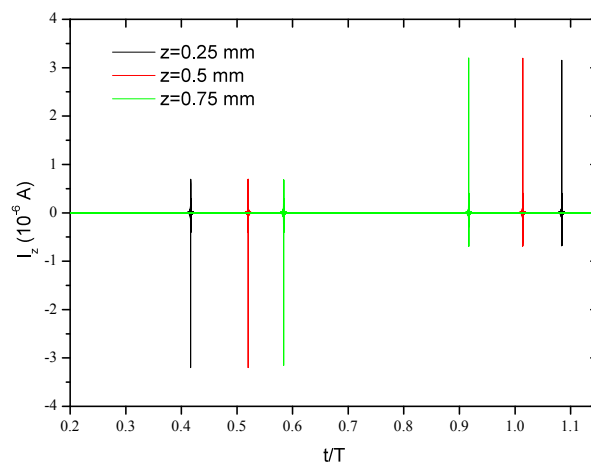
(a) $m = 100$.(b) $m = 1000$.(c) $m = 10000$.

Figure 3.8: Fourier series representation of the point current within a parallel-plate waveguide of distance $d = 1$ mm at different positions for 100, 1000 and 10000 harmonics (a-c), respectively.

where ϵ_0 is the free-space permittivity. Then, the electric field $\mathbf{E}_m = E_{\rho m} \hat{\rho} + E_{z m} \hat{z} = -\nabla \phi_m - j\omega_m A_{z m} \hat{z}$ can be calculated using (3.18a), whose components are

$$\begin{cases} E_{\rho m} = \frac{-j}{\omega_m \mu_0 \epsilon_0} \frac{\partial^2 A_{z m}}{\partial \rho \partial z} & (3.32a) \\ E_{z m} = \frac{-j}{\omega_m \mu_0 \epsilon_0} \frac{\partial^2 A_{z m}}{\partial z^2} - j\omega_m A_{z m}. & (3.32b) \end{cases}$$

Substituting the value of the vector potential given by (3.28) into (3.32) we can rewrite the components of the electric field as

$$\begin{cases} E_{\rho m} = \xi \int_0^d \frac{\partial^2 g_m(\mathbf{r}; z')}{\partial \rho \partial z} \tilde{c}_m(z') e^{j\tilde{\delta}_m(z')} dz' & (3.33a) \\ E_{z m} = \xi \int_0^d \left[\frac{\partial^2 g_m(\mathbf{r}; z')}{\partial z^2} + (mk_m)^2 g_m(\mathbf{r}; z', \hat{z}) \right] \tilde{c}_m(z') e^{j\tilde{\delta}_m(z')} dz' & (3.33b) \end{cases}$$

where $\xi \equiv j \frac{e}{\omega_m \epsilon_0}$.

The main difference between the electric field evaluated with the point current model and the one done with the uniform current model (Section 3.2.1) is the appearance of a radial component. But this component is only important near the source, and it has shown to be around 5 orders of magnitude smaller than the z component of the field for large values of ρ . This is expected since both models of the current must yield the same results at the far-field region. It must be remarked that the near field decays faster for the high harmonics than for the fundamental one, whose frequency lies closer to the carrier frequency. This results in some differences between the electromagnetic fields evaluated with both models near the source for the first harmonic, as it will be shown later.

An accurate evaluation of the electric field and, subsequently, of the radiated power spectrum, requests many terms in the image series (3.29) in order to suitably represent the Green function due to the slow convergence of the series. This makes impractical the calculation of the vector potential at several points to integrate and calculate the electric field, and the same can be said for the evaluation of the space-integral of the time-averaged Poynting vector. In order to circumvent this problem some acceleration techniques [Ewald 1921, Park 1998, Kustepeli 2000, Capolino 2005, G. Valerio 2007, Gimeno 2009] have been applied to that series which reduced noticeably the time in the calculation of the electric and magnetic fields.

Once the electromagnetic fields are known, the Poynting vector can be found and the integral of its time-average value evaluated on the side walls of an imaginary cylinder of radius $\rho = L$ surrounding the source current and its images, as done in the previous model. Therefore, we substitute the fields given by (3.30) and (3.33) into (3.20) to calculate the radiated power as follows:

$$P_m^{rad} = \lim_{\rho \rightarrow \infty} \left\{ \frac{1}{2} \int_{\varphi=0}^{\varphi=2\pi} \rho d\varphi \int_{z=0}^{z=d} \text{Re} \left[(E_{\rho m} \hat{\rho} + E_{z m} \hat{z}) \times H_{\varphi m}^* \hat{\varphi} \right] \cdot \hat{\rho} dz \right\}. \quad (3.34)$$

The first term of the integral above does not contribute to the radiated power since $\hat{\rho} \times \hat{\varphi} = \hat{z}$, which is perpendicular to the unit vector $\hat{\rho}$, but the second term provides the radiation that, for practical purposes, will be evaluated at a finite distance $\rho = L$ far enough from the source as to be considered the far-field contribution.

3.3 Results

The electromagnetic fields obtained with both models of the current are presented and compared in this section. In Fig. 3.9 the real and imaginary parts of the z component of the electric field are shown vs. the distance over the microwave wavelength ratio for the first and third harmonic of the Fourier series. It must be remarked that only the odd harmonic provide non-zero values of the electromagnetic field.

Note the excellent agreement between the results obtained with both models of the current even for points near the source, except for the imaginary part of the magnetic field of the first harmonic near the source (see Fig. 3.10b). This discrepancy arises because the curl of the vector potential for the uniform current model introduces a pure imaginary factor that decays as $-\rho^{-3/2}$, which is negligible far from the source. However, near the source this term appears as a result of the uniform current model that assumed the presence of an unbounded source, what differs from the reality more remarkably near the actual point charge. This factor tends to minus infinity close to the source point, what predicts a singularity in the imaginary part of the magnetic field near the source (see (3.19b)), whereas for the point current model the imaginary part of the magnetic field for the fundamental harmonic tends to zero near the source. As it was commented above, the near field for higher harmonics than the fundamental one decays faster beyond a certain distance, what explains why this discrepancy is not observed in the magnetic field for the third harmonic. Nevertheless, the values of the magnetic field calculated with both models of the current beyond a certain distance agree very well with each other, as it has been pointed out above.

It must be remarked that the frequency in the oscillations of the electric and magnetic fields for the third harmonic is higher than for the first one, what implies that the high harmonics of the radiated power spectrum are more expensive to calculate. Since the high harmonics oscillate more rapidly than the low ones, the number of sampling points that must be considered in the numerical calculation of the integral (3.34) must be larger as the harmonic number increases to ensure the accuracy of the cubature used. This entails that the evaluation of the radiated power spectrum for the high harmonics will be less accurate than for the low harmonics with the same number of sampling points. The results of the radiated power spectrum shown later, as well as the ones of the electric and magnetic fields, have been obtained using the Gauss-Legendre cubature in the calculation of (3.30), (3.33) and (3.34) with enough number of sampling points as to ensure that the results are accurate enough.

The radiated power spectrum of a single electron in resonance with the electromagnetic field of a parallel-plate waveguide for order of multipactor one has been plotted in Fig. 3.11 using (3.22), and evaluating numerically the integral (3.34) with $\rho = 1$ m. The distance between the plates is $d = 1$ mm and the microwave frequency $f = 1$ GHz. The initial velocity of the secondary electrons was assumed to be $v_0 = 3.68$ eV, the RF voltage $V_{RF} \approx 86.32$ V and the phase of resonance $\alpha_{res} = 50$ deg. Note the perfect agreement between the radiated power spectrum predicted by both models of the current for the first 5 non-vanishing harmonics. The number of points considered in the calculation of the integral (3.34) for the highest harmonic was 100 for the evaluation of the Poynting vector at $\rho = 1$ m. This distance implies around 3 times the microwave wavelength, thus around 30 times the wavelength associated to the harmonic $m = 9$, so 100 points seem to be enough in the Gauss-Legendre cubature to evaluate accurately the radiated power spectrum for this harmonic.

Note that the radiated power spectrum plotted in Fig. 3.11 shows a decrease in the power levels following a $1/m$ behavior, as predicted by (3.22), except for the harmonic $m = N$, whose power level is maximum. Note also that, as expected, the maximum in the power spectrum lies always on the microwave frequency, f , regarding the order of multipactor, N . Nevertheless, as the frequency associated to the m -th harmonic of the electron current is given by mf/N , the maximum in the power spectrum occurs at the harmonic that coincides

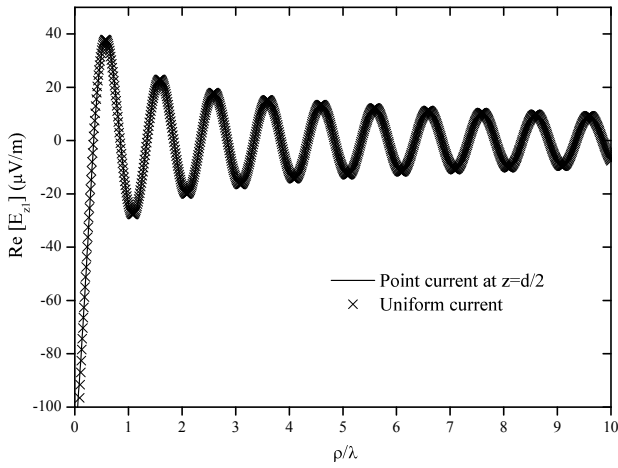
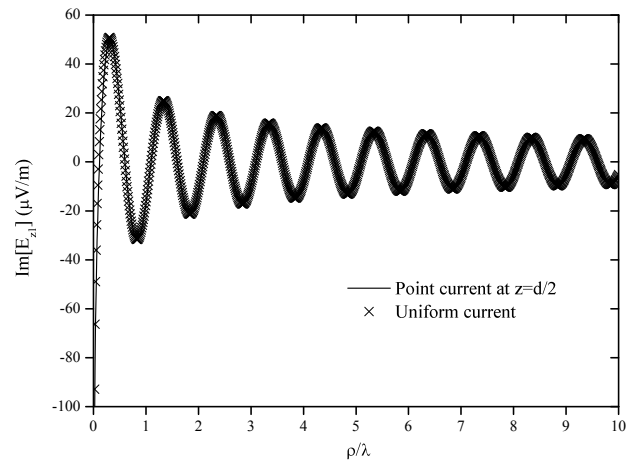
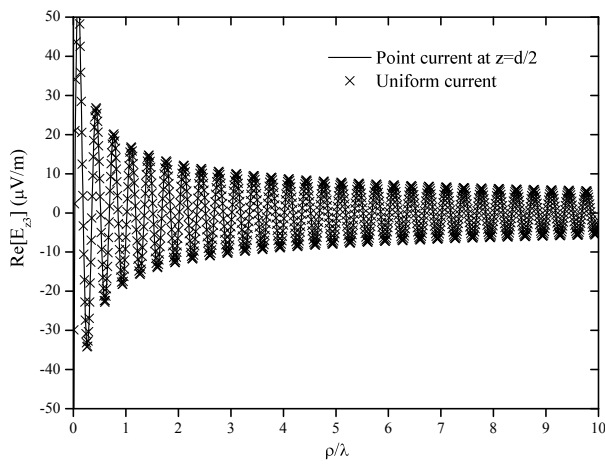
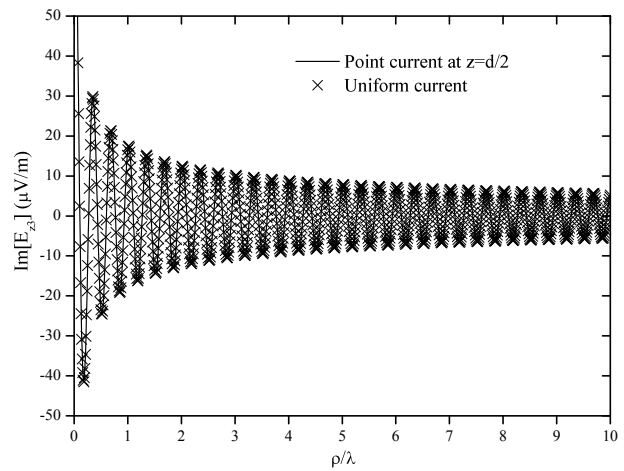
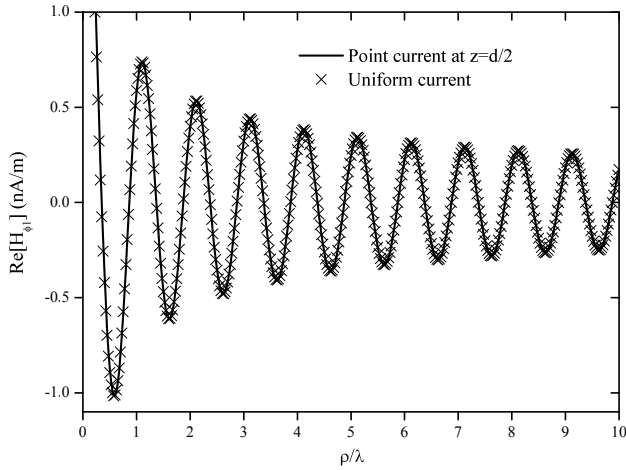
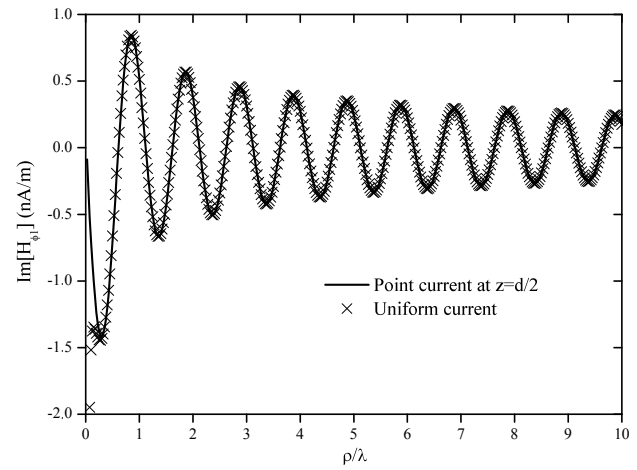
(a) $\text{Re} [E_{z1}]$.(b) $\text{Im} [E_{z1}]$.(c) $\text{Re} [E_{z3}]$.(d) $\text{Im} [E_{z3}]$.

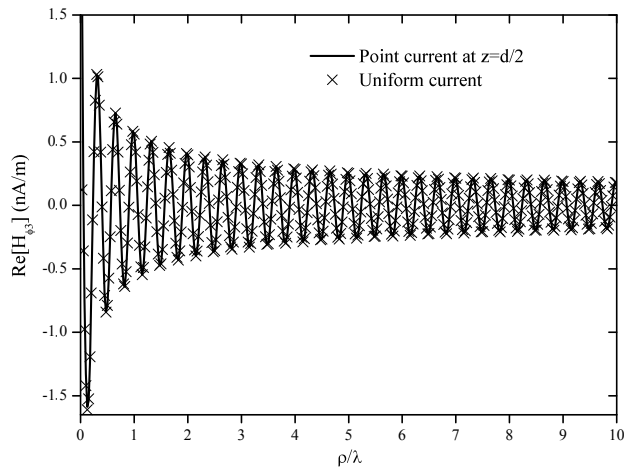
Figure 3.9: Vertical component of the electric field vs. ρ/λ for the first (top) and third (bottom) Fourier harmonics. Like for the uniform current model, in this case the values of the electric field for the even harmonics are null because of the odd symmetry of the velocity function. The crosses show the results obtained with the uniform current model and the solid line the ones with the point current model in the center of the region between the plates.



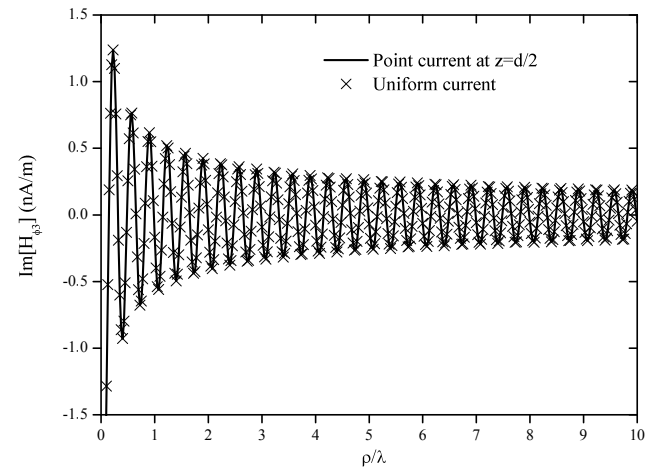
(a) $\text{Re} [H_{\phi_1}]$.



(b) $\text{Im} [H_{\phi_1}]$.



(c) $\text{Re} [H_{\phi_3}]$



(d) $\text{Im} [H_{\phi_3}]$.

Figure 3.10: Azimuthal component of the magnetic field vs. ρ/λ for the first (top) and third (bottom) Fourier harmonics. Due to the symmetry of the velocity function, the values of the magnetic field corresponding to the odd harmonics are null. The crosses show the results obtained with the uniform current model and the solid line the ones with the point current model in the center of the region between the plates.

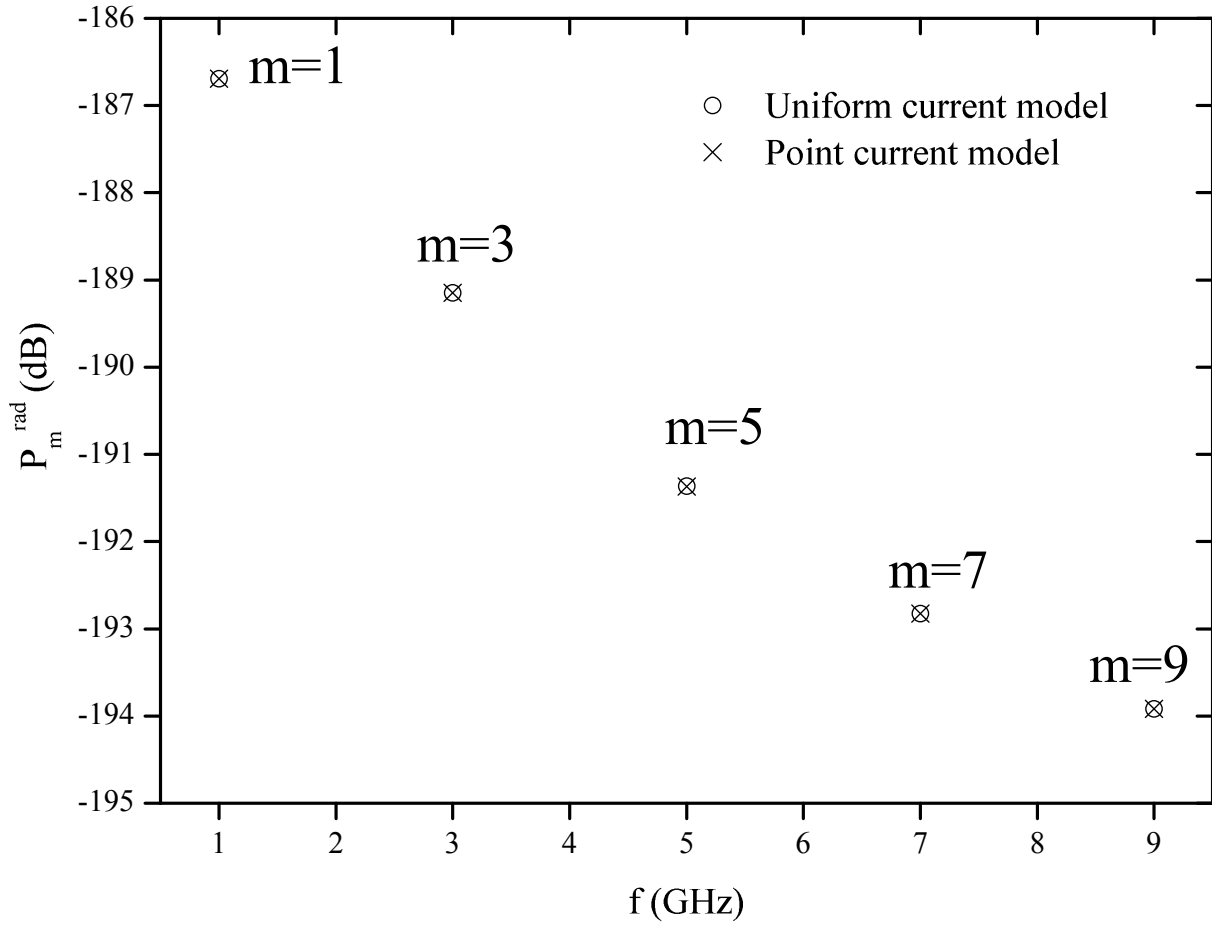


Figure 3.11: Radiated power spectrum of a multipactor discharge within a parallel-plate waveguide obtained with both models of the current.

with the order of multipactor.

In Fig. 3.12 the radiated power spectrum has been plotted for different orders of resonance, N . It can be observed that the harmonics appear at odd multiples of f/N , which means that harmonics will be generated at lower frequencies than the RF signal frequency for multipactor orders $N > 1$. The radiated power spectrum predicted by (3.22) is shown together with the one obtained with a PIC code for comparison [Vicente 2005], demonstrating the excellent agreement, as well, with this method. The results obtained with the PIC code show the radiated power spectrum of a single electron driven by the microwave field at the center of the cross-section of a rectangular cavity where the electric field is the same as in the parallel-plate considered. In all these plots the RF frequency is $f = 1$ GHz, what coincides with the harmonic that exhibits the highest radiated power level.

Regarding the third harmonic detection technique, the results shown in Figs. 3.11 and 3.12 imply that, for the case of multipactor order $N = 1$, the mentioned third harmonic coincides indeed with the harmonic $m = 3$, being detected at a frequency three times higher than the RF one. As it is well known, this harmonic is chosen for detecting multipactor because it is the one with the highest power level apart from the main one ($m = 1$)

at the RF frequency f , which is obscured by the carrier in the experiments. However, for higher orders of multipactor more harmonics appear at both sides of the RF carrier at odd multiples of f/N . For instance, in Fig. 3.12c the radiated power of the first harmonic is predicted at 200 MHz, what could be used for detecting multipactor of order higher than one, since its amplitude is close to the one of the driven frequency, and it is not obscured by the carrier. Similarly, the radiated power spectrum for $N = 11$ plotted in Fig. 3.12d shows that the first harmonic is also predicting a power level comparable to the one corresponding to the microwave frequency. In these cases, where the harmonics different to the order of multipactor are propagated and are not obscured by the carrier, they could give a more precise reference for detecting multipactor than the third harmonic detection technique.

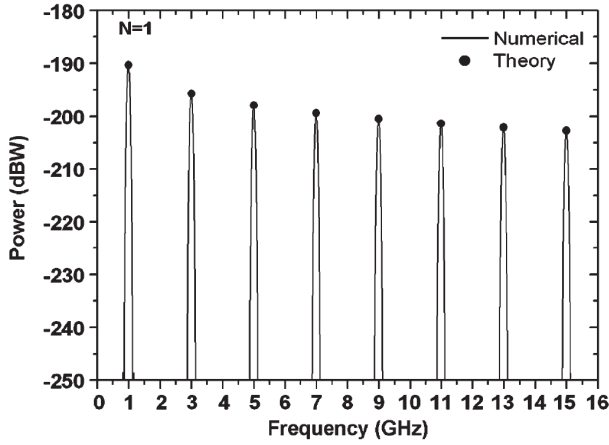
It is important to understand that the radiated power spectrum plotted in Figs. 3.11 and 3.12 shows the power spectrum radiated by a single electron within a parallel-plate waveguide, however, since the multipactor current is directly proportional to the number of electrons involved in the multipactor discharge [Hatch 1958], the power emitted by N_e electrons in resonance with the microwave field is simply given by $N_e^2 P_m^{rad}$. Some authors have proposed values for the number of electrons at the steady-state multipactor stage [Vaughan 1988], suggesting typical values of the electron population around $N_e = 10^8$. The radiated power spectrum of the plot for the cases where this applies should be, therefore, +160 dB shifted, predicting more realistic values of the radiated power spectrum. Therefore, an accurate evaluation of the number of electrons in the multipactor saturation must be found in order to predict accurately the power radiated by the multipactor current at the saturation stage.

Finally, the good agreement between the radiated power spectrum obtained with both models of the current validates mutually the formulae, suggesting no major error existing in the formulation of (3.22) within the limits imposed by the “effective electron” model. As it has been mentioned above, the space charge effects have not been considered in the equation of motion of the electron cloud within the parallel-plate waveguide, and the estimations of the number of electrons predicted in the literature have not been confirmed yet. In Chapter 5, the equations of motion of the electron cloud within a parallel-plate waveguide considering the space charge effects will be solved, showing a natural limit in the number of electrons released by secondary emission. Together with the new equations of motion, an analytical estimation of the electron density at the steady-state multipactor will be presented.

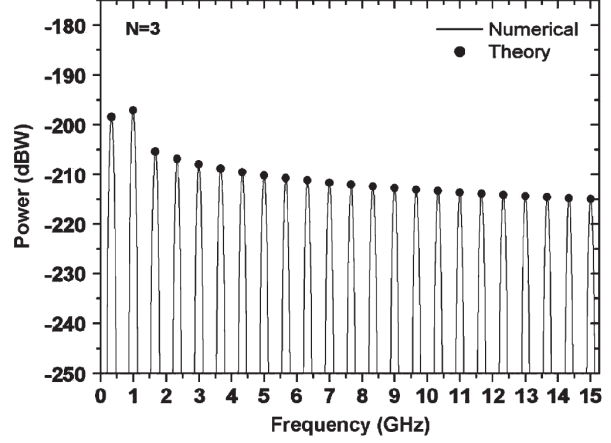
3.4 Summary

The radiated power spectrum of the electron cloud produced by a multipactor discharge within a parallel-plate waveguide has been calculated by the “effective electron” model, obtaining an analytical expression whose validity has been confirmed by other methods. An interesting result is that, according to the formula that has been found, the radiated power spectrum of an electron under multipactor regime does not depend on the fd product, unlike the multipactor breakdown voltage [Hatch 1958, Vaughan 1988]. In fact, the power level is proportional to f/d for all the harmonics, if working with a fixed fd product. This implies, for instance, that the predicted harmonic levels for real low band waveguides (low frequency, large gap) would be lower than for high band ones, even if working with the same fd product. In addition, multipactor in typical large gap structures, such as bandpass filters, would generate considerably lower harmonics than other structures with shorter gaps, such as transformers or low-pass filters. Such implications should be also considered when measuring multipactor in real devices.

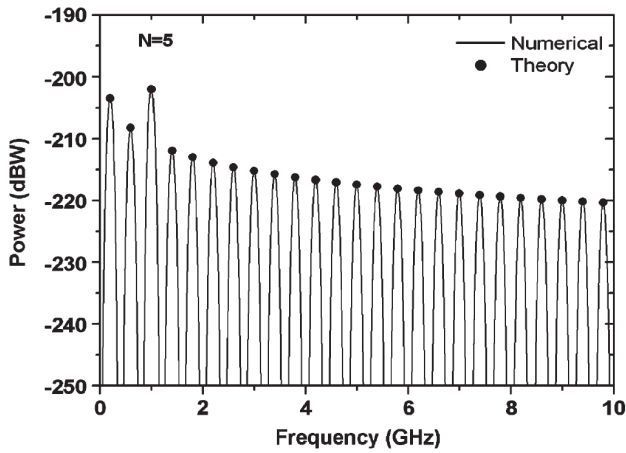
Another feature of the radiated power spectrum presented is the prediction of harmonics at frequencies lower than the carrier one for orders of multipactor bigger than one. This opens the possibility of extending



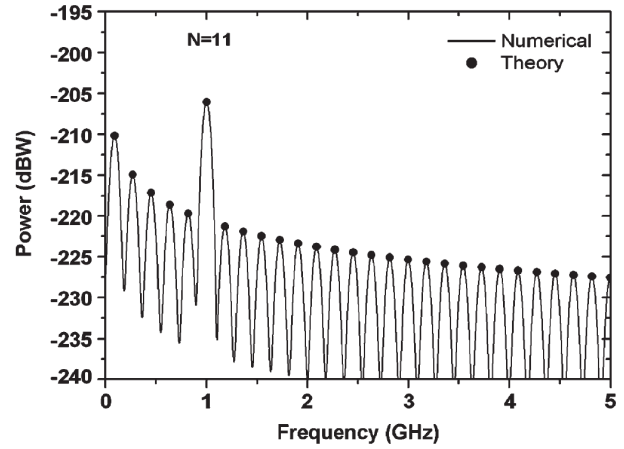
(a) $N = 1$, $V_{RF} = 30$ V, $d = 1$ mm and $\alpha_{res} = 92.49$ deg.



(b) $N = 3$, $V_{RF} = 383.64$ V, $d = 5$ mm and $\alpha_{res} = 101.96$ deg.



(c) $N = 5$, $V_{RF} = 412.34$ V, $d = 7$ mm and $\alpha_{res} = 97.15$ deg.



(d) $N = 11$, $V_{RF} = 953.14$ V, $d = 15.65$ mm and $\alpha_{res} = 93.3$ deg.

Figure 3.12: Radiated power spectrum of the multipactor current within a parallel-plate waveguide for different orders of multipactor, N . All the simulations have been obtained with $f = 1$ GHz and $v_0 = 3.68$ eV. The dots correspond to the radiated power spectrum obtained with (3.22) and the lines have been obtained with a PIC code.

the third harmonic detection technique to the search of other harmonics that can propagate, which are not obscured by the carrier of the signal, which may give a more precise reference for detecting multipactor than the observation of the third harmonic.

The next step in the evaluation of the radiated power spectrum of a multipactor discharge is the consideration of the space charge effects in the motion of the electron cloud produced within the parallel-plate waveguide. The equations of motion of the electron cloud within the parallel-plate waveguide taking into account the space charge effects due to the presence of the boundaries will be solved in Chapter 5 analytically. Once the analytical solution of the equations of motion will be shown, an estimation of the maximum number of electrons in the saturation will be presented like a natural consequence of the rupture of the resonance condition by the interaction of the electron cloud with its image charge through the metal plates.

It would be interesting, therefore, to develop the current produced by the electron cloud taking into account the space charge effects in a Fourier series applying the same reasonings done here. In this case, the velocity is not a periodic signal anymore, since the electron density of the electron cloud appears explicitly in the expression of the velocity, which increases with time by the secondary emission. Nevertheless, some approximations to this problem may be found for a relatively slow increase of the electron population, near above the multipactor threshold, when the velocity function would not change abruptly and it could be considered as a quasi-periodic signal. Another possibility is the consideration of the current once the saturation level has been reached, for which the velocity is a periodic function if certain conditions are satisfied, as it will be explained in Chapter 5.

The analysis of the radiated power spectrum produced by a multipactor discharge together with the study of the saturation may lead towards an unambiguous criterion to uniquely assess the multipactor onset, an open problem that has not been solved yet, and for which the contribution of this thesis is intended to help in the joint success of this task.

Roots of the cross-product of Bessel functions

Contents

4.1	Introduction	63
4.2	Theory	64
4.2.1	Roots of $TM_{0,s}$ modes	65
4.2.2	Roots of $TM_{\nu,s}$ modes	68
4.2.3	Roots of $TE_{\nu,s}$ modes	70
4.3	Main results	72
4.4	Summary	77

4.1 Introduction

The two cross-product combinations of Bessel functions and their derivatives appear frequently in physical problems having cylindrical [Stratton 1941] or spherical [Boyer 1969] symmetry in different fields such as fluid mechanics [Bauer 1988], mechanical [Olçer 1968] or electrical engineering [Marcuvitz 1951]. The roots of the cross-product of Bessel functions and their derivatives represent the eigenvalue solutions of problems like the accurate simulation of the behavior of discontinuities involving coaxial geometries. This is a basic staple in modern CAD tools for designing waveguide networks [Gimeno 1996, Gimeno 1997, Arndt 2004]. The computation of the radiated field produced by an open-ended coaxial probe, a very useful tool in electromagnetic diagnosis, also needs the calculation of these roots [Mosig 1981, Yung 1984, Noh 1999, Lee 1996, Panariello 2001, Asvestas 2006]. Finally, the representation of the electromagnetic field within curved waveguides [Petrusenko 2001], as well as the prediction of the radiated power spectrum of charged particles within accelerating cavities [Nagesh 2005], also require the efficient and fast calculation of these roots. An algorithm for the efficient numerical calculation of the roots of the cross-product of Bessel functions and their derivatives has been developed especially for the last problem in order to improve the speed in the calculation of the radiated power spectrum of a multipactor current within a coaxial waveguide.

This work also opens the possibility of studying the problem of the radiated power spectrum of a multipactor discharge within coaxial geometries. There has been an article dealing with this problem [Nagesh 2005], but no image theory has been applied to this problem nor an acceleration technique has been proposed to the evaluation of the Green function of the coaxial waveguide. This algorithm intends to improve the speed in the evaluation of the radiated power spectrum produced by a multipactor discharge within a coaxial waveguide. However, the study of the image method for the coaxial waveguide has not been solved yet to the best of our knowledge, which could bring a new insight into the problem of the multipactor radiation for coaxial geometries.

Many studies have been realized to calculate the roots of these functions [McMahon 1894, Bridge 1962, Laslett 1962, Bauer 1964, Cochran 1966b, Salchev 1973, Koss 2004], but they have not provided a globally convergent algorithm or, in the best cases, they have found solutions only valid for certain extreme values of the coaxial cable aspect ratio q , or the order of the involved Bessel functions.

In this chapter the summary of the work presented in [Sorolla 2011] together with the optimization of the algorithm presented in [Sorolla 2012] are described. The optimization of the algorithm described in the last reference exhibited a dramatically decrease in the amount of iterations needed to find the first root for $\nu = 1$ of the TE-mode with respect to the previous algorithm. Moreover, the optimization of the method extended the range of q for which the algorithm converges by optimizing the position of the seed in the root search within the boundaries of the search intervals. The bounds of q that ensure the convergence are determined by the numerical limits of floating-number implementation.

4.2 Theory

The problem of the radiation produced by a current source within a coaxial waveguide has been solved by calculating the electromagnetic fields using the dyadic Green's functions for coaxial geometries [Tai 1983]. The calculation of the Green's function implies the search of the roots of the functions

$$g_\nu(q, x) \equiv J_\nu(qx)Y_\nu(x) - J_\nu(x)Y_\nu(qx) \quad (4.1a)$$

$$\tilde{g}_\nu(q, x) \equiv J'_\nu(qx)Y'_\nu(x) - J'_\nu(x)Y'_\nu(qx) \quad (4.1b)$$

where $J_\nu(x)$ and $Y_\nu(x)$ are the Bessel function of first and second kind, respectively, and $J'_\nu(x)$ and $Y'_\nu(x)$ are the first derivatives of the Bessel functions with respect to x . The coaxial aspect ratio $q = b/a$ has been defined, where a and b are the inner and the outer radius of the coaxial waveguide, respectively. The roots of $g_\nu(q, x)$ and $\tilde{g}_\nu(q, x)$ are named $c_\nu^{(s)}$ and $\tilde{c}_\nu^{(s)}$, respectively, and since $x = \lambda a$, they define the cut-off wavelength of the TM and the TE modes, respectively. The wavelength of the signal $\lambda = c/f$ relates the speed of light in free-space, c , to the signal frequency, f , what allows to calculate the cut-off frequency of each mode by knowing the values of the above-mentioned roots as follows:

$$\left\{ \begin{array}{l} f_\nu^{(s)} = \frac{ca}{c_\nu^{(s)}} \\ \tilde{f}_\nu^{(s)} = \frac{ca}{\tilde{c}_\nu^{(s)}} \end{array} \right. \quad (4.2a)$$

$$\left\{ \begin{array}{l} f_\nu^{(s)} = \frac{ca}{c_\nu^{(s)}} \\ \tilde{f}_\nu^{(s)} = \frac{ca}{\tilde{c}_\nu^{(s)}} \end{array} \right. \quad (4.2b)$$

where $f_\nu^{(s)}$ and $\tilde{f}_\nu^{(s)}$ define the cut-off frequencies of the TM and the TE modes, respectively.

In order to calculate the radiated electromagnetic fields produced by a current within a coaxial waveguide a certain number of roots ($s = s_{max}$) for $\nu = 0$ and a certain maximum index ($\nu = \nu_{max}$) will be needed to define accurately the Green function and, consequently, the electromagnetic fields. As it will be shown later, the roots of $g_{\nu-1}(q, x)$ are needed to obtain the ones of $g_\nu(q, x)$, Thus, the roots for $\nu = 0$ are calculated firstly and the rest of roots are found in ascending order of ν , defining an inverted pyramidal scheme where the first

roots are shown on the top (the same holds for the roots of $\tilde{g}_\nu(q, x)$):

$$\left\{ \begin{array}{l} c_0^{(1)}, c_0^{(2)}, \dots, c_0^{(s_{max}-\nu_{max})}, \dots, c_0^{(s_{max}-1)}, c_0^{(s_{max})} \\ c_1^{(1)}, c_1^{(2)}, \dots, c_1^{(s_{max}-\nu_{max})}, \dots, c_1^{(s_{max}-1)} \\ \vdots \\ c_{\nu_{max}}^{(1)}, c_{\nu_{max}}^{(2)}, \dots, c_{\nu_{max}}^{(s_{max}-\nu_{max})} \end{array} \right\}$$

It is required that $s_{max} \geq \nu_{max} + 1$ in order to calculate the last root of the scheme. For instance, if p roots are requested for $\nu_{max} = m$ to reach the desired accuracy in the calculation of the electromagnetic fields, the expression $s_{max} = p + m$ must be satisfied.

4.2.1 Roots of $\text{TM}_{0,s}$ modes

To calculate the first set of roots of $g_0(q, x)$ an auxiliary function is used following a similar approach as in [Segura 1998]

$$G_0(q, x) \equiv \frac{g_0(q, x)}{g_0'(q, x)} \quad (4.3)$$

since the roots of $g_0(q, x)$ and $g_0'(q, x)$ never coincide [Cochran 1966a]. Thus, the roots of $G_0(q, x)$ and $g_0(q, x)$ are the same, with the advantage that $G_0(q, x)$ shows a tangent-like function behavior, as it is shown next. This, indeed, guarantees the success of the Newton-Raphson (NR) algorithm [Press 1992] in the root search since all the approximations along the iterative process will lie inside the interval defined by the branches of the function $G_0(q, x)$.

Let us first calculate $G_0'(q, x_0)$ when $G_0(q, x_0) = 0$:

$$G_0'(q, x_0) = \frac{(g_0'(q, x_0))^2 - g_0(q, x_0)g_0''(q, x_0)}{(g_0'(q, x_0))^2} = 1 \quad (4.4)$$

since $g_0(q, x_0) = 0$ in this case.

Let $z_0^{(s)}$ be the positive roots of $g_0'(q, x)$ i.e. the extremes of $g_0(q, x)$

$$z_0^{(s)} = x \in (0, \infty) \mid g_0'(q, x) = 0$$

and let us study the asymptotes of the auxiliary function $G_0(q, x)$ in these limits taking into account the periodic character of the function $g_0(q, x)$ [Gray 1895]:

$$\lim_{x \rightarrow z_0^{(s)(-)}} \frac{\text{sgn}[g_0(q, x)] \text{abs}[g_0(q, x)]}{\text{sgn}[g_0'(q, x)] \text{abs}[g_0'(q, x)]} = \left\{ \begin{array}{l} + \left(\frac{\lim_{x \rightarrow z_0^{(s)(-)}} \text{abs}[g_0(q, x)]}{\lim_{x \rightarrow z_0^{(s)(-)}} \text{abs}[g_0'(q, x)]} \right) \\ - \left(\frac{\lim_{x \rightarrow z_0^{(s)(-)}} \text{abs}[g_0(q, x)]}{\lim_{x \rightarrow z_0^{(s)(-)}} \text{abs}[g_0'(q, x)]} \right) \end{array} \right\} = +\infty \quad (4.5)$$

The limits from the other side are

$$\lim_{x \rightarrow z_0^{(s)}(+)} \frac{\operatorname{sgn}[g_0(q, x)] \operatorname{abs}[g_0(q, x)]}{\operatorname{sgn}[g'_0(q, x)] \operatorname{abs}[g'_0(q, x)]} = \left\{ \begin{array}{l} + \left(\frac{\lim_{x \rightarrow z_0^{(s)}(+)} \operatorname{abs}[g_0(q, x)]}{\lim_{x \rightarrow z_0^{(s)}(+)} \operatorname{abs}[g'_0(q, x)]} \right) \\ - \left(\frac{\lim_{x \rightarrow z_0^{(s)}(+)} \operatorname{abs}[g_0(q, x)]}{\lim_{x \rightarrow z_0^{(s)}(+)} \operatorname{abs}[g'_0(q, x)]} \right) \\ - \left(\frac{\lim_{x \rightarrow z_0^{(s)}(+)} \operatorname{abs}[g_0(q, x)]}{\lim_{x \rightarrow z_0^{(s)}(+)} \operatorname{abs}[g'_0(q, x)]} \right) \\ + \left(\frac{\lim_{x \rightarrow z_0^{(s)}(+)} \operatorname{abs}[g_0(q, x)]}{\lim_{x \rightarrow z_0^{(s)}(+)} \operatorname{abs}[g'_0(q, x)]} \right) \end{array} \right\} = -\infty \quad (4.6)$$

Furthermore, due to the periodicity of $g_0(q, x)$ we know that there is a single root in between two extrema, thus, between two roots of $g'_0(q, x)$ there is a single zero of the function $G_0(q, x)$.

These properties show that G_0 resembles a tangent-like function. In Fig. 4.1 the auxiliary function $G_0(q, x)$ is plotted using solid line together with the seeds used in the root search for $\nu = 0$, represented by dots, for two extreme values of the parameter q . The seeds of the root search are chosen accordingly to McMahan's expansion formula [McMahan 1894]. Note that the s -th seed lies within the branch corresponding to the same index of the root, and, since McMahan's expansion formula provides a more precise approximation the larger the value of the root, the consecutive seeds corresponding to larger values of s are expected to lie within the corresponding branches, too. This guarantees the success of the root search using McMahan's expansion formula as seed for $\nu = 0$.

The NR iteration formula needs the calculation of the first derivative of the auxiliary function. Therefore, recalling (4.3) and (4.4) we can write the root search formula as

$$X_{n+1} = X_n - \frac{G_0(q, X_n)}{G'_0(q, X_n)} = X_n - \left(\frac{g'_0(q, X_n)}{g_0(q, X_n)} - \frac{g''_0(q, X_n)}{g'_0(q, X_n)} \right)^{-1}, \quad (4.7)$$

where the prime indicates derivative with respect to x , with

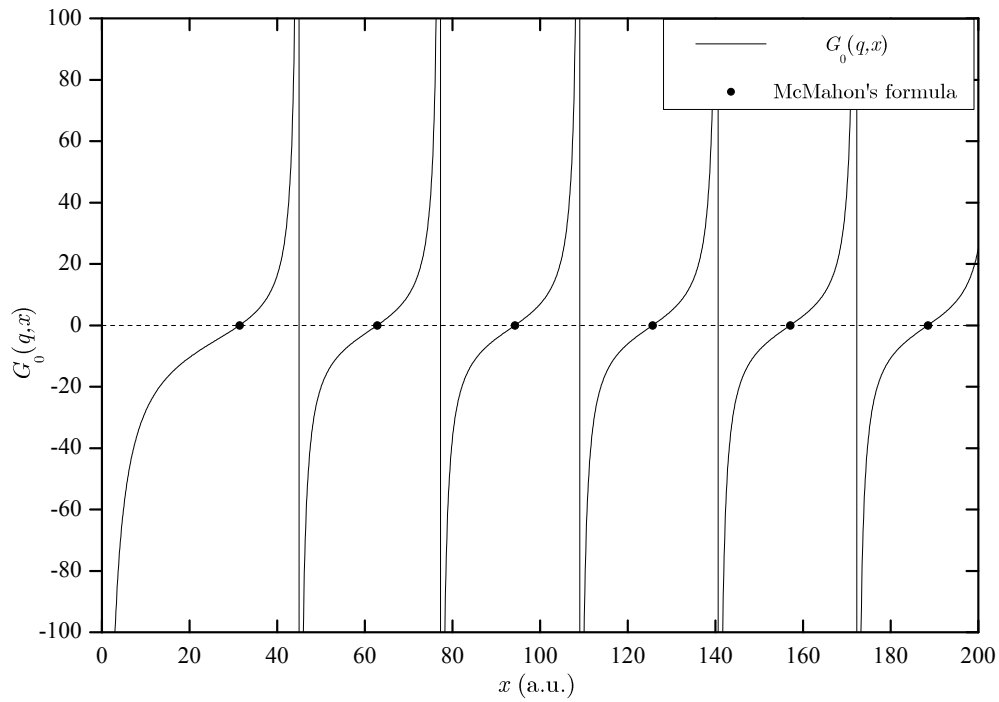
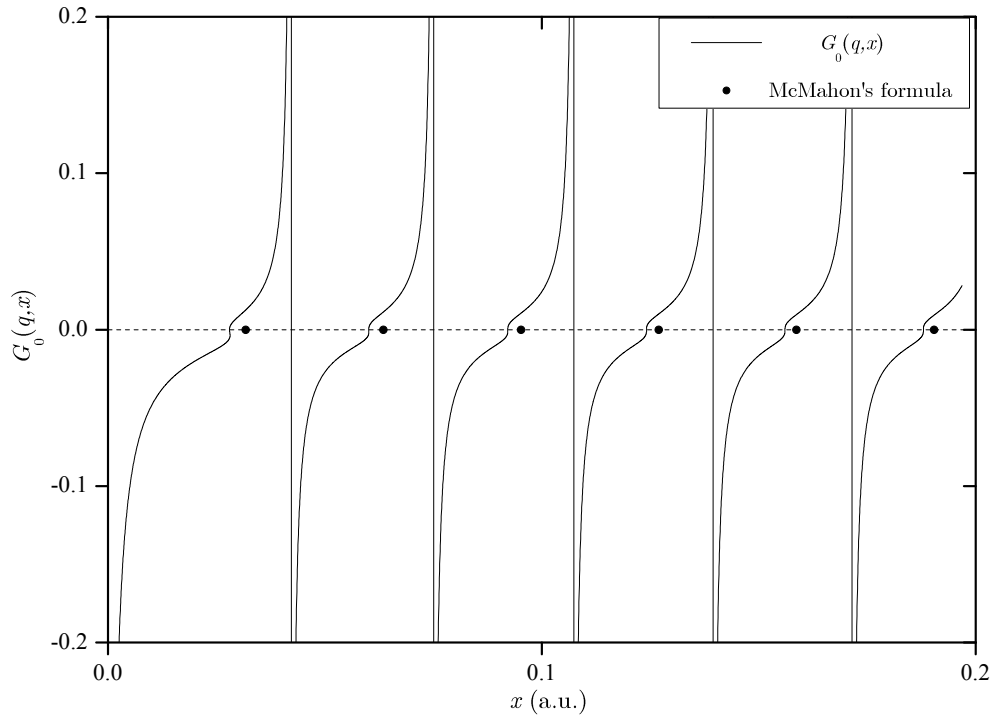
$$g'_0(q, x) = [J'_0(qx)Y_0(x) - J_0(x)Y'_0(qx)] + q [J_0(qx)Y'_0(x) - J'_0(x)Y_0(qx)], \quad (4.8)$$

$$g''_0(q, x) = A_0(x) + 2qB_0(x) + q^2C_0(x) \quad (4.9)$$

and

$$\left. \begin{array}{l} A_0(x) = J''_0(qx)Y_0(x) - J_0(x)Y''_0(qx) \\ B_0(x) = J'_0(qx)Y'_0(x) - J'_0(x)Y'_0(qx) \\ C_0(x) = J_0(qx)Y''_0(x) - J''_0(x)Y_0(qx). \end{array} \right\} \quad (4.10)$$

The algorithm to calculate the roots of $g_0(q, x)$ requests as input the ratio q and the desired maximum amount of roots, s_{max} , that are to be calculated for $\nu = 0$. It is crucial to remember that, according to the pyramidal scheme, s_{max} is not independent of the largest order ν_{max} for which the p roots are searched (see pyramidal scheme). The desired accuracy and the maximum amount of iterations are given by eps and i_{max} , respectively, where eps has been chosen equal to the machine precision in the following. The algorithm to obtain the set of roots for $\nu = 0$ is then summarized in **Algorithm 1**.

(a) $q = 1.1$.(b) $q = 100$.Figure 4.1: Auxiliary function (solid line) and McMahon's expansion formula (dots) for the roots of (4.1a) for $\nu = 0$.

Algorithm 1 Calculate $c_0^{(s)} \quad \forall s \in [1, s_{max}]$

Input: q, ν_{max}, s_{max} ; **Output:** $c_0^{(s)}$; **Constants:** eps, i_{max} ;

while $(s_{max} - \nu_{max}) \geq 1$ **do**

for $s = 1$ to s_{max} **do**

$i := 0$; $err := 1$

$X_i := \frac{s\pi}{(q-1)}$ {Seed for the s -th root (McMahon).}

while $(err > eps \wedge i \leq i_{max})$ **do**

$X_{i+1} := X_i - \frac{G_0(q, X_i)}{G'_0(q, X_i)}$

$err := \text{abs} \left[\frac{X_{i+1} - X_i}{X_{i+1}} \right]$

$i := i + 1$

$c_0^{(s)} := X_i$

4.2.2 Roots of $\text{TM}_{\nu,s}$ modes

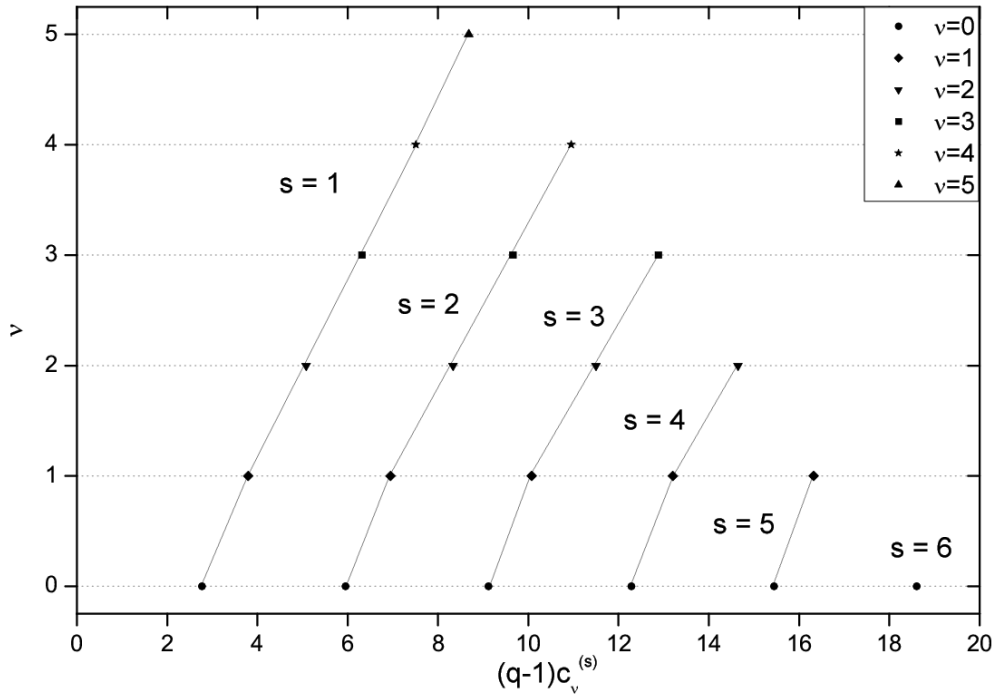
It has been observed that the function $g_\nu(q, x)$ presents one and only one root in between two consecutive roots of $g_{\nu-1}(q, x)$ for any value of q and ν [Boyer 1969]. The interlacing property of the roots ensures the good performance of the algorithm, since the roots of the set $\mathcal{C}_\nu = \left\{ c_\nu^{(s)} \mid g_\nu(q, c_\nu^{(s)}) = 0, s, \nu \in \mathbb{N} \right\}$ are bounded by the roots of $\mathcal{C}_{\nu-1}$ as follows:

$$c_{\nu-1}^{(s)} < c_\nu^{(s)} < c_{\nu-1}^{(s+1)} \quad \forall \nu > 0. \quad (4.11)$$

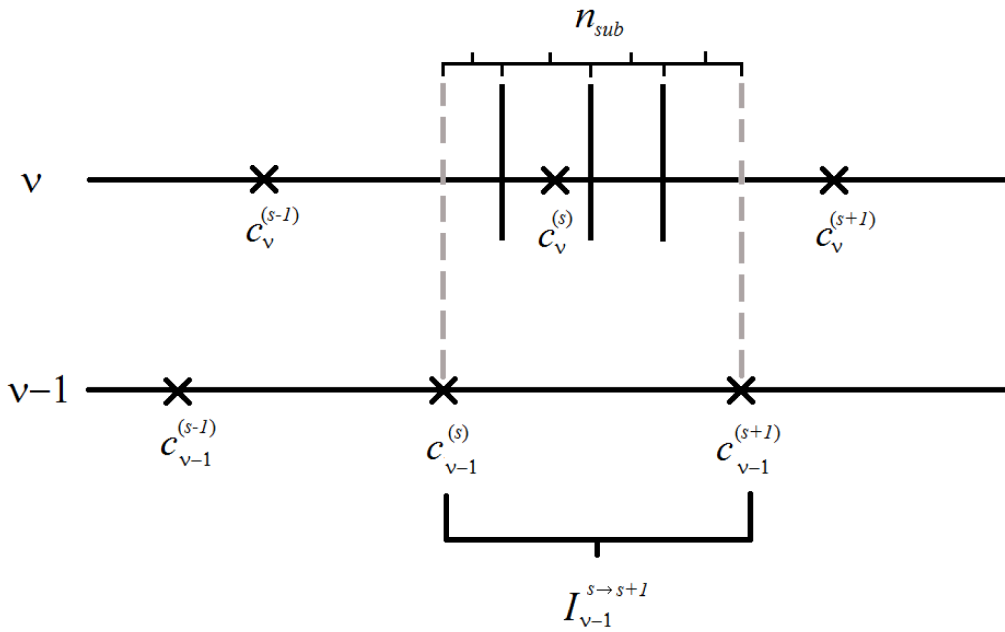
Thus, to find the roots for $\nu > 0$, the set \mathcal{C}_0 is used as basic set from which the rest of roots will be found using the original function $g_\nu(q, x)$. The interlacing property can be observed in Fig. 4.2a, where the roots of the function $g_\nu(q, x)$ for $q = 100$ and different ν -orders are shown. The search interval of each root for the order ν is, therefore, well-established by the interlacing properties and defined by

$$I_{\nu-1}^{s \rightarrow s+1} \in (c_{\nu-1}^{(s)}, c_{\nu-1}^{(s+1)}) \quad \forall \nu > 0$$

which is split into n_{sub} subintervals (see Fig. 4.2b). The division of that interval in subintervals is done in order to ensure the convergence of the method when the approximation of the root lies outside $I_{\nu-1}^{s \rightarrow s+1}$. The seed is placed slightly above the beginning of the first subinterval by ϵ , a quantity that is fixed by the maximum among the quantities: “machine precision times the interval length” and “machine precision” (see **Algorithm 2**). Then, the NR iteration is applied and, if some approximation to the root lies outside the interval defined by the interlacing property, the seed is placed at the beginning of the next subinterval and so on till the solution converges inside $I_{\nu-1}^{s \rightarrow s+1}$. The quasi-periodicity of the cross-product of Bessel functions [Salchev 1973] ensures that, placing the seed within some of the subintervals, the NR algorithm will necessarily converge. The typical values of n_{sub} chosen are between 5 and 10, observing that the algorithm had to restart the root search within the second interval in the worst case, as it will be shown later. The procedure to calculate the roots of the function $g_\nu(q, x)$, $c_\nu^{(s)}$, till $\nu = \nu_{max}$ is reached requests the same input parameters as the **Algorithm 1** plus the s_{max} roots: $c_0^{(s)}$. The steps to follow are summarized in **Algorithm 2**.



(a) Interlacing properties.



(b) Definition of sub-intervals.

Figure 4.2: All the roots calculated by the algorithm for $s_{max} = 6$, $\nu_{max} = 5$ and $q = 100$ (top). Sketch showing how the interval $I_{\nu-1}^{s \rightarrow s+1}$ is split into an arbitrary number of subintervals n_{sub} (bottom).

Algorithm 2 Calculate $c_\nu^{(s)} \quad \forall (s, \nu), s \in [1, s_{max} - \nu], \nu \in [1, \nu_{max}]$

Input: $c_0^{(s)}, \nu_{max}, s_{max}$; **Output:** $c_\nu^{(s)}$; **Constants:** eps, ϵ, n_{sub} ;

for $\nu = 1$ to ν_{max} **do**

for $s = 1$ to $s_{max} - \nu$ **do**

$i := 0; err := 1; count := 0;$

$\epsilon := max \left\{ eps \cdot \left(c_{\nu-1}^{(s+1)} - c_{\nu-1}^{(s)} \right), eps \right\};$

$delta := \frac{\left(c_{\nu-1}^{(s+1)} - c_{\nu-1}^{(s)} \right)}{n_{sub}};$

while $(err > eps \wedge count < n_{sub})$ **do**

$X_i := c_{\nu-1}^{(s)} + \epsilon + count \cdot delta$

$count := count + 1$

while $\left(X_i \geq c_{\nu-1}^{(s)} \wedge X_i < c_{\nu-1}^{(s+1)} \wedge i \leq i_{max} \right)$ **do**

$X_{i+1} := X_i - \frac{g_\nu(q, X_i)}{g'_\nu(q, X_i)}$

$err := abs \left[\frac{X_{i+1} - X_i}{X_{i+1}} \right]$

$i := i + 1$

$c_\nu^{(s)} := X_i$

4.2.3 Roots of $TE_{\nu,s}$ modes

To calculate the set of roots of (4.1b) for $\nu = 0$ the property $\mathcal{Z}'_0(x) = -\mathcal{Z}_1(x)$ [Abramowitz 1970] is used, where $\mathcal{Z}_\nu(x)$ is any of the two Bessel functions, either $J_\nu(x)$ or $Y_\nu(x)$. This property leads to $c_1^{(s)} = \tilde{c}_0^{(s)}$, ($s = 1, 2, 3, \dots$), thus, the set of roots of $\tilde{g}_\nu(q, x)$ for $\nu = 0$ is already given since it is the same as the set of roots of $g_\nu(q, x)$ for $\nu = 1$, previously calculated. The interlacing property:

$$\tilde{c}_{\nu-1}^{(s)} < \tilde{c}_\nu^{(s)} < \tilde{c}_{\nu-1}^{(s+1)} \quad \forall \nu > 0 \quad (4.12)$$

is also valid for all the roots except for $\tilde{c}_1^{(1)}$ since it lies before $\tilde{c}_0^{(1)}$ [Truell 1943]. This root is, therefore, searched inside the interval $\tilde{I}_0 \in \left(\delta, \tilde{c}_0^{(1)} \right)$, where δ is an arbitrary number smaller than the root to be found, and $\tilde{c}_0^{(1)} \equiv c_1^{(1)}$ has been calculated previously. In the algorithm $\delta = 10^{-3}$ has been chosen, since the smallest root that can be found by our algorithm corresponds to $q = 1000$ and, in this case, the searched root is around $1.8 \cdot 10^{-3}$. Once this root has been found the remaining ones are automatically calculated following the same inverted pyramidal scheme and relying on the subdivision of the intervals performed by the roots of the previous ν -order, as described above. Note that the index s for the roots of $\tilde{g}_\nu(q, x)$ does not correspond to the one of McMahon's expansion since smaller roots than predicted for $s = 1$ are found [Truell 1943, Dwight 1948]. Thus, the index s is shifted by one in this case with respect to McMahon's nomenclature for the roots of this function.

The algorithm to calculate the set of roots $\tilde{C}_\nu = \left\{ \tilde{c}_\nu^{(s)} \mid \tilde{g}_\nu \left(q, \tilde{c}_\nu^{(s)} \right) = 0, s, \nu \in \mathbb{N} \right\}$ till reaching the order ν_{max} is presented in **Algorithm 3**.

Algorithm 3 Calculate $\tilde{c}_\nu^{(s)} \quad \forall (s, \nu), s \in [1, s_{max} - \nu], \nu \in [0, \nu_{max}]$

Input: $c_1^{(s)}, \nu_{max}, s_{max}$; **Output:** $\tilde{c}_\nu^{(s)}$; **Constants:** $eps, \epsilon, n_{sub}, \delta$;

$\tilde{c}_0^{(1)} := \delta$ {This root is discarded later, since it is only an artificial bound to find the first root for $\nu = 1$.}

$\tilde{c}_0^{(s)} := c_1^{(s-1)} \quad \forall s \in [2, s_{max}]$

for $\nu = 1$ to ν_{max} **do**

for $s = 1$ to $s_{max} - \nu$ **do**

$i := 0$; $err := 1$; $count := 0$;

$\epsilon := \max \left\{ eps \cdot \left(\tilde{c}_{\nu-1}^{(s+1)} - \tilde{c}_{\nu-1}^{(s)} \right), eps \right\}$;

$delta := \frac{\left(\tilde{c}_{\nu-1}^{(s+1)} - \tilde{c}_{\nu-1}^{(s)} \right)}{n_{sub}}$;

while $(err > eps \wedge count < n_{sub})$ **do**

$X_i := \tilde{c}_{\nu-1}^{(s)} + \epsilon + count \cdot delta$

$count := count + 1$

while $\left(X_i \geq \tilde{c}_{\nu-1}^{(s)} \wedge X_i < \tilde{c}_{\nu-1}^{(s+1)} \wedge i \leq i_{max} \right)$ **do**

$X_{i+1} := X_i - \frac{\tilde{g}_\nu(q, X_i)}{\tilde{g}'_\nu(q, X_i)}$

$err := \text{abs} \left[\frac{X_{i+1} - X_i}{X_{i+1}} \right]$

$i := i + 1$

$\tilde{c}_\nu^{(s)} := X_i$

4.3 Main results

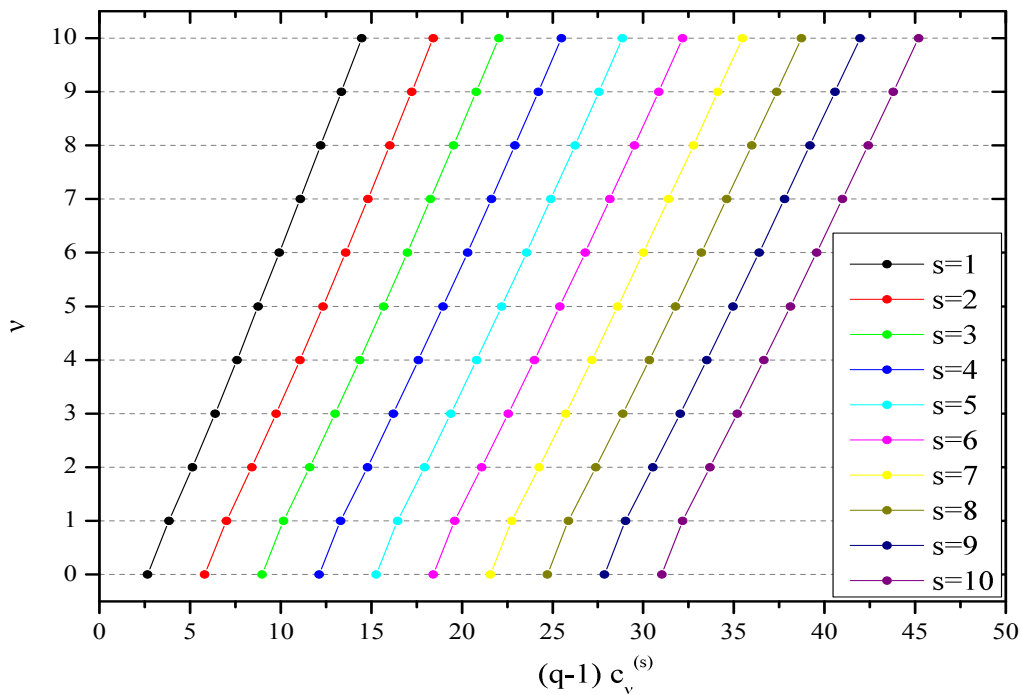
In this section the roots of the two functions (4.1) are shown for two extreme values of the coaxial cable aspect ratio ($q = 1.001$ and $q = 1000$) in order to check the reliability of the algorithm for limiting cases. This ensures that the algorithm will work as well for ratios of q as they are found in practical applications. For these two extreme values the interlacing properties of the roots of both, the cross-product of Bessel functions and their derivatives, are verified.

As for low values of q and for a given s the roots of (4.1) lie very close to each other as ν increases, and the interlacing properties cannot be easily verified by visual inspection, we represent the roots for $q = 1.001$ in tabular format normalized by the quantity $(q - 1)$. In Table 4.1 the 10 first roots of (4.1a) for values of ν from 0 to 5 are shown. In Table 4.2 the 11 first roots of (4.1b) for values of ν from 1 to 5 for the same value of q are shown. The reason why the roots in Table 4.2 for $\nu = 0$ are not shown is because they are the same as those ones of Table 4.1 for $\nu = 1$ as it was pointed out before. It can be seen that the values of the normalized roots tend to multiples of π , as expected when $q \rightarrow 1$ since this limit corresponds to the solution of the eigenvalues of the parallel-plate waveguide [Cochran 1966b]. The results certify that the interlacing property of the roots of both functions hold for all of them.

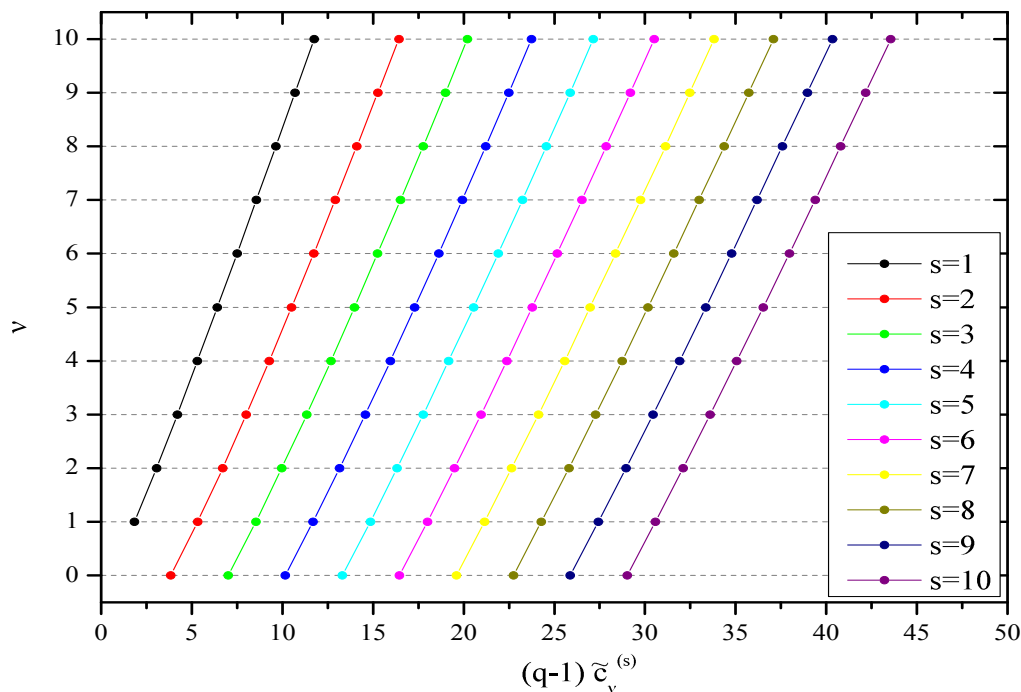
For large values of q the verification of the interlacing property can be easily performed by visual inspection. The 10 first roots of the cross-product of Bessel functions and the ones of the cross-product of their derivatives are shown for the 10 first values of ν for $q = 1000$ in Fig. 4.3, top and bottom, respectively. In this case it can be noticed that the roots of (4.1a) tend to the ones of the Bessel function of the first kind, that is, the roots of $J_\nu(qx) = 0$; while the roots of (4.1b) tend to the ones of the derivative $J'_\nu(qx) = 0$, as expected for large values of q [Kline 1948].

In order to show the efficiency of the roots search the number of iterations needed to reach machine precision for the first root of the functions defined in (4.1) is represented in Fig. 4.4. The convergence study of the first root of g_ν (see Fig. 4.4a) shows that the number of iterations needed to reach machine-precision accuracy increases as ν grows for a given q , though the convergence seems to depend more on q than on the index of the Bessel functions. Namely, for a given ν , the convergence is more quickly attained as the ratio q decreases and gets close to one. This is due to the fact that McMahan's expansion provides a better estimate of the roots as the ratio $s/(q - 1)$ increases. Another reason to explain why the algorithm needs less iterations for lower values of q than for larger ones is due to the fact that the algorithm places the seed slightly above the value of $c_{\nu-1}^{(s)}$ to find the root $c_\nu^{(s)}$. Thus, as the root lies closer to the seed for smaller values of q than for larger ones (compare results in Table 4.1 with those of Fig. 4.3) the convergence is more quickly attained for $q \rightarrow 1$. The fast and accurate character of the algorithm to find all the roots of functions (4.1) for any ν is, indeed, based on the knowledge of the set \mathcal{C}_0 and the properties of its elements with respect to the roots for higher orders ν . Nevertheless, the plot shows that in the worst case, corresponding to $(q - 1) = 1000$, the algorithm only needs six steps to reach machine-precision accuracy for $\nu = 100$, which reflects its fast performance.

It must be remarked that the eventual jump of the seed (cf. Figure 4.2b and Section 4.2.2) to the beginning of the second or the third subintervals when the approximation to the root lies outside the search interval has been recorded and taken into account in the plot of Figure 4.4. The convergence study of the root search for $n_{sub} = 10$ shows the presence of the jump of the seed to the second and the third subintervals for values of q above $q = 5$ and $q = 50$, respectively. No jump of the seed beyond the third subinterval was observed for values of q below $q = 1000$ for ν and s ranging from 0 to 100 and from 1 to 100, respectively. The appearance of jumps in the seed to the next subintervals does not follow a clear tendency with the parameter q or the index ν , since it depends on the slope of the function $f_\nu(q, x)$ evaluated at $x = c_{\nu-1}^{(s)}$, the NR iteration approximating



(a) Roots of $g_\nu(q, x)$.



(b) Roots of $\tilde{g}_\nu(q, x)$.

Figure 4.3: Roots of (4.1) for $q = 1000$.

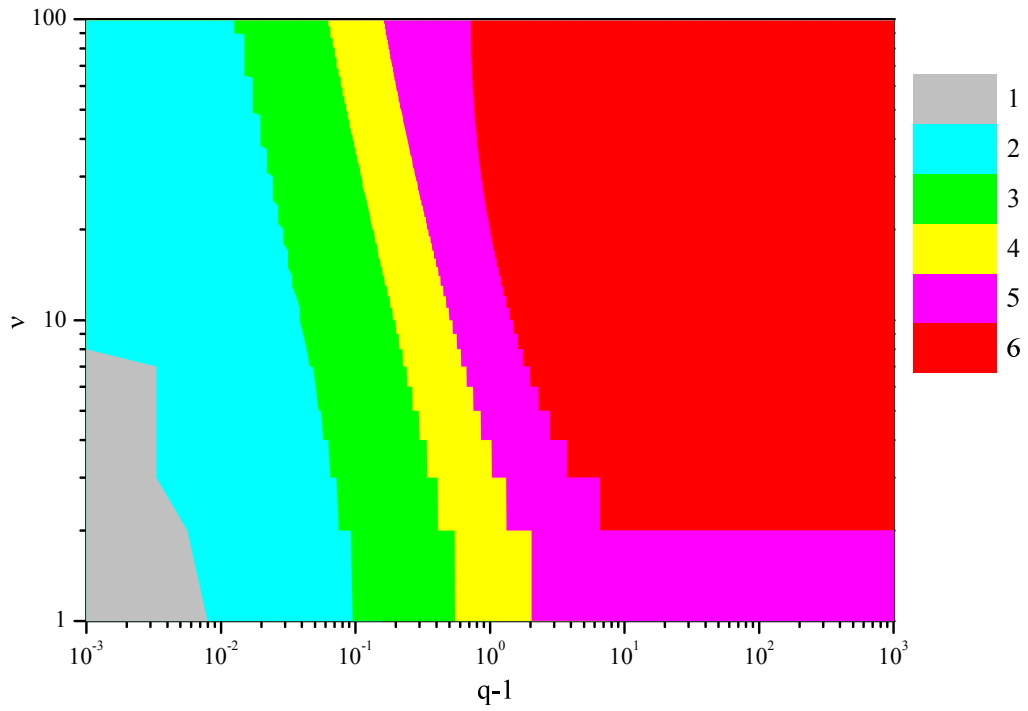
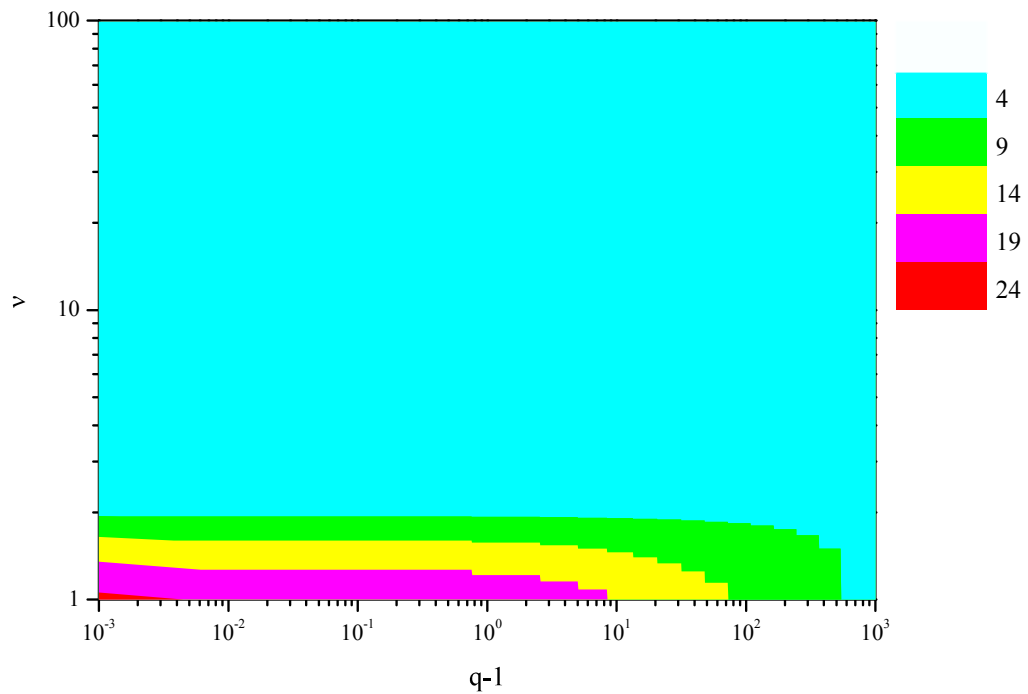
(a) Convergence of the root search $c_\nu^{(1)}$.(b) Convergence of the root search $\tilde{c}_\nu^{(1)}$.

Figure 4.4: Iterations needed to reach machine accuracy in the root search of the first roots of the functions (4.1).

the root within or outside the search interval defined by $I_{\nu-1}^{s \rightarrow s+1}$.

For example, for $q = 5$, jumps to the second subinterval were recorded for values of ν between 21 and 55 for few values of the root index, s . For $\nu = 21$ it was observed the jump of the root approximation to the second subinterval only for $s = 18, 19$. For $\nu = 55$ this jump was observed only for $s = 44, 45$. The behavior of the jump of the seed to the second subinterval for intermediate values of ν was different, for instance, for $\nu = 41$ this occurred for the roots lying from $s = 33$ to $s = 43$.

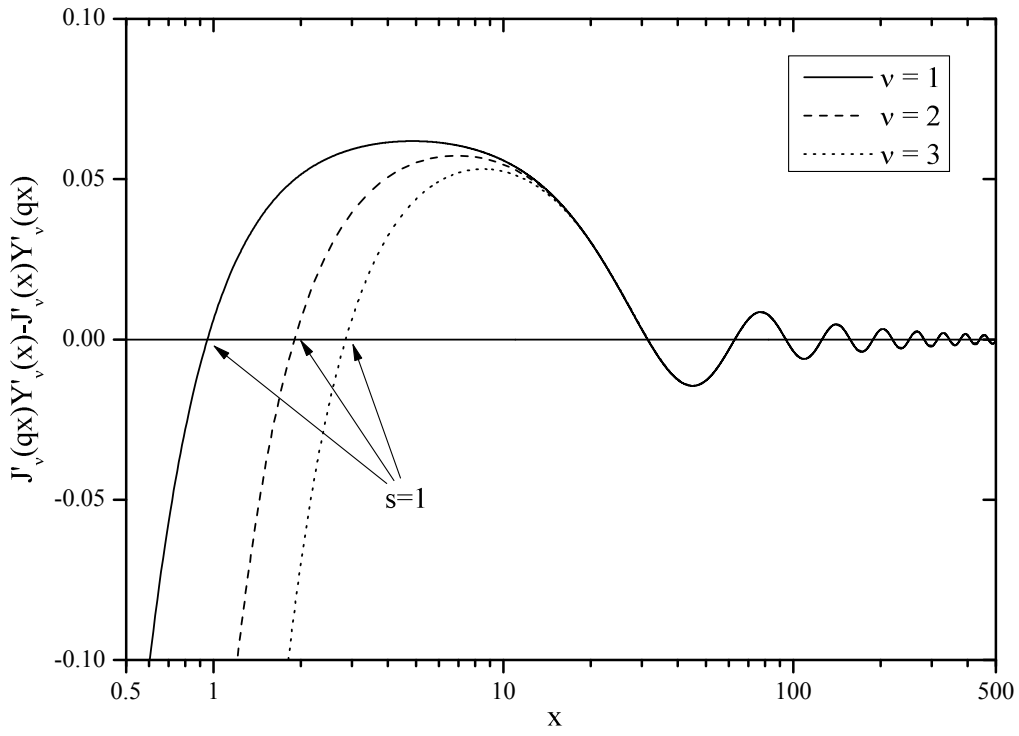
For $q = 1000$ the presence of the jumps of the seed to the next subintervals was observed for values of ν from 2 to 47. For values of ν below 15 the jump to the third subinterval occurred in few cases for large values of the root index, s (between 70 and 90). For big values of ν the jump occurred only to the second subinterval for few roots (typically 8 for each value of ν). It has also been observed that the number of roots for which this jump occurs decreases as the index ν grows, disappearing the presence of jumps for $\nu > 47$.

Figure 4.4b shows that the convergence of the first root of \tilde{g}_ν is mainly achieved in four or less iterations for any value of q as long as ν is larger than one, reflecting the fast performance of the root search. It is worthwhile to mention that, unlike the convergence of the search of $c_\nu^{(1)}$, the number of iterations needed to find $\tilde{c}_\nu^{(1)}$ is practically independent of q , except for the first order, showing a satisfactory performance of the root search for any order. The exception to the fast convergence of the algorithm occurs for $\nu = 1$, where the algorithm needs up to 24 iterations to converge for $q = 1.001$, though it is better compared to the previous algorithm [Sorolla 2011], where 81 iterations were required for $q = 1.01$. Although the comparison is made for different values of q it must be noted that the lower the coaxial cable aspect ratio the worse the convergence speed. The current algorithm finds the first root 4 times faster than the previous one and, moreover, for a smaller value of q .

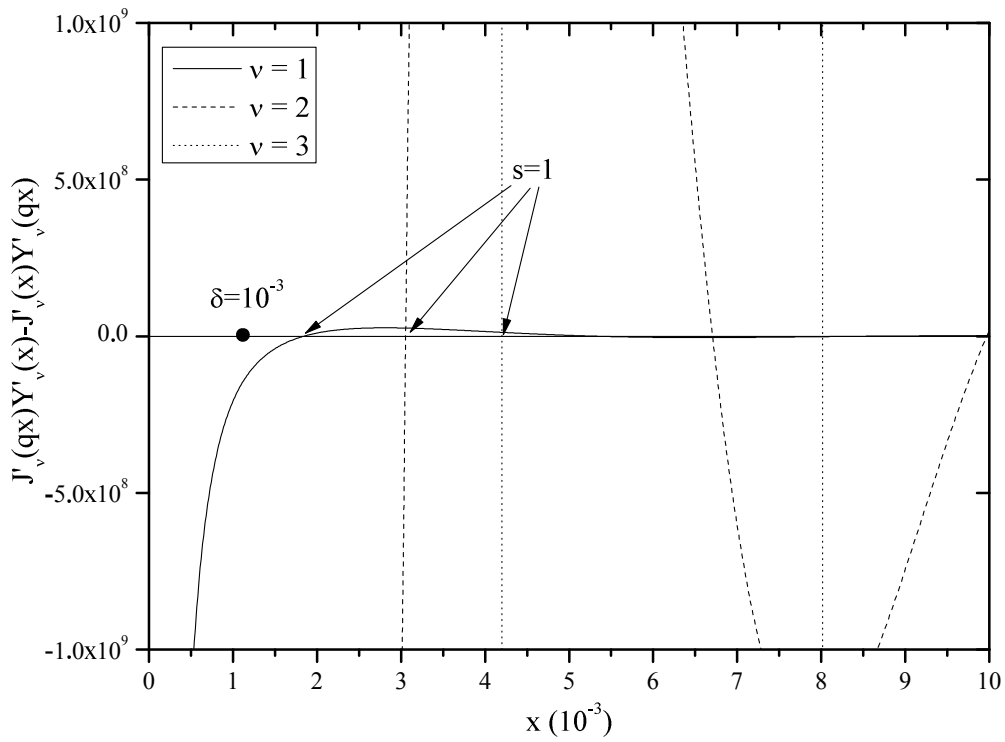
The reason of the slow performance in the root search of $\tilde{c}_\nu^{(1)}$ is twofold: the seed to calculate $\tilde{c}_1^{(1)}$ is placed slightly above δ within the interval $\tilde{I}_0 \in (\delta, c_1^{(1)})$, and this may lie far away from the actual root; the second reason is that the slope of the function $\tilde{g}_1(q, x)$ is very steep close to the origin, what makes the convergence of the NR algorithm difficult to converge when the seed is far from the root. Let us remind that the lower bound of the search interval was optimized to lie close to the first root for $q = 1000$ (see Fig. 4.5b) and the NR algorithm in this case needs only four steps as it is shown in cyan in Fig. 4.4b. For lower values of q the first root for $\nu = 1$ lies far above the lower bound of the search interval, what slows down the convergence. Nevertheless, all the roots $\tilde{c}_\nu^{(s)}$ are calculated based on the knowledge of $\tilde{c}_{\nu-1}^{(s)}$. Therefore, the drawback found in the root search of the first root of $\tilde{g}_1(q, x)$ does almost not affect the whole performance of the algorithm since, once the value of $\tilde{c}_1^{(1)}$ is found, the procedure calculates the rest of the roots very efficiently for any value of ν and q .

It must be mentioned that the algorithm still works for values of $q > 1000$ as long as the amount of roots requested for $\nu = 0$, s_{max} , and the largest order of the Bessel functions, ν_{max} , are not too big. For example, the algorithm is still able to find the roots for $q = 2000$ when $s_{max} = \nu_{max} = 30$ but when these values were increased to 40, the values of the argument of the Bessel functions were so small such that underflow error messages were received. On the other hand, the calculation of the roots of the cross-product of Bessel functions for extreme values of the coaxial cable aspect ratio have already been developed by other authors using the asymptotic expansion of the Bessel functions for small or big arguments [McMahon 1894, Laslett 1962, Cochran 1966b].

The average number of iterations needed to calculate the eigenvalues of the TM-modes is around 6 per roots for $q > 3$ and around 2 for $q < 1.1$. For the TE-modes the behavior of the convergence is in general a bit better, apart from the fact that for low values of q the convergence for $\nu = 1$ is very slow for the reasons mentioned above. In the end, the overall effect is that the average number of iterations in the search of the eigenvalues of



(a) $q = 1.1$.



(b) $q = 1000$.

Figure 4.5: Plots of the function $\tilde{g}_\nu(q, x)$.

TM- and TE-modes is very similar. The previously developed algorithms that analyzed the calculation of the roots of (4.1) were based either on the approximation by a series [McMahon 1894, Bridge 1962], sometimes only valid for asymptotic values of q or ν [Laslett 1962, Cochran 1966b], or on the solution of an eigenvalue problem in a fast and efficient way as most recent works have done [Gimeno 1996, Gimeno 1997, Ruiz-Cruz 2004, de la Rubia 2005]. These last studies showed very efficient calculation of the eigenvalues of more general structures, though the accuracy presented for coaxial cables was lower than the one achieved with the algorithm presented in this article. Nevertheless, as the computational cost to solve a linear eigenvalue problem grows with the square of the amount of roots, the method presented here is much more efficient when a large number of roots is requested, since its computational cost grows only linearly.

4.4 Summary

A globally convergent algorithm to find a large amount of roots of the cross-product of Bessel functions and their derivatives has been developed for the first time for a large range of values of the parameter q and the order ν . Its efficiency has been checked analyzing the amount of iterations needed to reach convergence up to the 14-th digit, underlining its good performance. The algorithm with the detailed steps to follow has been depicted in pseudo-code, showing the easy implementation using the Newton-Raphson iteration scheme.

In average, approximately only 6 iterations per root are required considering two extreme values of the parameter q , with the exception of the first root of the cross-product of derivatives of Bessel functions (TE modes). However, this isolated case only affects slightly the overall performance of the algorithm.

The speed of the algorithm has been tested for $q = 1.001$ and $q = 1000$, showing a speed of 81000 and around 16000 roots per second, respectively, all calculated on a current desktop computer (Intel 4-core 2.4 GHz).

Table 4.1: Roots of $g_\nu(q, x)$ for $q = 1.001$.

		$(q-1)c_\nu^{(s)}$				
$s \backslash \nu$	0	1	2	3	4	5
1	3.14159261384070	3.14159277283666	3.14159324982459	3.14159404480405	3.14159515777465	3.14159658873654
2	6.28318528730424	6.28318536680294	6.28318560529729	6.28318600278670	6.28318655927254	6.28318727475406
3	9.4247794751978	9.42477800051970	9.42477815951523	9.42477842450749	9.42477879549898	9.42477927248715
4	12.5663706044217	12.5663706441725	12.5663707634179	12.5663709621625	12.5663712404052	12.5663715981467
5	15.7079632599985	15.7079632917983	15.7079633871946	15.7079635461920	15.7079637687865	15.7079640549799
6	18.8495559149138	18.8495559414141	18.8495560209108	18.8495561534082	18.8495563389043	18.8495565773960
7	21.9911485694487	21.9911485921646	21.9911486603049	21.9911487738743	21.9911489328691	21.9911491372929
8	25.1327412237482	25.1327412436240	25.1327413032459	25.1327414026220	25.1327415417425	25.1327417206116
9	28.2743338778918	28.2743338955588	28.2743339485548	28.2743340368878	28.2743341605521	28.2743343195481
10	31.415926519259	31.4159265478225	31.4159265955208	31.4159266750207	31.4159267863192	31.4159269294122

Table 4.2: Roots of $\tilde{g}_\nu(q, x)$ for $q = 1.001$.

ν	$(q-1)\tilde{c}_\nu^{(s)}$				
s	1	2	3	4	5
$1 (10^{-3})$	0.9995002914791958	1.999000582958197	2.9985000874437121	3.998001165915639	4.997501457393846
2	3.14159293183281	3.14159340882063	3.14159420380024	3.14159531677170	3.14159674773360
3	6.28318544630149	6.28318568479540	6.28318608228523	6.28318663877034	6.28318735425205
4	9.42477805351680	9.42477821251291	9.42477847750602	9.42477884849725	9.42477932548451
5	12.5663706839191	12.5663708031668	12.5663710019127	12.5663712801540	12.5663716378951
6	15.7079633235970	15.7079634189947	15.7079635779910	15.7079638005860	15.7079640867774
7	18.8495559679116	18.8495560474122	18.8495561799068	18.8495563654032	18.8495566038958
8	21.9911486148778	21.9911486830198	21.9911487965874	21.9911489555840	21.9911491600060
9	25.1327412634983	25.1327413231240	25.1327414224935	25.1327415616179	25.1327417404876
10	28.2743339132224	28.2743339662221	28.2743340545521	28.2743341782166	28.2743343372131
11	31.4159265637216	31.4159266114206	31.4159266909218	31.4159268022147	31.4159269453126

Multipactor saturation

Contents

5.1	Introduction	81
5.2	Multipactor breakdown with space charge effects	82
5.2.1	Equations of motion of the electron sheet	83
5.2.2	Stability of the multipactor discharge	85
5.3	Mechanisms of saturation	92
5.3.1	Impact energy limit mechanism	94
5.3.2	Returning limit mechanism	95
5.4	Range of validity of the saturation mechanisms	101
5.5	Summary	104

5.1 Introduction

In order to detect the presence of multipactor some experimental methods have been proposed in the literature, like the third harmonic detection technique [Udiljak 2003], which proposes the search of the third harmonic of the radiated power spectrum of the electron cloud current to witness the presence of the discharge. As the electron population cannot grow indefinitely there must be a mechanism that limits the number of electrons released by secondary emission, i.e., the saturation mechanism. On the other hand, the intensity of the radiated power spectrum depends on the number of electrons involved in the discharge [Sorolla 2008], and the detection is supposed to take place when the saturation is reached. Therefore, the study of the multipactor saturation is important in order to estimate the number of electrons in the steady-state and establish a measurable criterion for the discharge onset, since a criterion to determine whether multipactor has unambiguously occurred does not exist yet.

The parallel-plate waveguide is a good model to study many structures like irises or small gaps where the electric field is reasonably homogeneous [Woode 1990]. The physical mechanism to explain the classical multipactor breakdown has been studied by several authors. Initially, analytical expressions for the equations of motion of the electrons within a parallel-plate waveguide were found without considering space charge effects [Hatch 1954, Vaughan 1988]. They were used to explain the conditions that lead to the multipactor onset and to calculate the voltage threshold that would trigger the electron avalanche. Nevertheless, they could not predict a limit in the amount of electrons released by secondary emission, though a tentative description of the saturation taking into account the thermal spread in the initial velocity of the secondary electrons, and the consequent bunch breakup produced by the mutual repulsion between electrons, was considered [Vaughan 1988].

Other authors have studied the multipactor discharge using a PIC (Particle-In-Cell) code considering the thermal effects and the change of the total electric field due to the presence of the boundaries on the electron cloud as well [Riyopoulos 1995, Riyopoulos 1997, Gopinath 1998, Buyanova 2010]. Their works showed the limit in the increase of the electron population and remarked the importance of the interaction of the electron cloud with its image through the metallic boundaries to explain the achievement of steady-state multipactor. The spread in the initial velocity of secondary electrons also explained the multipactor saturation by the de-bunching of the electron cloud against the phase-focusing effect. Other works have been developed to study the saturation of multipactor discharge in more general geometries or with different approaches [Kishek 1995, Kishek 1996, Ang 1998, Kishek 1997, Somersalo 1998, Gorshkova 1999, Blyakhman 2000, Semenov 2007, Coves 2008]. However, the mono-energetic model of secondary emission has been proposed in this chapter model as a good approximation to describe the steady-state multipactor under certain conditions. It was suggested that steady-state multipactor, if it exists, may be adequately described by a single sheet model [Kishek 1996]. Furthermore, it has been shown that, when fluctuations in the initial energy distribution of the secondary electrons are small enough and the SEY is slightly larger than one, the steady-state with a tight bunch preventing bunch breakup may occur [Riyopoulos 1997].

Therefore, in this chapter, like in Chapter 2, the initial velocity of all secondary electrons is assumed to be constant and the impacts against the metal plates are assumed to imply a SEY slightly above unity, so that the presented calculations of the saturation charge density are a good approximation of the saturation levels found near above the multipactor threshold. Nevertheless, as multipactor breakdown is usually detected near the threshold, the saturation levels calculated in these conditions are representative of steady-state multipactor.

The results of the electron population evolution obtained show that the image charge of the electron sheet has a strong influence on the appearance of the steady-state multipactor, as it will be presented later. Two mechanisms of saturation have been identified to explain the multipactor saturation for order one of resonance (see Section 2.2). The conclusions of this chapter agree with those ones already found by other authors: the decrease in the impact energy of the electron cloud with the increase of the electron surface density till reaching the unity SEY [Kishek 1995, Riyopoulos 1997, Kishek 1997], and the transient from double-sided to single-sided multipactor by the attraction of the electron cloud by its image through the plates [Buyanova 2010]. These two effects have also been identified in this work as the mechanisms to explain the multipactor steady-state.

We will model the electron cloud by an infinitely thin sheet and calculate the equations of motion within a parallel-plate waveguide excited by the Transverse-Electromagnetic (TEM) mode taking into account space charge effects. The equations of motion of the electron sheet will be presented (for details see Appendix C) and a description of the physical mechanisms that lead the electron cloud to the saturation stage provided by this model will be done. The analysis of the stability of the electron population growth will be developed and employed to explain how the multipactor steady-state is attained.

5.2 Multipactor breakdown with space charge effects

The electron cloud generated during the discharge in parallel-plate geometries has traditionally been modeled by an infinitely thin, flat and continuous charge distribution (electron sheet) [Vaughan 1988, Kishek 1995, Riyopoulos 1997, Coves 2008] using the theory of Sombrin [Sombrin 1983] in which the initial speed of all the secondary electrons is the same. Analogously to [Kishek 1995], the self-field of the electron sheet when calculating its equations of motion has been considered to take into account the space charge effects in the motion of the electron cloud.

Like in Chapter 2, the SEY model of Vaughan [Vaughan 1989] has been chosen to calculate the electron population growth along the time evolution. The dependency of the first cross-over point of the material of the plates on the electron density at the steady-state will be studied, showing an important influence on the maximum charge density of the electron cloud in the saturation.

5.2.1 Equations of motion of the electron sheet

Let us consider the set of electrons within the region between the plates represented in Fig. 5.1a that describes the electron cloud produced by the multipactor discharge in a parallel-plate waveguide. This can be modeled by an unbounded 2D continuous charge distribution whose surface charge density is $\Sigma = -e\sigma$, where $-e$ is the electron charge and $\sigma[\text{m}^{-2}]$ is the electron surface density of the sheet. The charge distribution is assumed to move in one dimension along the z axis between the plates of the waveguide (see Fig. 5.1b). As the plates of the waveguide are supposed to have infinite dimensions, edge effects are not present and the electric field within the region between the plates can be calculated analytically. It is assumed that all the secondary electrons are released from the plates at the same time and with the same initial velocity. Thus, the motion of a single electron of the sheet taking into account the interaction with the rest of the electrons is calculated, since it is representative for the motion of the electron sheet. The electric field evaluated at the position of a single electron belonging to the sheet will be calculated applying the superposition principle: the total electric field will be the sum of the generator field plus the field produced by the electron sheet between the parallel-plates without the contribution of the single electron whose motion is considered.

The infinite parallel-plate waveguide is excited with the fundamental mode, thus, the electric field coming from the generator points the z -axis and is given by:

$$\mathbf{E}_{\text{RF}}(t) = \frac{V_{\text{RF}}}{d} \cos(\omega t) \hat{\mathbf{z}} \quad (5.1)$$

where V_{RF} is the RF voltage, ω is the angular frequency of the RF signal and d is the distance between the plates (see Fig. 5.1b).

The electric field provided by the electron sheet is oriented along the z -axis, and it is described by a piecewise function where the electron sheet introduces a discontinuity at $z = z'(t)$ [Stakgold 1979]:

$$\mathbf{E}_{\text{sheet}}(z, t) = \begin{cases} \mathbf{E}_{\text{below}} = \frac{-e\sigma[z'(t)-d]}{\epsilon_0 d} \hat{\mathbf{z}}, & 0 \leq z < z'(t) \\ \mathbf{E}_{\text{above}} = \frac{-e\sigma z'(t)}{\epsilon_0 d} \hat{\mathbf{z}}, & z'(t) < z \leq d \end{cases}$$

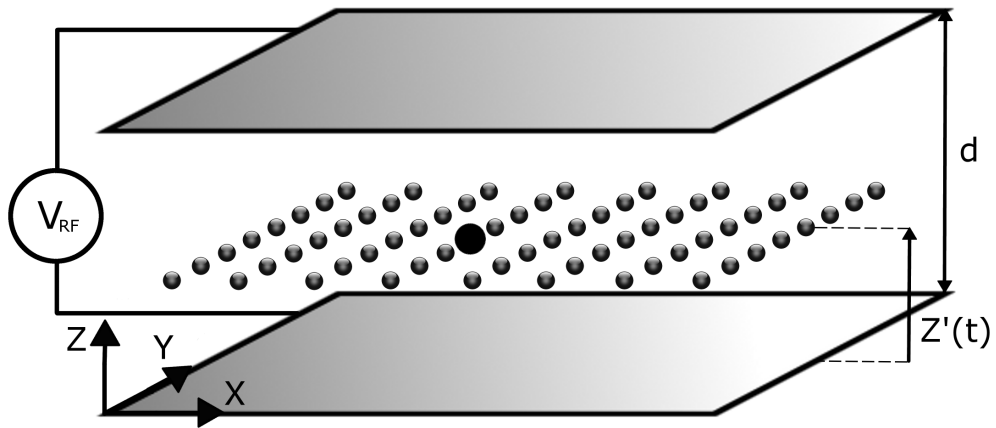
where ϵ_0 is the vacuum permittivity.

Our goal is to find an expression for the position of the electron sheet, $z'(t)$, and its velocity, $\dot{z}'(t)$, as function of time. To do so, we are going to apply the total electric field on a single electron of the sheet. By the superposition principle the total electric field will be

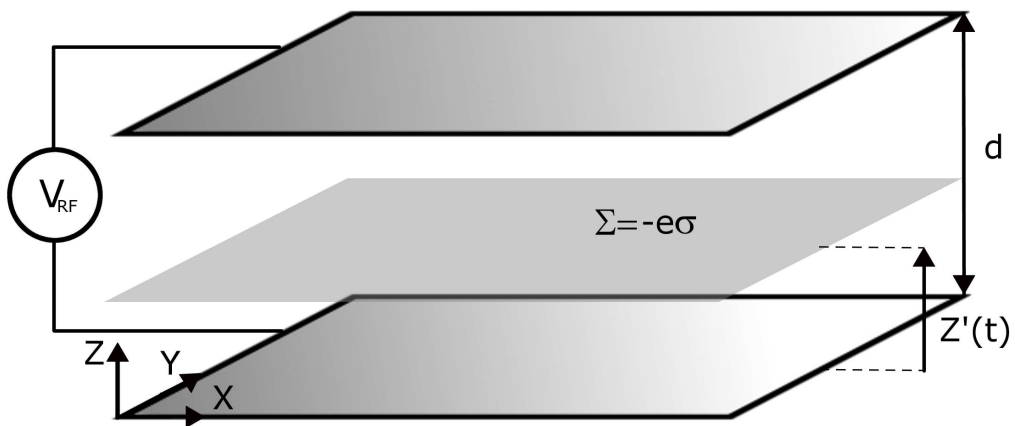
$$\mathbf{E}_{\text{total}}(t) = \mathbf{E}_{\text{RF}}(t) + \mathbf{E}_{\text{sheet}}(z = z'(t), t) \quad (5.2)$$

To calculate $\mathbf{E}_{\text{sheet}}(z = z'(t), t)$ the approach of [Griffiths 1999] has been followed: the electric field at a point on a conductor is the mean value of the electric fields above and below the discontinuity evaluated at that point, $z'(t)$. Thus, we can write the total electric field on a single electron of the sheet as:

$$\mathbf{E}_{\text{total}}(t) = \left(\frac{V_{\text{RF}}}{d} \cos(\omega t) - \frac{e\sigma(z'(t)/d - 1/2)}{\epsilon_0} \right) \hat{\mathbf{z}} \quad (5.3)$$



(a) Sketch of the electron cloud. Note that the equations of motion are found for the electron represented by the big black sphere.



(b) Electron sheet model of the electron cloud.

Figure 5.1: Electron cloud produced by a multipactor discharge predicted by Sombrin's model within a parallel-plate waveguide.

The first term represents the field from the generator and the second the field from the image charges induced by the electron sheet due to the presence of the plates, as it has already been identified in [Kishek 1995].

If the Lorentz force is applied to an electron of the sheet (e.g. the black one in Fig. 5.1a) neglecting the magnetic field, we find a differential equation that can be solved analytically. The details of the solution of that differential equation are shown in Appendix C. Thus, the velocity of the electron sheet can be written

$$\begin{aligned} \dot{z}'(t) = & (v_0 + \bar{z}_\sigma \omega \sin \phi_1) \cosh \left(\frac{\delta\phi}{\sqrt{K_\sigma}} \right) - \frac{\omega}{\sqrt{K_\sigma}} \left(\frac{d}{2} - z'_0 + \bar{z}_\sigma \cos \phi_1 \right) \sinh \left(\frac{\delta\phi}{\sqrt{K_\sigma}} \right) + \\ & - \bar{z}_\sigma \omega \sin(\phi_1 + \delta\phi) \end{aligned} \quad (5.4)$$

and the position is:

$$\begin{aligned} z'(t) = & \frac{d}{2} + \bar{z}_\sigma \cos(\phi_1 + \delta\phi) + \sqrt{K_\sigma} \left(\frac{v_0}{\omega} + \bar{z}_\sigma \sin \phi_1 \right) \sinh \left(\frac{\delta\phi}{\sqrt{K_\sigma}} \right) + \\ & + \left(z'_0 - \frac{d}{2} - \bar{z}_\sigma \cos \phi_1 \right) \cosh \left(\frac{\delta\phi}{\sqrt{K_\sigma}} \right) \end{aligned} \quad (5.5)$$

where v_0 is the initial velocity of the electron sheet when leaving the initial plate located at z'_0 at the instant t_1 , and ϕ_1 is the phase of the RF field at t_1 ; $\delta\phi$ is the phase shift between the phase for any subsequent instant t ($\phi = \omega t$) and ϕ_1 ($\delta\phi = \omega(t - t_1)$); the quantity \bar{z}_σ is given by the expression

$$\bar{z}_\sigma = \frac{\epsilon_0 V_{RF}}{e\sigma(1 + K_\sigma)}$$

where K_σ is a dimensionless parameter defined by

$$K_\sigma \equiv \frac{\epsilon_0 m_e \omega^2 d}{\sigma e^2},$$

m_e being the electron mass. The parameter K_σ stands for the intensity of the interaction between the electron sheet and its image, since it is easy to prove that, as σ tends to zero, \bar{z}_σ tends to $eV_{RF}/m_e\omega^2 d$ and (5.4) and (5.5) tend to the expressions obtained in the literature where space charge effects are neglected [Vaughan 1988, Hatch 1954].

5.2.2 Stability of the multipactor discharge

The time evolution of the electron population has been calculated using the equations of motion introduced in Section 5.2.1 for different values of the initial velocity, frequency, distance, voltage and the first cross-over point of the SEY. The phase of resonance is obtained using the ‘‘effective electron’’ model, since the initial electron surface density has been taken low enough as to represent accurately this model at the beginning of the motion ($\sigma \leq 10^{-6} \text{ m}^{-2}$). The simulations were carried out during hundreds of periods of the signal and they all showed a limit in the increase of the surface electron density (see e.g. Fig. 5.2). When the RF voltage is near above the breakdown voltage threshold (SEY slightly above unity) the simulations showed that the ceiling in the evolution of σ with time for multipactor of order one is reached in different ways.

For very low values of the RF voltage the electron surface density reaches a constant value in the steady-state as it is shown in Fig. 5.2a for $V_{RF} = 30 \text{ V}$ and in Fig. 5.2b for $V_{RF} = 70 \text{ V}$. However, when the voltage increases, the steady-state is characterized by a fast oscillation of σ , what can exhibit different behaviors. The

electron surface density may oscillate chaotically below a certain limit which is never exceeded (see the case for $V_{RF} = 60$ V in Fig. 5.2a), or if the voltage is too high, the values of σ exhibit big oscillations without a well-defined top limit. Interestingly, the electron population growth with space charge effects may exhibit different behaviors as time passes. An example of this is plotted in Fig. 5.2b for $V_{RF} = 1400$ V, where the steady-state seems to have been reached when the chaotic oscillations of σ appear but after a certain instant the fast variations exhibit a coherent behavior.

The different ways for the multipactor discharge to reach the steady-state can be explained by analyzing the stability factor of the resonant motion of the electron sheet. For example, for very low values of the RF voltage, but still able to fulfill the conditions of resonance, and for impact energies higher than the first cross-over point, the electron sheet impacts against the plates with enough energy so that its charge increases gradually. Above a certain value of σ , the image charge of the electron sheet with respect to the initial plate is able to slow down the motion of the electron cloud so that the impact energy against the opposite plate decreases wandering around, before converging to the first cross-over point. In Fig. 5.3 the impact energy vs. the electron surface density for the cases obtained with $V_{RF} = 30$ V and $V_{RF} = 70$ V presented in Fig. 5.2 shows that the saturation is, indeed, attained when the impact energy reaches the first cross-over point. In these cases the mechanism that describes the process of saturation has been named “impact energy limit” model. This mechanism consists of the decrease of the impact energy as the electron surface density increases, but maintaining the stability of the resonance till the impact energy reaches the first cross-over point, when the electron population does not increase anymore. When the voltage is higher, such that the electron sheet returns to the initial plate attracted by its image before reaching the opposite plate, the maximum value of the electron surface density can be predicted by the “returning limit” model. Both models will be mathematically developed later.

In order to understand the mechanisms that lead the multipactor breakdown to the steady-state let us study the stability of the motion of the electron sheet for each case. To do so, the stability factor as presented in Section 2.4

$$|G| \equiv \left| \frac{\partial \phi}{\partial \phi_1} \right|_{\phi=\phi_1+\pi}$$

is calculated using (5.5) to determine whether the resonant motion is stable or not. Therefore, using the definition of F employed in Section 2.4, the stability factor for order of multipactor one can be written as

$$\begin{aligned} G &= \frac{\partial F / \partial \phi_1}{\partial F / \partial \phi} \Big|_{\phi=\phi_1+\pi} = \\ &= \frac{v_0 / \omega \cosh \left(\pi / \sqrt{K_\sigma} \right) - [d/2 + (K_\sigma + 1) z_\sigma \cos \phi_1] h_\sigma}{(d/2 + z_\sigma \cos \phi_1) h_\sigma - z_\sigma \sin \phi_1 \left[1 + \cosh \left(\pi / \sqrt{K_\sigma} \right) \right] - v_0 / \omega \cosh \left(\pi / \sqrt{K_\sigma} \right)} \end{aligned}$$

where $h_\sigma \equiv \frac{\sinh(\pi/\sqrt{K_\sigma})}{\sqrt{K_\sigma}}$.

The stability factor is plotted in Figs. 5.4a and 5.4b as function of σ for different values of the initial phase ϕ_1 applying the resonance condition for order of multipactor one, i.e., $\phi = \phi_1 + \pi$. For example, the stability factor plotted in Fig. 5.4a for $V_{RF} = 30$ V and $\phi_1 = 1.6$ rad shows that the resonant motion of the sheet is stable for values of $\sigma \lesssim 3.5 \cdot 10^{12} \text{ m}^{-2}$. Part of the motion, together with the phase evolution of the impacts of the multipactor discharge, corresponding to the cases presented in Fig. 5.2 are shown in Fig. 5.5. The two top figures show the position of the electron sheet and the value of σ vs. time, and the two bottom figures show the impact phase, ϕ_n , vs. the initial one, ϕ_{n-1} . It must be noted that the resonance phase changes as the value of σ

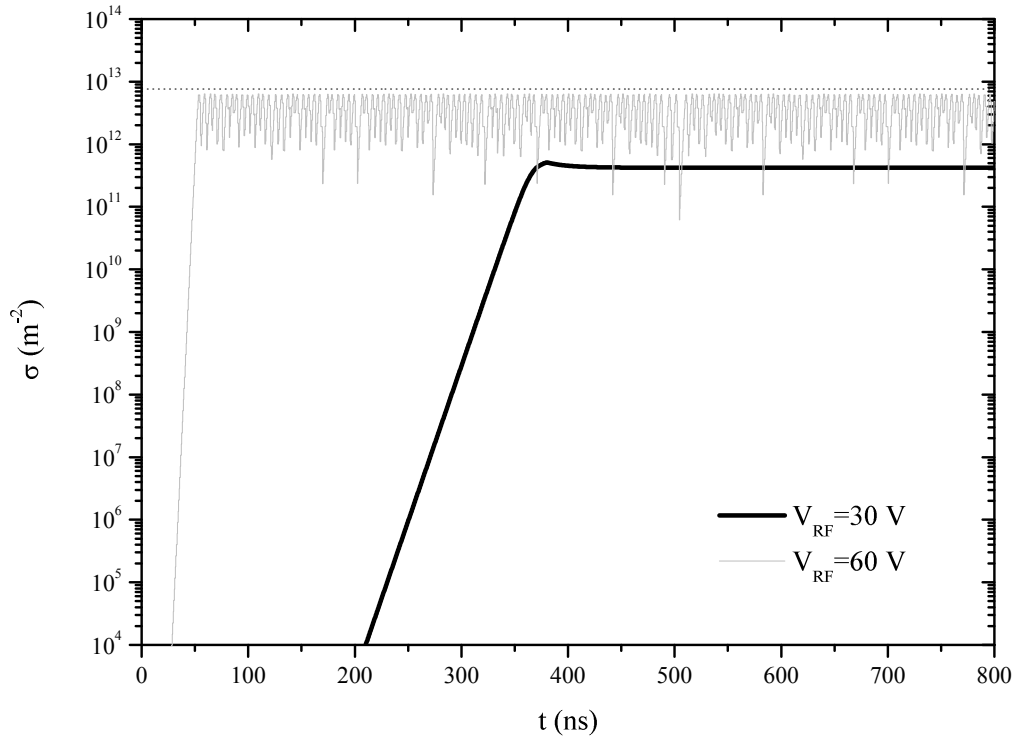
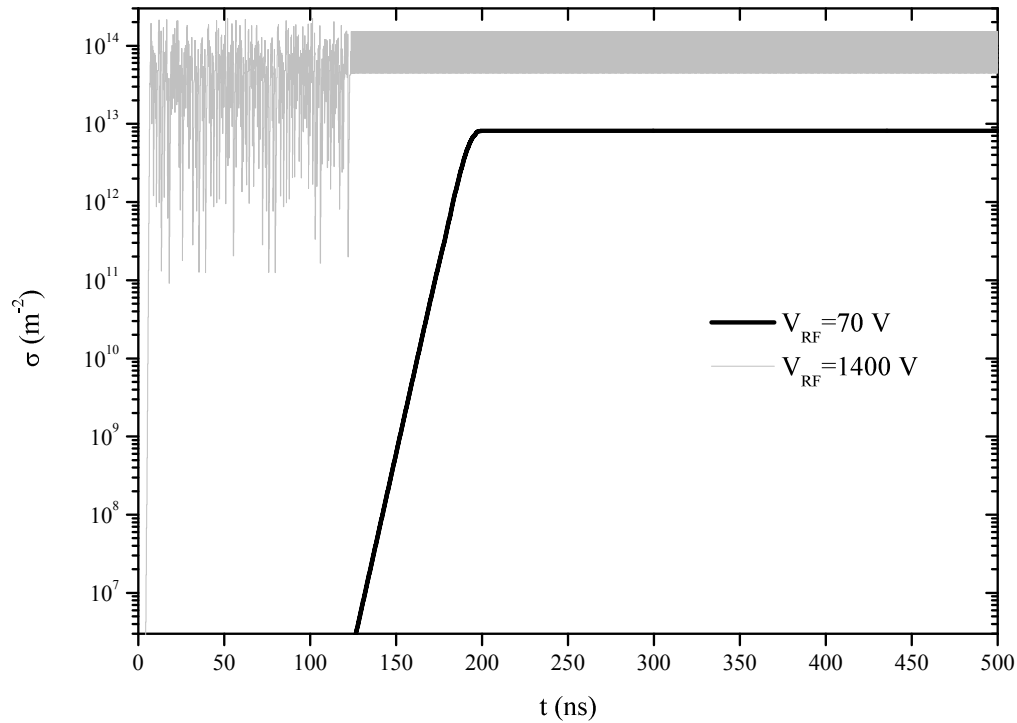
(a) $f = 1$ GHz, $d = 1$ mm, $v_0 = 3.68$ eV, $E_1 = 20$ eV.(b) $f = 5$ GHz, $v_0 = 2$ eV, $E_1 = 50$ eV.

Figure 5.2: Evolution of the electron surface density. (a) For $V_{RF} = 30$ V, $\phi_1 = 1.06$ rad and for $V_{RF} = 60$ V, $\phi_1 = 1.6$ rad. (b) For $V_{RF} = 70$ V, $d = 0.2$ mm and $\phi_1 = 1.1$ rad and for $V_{RF} = 1400$ V, $d = 1$ mm and $\phi_1 = 2$ rad.

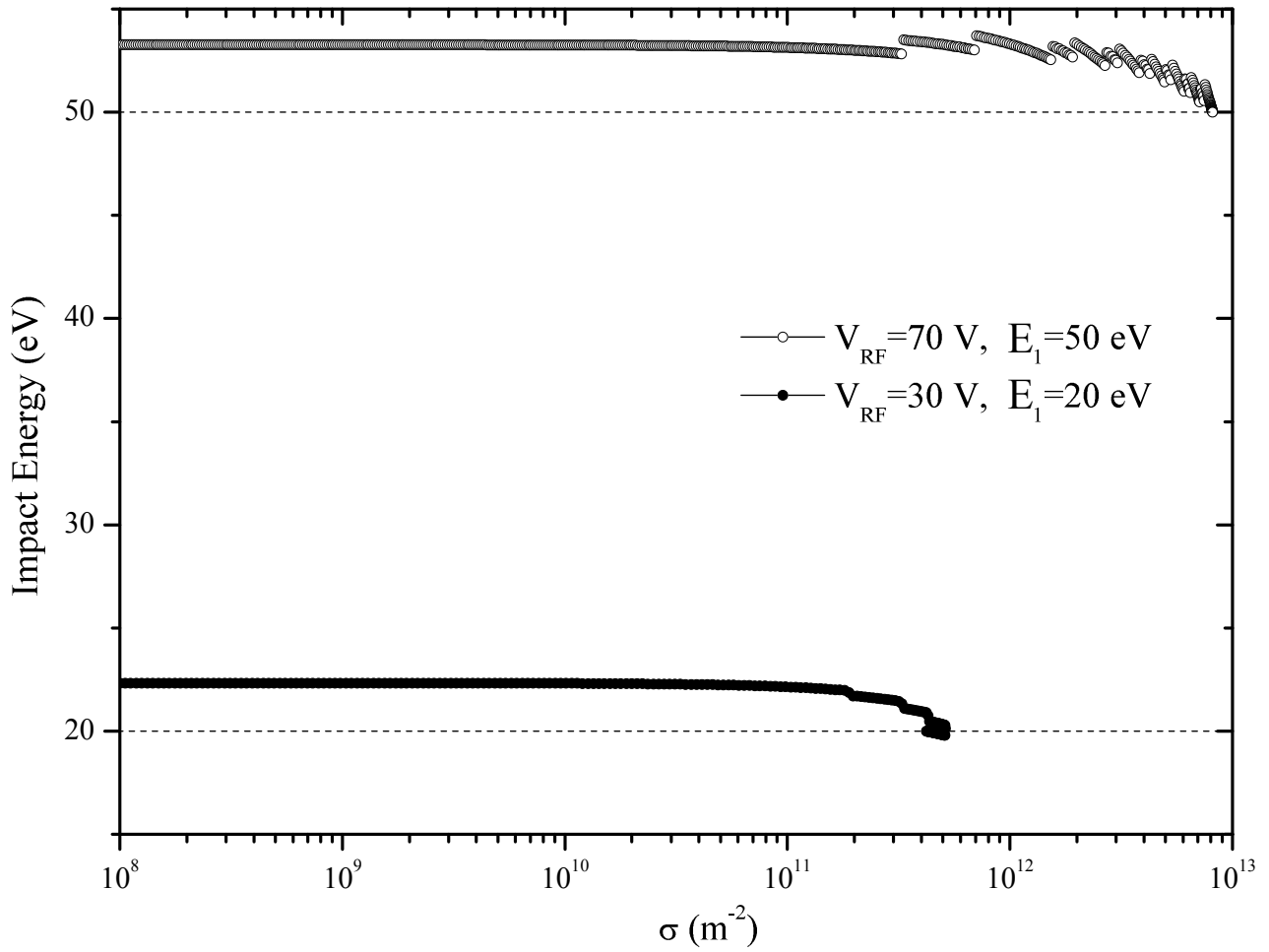


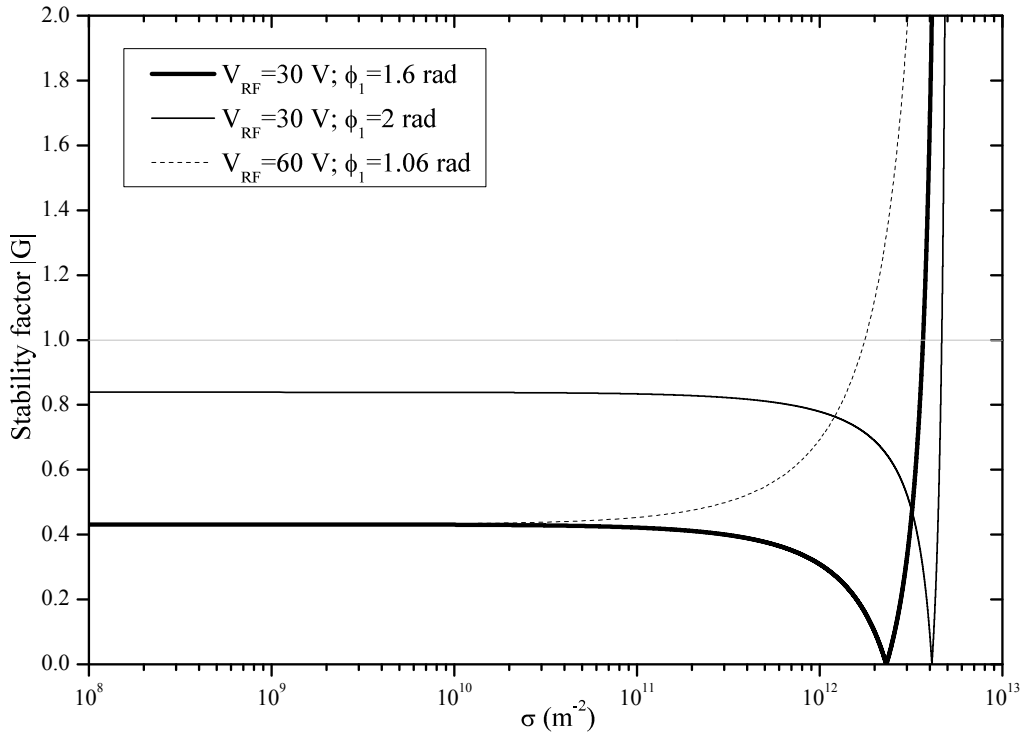
Figure 5.3: Impact energy as function of σ for $f = 1$ GHz, $d = 1$ mm, $v_0 = 3.68$ eV and $\phi_1 = 1.6$ rad (black dots) and $f = 5$ GHz, $d = 0.2$ mm, $v_0 = 2$ eV and $\phi_1 = 1.1$ rad (circles).

grows (see Figs. 5.5c and 5.5d), this is the reason why the stability factor has been plotted for different values of ϕ_1 . Interestingly, Figs. 5.5c and 5.5d show that for low voltages (represented by crosses) the resonant phase seems to increase slowly as the electron surface density grows. On the contrary, for higher voltages (represented by dots) the evolution of the initial phase changes more remarkably. The first case corresponds to the one when the value of the RF voltage is low enough so that σ does not overcome the values that would lead to an unstable resonant regime for the attained resonant phases. The second case shows that, at a certain instant, the resonance becomes unstable because the value of σ for the corresponding value of ϕ_1 entails a value of $|G|$ above unity.

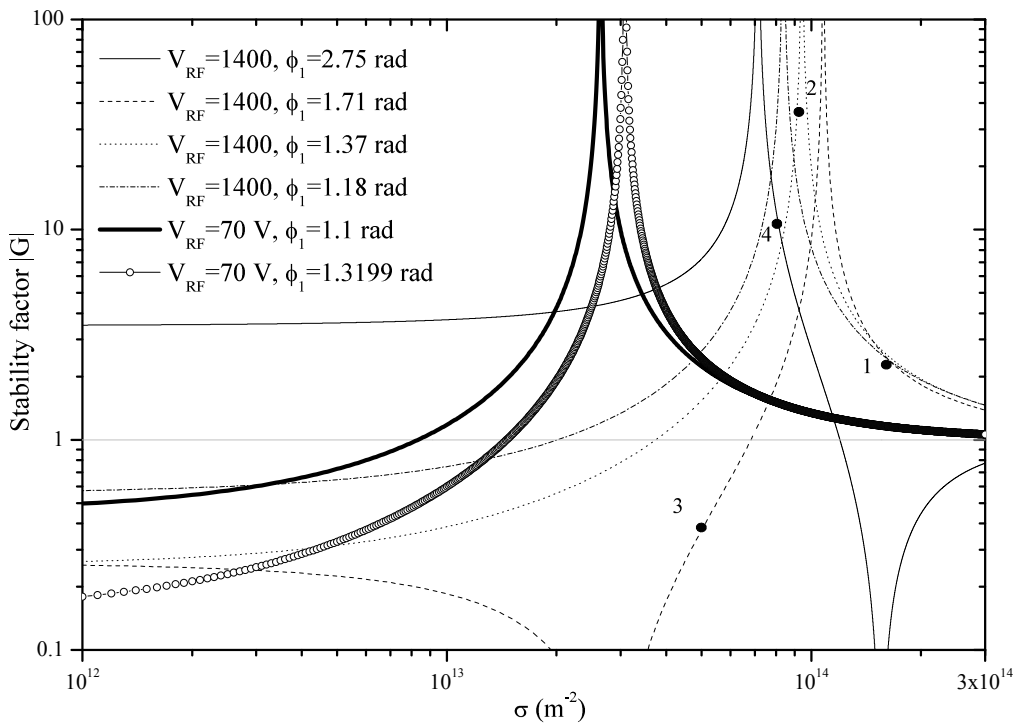
For instance, Fig. 5.3 shows that the electron surface density in the steady-state for $V_{RF} = 30$ V is around $\sigma = 5 \cdot 10^{11} \text{ m}^{-2}$, while Fig. 5.5c shows that the resonant phase ranges from $\phi_1 = 1.6$ rad, at the beginning of the motion, to $\phi_1 = 2$ rad in the saturation, whereas the stability factor stays below unity as long as σ stays below $4 \cdot 10^{12} \text{ m}^{-2}$ (see Fig. 5.4a). Analogously, the evolution of the resonant phase for $V_{RF} = 70$ V (plotted in Fig. 5.5d) shows that the stability factor (Fig. 5.4b) lies below one as the resonant phase evolves from $\phi_1 = 1.1$ rad to $\phi_1 = 1.3199$ rad. Although the stability factor for $\phi_1 = 1.1$ rad is in the limit of unity close to the saturation value of σ ($8 \cdot 10^{12} \text{ m}^{-2}$ according to Fig. 5.3), the evolution of the resonant phase towards $\phi_1 = 1.3199$ rad changes the profile of $|G|$ such that the maximum value of σ that keeps the stability factor below one increases, too, lying around $\sigma = 1.5 \cdot 10^{12} \text{ m}^{-2}$ (see Figs. 5.4b and 5.5d).

Due to the presence of the image charge, the consequences of the electron population growth are the decrease of the impact energy and the increase of the resonant phase. The overall effect by the increase of the electron population is equivalent to a reduction of the electric field in the “effective electron” model without space charge effects. One important difference between these two scenarios is that, as σ grows, the resonant phase increases and the stability factor changes in such a way that the resonant motion of the electron becomes stable for values of σ that would previously lead to unstable regimes (see e.g. Fig. 5.4a for $V_{RF} = 30$ V for $\phi_1 = 1.6$ rad and $\phi_1 = 2$ rad). Another difference is that the intensity of the electric field induced by the image charge changes not only with time, but with the position of the sheet, too. There are, thus, two facts that explain why in this case the saturation results in a constant electron surface density: 1) The resonant phase increases with σ (see crosses in Figs. 5.5c and 5.5d); 2) the maximum value of σ that yields a stability factor below unity increases with ϕ_1 (see Fig. 5.4a). These two effects allow the electron population to increase with the subsequent decrease of the impact energy until the first cross-over point is reached. This occurs before the value of σ that would entail a stability factor above one is attained when the growth rate is moderate. Thus, the calculation of the surface charge density in the steady-state obtained with the “impact energy limit” model is justified as long as the RF voltage is low enough to ensure that the SEY lies near above one during the increase of the electron population.

As it is shown next, the stability break is more likely to occur at some moment of the electron avalanche onset as the voltage increases. For higher voltages, the electron cloud also exhibits at the beginning a periodic motion (see Fig. 5.6b) but with the electron population increasing faster. Above a certain value of σ the stability factor exceeds unity marking the presence of an unstable resonance. The initial and final phases between successive impacts split up and resonance breaks. At this stage the image charge through the metal plates reduces the speed of the electron sheet and diminishes its impact energy against the opposite plate inducing a SEY close to unity (e.g. for impact **7** in Fig. 5.5a, the value of σ did not change significantly with respect to what occurred after impact **6**); or the impact can entail a low SEY with the subsequent decrease of the electron population (e.g. impacts **8** and **9** in Fig. 5.5a). The initial phase and the attraction between the sheet and its image imply the return of the electron cloud to the initial plate decreasing (e.g. impact **10** in Fig. 5.5a) or increasing (e.g. impact **1** in Fig. 5.5b) the electron surface density, respectively. In the first case, the minimum value of σ that provokes the return of the sheet to the initial plate for any value of the initial phase, inducing

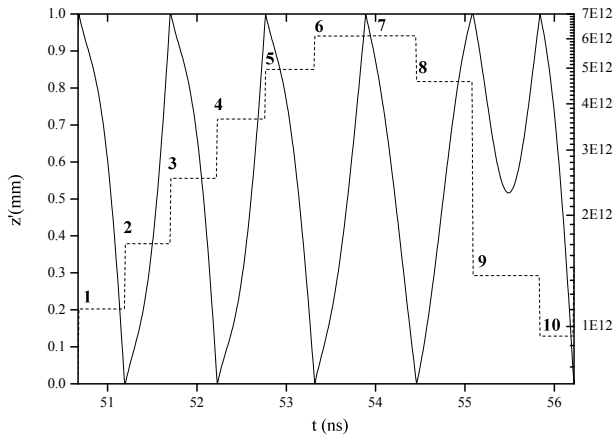


(a) Stability factor for the case of Fig. 5.6a.

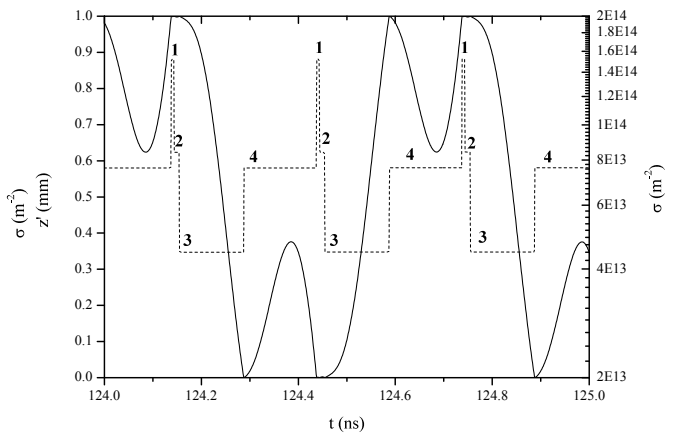


(b) Stability factor for the case of Fig. 5.6b.

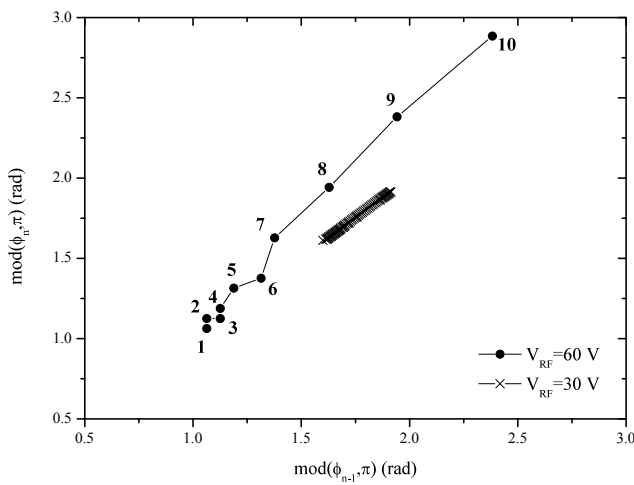
Figure 5.4: The stability factor calculated for different values of the initial phase corresponding to the cases presented in Fig. 5.6.



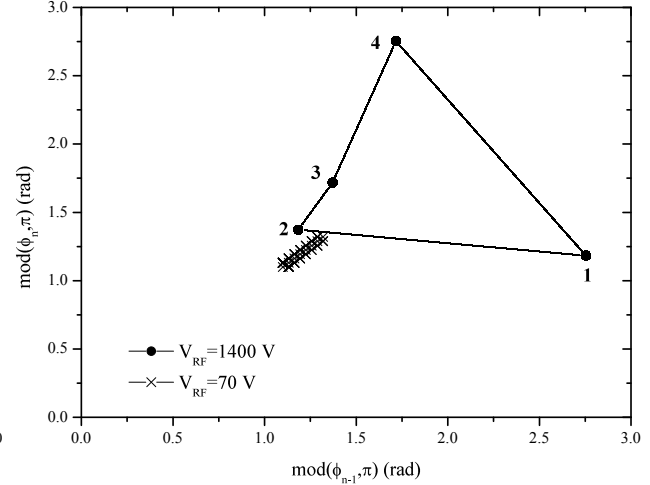
(a) Position and electron surface density for the high voltage case presented in Fig. 5.6a.



(b) Position and electron surface density for the high voltage case presented in Fig. 5.6b.



(c) Phase evolution of part of the motion shown in Fig. 5.6a.



(d) Phase evolution of part of the motion shown in Fig. 5.6b.

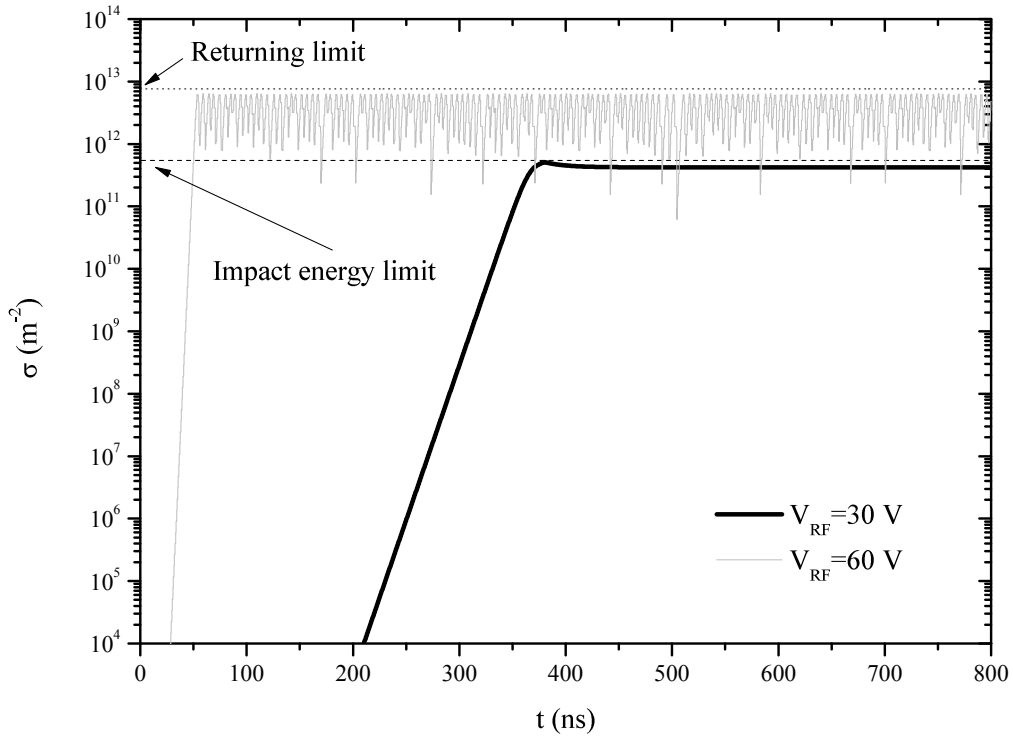
Figure 5.5: Analysis of the motion of the electron sheet for the cases shown in Fig. 5.6. (a) shows the motion (solid) and the electron surface density (dashed) during a short time slot for $V_{RF} = 60$ V presented in Fig. 5.6a; (b) shows the coherent part of the motion (solid) and the electron surface density (dashed) (after $t = 124$ ns) for $V_{RF} = 1400$ V presented in Fig. 5.6b; (c) and (d) show the phase at each impact, ϕ_n , vs. the one at the previous impact, ϕ_{n-1} , corresponding to the motion of the cases shown in Figs. 5.6a and Fig. 5.6b.

a SEY below unity, is identified as the saturation level, σ_{sat} in the “returning limit” model. The calculation of this value will be presented later and it is represented by the dotted line in Fig. 5.6. When the RF voltage is low enough, the impact energy in the collision against the initial plate lies below the first cross-over point and the electron surface density never goes above σ_{sat} (see Fig. 5.6a). On the contrary, when the RF voltage is much higher the initial phase may provoke a high impact energy against the initial plate with a SEY larger than unity, exceeding the value of σ_{sat} predicted by the “returning limit” model. An example of this is shown in Fig. 5.6b, where the maximum electron surface density exceeds the value obtained with this model when the voltage is too high.

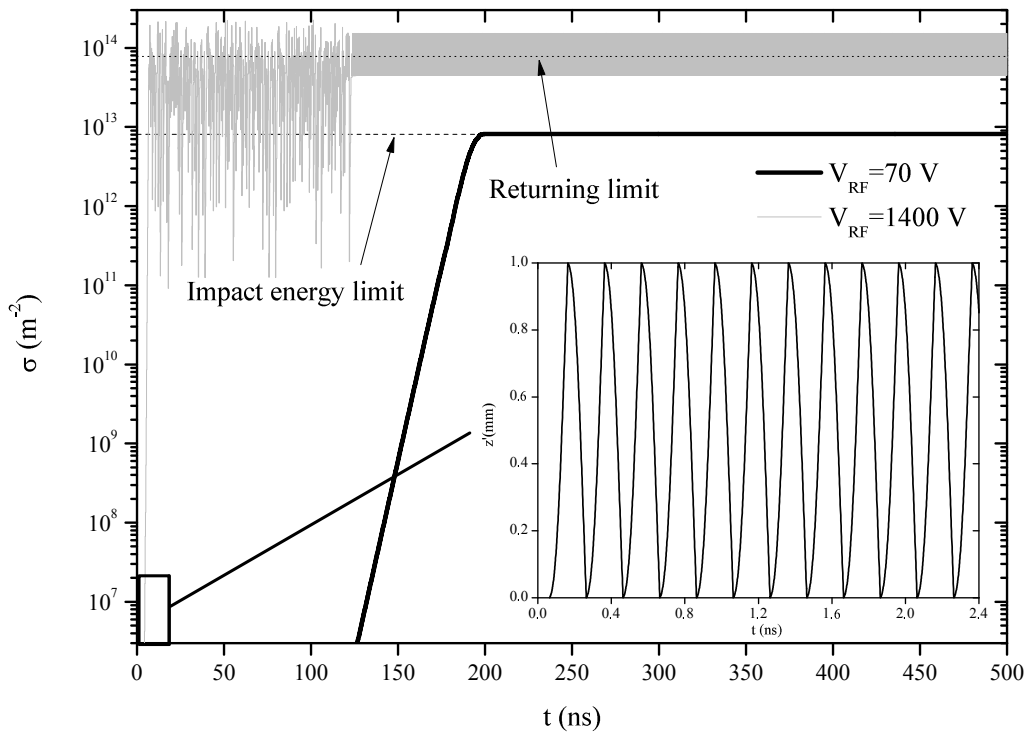
The presence of three regions can be noted in the growth of the electron surface density obtained for $V_{RF} = 1400$ V in Fig. 5.6b. Initially, the electron sheet moves in resonance with the RF field increasing σ quickly till the electron surface density overcomes the value for which the stability factor lies above one. From then on, the coherent motion of the electron sheet is destroyed and the electron population oscillates chaotically around the maximum value predicted by the “returning limit” model. However, after $t = 124$ ns, another type of resonant motion is found, differently of the initial one. In Fig. 5.5b the position of the sheet corresponding to the beginning of this part of the motion, where σ oscillates between two well-defined values, exhibits a multipactor resonance of order 3. In Fig. 5.5d the phase evolution from the beginning of this part of the motion till the end of the simulation shows a stable 4-cycle phase diagram which provides us with the values of the impact phases to evaluate the stability factor according to the value of σ obtained. The dots of the phase diagram show in Fig. 5.4b the evolution of the stability factor at each impact. Indeed, when the sheet reaches a high electron surface density (impact **1**) the resonance becomes unstable and the initial phase induces a low energy impact (impacts **2** and **3**), but when the value of σ has decreased below $5 \cdot 10^{13} \text{ m}^{-2}$ the phase at **3** is favorable to an impact against the opposite plate $\pi/3$ rad later (impact **4**). However, with the increase of the electron surface density the resonance becomes unstable once more with the particularity that the next impact leads to the initial phase and to the electron surface density of dot **1**. Therefore, this cycle repeats, and the oscillation in the values of σ limits the electron population growth in the steady-state, though the maximum value of the electron surface density lies above σ_{sat} predicted by the “returning limit” model.

5.3 Mechanisms of saturation

Therefore, when the RF voltage is not too high the steady-state can be explained by the two mechanisms described in what follows. The values of the surface electron density in the steady-state predicted by the “impact energy limit” model is shown in Fig. 5.6 for $V_{RF} = 30$ V and $V_{RF} = 60$ V. Note the good agreement between the predictions obtained with the numerical solution of (5.6) and the simulations of the electron population increase with the equations of motion. On the other hand, the maximum electron surface density predicted by the “returning limit” agrees with the case shown in Fig. 5.6a for $V_{RF} = 60$ V but it does not agree with the case represented in Fig. 5.6b for $V_{RF} = 1400$ V. It has been shown that in this case the voltage is so high that the stability is broken before reaching the steady-state, provoking oscillations in the values of σ beyond the maximum electron surface density predicted by the “returning limit” model.



(a) $f = 1$ GHz, $d = 1$ mm, $v_0 = 3.68$ eV, $E_1 = 20$ eV.



(b) $f = 5$ GHz, $v_0 = 2$ eV, $E_1 = 50$ eV.

Figure 5.6: Evolution of the electron surface density. (a) For $V_{RF} = 30$ V, $\phi_1 = 1.06$ rad and for $V_{RF} = 60$ V, $\phi_1 = 1.6$ rad. (b) For $V_{RF} = 70$ V, $d = 0.2$ mm and $\phi_1 = 1.1$ rad and for $V_{RF} = 1400$ V, $d = 1$ mm and $\phi_1 = 2$ rad.

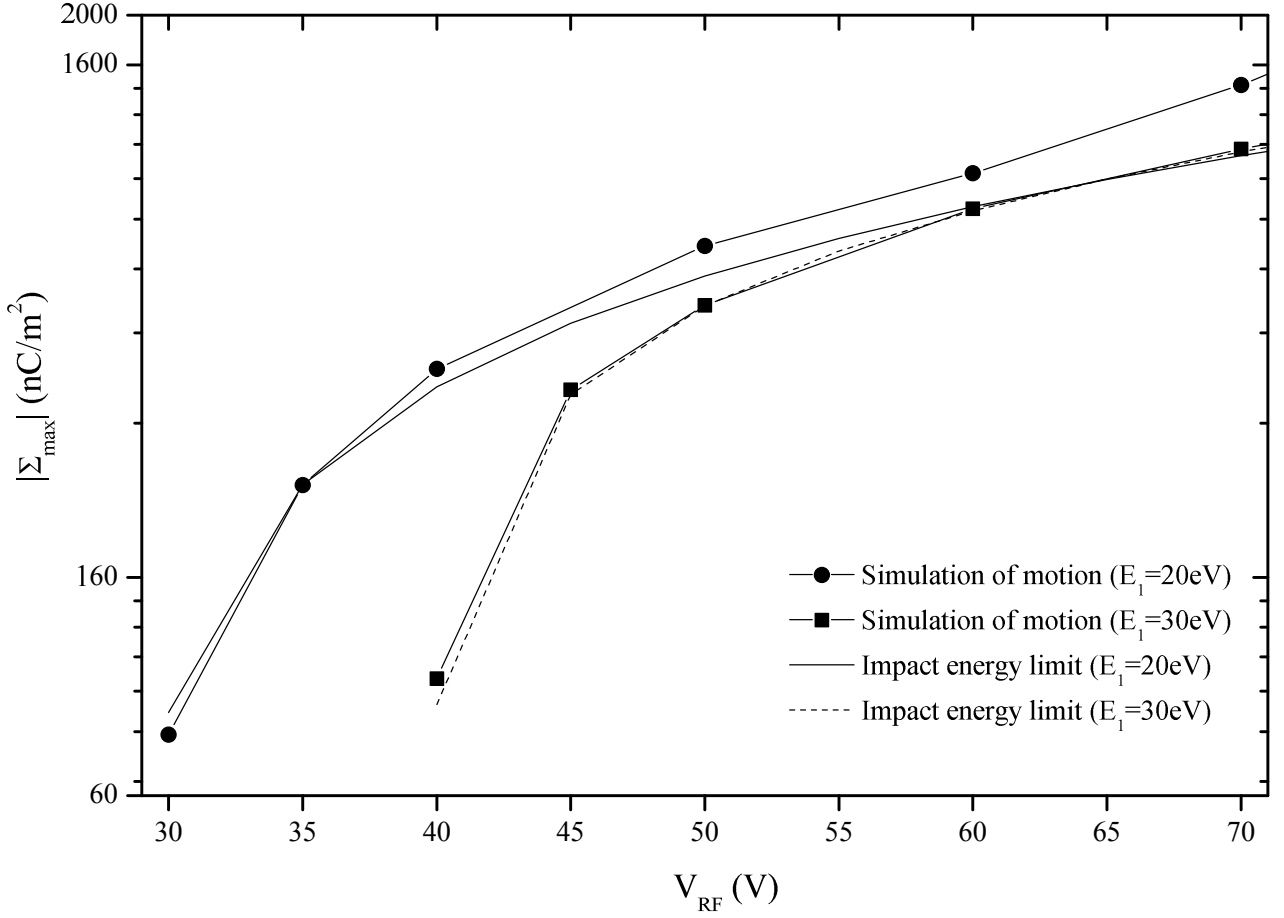


Figure 5.7: Steady-state surface charge density vs. RF voltage for $f = 1$ GHz, $d = 1$ mm and $v_0 = 3.68$ eV obtained with the equations of motion and with (5.6).

5.3.1 Impact energy limit mechanism

In this model, the value of σ_{sat} for which the resonance condition is fulfilled and the impact energy is equal to the first cross-over point is calculated as the solution of the following system of equations:

$$\left. \begin{aligned} d - z'[\delta\phi = \pi; \sigma = \sigma_{sat}] &= 0 \\ \sqrt{\frac{2eE_1}{m_e}} - z'[\delta\phi = \pi; \sigma = \sigma_{sat}] &= 0 \end{aligned} \right\} \quad (5.6)$$

that represents the classical system of equations to find the resonance condition. In this case the unknowns are the resonant phase and the density of electrons as the new variable. The values of f , d and v_0 are fixed in (5.4) and (5.5) and V_{RF} is calculated using the “effective electron” model as presented in Chapter 2 to ensure the multipactor occurrence of order one. Thus, the value of σ that verifies both equations is calculated and identified as σ_{sat} .

The value of the electron surface density as solution of the system of equations is compared with the results obtained with (5.4) and (5.5) by recording the electron growth during more than 900 periods using the SEY model of Vaughan. The RF voltage has been varied and the maximum electron surface density recorded for

each case. The results of the surface charge density ($\Sigma = -e\sigma$) obtained with the equations of motion are compared with the solution of (5.6) in Fig. 5.7 for two different values of E_1 . The agreement certifies that the multipactor saturation obtained with the equations of motion of the electron sheet in this case can be explained by the “impact energy limit” mechanism. Note that the maximum surface charge density obtained with two different values of the first cross-over point, E_1 , differ noticeably for low voltages, decaying in the low voltage region. This can be understood by the fact that, for a given voltage, the electron sheet impacting against a material with $E_1 = 30$ eV increases its charge till the impact energy reaches the first cross-over point; the electron sheet subject to the same voltage impacting against a material with $E_1 = 20$ eV has still some energy to increase its charge, however. In the high voltage region, the condition of the synchronous motion of the electron sheet with the RF signal has more influence on the solution of (5.6). Therefore, the “impact energy limit” mechanism predicts the same surface charge density of saturation independently of the first cross-over point for high voltages.

5.3.2 Returning limit mechanism

The calculation of the surface charge density of saturation described by the second mechanism is more cumbersome. As it was explained above, there is a minimum charge for which the image of the electron cloud with respect to the initial plate pulls the electron sheet back to this plate for any value of the initial phase before reaching the opposite plate. This model is based on the assumption that the collision against the initial plate entails a low impact energy and, thus, a decrease of the electron density, fixing so a maximum limit for σ , which is identified like the value of saturation of this model. Accordingly, the model assumes that the value of the first cross-over point of the SEY is much higher than the initial velocity so that E_1 does not play any role in the motion that fixes the value of σ_{sat} , which induces the return of the electron sheet to the initial plate, as long as the RF voltage is not too high. If the RF voltage produces a too intense electric field, or the first cross-over point is too small, the impacts against the initial plate may provoke an uncommon increase of the electron population and the electron surface density of saturation will lie above the maximum one predicted by this model.

Let us find the maximum surface charge density predicted by this model by establishing the condition of returning to the initial plate and defining the implicit function $|\Sigma(\phi_1, \delta\phi)| = |e\sigma(\phi_1, \delta\phi)|$ as

$$|\Sigma(\phi_1, \delta\phi)| : z'(z'_0, v_0, f, d, V_{RF}, \phi_1, \delta\phi; |\Sigma|) \equiv 0 \quad (5.7)$$

The function $|\Sigma(\phi_1, \delta\phi)|$ represents the value of the surface charge density of the electron sheet, leaving the initial plate at ϕ_1 , needed to cause the impact against the initial plate after the time (phase) span $\delta\phi$. This function has been plotted vs. ϕ_1 and $\delta\phi$ in Fig. 5.8, and it is clear that, for a given $\delta\phi$, there is an initial phase ϕ_1 for which the density of electrons presents a local maximum. This can be understood by noting that, for $\delta\phi$ and $|\Sigma|$ fixed, there is a certain value of the initial phase for which the speed of the electron sheet flying from the initial to the opposite plate is maximal (see Fig. 5.9 for an example). Therefore, it is natural to expect a local maximum at the minimum charge needed to force the electron sheet to return to the initial plate near the phase for which the maximum of the speed of the electron sheet is found. Below and above that phase, the speed of the sheet is lower, and the minimum charge, $|\Sigma_{max}|$, needed to slow down the electron sheet by its image in order to induce the impact against the initial plate is expected to be lower, too. The local maximum surface charge density of (5.7), $|\Sigma_{max}|$, is represented as function of $\delta\phi$ in Fig. 5.10. Note in this plot that, for a sufficiently big phase span, $\delta\phi$, the local maximum of the surface charge density, depicted in Fig. 5.8, tends to a constant value, what allows us to identify that value as the saturation surface charge density searched by

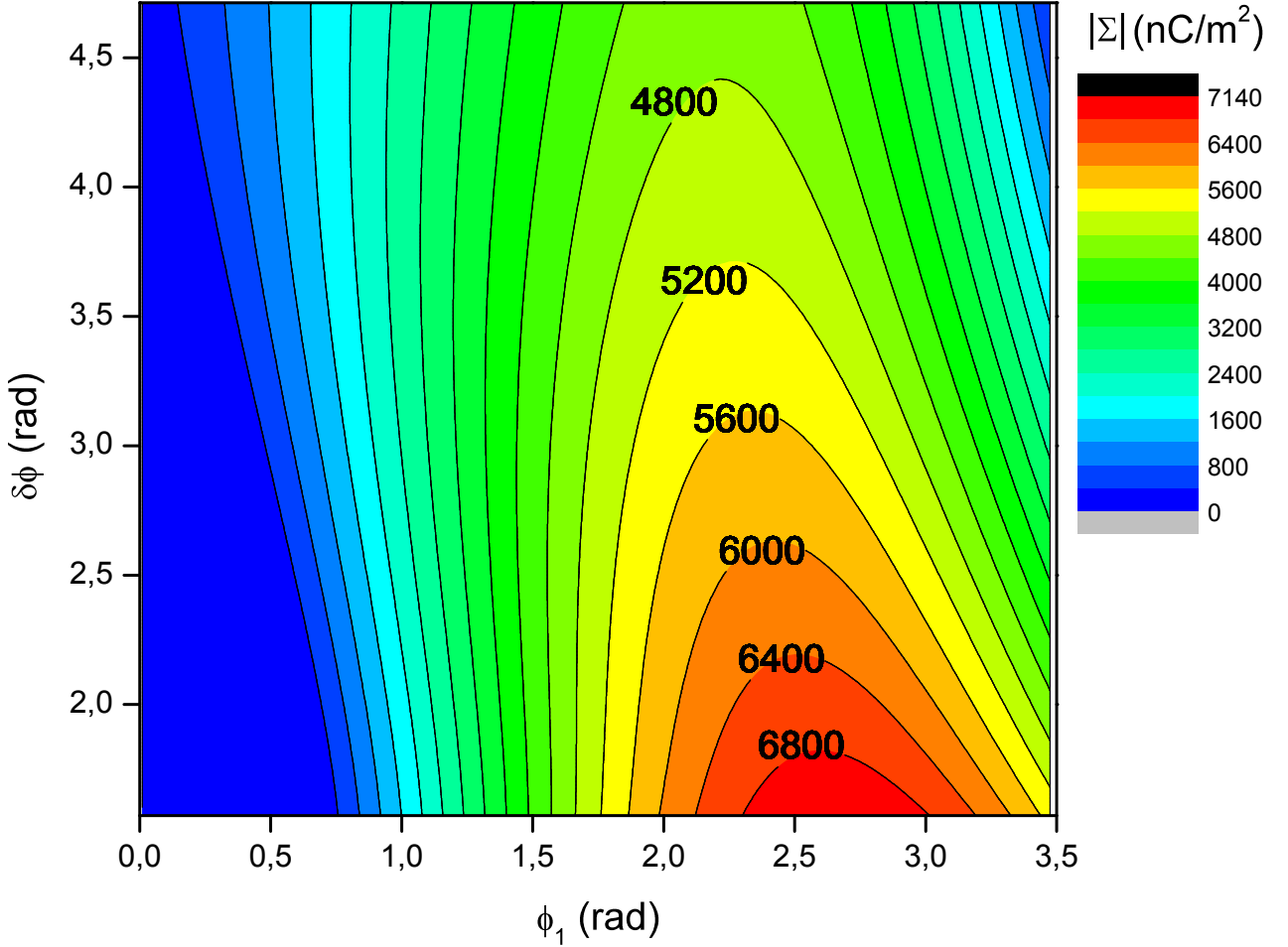


Figure 5.8: Surface charge density obtained by (5.7) vs. ϕ_1 and $\delta\phi$ for $f = 2$ GHz, $d = 1$ mm, $V_{RF} = 300$ V and $v_0 = 3.68$ eV.

this model. This model can be employed to describe the multipactor saturation provided that the electron sheet does not impact with the opposite plate before.

To calculate the analytical expression that links the RF voltage to the maximum charge that the electron sheet can hold under multipactor resonance in the steady-state, (5.5) is used to rewrite (5.7) as follows:

$$\frac{\epsilon_0 V_{RF}}{e\sigma(1 + K_\sigma)} \left\{ \left[\cosh\left(\frac{\delta\phi}{\sqrt{K_\sigma}}\right) - 1 \right] \cos\phi_1 - \sqrt{K_\sigma} \sinh\left(\frac{\delta\phi}{\sqrt{K_\sigma}}\right) \sin\phi_1 \right\} + \frac{d}{2} \left[\cosh\left(\frac{\delta\phi}{\sqrt{K_\sigma}}\right) - 1 \right] - \frac{v_0 \sqrt{K_\sigma}}{\omega} \sinh\left(\frac{\delta\phi}{\sqrt{K_\sigma}}\right) = 0 \quad (5.8)$$

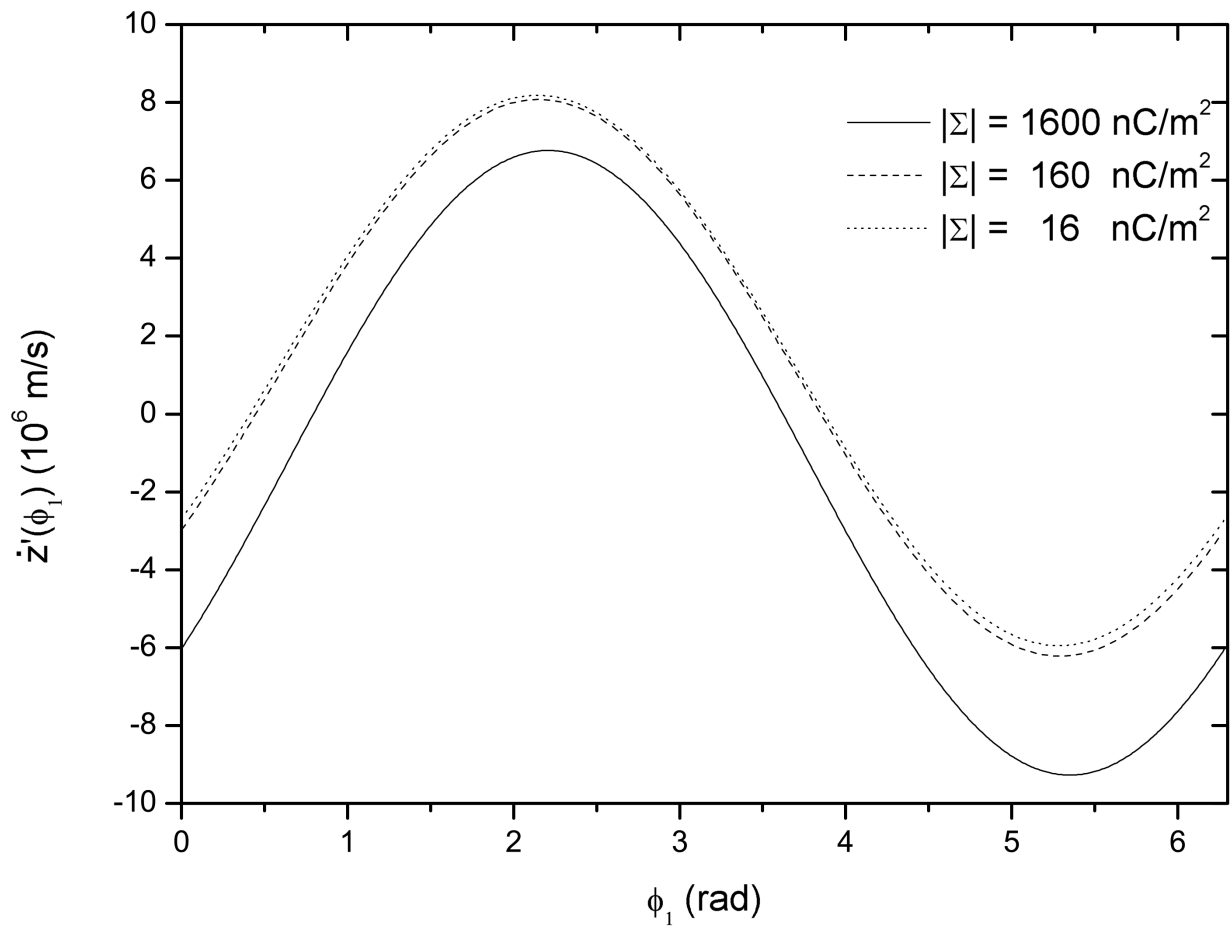


Figure 5.9: Velocity of the electron sheet for $f = 2$ GHz, $d = 1$ mm, $\delta\phi = 2$ rad and $v_0 = 3.68$ eV for different values of the surface charge density.

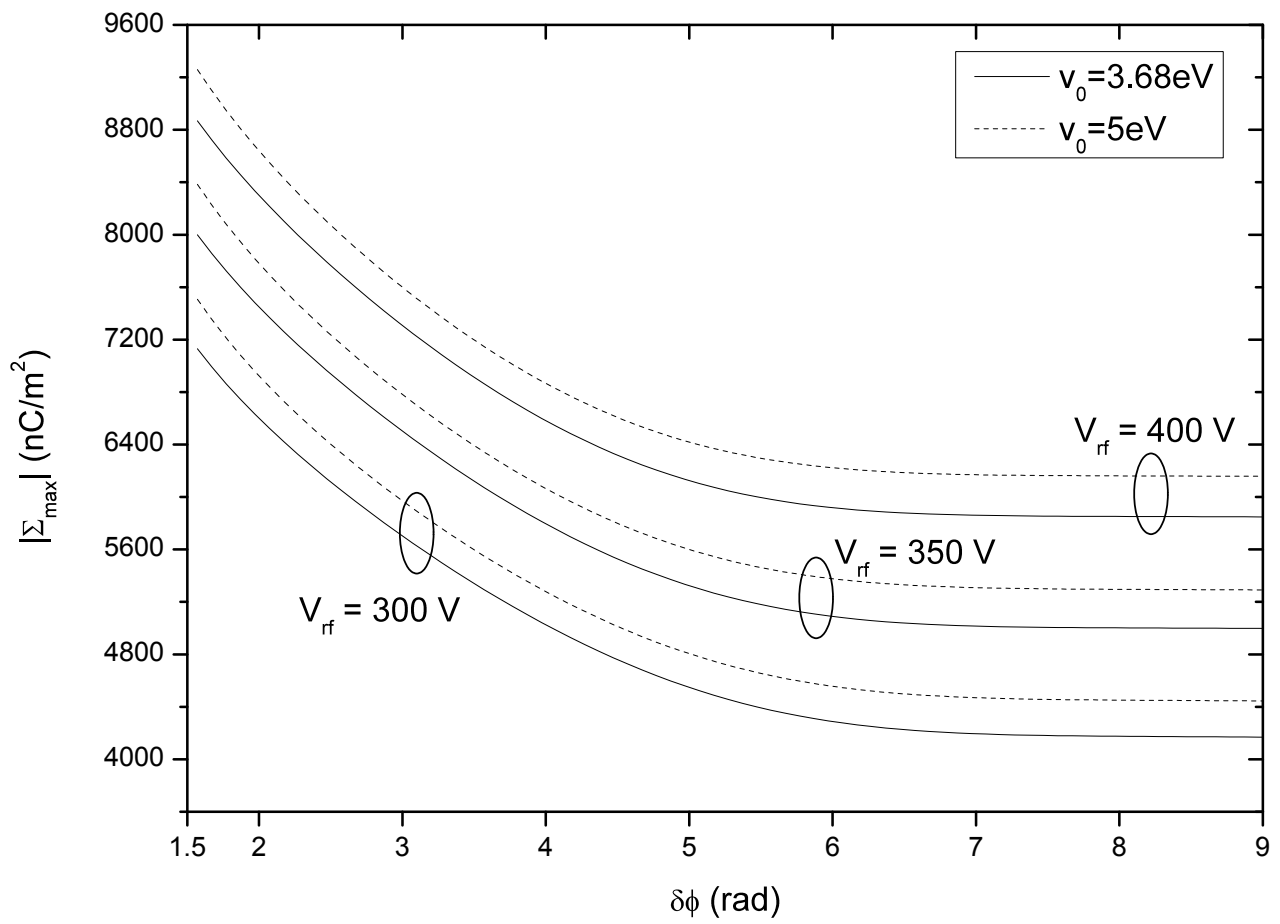


Figure 5.10: Maximum surface charge density of the function defined by (5.7) vs. $\delta\phi$ for different parameters.

Factoring out the trigonometric terms and rearranging them, (5.8) can be written as

$$\frac{\epsilon_0 V_{RF}}{e\sigma(1+K_\sigma)} \sqrt{\cosh^2\left(\frac{\delta\phi}{\sqrt{K_\sigma}}\right) + K_\sigma \sinh^2\left(\frac{\delta\phi}{\sqrt{K_\sigma}}\right)} \cdot \sin(\phi_1 - \beta) + \frac{d}{2} \cosh\left(\frac{\delta\phi}{\sqrt{K_\sigma}}\right) + \frac{v_0 \sqrt{K_\sigma}}{\omega} \sinh\left(\frac{\delta\phi}{\sqrt{K_\sigma}}\right) = 0 \quad (5.9)$$

where $\beta = \arctan\left(\frac{1}{\sqrt{K_\sigma}}\right)$. For large values of the argument of the hyperbolic trigonometric functions, $\cosh(\delta\phi/\sqrt{K_\sigma}) \simeq \sinh(\delta\phi/\sqrt{K_\sigma})$, and (5.9) reduces to

$$\frac{\epsilon_0 V_{RF}}{e\sigma\sqrt{1+K_\sigma}} \sin(\phi_1 - \beta) - \frac{d}{2} + \frac{v_0 \sqrt{K_\sigma}}{\omega} = 0 \quad (5.10)$$

provided that $\frac{\delta\phi}{\sqrt{K_\sigma}} \gg 1$. That condition ensures the maximum value of the surface charge density, as solution of (5.7), to be stable (see Fig. 5.10). As (5.10) is independent of $\delta\phi$, ϕ_1 can be isolated resulting in:

$$\phi_1(\sigma) = \arcsin\left\{\frac{e\sigma\sqrt{1+K_\sigma}}{\epsilon_0 V_{RF}} \left(\frac{d}{2} - \frac{v_0 \sqrt{K_\sigma}}{\omega}\right)\right\} + \beta \quad (5.11)$$

The maximum of the function $\sigma(\phi_1, \delta\phi \gg \sqrt{K_\sigma})$ can be found by using

$$\frac{d\sigma}{d\phi_1} \equiv \left(\frac{d\phi_1}{d\sigma}\right) \Big|_{\sigma=\sigma_{max}}^{-1} = 0$$

and its value can be calculated by solving the equation

$$\frac{(e\sigma_{max})^2 (1+K_{\sigma_{max}})}{\epsilon_0^2 V_{RF}^2} \left(\frac{d}{2} - \frac{v_0 \sqrt{K_{\sigma_{max}}}}{\omega}\right)^2 = 1 \quad (5.12)$$

After some algebraic manipulations and replacing $e\sigma_{max}$ by $|\Sigma_{max}|$ we find the maximum surface charge density as function of the input voltage

$$V_{RF} = \frac{d}{2\epsilon_0} \sqrt{1+K_{\sigma_{max}}} \left|1 - \sqrt{\frac{\Sigma_0}{|\Sigma_{max}|}}\right| |\Sigma_{max}| \quad (5.13)$$

where $\Sigma_0 = \frac{4v_0^2 m_e \epsilon_0}{ed}$ provides the minimum value of the saturation charge, coming from the condition $V_{RF} \rightarrow 0$, and resulting in

$$|\Sigma_{max}| \geq \frac{4v_0^2 m_e \epsilon_0}{ed} \quad (5.14)$$

providing the bottom limit to the charge for which the electron will return to the initial plate for any value of ϕ_1 under the above-mentioned conditions. This expression shows that the minimum saturation level, when it can be described by the ‘‘returning limit model’’, does not depend on the frequency, but on the initial velocity of the electrons and on the gap distance between the plates. Indeed, it is natural to expect that the bigger the initial velocity the higher the minimum surface charge density so that the image charge is strong enough to pull back

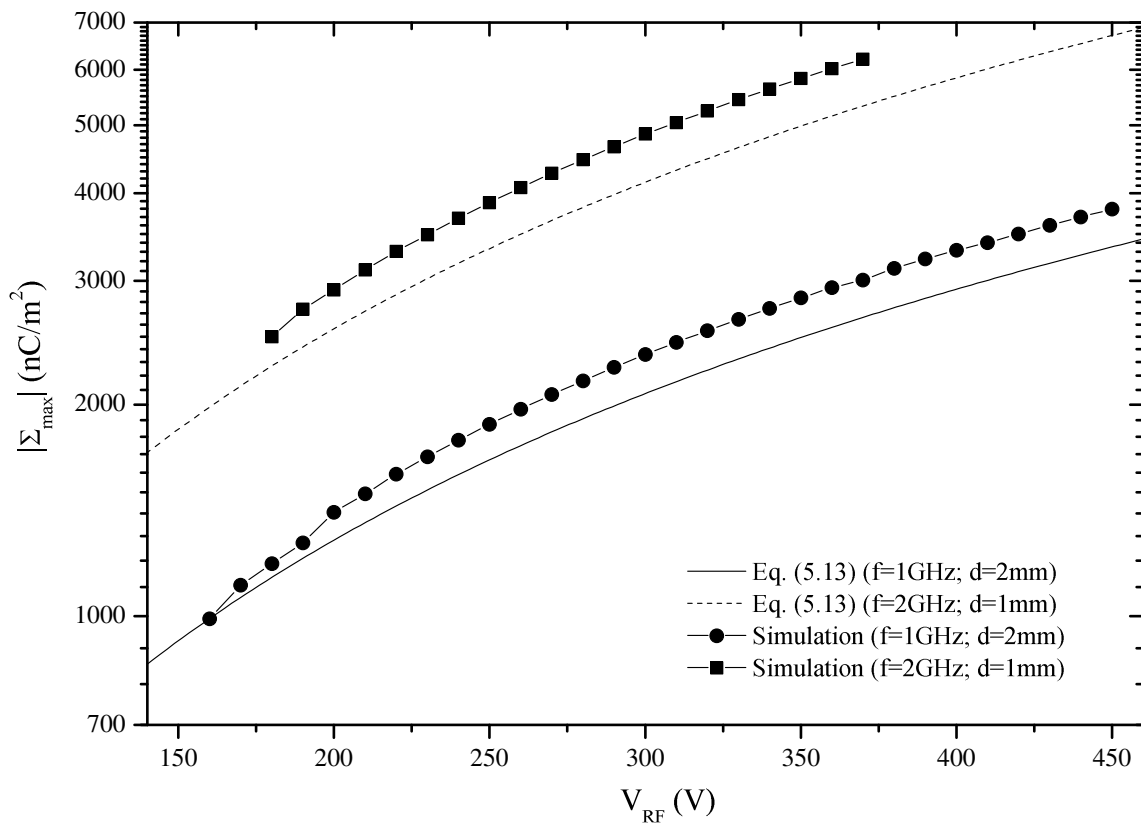


Figure 5.11: Maximum surface charge density vs. the RF voltage obtained with the simulations and with the predictions made by the “returning limit” model for $v_0 = 3.68$ eV. The maximum secondary-electron-yield is two.

the electron cloud to the initial plate. On the other hand, as the gap distance decreases, for a given voltage, the electric field increases and therefore, the minimum surface charge density must increase in order to counteract the RF field and to pull back the electron cloud to the birth plate. Several examples of $|\Sigma_{max}|$ as function of the voltage are shown in Fig. 5.11. The values of the maximum surface charge density obtained with the simulations of the motion of the electron sheet are slightly higher than the ones predicted by the “returning limit model”, though they never differ by more than the maximum SEY considered (in this case $\max\{\text{SEY}\} = 2$). This can be explained by taking into account that (5.13) predicts the minimum surface charge density above which the electron sheet will return to the initial plate for any initial phase; however, nothing forbids the surface charge density to overcome that prediction if its value is below and after some impact increases above it. This can be verified noting the fact that discrepancies between both results are always within the margin given by the maximum SEY.

5.4 Range of validity of the saturation mechanisms

As it has been mentioned before, the two identified mechanisms of saturation to describe the multipactor saturation for resonance of order one are based on the assumption that the spectrum of the initial velocity of secondary electrons is mono-energetic, so that the spread of the electron cloud due to the mutual repulsion of electron populations with different initial velocities is neglected. Furthermore, the “impact energy limit mechanism” assumes that for low RF voltages, the electron population grows slowly and the image charge does not alter the stability of the resonant motion of the electron sheet, reaching a stable value of the surface charge density for which the impact energy tends to the first cross-over point; on the other hand, the “returning limit” mechanism assumes that above a certain surface charge density, the electron sheet, attracted by its image, impacts against the initial plate provoking a decrease of the electron population as long as the RF voltage is not too high as to induce a SEY above unity.

Nonetheless, it has been observed that the voltage, the gap distance, the first cross-over point associated to the SEY curve or the initial velocity, limit the validity of these mechanisms to explain the multipactor saturation. For high voltages the charge of the electron sheet increases gradually after each impact till the moment when the image charge breaks the resonant motion of the electron sheet with the RF field. If the voltage is not too high (the gap distance or the first cross-over point are not too small) the rupture of the resonance by the return of the electron cloud to the initial plate attracted by its image leads to a low impact energy collision decreasing its charge, and limiting the maximum surface charge density as described before. However, if the voltage is too high or the distance between plates too small, the electron sheet may reach the opposite plate increasing even more its charge if the energy of collision is high enough despite of the solution provided by (5.13). Another possibility is that the electron sheet returns to the initial plate with an impact energy above the first cross-over point, increasing its surface charge density even more than predicted by the “returning limit” model. This happens when the initial velocity and the first cross-over point approaches each other.

In Fig. 5.12 the saturation charge predicted by the two models proposed in this work together with the results obtained with the equations of motion exemplify the range of validity of these models. As the difference between the initial velocity and the first cross-over point of the SEY decreases, the maximum surface charge density increases drastically because the impact energy is likely to exceed the first cross-over point E_1 in every collision. Nevertheless, this limit is not very representative since, in a realistic scenario, the first cross-over point and the initial velocity lie far from each other. Note that the maximum surface charge density predicted by both models tends to the results obtained with the equations of motion as the first cross-over point moves

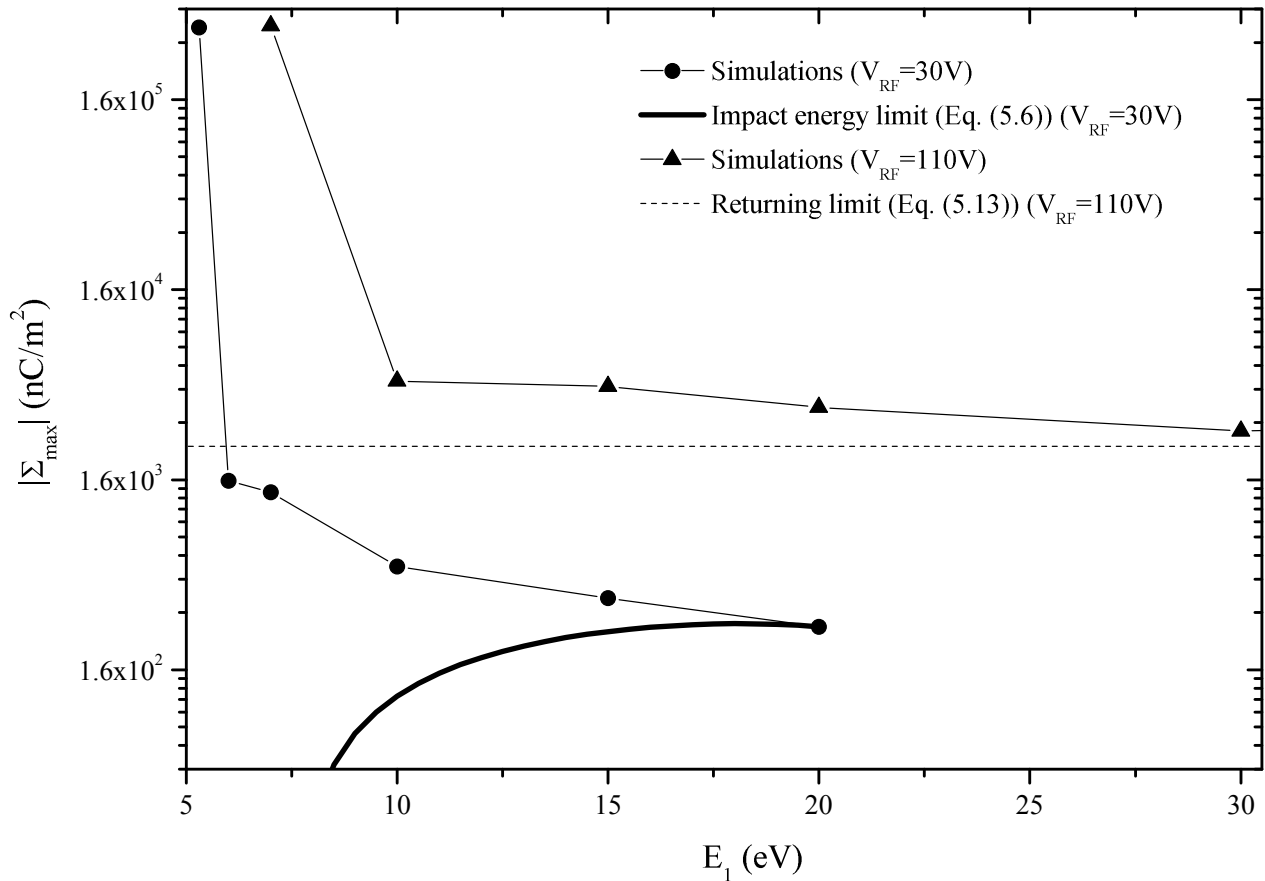


Figure 5.12: The surface charge density of saturation obtained by three methods: the maximum obtained by the simulation of the motion of the electron sheet (disks and triangles), the “returning limit” model (dashed line) and the “impact energy limit” model (thick solid line). Note how the maximum obtained by the equations of motion increases remarkably as E_1 tends to the initial velocity of the secondary electrons considered ($v_0=5$ eV).

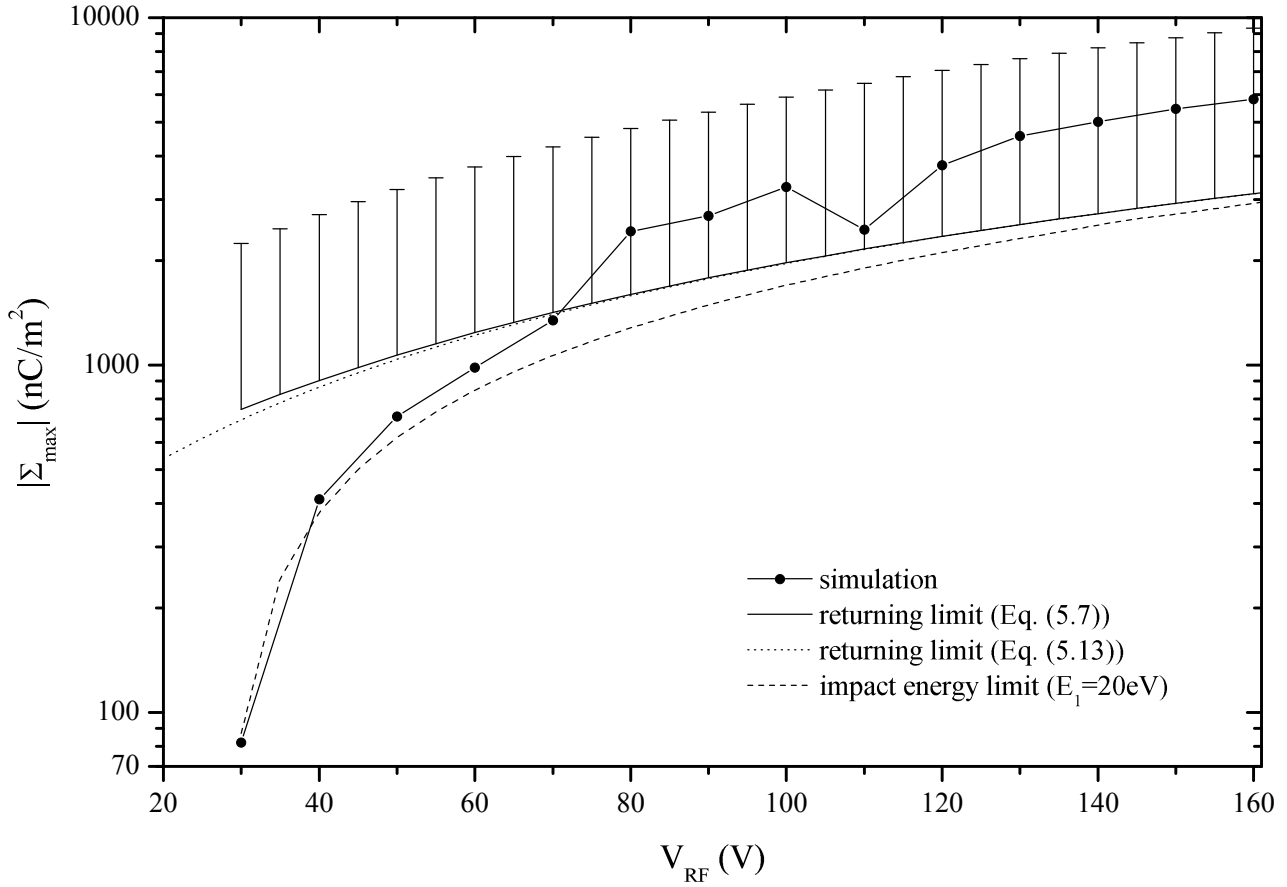


Figure 5.13: Comparison of the surface charge density of saturation vs. the RF voltage obtained with the equations of motion and by the “returning limit” and “impact energy limit” models for $f = 1$ GHz, $d = 1$ mm, $v_0 = 3.68$ eV and $E_1 = 20$ eV. The bars show the values of the surface charge density obtained with the “returning limit” model multiplied by the maximum SEY (two in this case).

away from the value of the initial velocity. The curve obtained with the equations of motion for $V_{RF} = 30$ V predicts a saturation surface charge density till a certain value of the first cross-over point is reached, because when the first cross-over point exceeds $E_1 = 20$ eV for that voltage, the conditions for multipactor to occur do not apply and the electron population does not grow anymore.

Figure 5.13 shows that the surface charge density of saturation predicted by the “impact energy limit” model fits well the values obtained with the equations of motion in the low-voltage region. Above a certain RF voltage the trend of $|\Sigma_{max}|$ changes and it seems to closely follow the predictions obtained by the “returning limit” model, that has been represented by the search of the stable maximum of (5.7) and by the analytic formula (5.13), showing practically the same results, validating the approximation done. The bars plotted in Fig. 5.13 show twice the value of σ obtained with the “returning limit” model, because in this case the maximum value of the SEY is two. The bars point that the discrepancies between the simulations and the values obtained with the “returning limit” model, though increasing with the voltage, they never go beyond the maximum SEY.

Therefore, though (5.4) and (5.5) are able to predict the electron population saturation, the magnitudes V_{RF} , d , v_0 and E_1 limit the validity of the two afore-mentioned models to explain the saturation mechanism. Their validity lies in the existence of electrons' initial velocity far from the first cross-over point, and in the presence of an electric field whose voltage lies near above the multipactor threshold and a gap distance big enough. In those cases, the mechanism of saturation of a multipactor discharge within a parallel-plate waveguide can be well explained by the models described above. These cases are, nevertheless, the most important ones since the smallest voltage (power) near above the multipactor threshold is searched in the design of microwave devices able to withstand high input powers without the risk of multipactor occurrence.

5.5 Summary

The electron cloud produced by a multipactor discharge has been modeled by a 2D homogeneous charge distribution and the equations of motion of the electron sheet driven by the RF electric field of the fundamental mode of an infinitely wide parallel-plate waveguide have been found and employed to simulate the electron population growth. The steady-state multipactor has been found and the surface charge density of saturation has been predicted by the "impact energy limit" and "returning limit" models. Their predictions have been compared with the simulations for voltages near above the breakdown threshold. In this limit the results obtained with both models have shown a good agreement with the ones provided by the equations of motion.

The equations of motion that have been found considering the space charge show that the resonance, the stability and the returning conditions studied in Chapter 2 change as the surface charge density increases. This study yields thus the possibility to find other types of resonances or other conditions under which the resonant motion of the electron cloud can occur by taking into account the electron surface density as a new variable in the equations of motion. The jump from a resonant order to a different resonance during the electron population growth has been observed and the study of the stability of the resonant motion of the electron cloud as function of the electron density has been done as well. The analysis of multipactor saturation in parallel-plate geometries can be extended to the study of the motion of two or more electron sheets representing the spread in the initial velocity as well. Other structures, for example coaxial or rectangular waveguides, can also be simulated following the same approach to analyze the steady-state multipactor.

For instance, the analytical motion of the electron cloud within a coaxial waveguide of large coaxial aspect ratio [Udiljak 2007] could be considered to find the surface charge of saturation and once it will be known, the radiated power spectrum using the efficient algorithm of the roots search of the cross-product of the Bessel functions could be calculated (see Chapter 4). For rectangular waveguides, the electron cloud may be modeled by a continuous distribution of charge on a thin layer whose profile follows the one of the electric field for the fundamental mode (TE_{10}) mode.

On the other hand, the presented results provide the possibility of evaluating the radiated power spectrum of a multipactor discharge considering the space charge effects. As the motion of the electron cloud within the parallel-plate waveguide taking into account the space charge is analytical, the same approach as that one presented in Chapter 3 can be done at the saturation stage. For this, the number of electrons in the steady-state predicted by the models developed here must be substituted into the equations of motion.

It would be interesting, therefore, to develop the electric current, produced by the electron cloud taking into account the space charge effects, into a Fourier series to find the radiated power spectrum for a more realistic case. Nevertheless, the velocity is not a periodic signal anymore when space charge effects are considered, since the electron population increases with time and this effect modifies the dynamics of the electrons. Thus,

the analysis of the radiated power spectrum produced by a multipactor discharge considering space charge effects could be done when the conditions to explain the saturation with the “impact energy limit” model apply. In this case the development of the current into a Fourier series could be done once the saturation level has been reached leading to a constant value of the surface charge density and the velocity is a periodic function. For the conditions when the maximum value of the surface charge density predicted by the “returning limit model” agrees with the maximum value obtained with the equations of motion, the value of $|\Sigma_{max}|$ predicted by (5.13) can be employed to calculate the radiated power spectrum considering space charge effects. For the cases when σ oscillates chaotically around a certain value in the steady-state, the current can be modeled using the time-average of the surface charge density or the study could be done using the Fourier transform of the velocity function.

This analysis and the presented results might help to establish a criterion for multipactor occurrence. Measurements of the radiated power spectrum of the electron cloud, using the third harmonic detection technique (or other harmonics), can be compared with the predicted radiated power spectrum of a multipactor discharge following the proposed study. The comparison could establish, indeed, a unique criterion to assess the multipactor onset unambiguously.

Corona breakdown

Contents

6.1	Transport theory of charged particles in gases	107
6.2	Corona breakdown	111
6.3	Ionization rate models	115
6.3.1	Woo's model	115
6.3.2	Lupan's model	116
6.3.3	Mayhan's model	116
6.3.4	Comparison of the ionization rates	117
6.4	Numerical solution of the corona equation	119
6.5	Results	120
6.5.1	Corona discharge in a parallel-plate waveguide	121
6.5.2	Corona discharge in a rectangular waveguide	124
6.5.3	Corona discharge in a circular waveguide	128
6.5.4	Corona discharge in a coaxial waveguide	136
6.5.5	Corona discharge in a rectangular cavity	142
6.5.6	Corona discharge of a monopole antenna	145
6.6	Summary	158

6.1 Transport theory of charged particles in gases

The onset of gas breakdown at high frequencies -also called corona discharge- has been analyzed by many authors from the beginning of the twentieth century [Ryan 1915, Margenau 1946, Herlin 1948a, Chown 1959, Brown 1951, MacDonald 1963, Mayhan 1969, Anderson 1986], citing only a few. The first analysis of corona breakdown at microwave frequencies incorporated physical aspects that were found in DC discharges, more well-known in the beginning of the twentieth century. Later, some authors started to recognize the differences between the high and the low frequency discharges. Whereas the electrons in a DC breakdown are continuously swept out by the field from the critical region, which forces the presence of a source of electrons produced by secondary effects on the electrodes to trigger the discharge, the gas ionization due to the electron motion driven by the RF fields is the physical phenomenon, together with diffusion and attachment, that control the breakdown in high frequency discharges.

Let us imagine an electron within a very low pressure gas accelerated by a uniform microwave electric field $\mathbf{E} = \mathbf{E}_0 e^{j\omega t}$ oscillating with a radian frequency ω . If the pressure is so low that the collision rate between

electrons and gas molecules is much lower than the RF frequency, we can integrate the collision-less equation of motion

$$m_e \frac{d\mathbf{v}}{dt} = -e\mathbf{E}_0 e^{j\omega t} \quad (6.1)$$

to give

$$\mathbf{v} = \mathbf{v}_0 + \frac{e\mathbf{E}_0}{m_e\omega} e^{j(\omega t + \frac{\pi}{2})} \quad (6.2)$$

and integrating again we obtain

$$\mathbf{r} = \mathbf{r}_0 + \mathbf{v}_0 t + \frac{e\mathbf{E}_0}{m_e\omega^2} e^{j\omega t}. \quad (6.3)$$

The quantities m_e and $-e$ are the mass and the charge of the electron, respectively.

The kinetic energy conveyed to the electrons driven back and forth by the microwave field is, therefore

$$T = \frac{1}{2} \frac{e^2 E_0^2}{m_e \omega^2}, \quad (6.4)$$

which cannot explain the electron avalanche produced when the corona onset arises if we consider the measured field strengths obtained for breakdown. The ionization energy of a gas molecule present in the air is of orders of eV, but the kinetic energy gained by the electrons by the presence of the electromagnetic fields is around meV. But let us calculate the mean-value of the energy density that the RF field transmits to the electrons within the gas. We know that the energy transfer from the electric field to an electric charge is found using Ohm's law. Thus, if we consider that the electron density within the gas is of n electrons per unit volume and that the current density is $\mathbf{J} = -en\mathbf{v}$, we can use the equations of motion to calculate the time-averaged energy density:

$$\langle \text{Re}(\mathbf{J}) \cdot \text{Re}(\mathbf{E}) \rangle = -en\mathbf{v}_0 \cdot \mathbf{E}_0 \langle \cos(\omega t) \rangle + \frac{ne^2 E_0^2}{2m_e\omega} \langle \sin(2\omega t) \rangle = 0. \quad (6.5)$$

It is then proven that the electrons can only gain energy from the microwave field by colliding randomly with the gas molecules until they reach enough energy to produce the ionization. It imposes thus the consideration of the impacts against the gas neutrals in the description of the corona breakdown at microwave frequencies. When the electron is accelerated by a uniform electric field and the pressure is not so low, the equation of motion of an electron can be written as follows [Lorentz 1909]:

$$m_e \left(\frac{d\mathbf{v}}{dt} \right) + m_e \nu_c \mathbf{v} = -e\mathbf{E}_0 e^{j\omega t} \quad (6.6)$$

where the second term on the LHS represents a net damping force produced by the random collisions of the electrons with the gas molecules. The collision frequency, ν_c , stands for the number of electron-molecule collisions per unit time. The pressure is a measure of the number of molecules in the gas, and it is intuitive to expect that the larger the amount of molecules, the larger the number of electron-neutral collisions per unit time. Therefore, as the experiments have shown [Nielsen 1937, Ryzko 1965] the collision frequency increases with the pressure and it does not depend on the electric field intensity in a first-order approximation.

Integrating the equation above we obtain for the velocity

$$\mathbf{v} = \mathbf{v}_0 e^{-\nu_c(t-t_0)} + \frac{-e\mathbf{E}_0 e^{j\omega t}}{m_e(j\omega + \nu_c)}. \quad (6.7)$$

However, the first term of the RHS decays very quickly as there are usually many collisions per unit time for the typical pressures under consideration. Therefore, the second term remains and allows us to calculate the averaged rate of energy gain of the electrons provided by the RF field as follows:

$$\langle \text{Re}(\mathbf{J}) \cdot \text{Re}(\mathbf{E}) \rangle = \frac{ne^2 E_0^2}{m_e} \left\langle \frac{\nu_c \cos \omega t + \omega \sin \omega t}{\nu_c^2 + \omega^2} \cdot \cos \omega t \right\rangle,$$

where the integration of $\sin \omega t \cdot \cos \omega t$ vanishes and it remains the integration of $\cos^2 \omega t$, which yields one half. Therefore the averaged rate of energy that the microwave field conveys to the electrons within the gas is

$$\langle \text{Re}(\mathbf{J}) \cdot \text{Re}(\mathbf{E}) \rangle = \frac{ne^2 E_0^2}{2m_e \nu_c} \left(\frac{\nu_c^2}{\nu_c^2 + \omega^2} \right).$$

The above expression has been obtained multiplying numerator and denominator by the collision frequency because it is interesting to define an effective electric field,

$$E_e^2 \equiv E_{rms}^2 \left(\frac{\nu_c^2}{\nu_c^2 + \omega^2} \right), \quad (6.8)$$

in order to find an analogy with the energy transfer for a DC signal, as it will be commented later, such that the averaged rate of energy gain of the electrons is

$$\langle \dot{P} \rangle = \frac{ne^2 E_e^2}{m_e \nu_c}. \quad (6.9)$$

As it is described in [Raizer 1991], the expression (6.9) is analog to the energy transfer from a DC field to the electrons of a gas if we replace E_e by the amplitude of an electrostatic field. Therefore, the effective electric field plays the role of a correction factor that is applied to the physical parameters that describe the DC discharge in order to suitable analyze the microwave corona breakdown. As the collision rate increases with the pressure, it is expected to retrieve the same results for microwave breakdown as for DC discharges when the pressure tends to atmospheric values, since in this case the effective electric field tends to E_{rms} , which does not depend on the microwave frequency. Obviously, the same limit is obtained when the RF frequency tends to zero. The study of the microwave discharge will show significant differences with respect to the DC breakdown especially for low pressures, as it is the case for space applications.

The expression (6.9) is also useful to understand the dependency of the energy transfer from the microwave field to the electron population on the collision frequency and, therefore, on the pressure. When the period of the microwave signal is much longer than the time between collisions of the electrons with the gas neutrals, an electron collides against many gas molecules within a period of the signal. As the collision rate increases with the pressure, we can imagine that for very high pressures, the electrons collide many times with the molecules within a period, and the impact energy is not controlled by the microwave field because the electrons cannot gain enough energy from the electric field before any collision. In this regime the energy transfer from the electric field to the electrons is not very efficient due to the random nature of the motion of the electrons mainly driven by the collisions rather than the RF field. On the contrary, if the signal frequency is too high, the electrons' position oscillates many times before impacting with a gas molecule and the collision energy is a random function that depends on the phase of the field at the impact instant. The energy transfer is not very efficient in this case, either. If we plot the averaged rate of energy gain of the electrons vs. the collision frequency we can

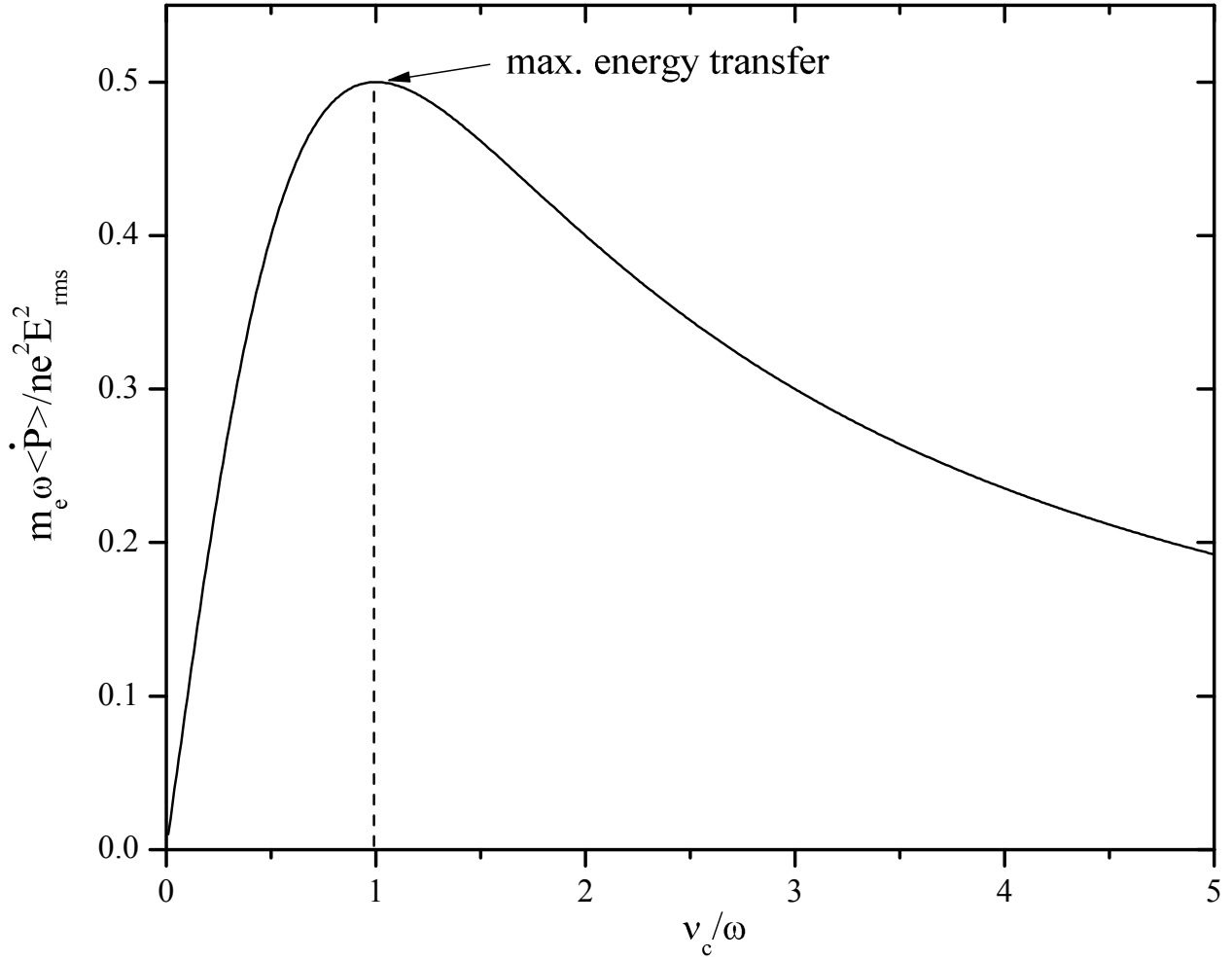


Figure 6.1: Normalized averaged energy transfer function from the microwave field to the electron gas as function of the normalized collision frequency.

see the maximum energy transfer just when the collision frequency equals the angular frequency (see Fig. 6.1). This is natural taking into account that when both, the collision and the microwave frequencies approach, the transit time between collisions tends to the period of the signal, and the electrons can acquire the maximum speed in the collision accelerated by the microwave electric field. The pressure for which the collision rate equals the angular frequency of the RF signal provides the condition for the maximum energy transfer, as it is studied next.

In order to find the maximum energy transfer let us rewrite (6.9) using (6.8) as follows:

$$\langle \dot{P} \rangle = \frac{ne^2 E_{rms}^2}{m_e} \left(\frac{1}{\nu_c \left(1 + \left(\frac{\omega}{\nu_c} \right)^2 \right)} \right). \quad (6.10)$$

We can define the new variable $x \equiv \frac{\nu_c}{\omega}$ in order to write the normalized version of the energy transfer from the

microwave field to the electron population within the gas as

$$\frac{m_e \omega \langle \dot{P} \rangle}{n e^2 E_{rms}^2} = \frac{1}{x (1 + x^{-2})}. \quad (6.11)$$

If we differentiate this expression with respect to x we get

$$\frac{m_e \omega}{n e^2 E_{rms}^2} \frac{d \langle \dot{P} \rangle}{dx} = - \frac{(1 + x^{-2}) - 2x^{-2}}{x^2 (1 + x^{-2})^2} = - \frac{1 - x^{-2}}{x^2 (1 + x^{-2})^2}.$$

In order to find the extreme of (6.11) we set the numerator of this expression to zero and we find that the physically meaningful solution that satisfies this condition corresponds to $x = 1 \rightarrow \nu_c = \omega$, as it was predicted before by physical reasonings. Note that the normalized maximum energy transfer from the microwave field to the electrons within the gas is 1/2 (see Fig. 6.1), what results from substituting E_e by $E_{rms}/2$ (see (6.9)) when $\nu_c = \omega$. This means that the maximum energy transfer for microwave frequencies is half the averaged rate of energy gain of electrons for DC signals.

As the collision frequency increases with pressure, the results above suggest that, for a given RF frequency, there is a pressure for which the energy transfer from the microwave field to the electrons is maximal. This implies, as it will be shown later, that the input power for which the corona discharge occurs at that pressure is minimal, since the maximum energy transfer from the electric field to the electron population applies at that pressure. It is natural to call this pressure the critical pressure, since it fixes the limit of the corona withstanding capabilities of the microwave device at a given frequency.

6.2 Corona breakdown

When the electrons collide with the gas neutrals, driven by the microwave field, some molecules can be ionized and some electrons released. On the other hand, the electrons tend to move away from the zones of high electron population density, trying to reach the chemical equilibrium leveling out the number of electrons per unit volume, process that is called diffusion. Furthermore, there is another loss mechanism that becomes important at high pressures, and that accounts for the attachment of the electrons to the neutrals by the affinity of the molecules to catch electrons. However, the presence of the attachment in the analysis of the corona breakdown does not change significantly the predicted breakdown threshold, except at high pressures.

The corona breakdown is produced when the intensity of the electric field is so high that the increase of the electron population by ionization is not compensated anymore by the diffusion loss of electrons and attachment. At this stage, the electron population grows dramatically producing an avalanche. The gas becomes conductive and a glowing emission is produced by the radiation of the accelerated particles [Ryan 1915, Akishev 1999], which may severely damage the microwave component due to the produced temperature increase.

In order to describe mathematically this process, let us consider an imaginary small volume within the gas (see Fig. 6.2), where the increase of the electron population by ionization results in a positive current flow across its surface, Γ_i . On the other hand, the local decrease of the electron population by diffusion will produce a current flow across the boundaries of the imaginary volume given by $\Gamma_D = \vec{\nabla} \cdot \mathbf{J}_D$. From ordinary kinetic theory considerations, the diffusion current can be expressed as [Kennard 1938]

$$\mathbf{J}_D = -\vec{\nabla} (Dn(\mathbf{r}, t)) \quad (6.12)$$

where the negative sign shows that the diffusion current flows in the direction of the maximum decrease of the electron population, since the gradient gives the direction of maximum increase of a scalar field. In this case, the scalar field, $n(\mathbf{r}, t)$, represents the electron population density at the position \mathbf{r} within the gas. The variable D is the diffusion coefficient, which is usually considered independent of the electric field, though some authors consider the influence of the RF field an important factor to describe it. Finally the ionization current flow is given by $\Gamma_i = (\nu_i - \nu_a) n(\mathbf{r}, t)$, where ν_i and ν_a are the number of electrons released by ionization and attached to the gas neutrals per unit time, respectively. In the definition of the flux Γ_i the attachment has been considered, defining a net ionization rate (or ionization frequency) by subtracting the attachment rate from the ionization one. The attachment rate is usually considered to be a single function of the pressure, but the ionization rate depends on the electric field and this, in general, depends on the position, thus the ionization frequency may, in general, depend on the position, too.

The first exhaustive analysis of the diffusion coefficient at microwave frequencies was made by [Kelly 1960], where the author found a good agreement between the proposed theoretical model of the diffusion coefficient and the measurements for O_2 . In [Kelly 1960] it is found for this gas the expression

$$Dp = 1.63 \cdot 10^6 \left[\text{Torr} \cdot \text{cm}^2 \cdot \text{s}^{-1} \right], \quad (6.13)$$

where the units are given in the CGS system, then p is expressed in Torr or mmHg. The diffusion coefficient found by [MacDonald 1963] for the same gas was

$$Dp = \left[29 + 0.9 \left(\frac{E_e}{p} \right) \right] \cdot 10^4 \left[\text{Torr} \cdot \text{cm}^2 \cdot \text{s}^{-1} \right]. \quad (6.14)$$

The comparison of both expressions shows a good agreement between the models as long as the pressure is not too low. Otherwise, the latter equation starts to deviate from the former one and the electric field starts to play an important role, obliging us to consider the dependency of the diffusion coefficient on the position. However, as it will be discussed later, the values of the ratio E_e/p for which the expressions of the ionization frequency are valid lie within the range for which both equations lead to the same diffusion coefficient.

If we recall the continuity equation we can consider these flows to write

$$\frac{\partial n}{\partial t} = \Gamma_i - \Gamma_D.$$

If we use the above-mentioned definitions of the current flows that account for the ionization and the diffusion, the continuity equation can be rewritten as

$$\frac{\partial n}{\partial t} = (\nu_i - \nu_a) n + D \nabla^2 n \quad (6.15)$$

where the diffusion coefficient has been assumed to be independent of the electric field and, therefore, of the position. The last equation is the usual expression of the corona equation, and the critical electric field is determined by the condition that the increase of the electron population by ionization and the electron loss produced by diffusion and attachment are balanced. This implies that the solution of the stationary equation

$$(\nu_i - \nu_a) n + D \nabla^2 n = 0 \quad (6.16)$$

together with the boundary conditions define the corona breakdown threshold.

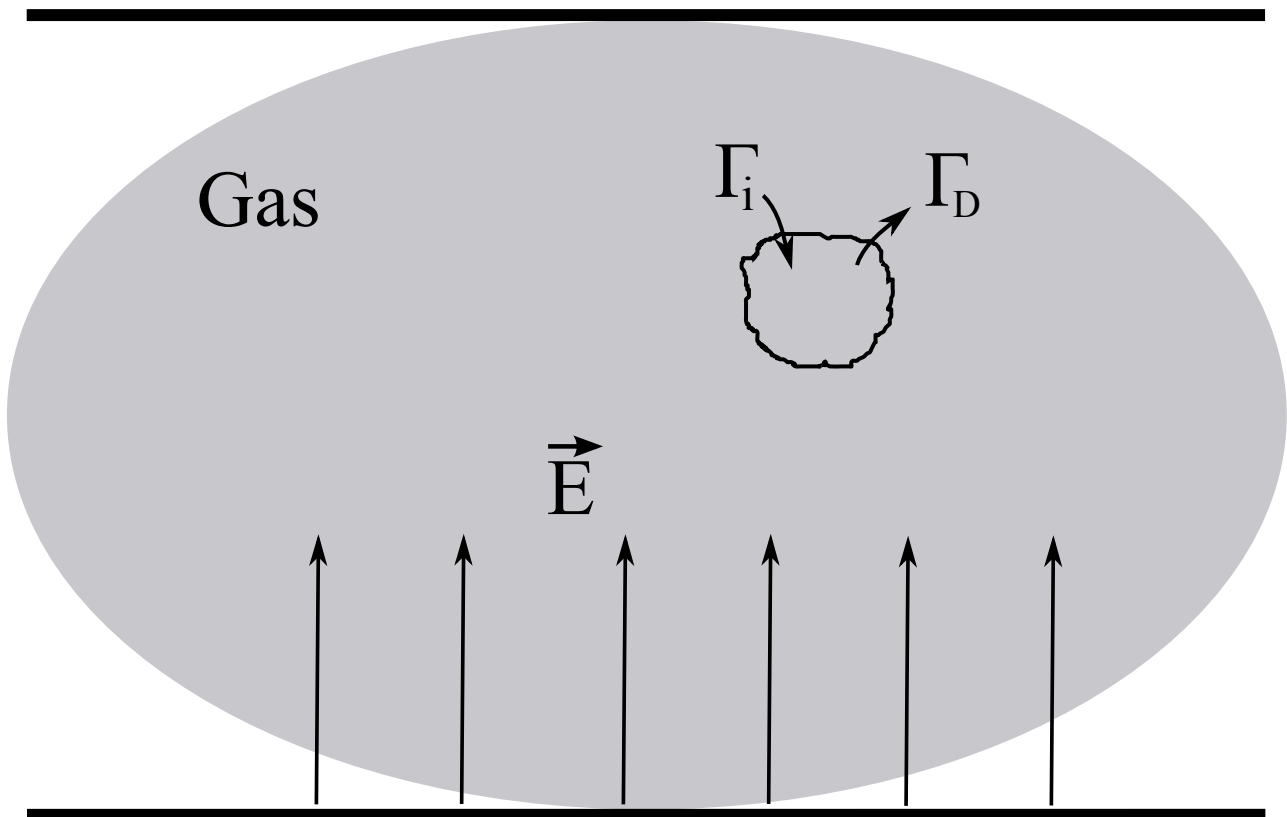


Figure 6.2: Sketch of gas transport properties within a parallel-plate waveguide.

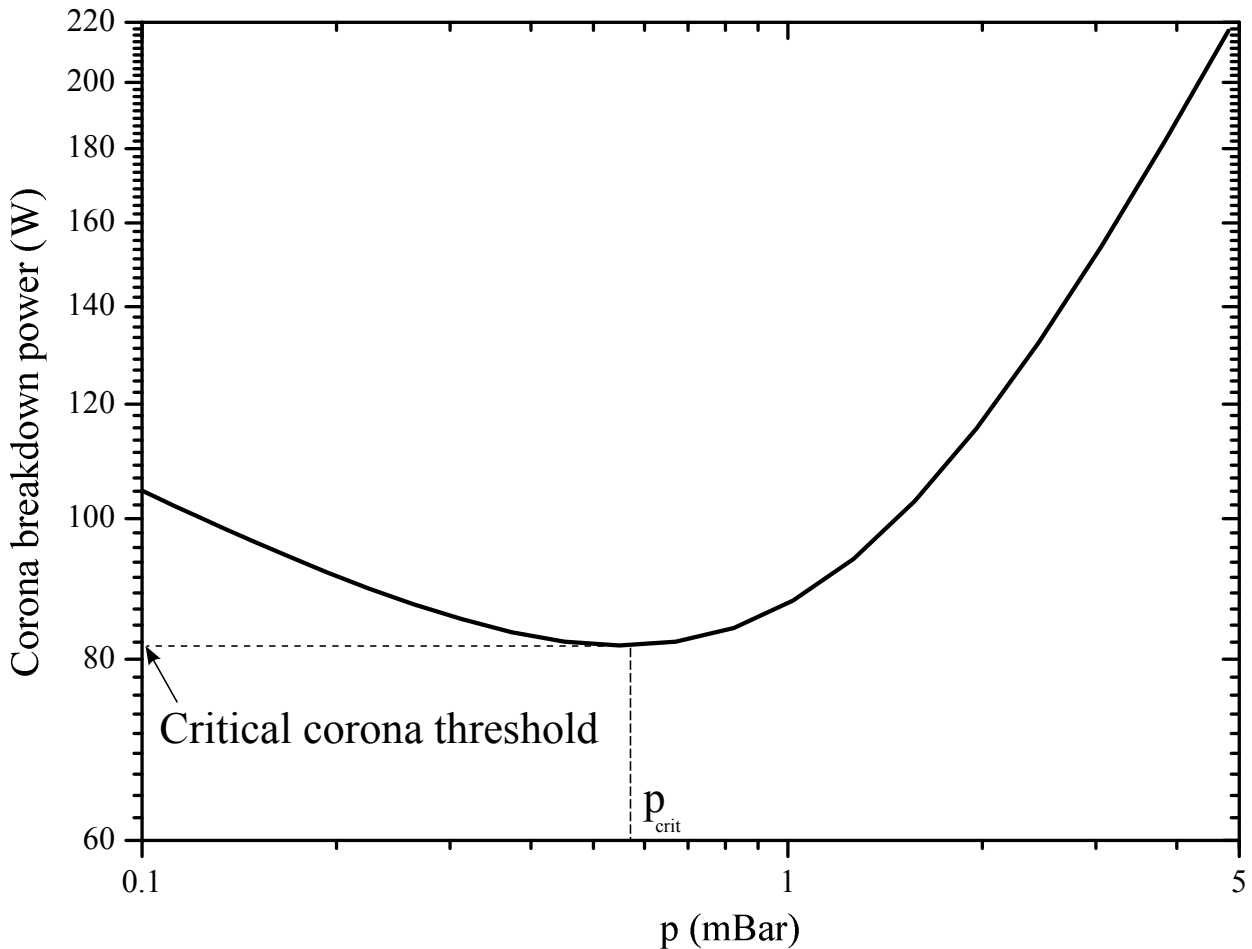


Figure 6.3: Example of the Paschen curve at microwave frequencies.

As we are going to deal with homogeneous dielectric materials, the analysis of the corona breakdown for perfect electric conductors implies the use of Dirichlet boundary conditions for the electron population density on the boundaries, since a grounded conductor acts like a sink of charges. Thus, the electrons of the gas recombine with the atoms within the lattice of the metal and the electric charge remains zero by the presence of the electron gas at the boundaries of the microwave device. Therefore, the solution of the corona equation for the following examples have been solved establishing the boundary conditions that set null the electron population density at the metal walls of the devices.

The plot of the corona breakdown power threshold vs. the pressure defines the Paschen curve [Paschen 1889] and it provides the minimum input power for which the corona discharge occurs. As it was commented in Sec. 6.1 and it will be shown later, the Paschen curve exhibits a minimum corona breakdown power threshold at the critical pressure (see Fig. 6.3).

The critical pressure is a very important parameter because it fixes the pressure that limits the performance of any microwave device subject to the space weather. At this pressure the corona breakdown threshold is minimal, limiting the input power that the device can withstand without the risk of corona breakdown. In order to predict the value of the critical pressure the dependency of the collision rate on the pressure must be known.

As it will be shown later, the value mostly found in the literature is $\nu_c = 5.3 \cdot 10^9 p$, where the pressure is given in Torr. Although the transport properties of the gas are expressed for the pressure given in Torr, the Paschen curve is commonly plotted for the pressure in mBar, but both cases will be used later interchangeably, according to the preference chosen in the corresponding reference. The relation between Torr and mBar is $1 \text{ Torr} \simeq 1013/760 \text{ mBar} \simeq 1.33 \text{ mBar}$.

According to the analysis made in Sec. 6.1 and the above-mentioned expression for the collision rate, the critical pressure will be found at:

$$\nu_c = \omega \rightarrow p_{crit} \text{ (mBar)} \simeq 1.6 f \text{ (GHz)}, \quad (6.17)$$

where f is the frequency of the RF signal. Below and above that pressure the corona threshold is higher, therefore, a good venting of the microwave devices, e.g. through appropriate venting holes, must be guaranteed to eliminate any residual gas. This procedure avoids the gas ionization and the corona discharge at low powers, since the corona breakdown threshold is always lower than the multipactor one, arising at much lower pressures.

6.3 Ionization rate models

In order to predict accurately the corona breakdown threshold an accurate model of the ionization rate is needed. The model must be able to relate the rate of ionizations produced within the gas with the amplitude of the electric field. The model must predict the increase of the ionization rate with the intensity of the electric field, since the energy transfer from the microwave field to the electrons is proportional to the square of the rms amplitude of the signal (see (6.9)).

The ionization rate for DC discharges has been measured by many authors for different gases [Sanders 1932, Jones 1953, Kuffel 2004] and some authors have applied the transport theory of charged particles in gases for AC signals in order to measure or describe the ionization rates at microwave frequencies numerically [Gould 1956, Rose 1957, MacDonald 1949, MacDonald 1959, Bell 1970]. However, analytical expressions relating explicitly the ionization frequency with the amplitude of the microwave electric field were proposed later [Mayhan 1971, Lupan 1978b, Woo 1984]. Other expressions for the ionization rate can be found in the literature showing slight differences with the cited ones, but the most representative ones or those most often found in the literature when analyzing the corona discharge have been considered in this manuscript.

6.3.1 Woo's model

In the following it has been named Woo's model of the ionization rate to the next parameter [Woo 1984]:

$$\nu_i = 5.14 \cdot 10^{11} p \exp \left\{ -73\alpha^{-0.44} \right\} \quad (6.18)$$

obtained for O₂ as the most representative gas among all the air elements, where the pressure is given in Torr and α is the parameter defined by

$$\alpha = E_e/p. \quad (6.19)$$

The expression for the ionization rate was extracted from [Druyvesteyn 1940, Dutton 1963] and considered that it is valid within the range $\alpha \in [32, 100]$ [$\text{V cm}^{-1} \text{ Torr}^{-1}$] with an error of 10%-20%. These units for α are going to be used along all this chapter following the CGS system of units, according to the literature and all the works developed in the study of gas discharges.

The collision frequency was described in [Woo 1984] using the results of [Nielsen 1937, Ryzko 1965] obtaining

$$\nu_c = 5 \cdot 10^9 p \sqrt{\frac{\alpha}{\alpha + 8}}. \quad (6.20)$$

This model takes into account the two-body attachment process, which occurs when an electron binds to an Oxygen molecule ($e + O_2$); and the three-body attachment occurring when an electron binds to two Oxygen molecules ($e + 2O_2$). These models are extracted from [Chatterton 1965, Harrison 1953, Chanin 1962] and it seems that they are valid within a narrow range of values of α , namely $0 < \alpha < 60$ [$V \text{ cm}^{-1} \text{ Torr}^{-1}$] and $0 < \alpha < 5$ [$V \text{ cm}^{-1} \text{ Torr}^{-1}$], respectively.

We will consider only the two-body attachment rate, which was found by the author and can be expressed as follows:

$$\nu_a = 7.6 \cdot 10^{-4} p \alpha^2 (\alpha + 218)^2 \quad (6.21)$$

where the pressure must be given in Torr.

6.3.2 Lupan's model

The name of this model comes from the author who found the expression of the ionization rate described in [Lupan 1978b]. The author proposes two expressions for the ionization rate as function of the effective electric field that are valid within the same range of validity for α as the previous model. The expressions are

$$\nu_i = 2.5 \cdot 10^7 p \left[1.45\sqrt{\alpha} + 0.01\sqrt{\alpha^3} \right] \exp \left[-\frac{278}{\alpha} \right] \quad (6.22a)$$

$$\nu_i = 8.35 \cdot 10^{-4} p \alpha^{5.34}. \quad (6.22b)$$

The author comments that both expressions seem to agree with the experimental measurements as long as $30 < \alpha < 100$ is satisfied, in the CGS system of units.

The author considers the collision rate between electrons and gas molecules as

$$\nu_c = 5.3 \cdot 10^9 p, \quad (6.23)$$

which is very similar to the one of the Woo model within the range of values of α for which the ionization rate is accurate enough.

Interestingly, the attachment rate coefficient is not considered in this work, but a correction factor is proposed to be subtracted in the variable α so as to fit the measurements to the proposed model of the ionization rate, beyond the above-mentioned range for which it is accurate.

6.3.3 Mayhan's model

The main work where the influence of the electron temperature on the ionization rate is taken into account is done by Mayhan's model [Mayhan 1971]. The author recalls the results presented in [Gould 1956, Light 1969] and proposes an expression for what he calls net ionization rate, where the attachment rate has been subtracted to the actual ionization rate. Though the transport properties of different gases are studied, the author considers the Nitrogen as the most important gas element for the air, obtaining the expression:

$$\nu_i = \frac{8.35 \cdot 10^{-4} (0.7885)^{2.67}}{\left[1 - \exp(-3395/T_v) \chi_{N_2}^{2.67} \right]} \frac{p |\mathbf{E}|^{5.24}}{(p^2 + \gamma^2)^{2.67}} - 6.4 \cdot 10^4 p \quad (6.24)$$

where p is given in Torr, T_v is the vibrational temperature of the N_2 constituent of air and χ_{N_2} is the molar fraction of N_2 present. For ambient conditions the vibrational temperature of the Nitrogen is not expected to be very high, therefore, the value of the exponential function is negligible and the denominator of the first factor can be approximated by one. Furthermore, the molar fraction of Nitrogen in air is around 0.78. Note how, under these approximations, the expression of the ionization rate is a slight modification of (6.22b).

The fact that this model takes into consideration the dependency of the common afore-mentioned parameters on the pressure, frequency and electric field strength, leads the model to apply a correction factor to the parameter α . The experiments show that the parameter α decreases with respect to the common definition, which is strictly valid only for very low pressures, or very high frequencies. Inspecting Fig. 4 of [Gould 1956] it can be established that the correction factor to the variable α is negligible as long as it is satisfied

$$\frac{f}{p} > c$$

where f is the RF frequency and c is the speed of light in vacuum. When the frequency decreases or the pressure increases much with respect to this expression, the effective electric field-to-pressure ratio starts to deviate from its common form. Unfortunately no analytical expression was proposed for this correction factor.

The author also considers the dependency of the collision frequency on the pressure, the electric field strength and the presence of contaminants, like CO_2 , CO , etc.... The collision frequency seems to change noticeably for very strong electric fields, doubling its value when α changed from 30 to 300 $[V \cdot cm^{-1} \cdot Torr^{-1}]$ for pure air. However the presence of different substances within the air did not alter noticeably the values of the collision rate. Mayhan presents a table with the values of the collision frequency vs. the effective electric field over pressure for different gases: pure air, air 10% CO_2 , etc.... However, the author mentions that the average of the collision rate over the table has been used in their analysis of the corona breakdown, which results in the well-known value of $\nu_c = 5.3 \cdot 10^9 p$, as the one of Lupan's model.

On the other hand, the diffusion coefficient proposed in this model is the same as (6.14), and the parameter γ is the pressure times the angular frequency over the collision rate. Choosing the average value of the latter, the variable γ can be written as follows:

$$\gamma = \frac{\omega}{5.3 \cdot 10^9} \cdot p$$

6.3.4 Comparison of the ionization rates

The ionization rates described above have been chosen as a sample of the models that can be found in the literature. In many occasions the models that appear in the literature are small variations or approximations of the ionization rates already proposed [Anderson 1986], and sometimes the proposed models are completely new [Tao 2008].

The validity of Mayhan's model seems not to be bounded by any value of the effective electric field over pressure, though strictly speaking a correction factor should be applied to the expression of the effective electric field and the dependency of the collision frequency on the electric field should be considered, too. As no analytical formula has been defined to express these dependencies, no author has considered these effects for Mayhan's model, or their works were confined within the range of validity of α defined above [Lupan 1978a, Lupan 1978b, Ney 1987, Rasch 2009].

The problems appear when the analysis of the corona breakdown threshold for open structures, like antennas, or for microwave devices where the field is strongly inhomogeneous, is required. In these cases, a wide range of values of α have to be considered in the solution of the corona equation outside the range of validity,

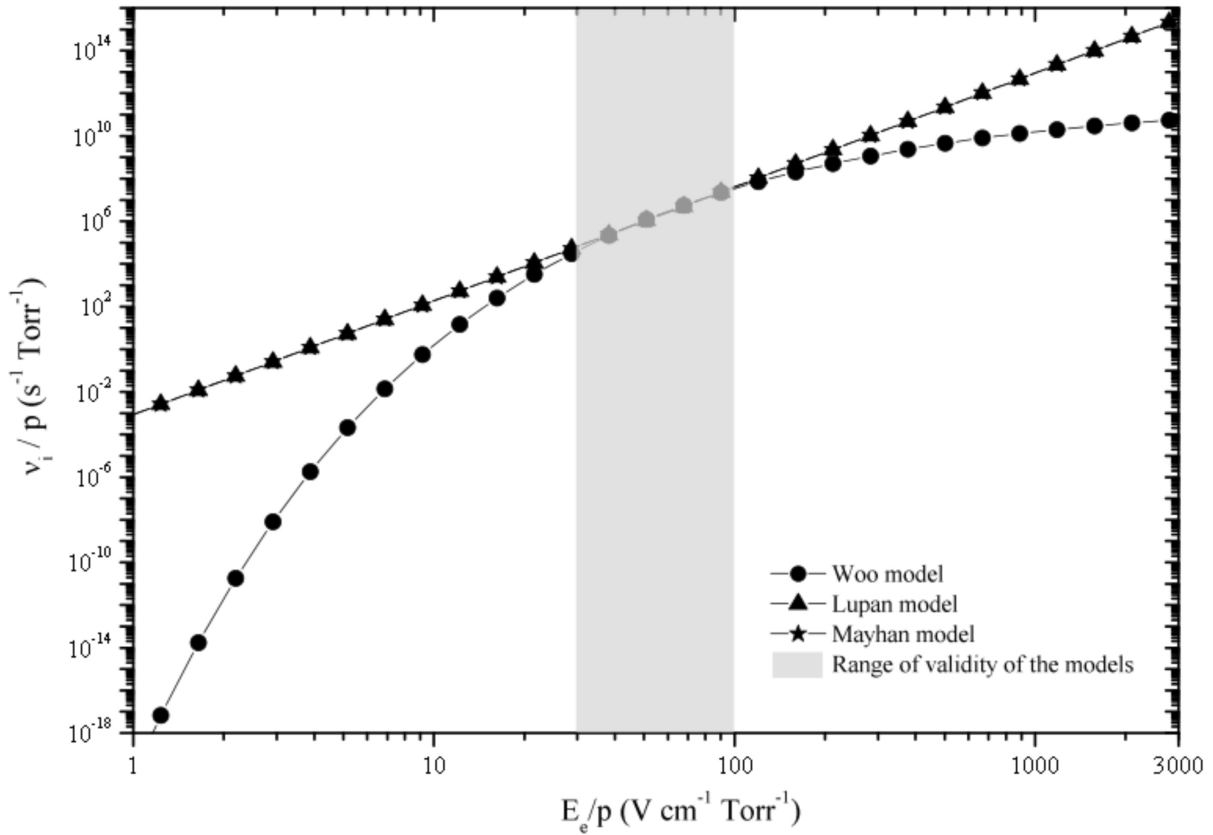


Figure 6.4: Comparison of the ionization rate obtained with three different models. The ionization rate has been plotted for $f = 994$ MHz and $p = 1.5$ Torr.

and the error in the solution of (6.16) due to the inaccurate model of the ionization rate is added to the inherent inaccuracy of the numerical technique applied to find the electric fields within the structure or when the corona equation cannot be solved analytically, what occurs in most of the cases.

The plot of Fig. 6.4 shows that the ionization rate of Lupan's and Mayhan's models behave in the same way with the variable α , however, Woo's model differs noticeably from the previous ones, decreasing drastically as the effective electric field over pressure lies outside the range of validity.

The range of values of α for which the models of Lupan and Woo are valid is represented by the gray area in Fig. 6.4. Note how the three models predict the same ionization rates within this zone. Fig. 6.5 shows a zoom of the ionization rates within the range of validity and it can be observed that the values of the ionization rate do not differ much in this region. Therefore, the predicted corona breakdown threshold obtained with the three models are expected to be similar when the electromagnetic field within the microwave device does not result in a wide spread of values of α needed to find the minimum breakdown power [Rasch 2009].

In general, the decrease of the ionization rate of the Woo model outside the range of validity will result in the overestimation of the corona breakdown threshold when solving the corona equation. The other two models follow the same tendency, but the later study of the corona breakdown threshold obtained with the three models will show some differences that will be discussed.

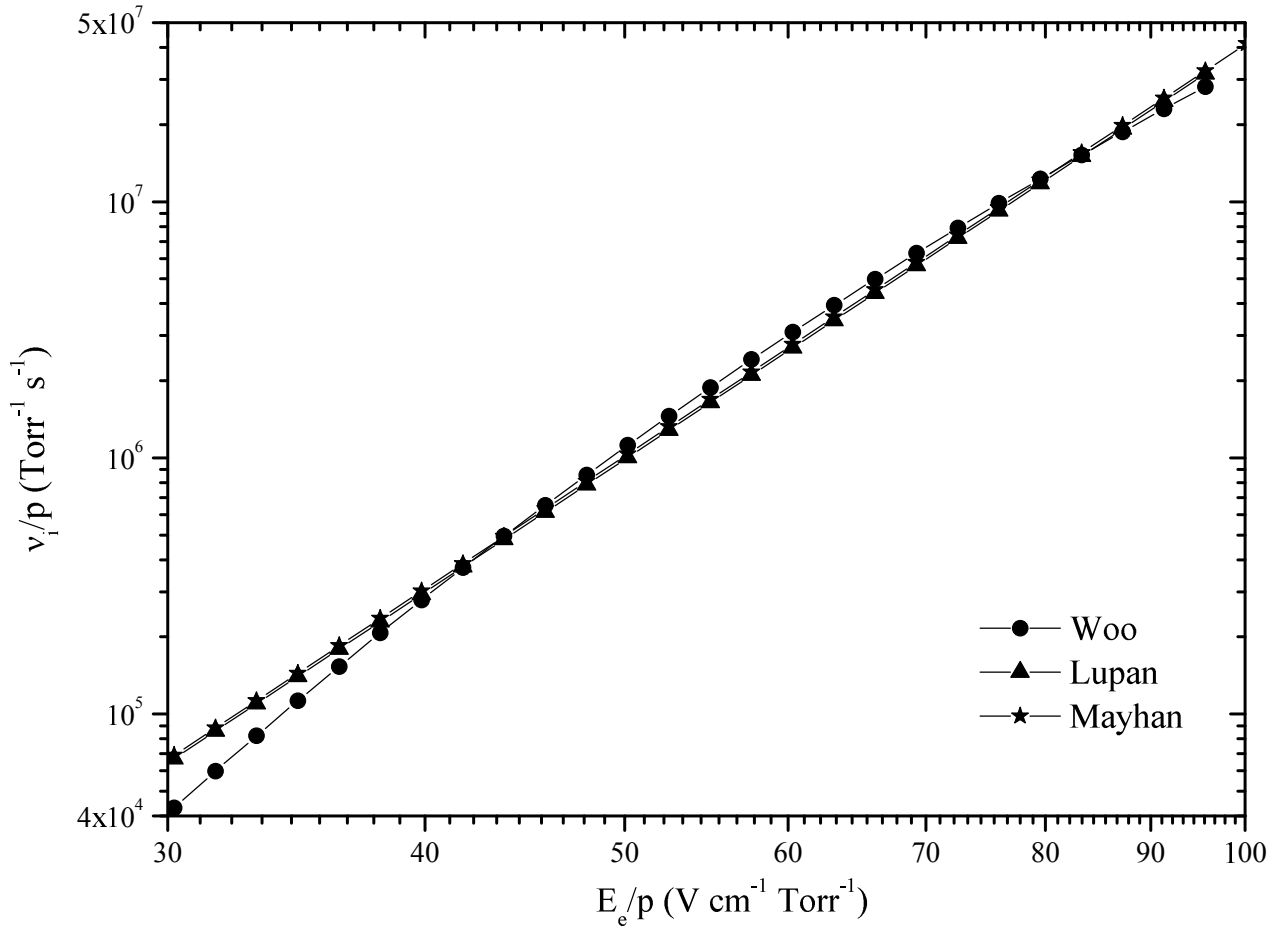


Figure 6.5: Ionization rate within the range of validity of α for the same parameters of Fig. 6.4.

6.4 Numerical solution of the corona equation

The corona equation (6.16) has been numerically solved using the Finite Elements Method (FEM). The examples that are going to be presented are separated into two cases: waveguides or cables, i.e., 2D structures, where the translational symmetry of the solution can be applied; cavities, resonators and open-structure problems, i.e., 3D geometries. In the first case, where the corona equation can be reduced to a 2D operator, the results that will follow have been obtained with an 2D Galerkin in-house FEM code based on the very pedagogical approach of the technique exhibited in [Polycarpou 2006]. The solution of the corona equation for closed cavities and open structures has been done using another in-house tool based on GetFEM [Renard 2010], adapted to the resolution of the corona equation.

The Finite Elements (FE) technique is based on the partition of the geometrical domain into canonical shapes. The choice of triangles and tetrahedra have been followed in this work for the 2D and the 3D problems, respectively. A set of linear interpolation functions is proposed as the approximated solution of the profile of the electron population density within each element. The unknowns of the interpolation function are placed on the vertices of the elements. By forcing the same unknown value at the node that is shared among neighboring

elements, the continuity of the numerical solution is guaranteed. Finally, the imposition of the Dirichlet boundary conditions at the boundary nodes results in the formation of a homogeneous system of equations where the unknowns are the values of the electron population density located at the mesh nodes. Since the system is homogeneous, the non-trivial values of the electron population density at the nodes of the mesh that satisfy the corona equation are calculated by setting the determinant to zero.

The coefficients of the corona equation depend on the ionization rate and the pressure. Then, the ionization rate depends on the rms electric field and this, in turn, on the input power. Therefore, the null-determinant condition sets an implicit function of the input power on the pressure. Finding the minimum power that sets the determinant to zero for each pressure defines the Paschen curve of the device.

The numerical modeling of the problem using the FEM can be summarized in the following steps:

1. Discretize the domain into finite elements.
2. Obtain the corresponding linear equation for a single element by first deriving the weak formulation of the differential equation.
3. Form the global system matrix of equations through the assembly of all the elements.
4. Impose Dirichlet boundary conditions.
5. Fix the pressure and find the minimum input power that sets the determinant of the global matrix to zero.

6.5 Results

The results of the eigenvalue problem applied to different examples appearing in the literature are going to be analyzed using the three ionization rate models presented before. The attachment rate of Woo's model has been used because it is the only model where the range of validity is specified, and this will be useful to understand the reliability of the Paschen curve obtained.

Fortunately, the devices that are going to be studied correspond to geometries where the electric field can be expressed analytically. However, the analytical solution of the electric field can only be found in few cases. Therefore, it is interesting to compare the corona breakdown threshold calculated using the electric field obtained by numerical methods, as it is the case for many realistic devices, with the Paschen curve obtained using the exact value of the electric field evaluated at the nodes of the mesh. It must be mentioned that the comparison between the results obtained with both methods for the 2D cases will be presented using the same number of triangles. The numerical method to obtain the electric field numerically has been chosen the same as to solve the corona equation. The commercial software HFSS is a code that applies the FEM and that has been utilized in the calculation of the electric fields of the problems analyzed next.

The solution of the eigenvalue problem described before provides the corona breakdown power threshold. The plot of the minimum input power for which the balance between the ionization gain and the diffusion loss of electrons occurs vs. pressure results in the Paschen curve. For higher input powers the diffusion of electrons will not be able to offset any more the increase of the electron population due to the ionization and the breakdown occurs.

Therefore, the Paschen curve of different devices is going to be analyzed in the following, together with a study of the convergence in order to analyze the impact of the mesh on the predicted values of the corona threshold. The influence of the nature in the calculation of the electric field in the solution of the corona equation

is also going to be analyzed. In view of the development of a new high power SMA connector, presented in Chapter 7, these studies are used to assess the implemented FEM-2D program and the available ionization rate models to design the connector and predict its corona breakdown withstanding capabilities.

6.5.1 Corona discharge in a parallel-plate waveguide

The first analysis of the corona breakdown threshold is going to be done for the unbounded parallel-plate waveguide separated a distance d and excited by the fundamental mode (TEM mode). In this case the electric field is uniform and points along the direction perpendicular to the plates (see Fig. 6.6). As the ionization rate is a scalar quantity, the rms is enough to describe the ionization rate which is also uniform within the region between the plates and can be expressed as

$$E_{rms} = \frac{V_{RF}}{\sqrt{2}d}. \quad (6.25)$$

This enables the calculation of the electron population density by solving analytically the corona equation (6.15).

This example intends to compare the results of the corona breakdown threshold obtained with different ionization rate models for a simple case where no influence of the method of solution on the predicted threshold could arise. As the ionization rate in this case is a constant, the electron density profile can be easily found by applying the method of separation of variables, which can be written

$$n(z, t) = n(z, 0) \sin \Lambda_m^{-1} e^{(\bar{\nu}_i - D/\Lambda_m^2)t}, \quad (6.26)$$

where Λ_m is the diffusion length and m is an integer that accounts for the m -th profile of the electron population density that satisfies the corona equation. The inverse of the diffusion length is given by $\Lambda_m^{-1} = (m\pi/d)$ and the corona breakdown condition is found by setting the exponent of the time-dependent part of (6.26) to zero. Indeed, when the ionization rate exceeds the value (D/Λ_m^2) , the electron population density grows exponentially, turning the gas into a conductor and triggering the corona discharge. In order to find the minimum voltage breakdown which onsets the corona discharge, the integer m must be equal one, in this case the corona breakdown condition reads:

$$\left(\bar{\nu}_i - D \left(\frac{\pi}{d} \right)^2 \right) = 0. \quad (6.27)$$

The diffusion coefficient is a function of the pressure and the ionization rate is a function of the rms electric field and the pressure. Thus, the corona breakdown threshold is obtained by calculating the rms electric field that satisfies (6.27) at a given pressure. By finding the root of (6.27) at each pressure the Paschen curve can be plotted.

6.5.1.1 Paschen curve

The Paschen curve obtained for a parallel-plate of distance $d = 4.744$ cm excited by a voltage generator at the frequency $f = 994$ MHz is plotted in Fig. 6.7. The plot shows the results obtained with the three ionization rate models together with the experimental measurements extracted from [MacDonald 1966].

The Paschen curve obtained shows that Mayhan's model predicts the lowest corona breakdown threshold. Observing Fig. 6.4 and Fig. 6.5 we can see that Mayhan's model yields the highest values of the ionization frequency, except around the middle value within the range of validity of the parameter α , where Woo's ionization

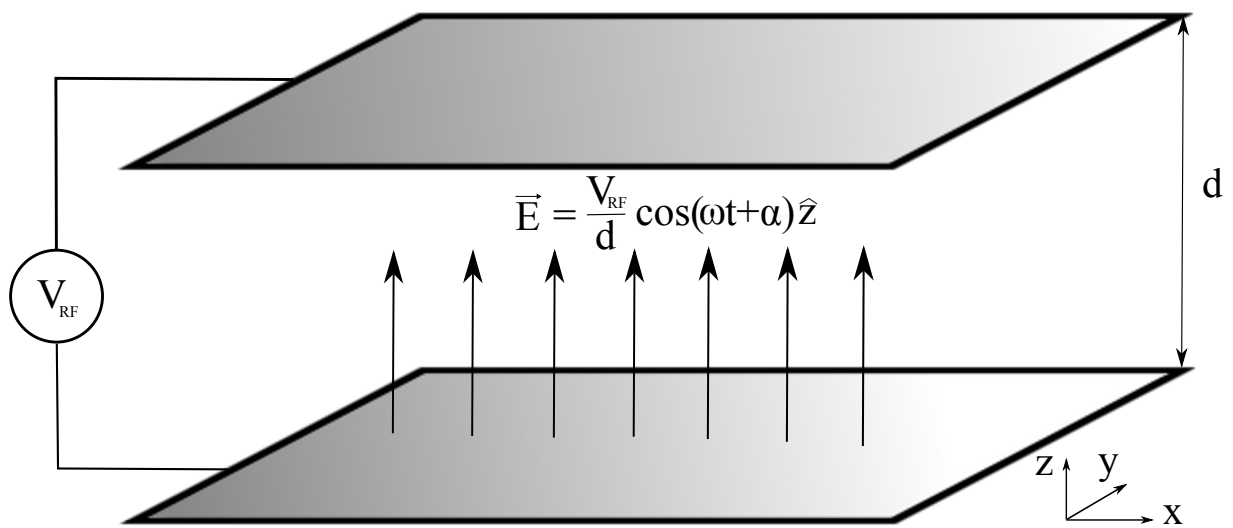


Figure 6.6: Sketch of a parallel-plate waveguide separated by a distance d .

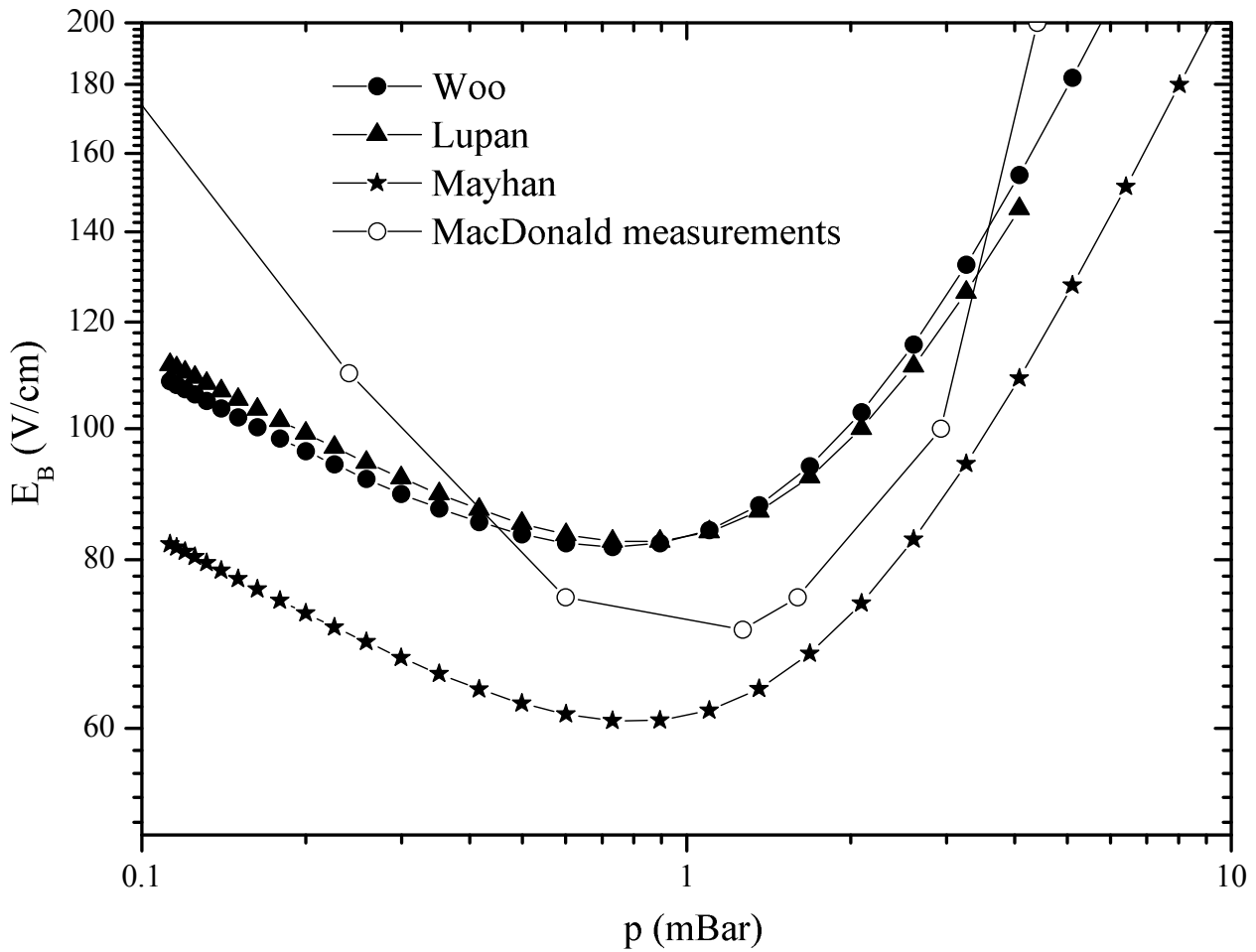


Figure 6.7: Paschen curve obtained with three ionization rate models for a parallel-plate waveguide of distance $d = 4.744$ cm excited at $f = 994$ MHz together with the measurements extracted from [MacDonald 1966].

rate model predicts the highest value of the ionization frequency (see Fig. 6.5). Nevertheless, for the rest of the domain of α , Mayhan's model exhibits the highest ionization frequency. It is thus natural that this model predicts the lowest corona breakdown threshold. Indeed, the higher the rate of electrons released by ionization for a given field strength, the bigger the ionization gain, so that the lower the input power needed to exceed the diffusion loss to trigger the discharge. On the other hand, the Paschen curve obtained with Woo's model exhibits the highest corona breakdown threshold, since the values of the ionization rate of this model are the lowest for most of the values of the effective electric field over pressure, as it is shown in Fig. 6.4.

By comparing the values of the ionization rate shown in Fig. 6.5 for the different ionization rate models it can be inferred that relatively small differences in the ionization frequency may lead to noticeable differences in the electric field breakdown and the corona breakdown power threshold, considering the results plotted in Fig. 6.7. An example of this effect is the fact that the results obtained with Woo's and Lupan's models lie quite close to each other, whereas Mayhan's model predicts a Paschen curve that lies noticeably below. It

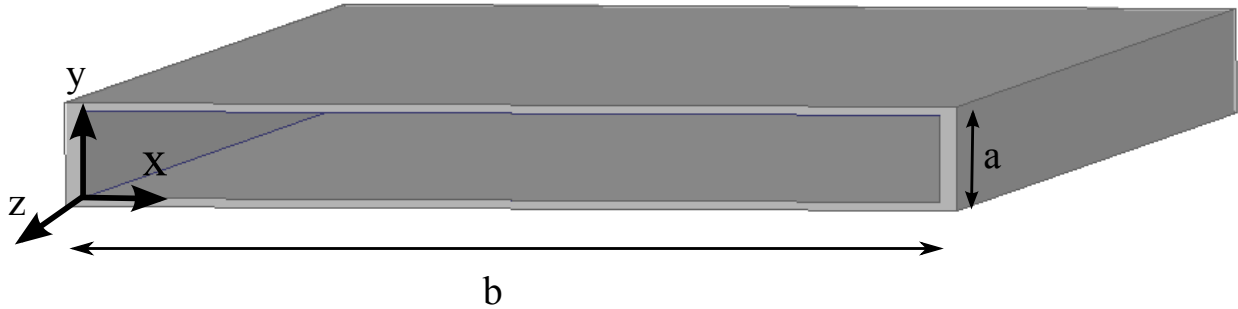


Figure 6.8: Sketch of the rectangular waveguide.

is also interesting to remark that the measurements lie in between the predictions obtained with the different ionization rate models around the critical corona threshold region, what suggests that the real values of the ionization rate model lie in between the ones corresponding to the presented models of ionization at this region of the Paschen curve. Interestingly, the measurements at the low and high pressure regions exhibit values of the corona breakdown power threshold much higher than the ones predicted by the ionization rate models presented in Section 6.3. This suggests that the real values of the ionization frequency must be smaller than the ones predicted by the described ionization models at low and high pressures.

Concerning the critical pressure, note how the measurements exhibit the minimum corona breakdown threshold around 1.3 mBar, close to $p_{crit} \simeq 1.57$ mBar, predicted by (6.17). However, the Paschen curve obtained with the three different ionization rate models show the minimum corona threshold at a lower pressure, around 0.8 mBar. It seems that the dependency of the ionization rate on the effective electric field over pressure is not able to predict accurately the pressure for which the corona threshold is minimal. However, the measurements show that the minimum corona threshold lies close to the value predicted by (6.17), what validates that expression.

6.5.2 Corona discharge in a rectangular waveguide

The second analysis of corona breakdown is going to be done for a rectangular waveguide with a small aspect ratio such that the breakdown threshold will be similar to the one of a parallel-plate. The sketch of the waveguide is shown in Fig. 6.8 whose height and width are $a = 1$ cm and $b = 10$ cm, respectively, so that the aspect ratio is $a/b = 0.1$. The exciting frequency that has been considered is $f = 1.5$ GHz, which lies between the cut-off frequency of the fundamental mode (TE_{10}) and the one of the higher-order mode.

The electric field in this case points along the y direction and reads [Pozar 1998a]:

$$\mathbf{E} = \frac{-j\omega\mu b}{\pi} A_{10} \sin \frac{\pi x}{b} \exp \{-j\beta z\} \hat{y}, \quad (6.28)$$

where $\mu = 4\pi \cdot 10^{-7}$ V · s/(A · m) is the free-space magnetic permeability, A_{10} is the electric field amplitude and β is the propagation constant, which is given by

$$\beta = \sqrt{\left(\frac{\omega}{c}\right)^2 - \left(\frac{\pi}{b}\right)^2} \quad (6.29)$$

for the fundamental mode of the rectangular waveguide. Therefore, as the ionization rate needs the rms value of the electric field, this can be found by the expression:

$$E_{rms} = \sqrt{\frac{\mathbf{E} \cdot \mathbf{E}^*}{2}}. \quad (6.30)$$

On the other hand, the relation between the electric field amplitude and the input power, P_{in} is given by

$$|A_{10}| = \sqrt{\frac{4\pi^2}{\omega\mu a^3 b \text{Re}[\beta]} P_{in}}. \quad (6.31)$$

In order to check the validity of the solutions obtained with the FEM-2D code, the corona analysis for the rectangular waveguide has been compared with the analytical solution for a parallel-plate waveguide of distance $d = a$ and an electric field equal to the maximum of the rectangular waveguide. For this, the relation between the maximum electric field amplitude and the input power must be found, which can be written as follows:

$$|E_{max}| = 2\sqrt{\frac{\omega\mu}{ab \text{Re}[\beta]} P_{in}}. \quad (6.32)$$

6.5.2.1 Convergence

For the study of the corona discharge, firstly we are going to analyze the convergence of the numerical method evaluating the evolution of the critical corona threshold as the number of elements increases. This quantity has been chosen for the convergence criterion since it is the most important parameter in the design of microwave components for space applications. The convergence was analyzed by calculating the relative error

$$\varepsilon_r(\%) = \frac{|P_n^{crit} - P_{n-1}^{crit}|}{P_n^{crit}} \cdot 100, \quad (6.33)$$

where P_n^{crit} is the critical corona threshold obtained in the n -th step.

The simulations were done increasing the number of triangles till the convergence was reached, established when the relative error decreased below 5% (see Fig. 6.9). In this case the convergence was found when using 7831 triangles.

6.5.2.2 Results

The simulations were only done with Woo's ionization rate model since the purpose in this section was not to compare the ionization models but to check the validity of the results obtained with the FEM-2D code for the later analysis. The plot of the Paschen curve for the rectangular waveguide obtained numerically with the FEM-2D code and with the analytical approximation of the parallel-plate are represented in Fig. 6.10.

It must be mentioned that the critical pressure predicted by both methods agree quite well, presenting the critical corona breakdown threshold around $p_{crit} = 2$ mBar, whereas (6.17) predicts $p_{crit} = 2.4$ mBar. On the other hand, the satisfactory agreement between the predicted Paschen curve predicted by both methods, with a discrepancy smaller than 10%, shows the suitability of the parallel-plate approximation for rectangular waveguides with small aspect ratio, and the reliability of the in-house software.

The small discrepancies can be explained by taking into account the different electric field profiles of the structures. The electric field within the rectangular waveguide is uniform along the y direction and it is maximal

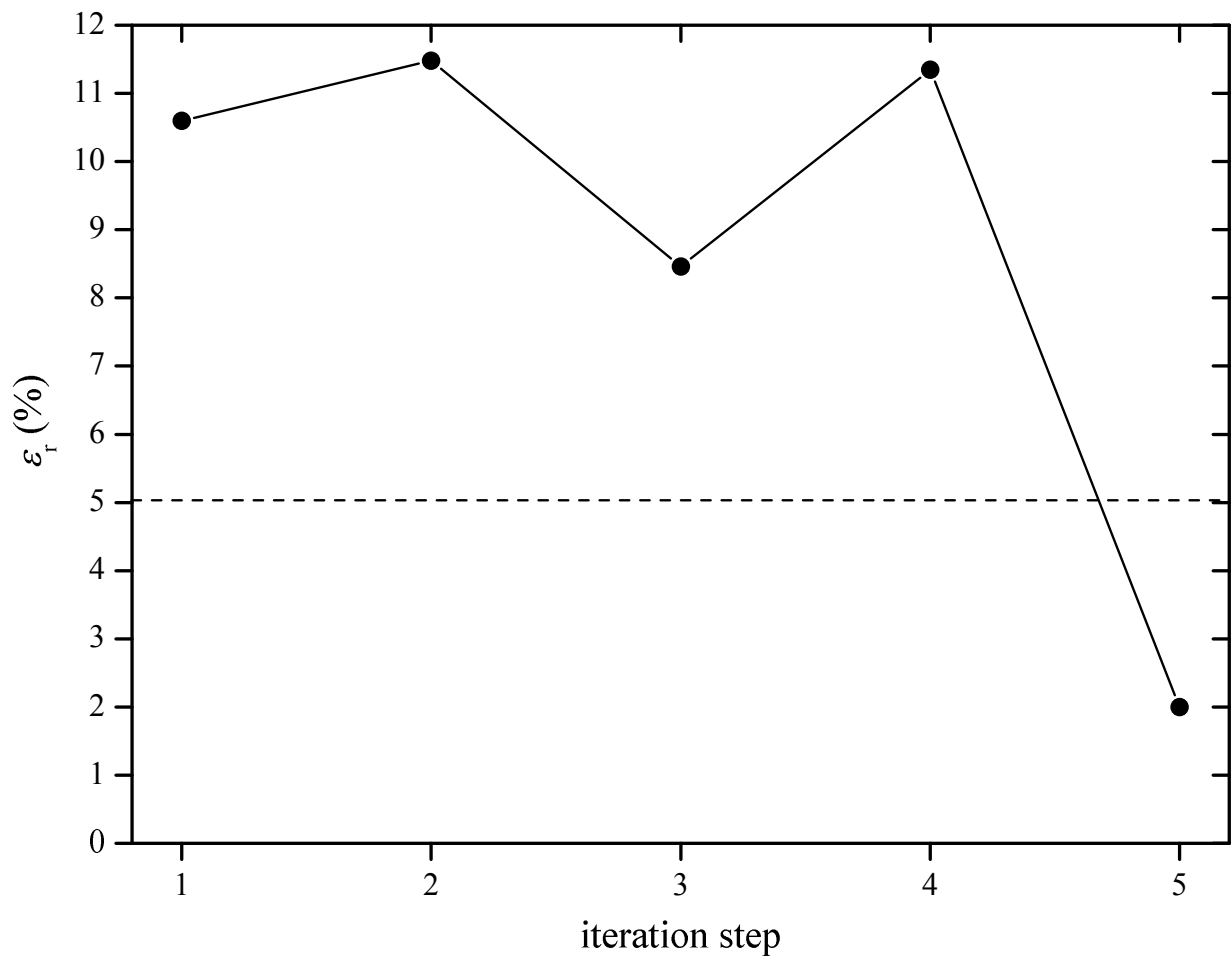


Figure 6.9: Convergence study of the Paschen curve for the rectangular waveguide calculated with the FEM-2D code.

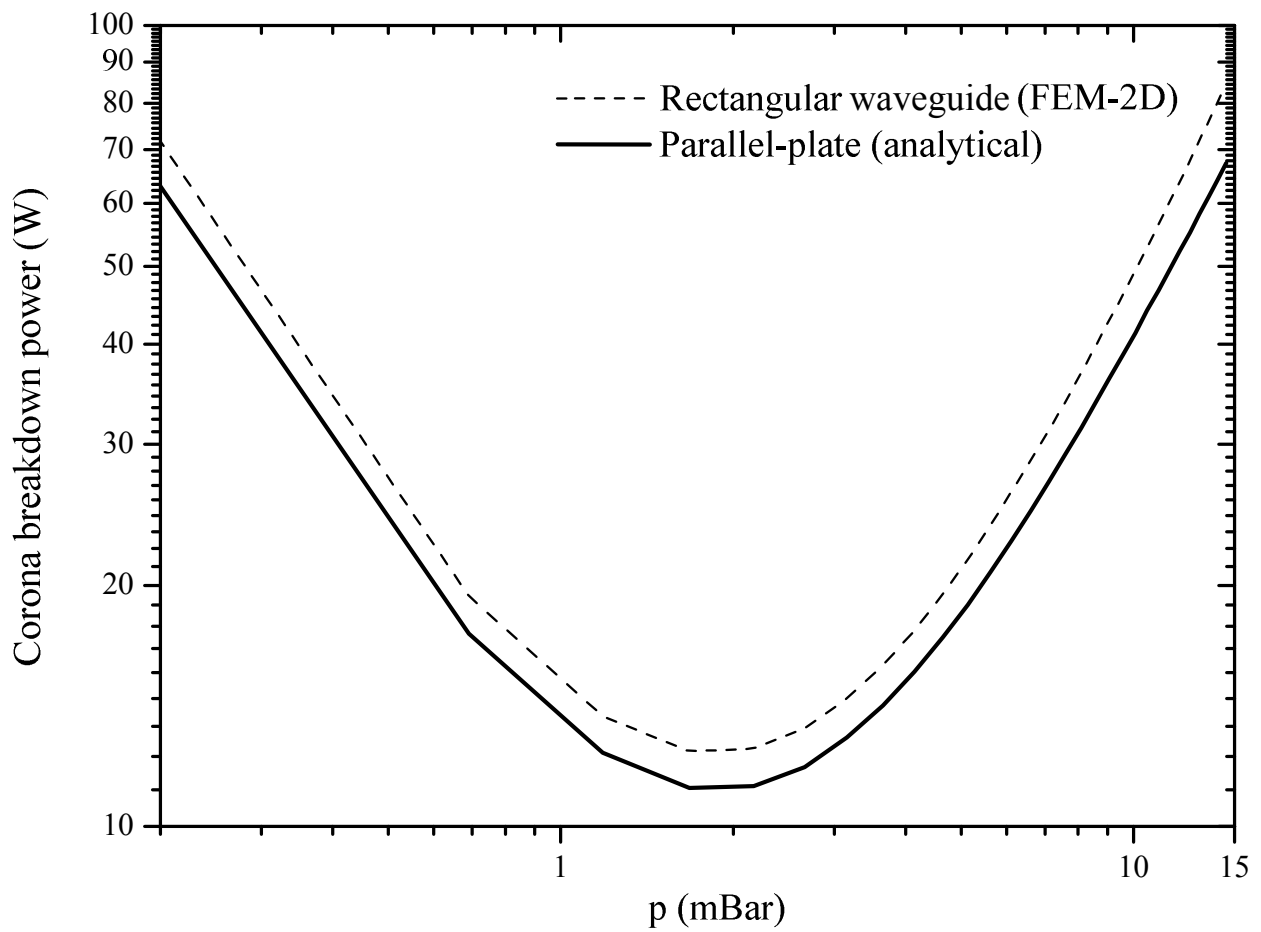


Figure 6.10: Paschen curve of the rectangular waveguide together with the one of a parallel-plate waveguide of distance $d = a$.

at $x = b/2$, decreasing as approaching the side walls. For the parallel-plate the maximum electric field of the rectangular waveguide has been assumed to be distributed within the space between the plates. It is, therefore, expected to need a higher input power in the rectangular waveguide to induce the discharge than for the parallel-plate, where the value of the electric field is the same across the whole structure. Moreover, the diffusion length of the rectangular waveguide is smaller than the one of the parallel-plate [Jordan 2006], what defines a higher corona breakdown power threshold for the rectangular [Brown 1951] than for the parallel-plate waveguide. These two factors account for the fact that the Paschen curve of the rectangular cavity lies above the one of the parallel-plate. This suggests the reliability of the in-house FEM-2D code in the calculation of the corona breakdown threshold for microwave devices where the corona equation cannot be solved analytically in light of the results that have been obtained.

6.5.3 Corona discharge in a circular waveguide

The next analysis of the corona discharge is going to be done for a circular cavity of radius $a = 1$ cm as presented in [Tomala 2005], where the fundamental mode of a circular waveguide, (TE_{11}), is excited with a frequency of $f = 10$ GHz. The sketch of the circular waveguide is shown in Fig. 6.11, and the analytical expressions for the components of the electric field of that mode read as follows: [Poazar 1998a]

$$E_\rho = \frac{-j\omega\mu}{k_c^2\rho} A \cos\phi J_1(k_c\rho) \quad (6.34a)$$

$$E_\phi = \frac{j\omega\mu}{k_c} A \sin\phi J_1'(k_c\rho), \quad (6.34b)$$

where J_1 and J_1' are the first-order Bessel function of the first kind and its derivative, respectively. The free-space permeability is defined by μ and the parameter $k_c = p'_{11}/a$ is the cut-off wave-number of the fundamental mode of the circular waveguide, which can be calculated by finding the first root of the derivative of the Bessel function, p'_{11} . Once the electric field is known, the rms value of the electric field, needed for the calculation of the ionization rate, is calculated using (6.30). The parameter A and the input power in the waveguide are related by the integration of the Poynting vector associated to the fundamental mode on the cross-section of the waveguide, and their relation is given by the expression

$$|A| = \frac{2k_c^2}{J_1(k_c a)} \sqrt{\frac{P_{in}}{\pi\omega\mu(p'_{11}{}^2 - 1)\text{Re}[\beta]}}. \quad (6.35)$$

Finally, the propagation constant β is given by

$$\beta = \sqrt{\left(\frac{2\pi f}{c}\right)^2 - \left(\frac{p'_{11}}{a}\right)^2} \quad (6.36)$$

where c is the speed of light in free-space.

6.5.3.1 Convergence

The convergence analysis of the FEM-2D for evaluating the Paschen curve of the circular waveguide is represented in Fig. 6.12 for the analytical and the numerical electric field. The results show that in the first steps the

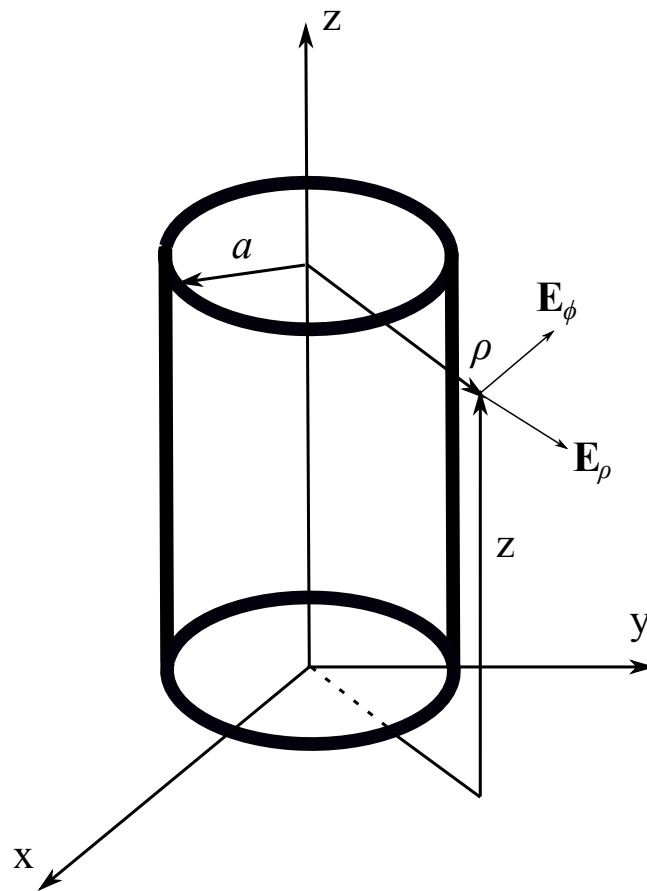


Figure 6.11: Sketch of the circular waveguide.

converge seems to have been attained for the analytical electric field as well as for the numerical. However, a further increase in the number of elements shows the growth of the relative error. At the end, the convergence for the analytical electric field was established when using 5886 triangles with a relative error below 2%, while the Paschen curve for the numerical field has not converged yet.

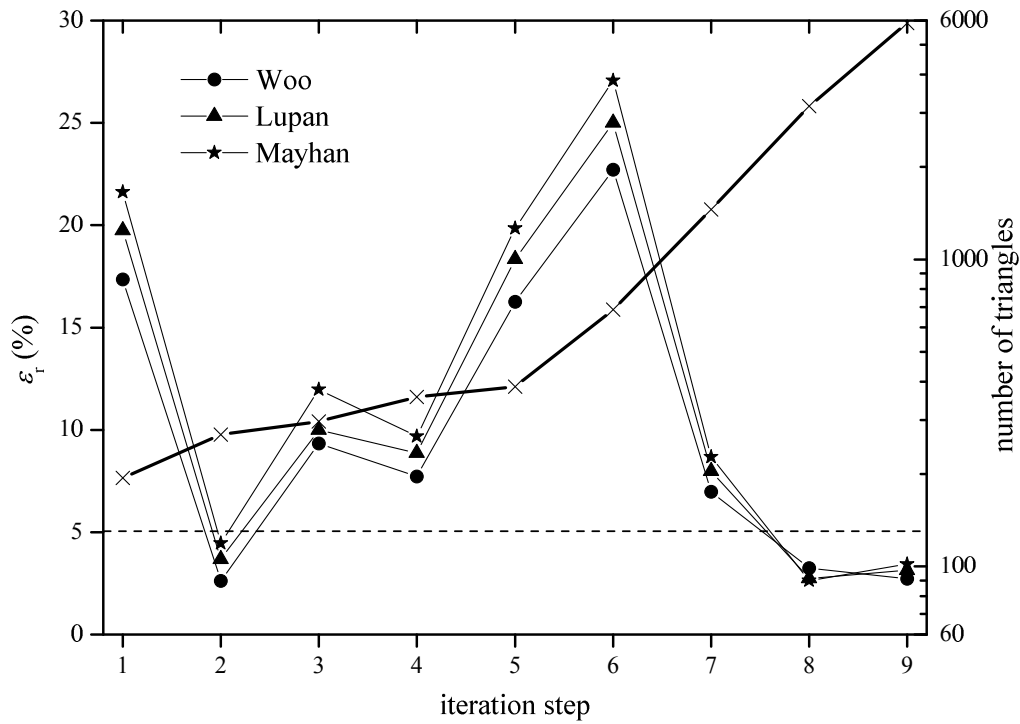
6.5.3.2 Paschen curve

The Paschen curve of the circular waveguide obtained with 5886 triangles elements using the analytical electric field is presented in Fig. 6.13. The predicted values of the corona breakdown threshold for different ionization rate models are plotted together with the results of the simulations presented in [Tomala 2005]. It can be seen that the values of the corona breakdown threshold predicted by Woo's and Lupan's models lie quite close to the results presented by Tomala, what is expected since the ionization model used in that work results in values of the ionization frequency very similar to the ones of Lupan's model. It can also be observed that Mayhan's model predicts a Paschen curve for the circular waveguide that lies relatively far below the ones predicted by the other models, as it was shown for the parallel-plate. Again, since Mayhan's ionization model exhibits the highest values of the ionization frequency, the solution of the corona equation using this model predicts the lowest corona breakdown threshold.

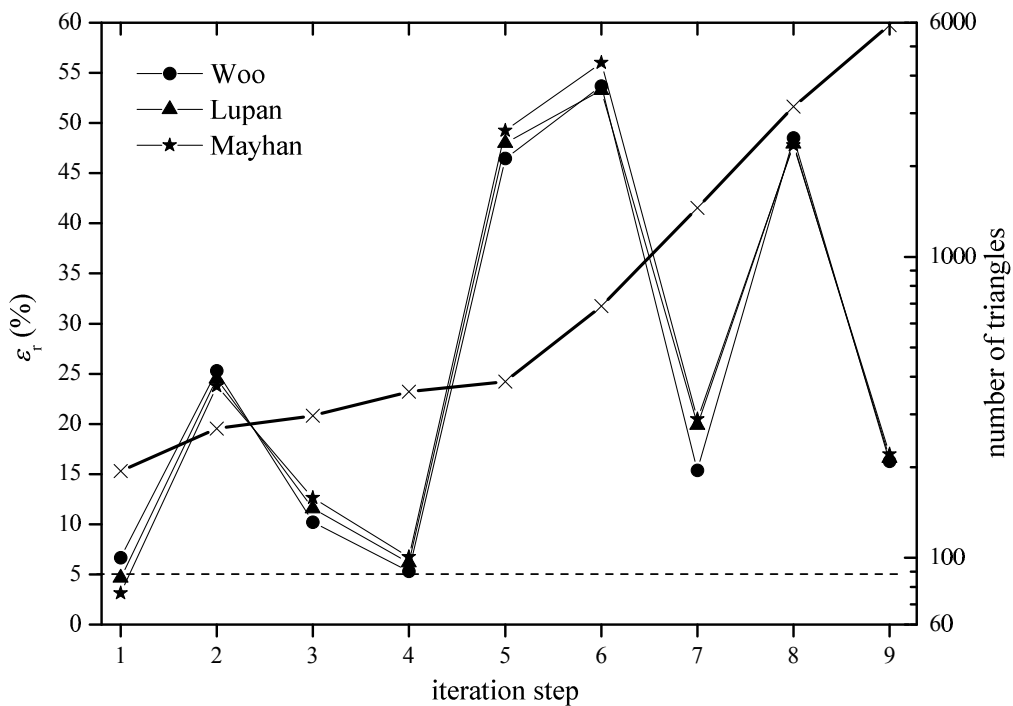
In Fig. 6.14 the critical pressure predicted by the different ionization models is represented vs. the number of elements used in the solution of the corona equation. Note that the predicted critical pressure for Woo's model lies below the ones obtained with the rest of the models for any number of elements. The critical pressure predicted by Lupan's model agrees quite well with the results of Tomala, what can be explained again by the fact that the ionization rate model chosen by Tomala is very similar to Lupan's one. Note as well how the critical pressure varies with the amount of triangles, showing that the mesh has some influence on the calculation of the critical pressure with the FEM. Therefore, although the critical pressure is supposed to depend only on the collision rate, it can be concluded from the results that the ionization rate and the mesh of the geometry have some influence on the qualitative behavior of the predicted critical pressure. It seems then, that the calculation of the critical pressure is influenced by the ionization rate, whose dependency on the collision rate must be correctly defined to avoid the calculation of a wrong critical pressure.

The predicted values of the critical pressure obtained with the numerical solution of the corona equation presented here wander around the same value exhibited by Tomala as the number of elements increases for any model of ionization (see Fig. 6.14). This is another indicator to assess that numerical convergence has been attained. Nevertheless, (6.17) predicts a value for the critical pressure around 16 mBar corresponding to the exciting frequency of the waveguide, 10 GHz, but the simulations presented here as well as the ones exhibited in [Tomala 2005] show the critical pressure lying around 10 mBar.

An inaccurate value of the collision frequency, which in reality is known to change with α [Mayhan 1971], and an inappropriate ionization rate model, could explain the discrepancies between simulations and measurements. However, the results presented here are compared with the predicted values of the corona threshold obtained by the method studied by Tomala, and the method presented here as well as the solution of the corona equation shown by Tomala, do not assume any dependency of the collision rate on the electric field. The same can be declared for the theory of the transport properties of charged particles within gases. Therefore, a possible explanation for the discrepancy between numerical results and theory is that the dependency of the ionization rate on the collision frequency for the models presented here, as in [Tomala 2005], are not correctly described for the prediction of the critical pressure. Interestingly, the study of this issue does not appear in the literature, nevertheless, for the moment no definitive explanation has been found for the discrepancy between simulations



(a) The electric field has been obtained **analytically**.



(b) The electric field has been obtained **numerically**.

Figure 6.12: Convergence study of the minimum corona breakdown threshold for the circular waveguide obtained with three different models of the ionization rate. The number of triangles used is represented by crosses.

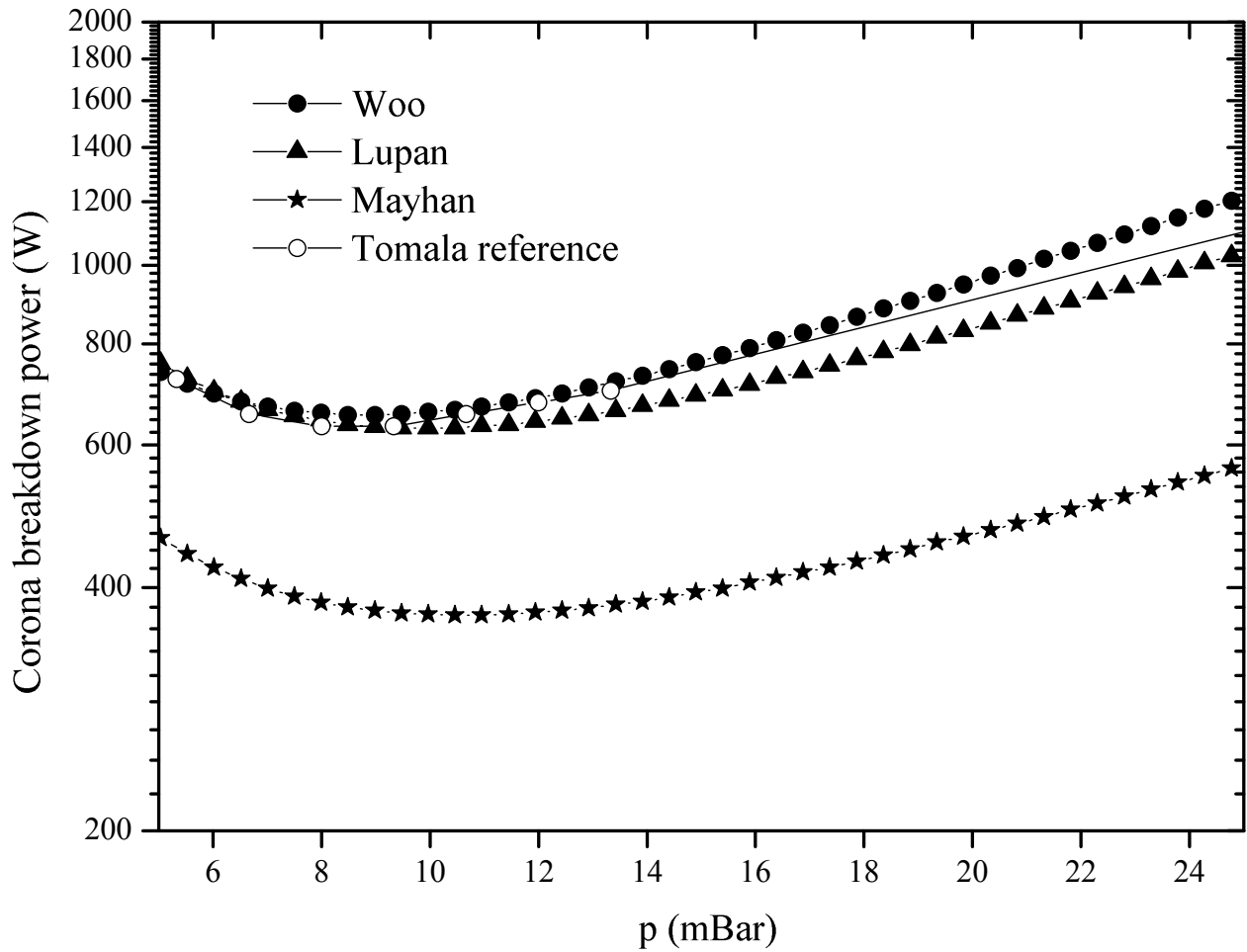


Figure 6.13: Paschen curve for the circular waveguide obtained with three different models of the ionization rate together with the simulations presented in [Tomala 2005]. The electric field has been obtained **analytically**.

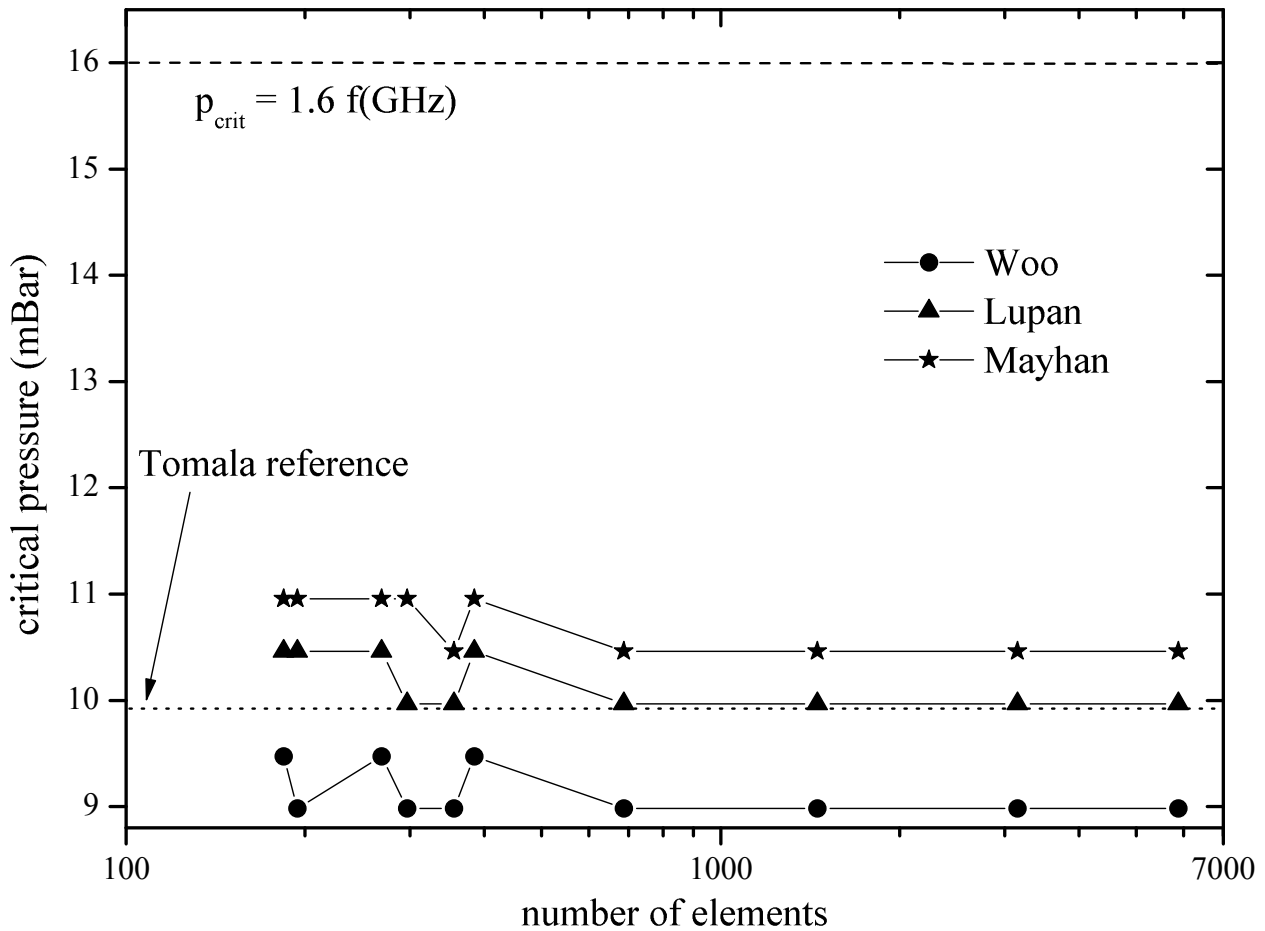


Figure 6.14: Convergence study of the critical pressure for the circular waveguide obtained with three different models of the ionization rate. The dashed line is the critical pressure predicted by (6.17) and the dotted line the predictions shown in [Tomala 2005]. The electric field has been obtained **analytically**.

and theory concerning the critical pressure.

6.5.3.3 Range of validity of parameter α

The last analysis concerns the evaluation of the percentage of nodes that lie outside the valid range of the parameter α to suitably describe the different ionization rate models. As the electric field is proportional to the square root of power, and the input of the corona equation is the electric field evaluated at the nodes of the mesh for 1 W rms input power, the value of (6.19) can be calculated at each node for any input power. From the values of pressure and power of each point of the Paschen curves obtained with the analytical and the numerical electric field, the value of (6.19) can be calculated at the mesh nodes.

The results are depicted in Fig. 6.15, where the plot shows that the Paschen curve at the low pressure region for Woo's and Lupan's models is well represented by their values of the ionization frequency since only few nodes are outside the valid range of values of α . The corona threshold predicted by Woo's and Lupan's models lie close to each other up to 11 mBar (see Fig. 6.13); at higher pressures the results start to differ, what corresponds to the region of the plot in Fig. 6.15 for which more than half of the nodes of the mesh exhibit values of α outside the range of validity. As it has been shown in Fig. 6.4, the value of Woo's ionization frequency outside the valid range of α is lower than the one of Lupan, thus the corona breakdown power threshold is expected to be higher than the one predicted by Lupan in this region. This is the reason why the Paschen curves obtained with Woo's and Lupan's models plotted in Fig. 6.13 start to deviate from each other at the high pressure region.

6.5.3.4 Summary

The analysis of the corona discharge done with the FEM-2D code for a circular waveguide has shown that the convergence is reached with less number of triangles when the electric field is analytical than for the numerical calculation of the field.

The ionization rate models predict different values of the corona breakdown power threshold. The case of Mayhan's model is more remarkable. Like in the parallel-plate waveguide, it exhibited much lower values of the corona breakdown powers than Woo's and Lupan's models. The results obtained with these models lie close to each other, and close to the reference values for values of (6.19) within the range of validity.

It has also been concluded that the ionization frequency model seems to have some influence on the predicted critical pressure obtained by the numerical solution of the corona equation, since the values that the different ionization rate models yield differ noticeably from the one that would be expected according to the theory expressed in (6.17).

The Paschen curve obtained with Woo's and Lupan's models predicted similar values of the corona threshold when most of the nodes of the mesh exhibited values of α within its region of validity. Moreover, these models predicted values of the corona threshold that lie close to the reference results presented by Tomala. Like in the parallel-plate waveguide, Mayhan's model exhibited lower values for the corona threshold though Fig. 6.4 does not show many differences in the values of Mayhan's model with respect to the rest of the models. This suggests that a small difference in the value of the ionization rate may lead to a noticeably different value of the corona breakdown power threshold.

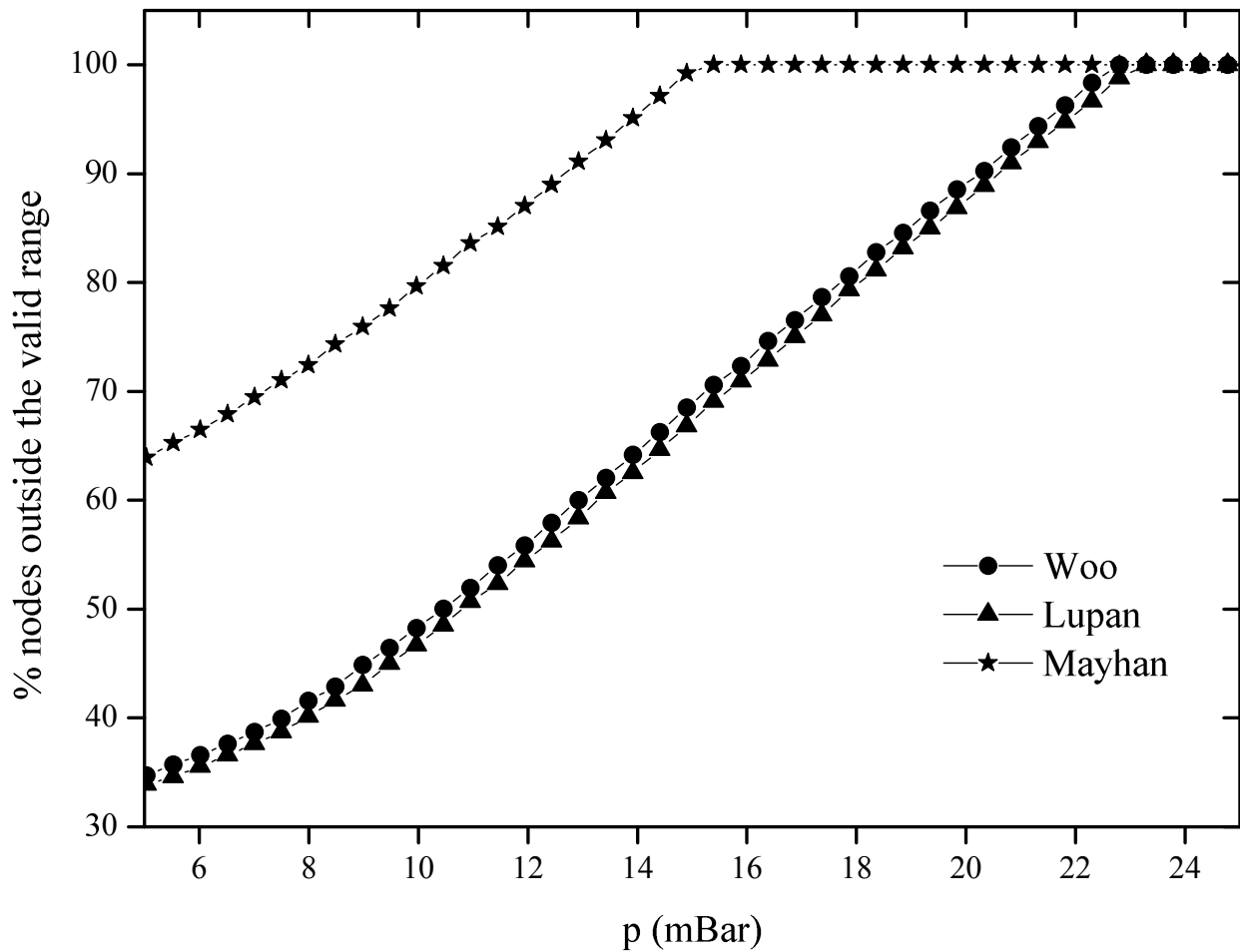


Figure 6.15: Percentage of nodes outside the range of validity for the parameter α to describe accurately the ionization rate models when the electric field of the circular waveguide has been obtained **analytically**.

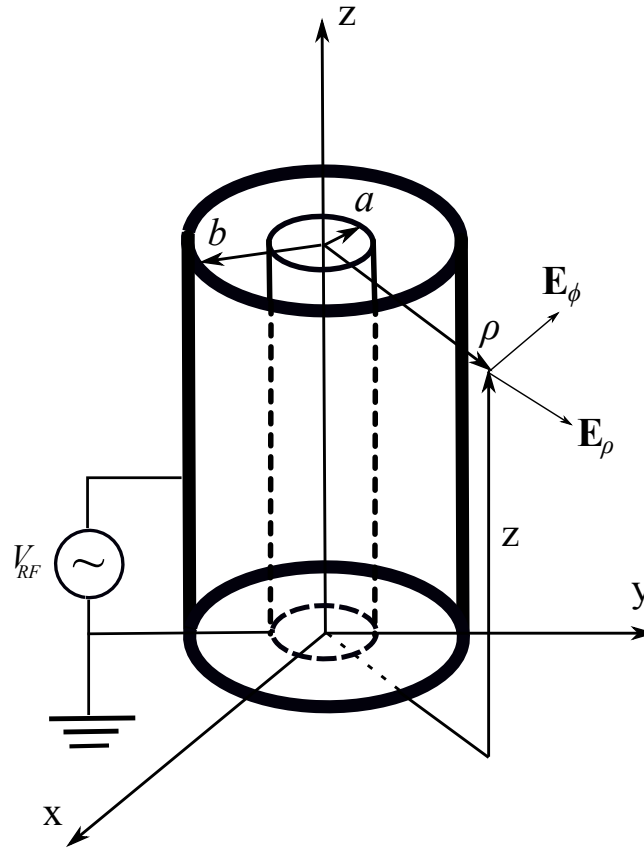


Figure 6.16: Sketch of the coaxial cable.

6.5.4 Corona discharge in a coaxial waveguide

The next analysis has been done for the coaxial waveguide presented in [Herlin 1948b] for a microwave frequency of $f = 3.125$ GHz, where a large coaxial cable aspect ratio is considered, $b/a = 15$ (see Fig. 6.16), provoking a quite inhomogeneous field between the electrodes. The values of the radii of the inner and outer conductor for this case are $a = 0.318$ mm and $b = 4.77$ mm, respectively.

The considered frequency is only able to excite the fundamental mode of the coaxial waveguide (the TEM mode), for which the electric field points along the radial direction and it is given by

$$E_\rho = \frac{V_{RF}}{\rho \ln b/a}, \quad (6.37)$$

where V_{RF} and ρ are the applied voltage between the electrodes and the radial coordinate, respectively (see Fig. 6.16). The relation between the rms input power, P_{in} , and the RF voltage applied between the conductors of an air-filled coaxial waveguide, V_{RF} , is given by

$$P_{in} \approx \frac{1}{2} \frac{V_{RF}^2}{60 \ln b/a}, \quad (6.38)$$

where the air impedance has been approximated by the free-space impedance $\eta \approx 120\pi \Omega$.

6.5.4.1 Convergence

The convergence analysis of the Paschen curve for the coaxial waveguide is represented in Fig. 6.17 for the analytical and the numerical electric field. Unlike the results obtained for the circular waveguide, in the coaxial the convergence is similar for both cases. At the 5-th step the relative error for the numerical electric field is smaller than for the analytical one, but although it is difficult to see, the relative error shown in Fig. 6.17b is slightly above the 5% delimited by the dashed line. The main difference between the convergence study for the analytical and the numerical electric fields is that Woo's model has not converged for the numerical electric field at the 10-th step (see Fig. 6.17b), while for the analytical all the models have converged at the last step (see Fig. 6.17a). The convergence was thus reached when using 8545 triangles within the space between the coaxial conductors.

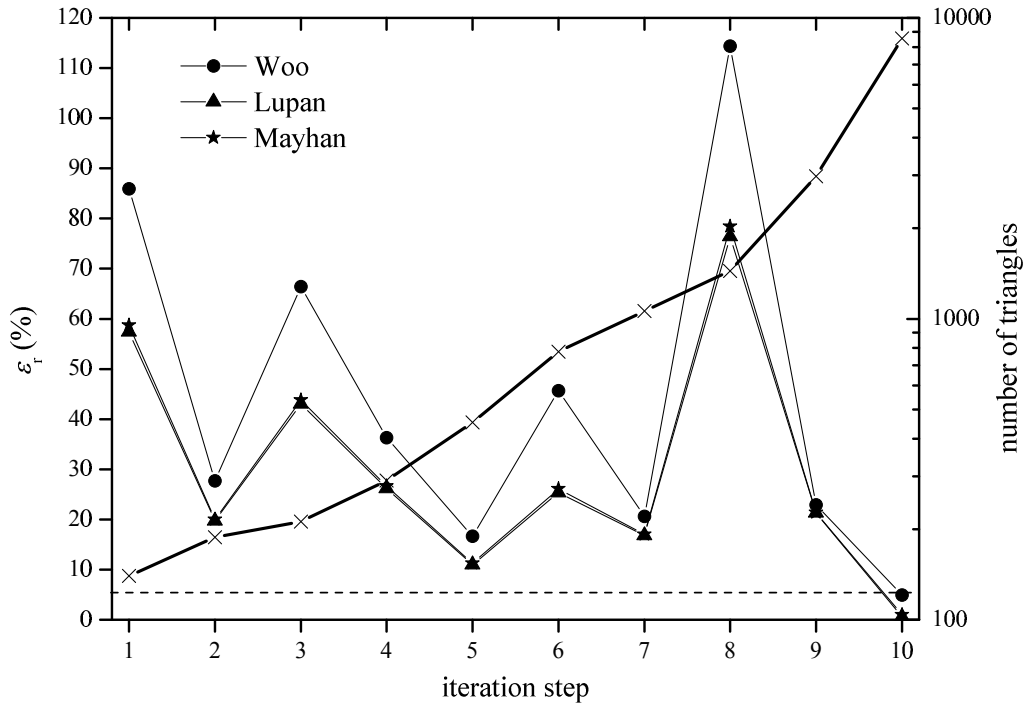
6.5.4.2 Paschen curve

The Paschen curve of the coaxial waveguide for this number of elements is plotted in Fig. 6.18 for different ionization rate models and the exact values of the electric field. The predicted values of the corona breakdown threshold are presented together with the measurements shown in [Herlin 1948b]. We can see that Woo's model agrees quite well with the author's measurements in the low pressure region. As it will be shown later, the values of α at the nodes of the mesh corresponding to every point of the Paschen curve obtained with Woo's model lie outside the range of validity. As Woo's ionization rate exhibits the lowest value of the ionization frequency outside the range of validity of α , in view of the good agreement between measurements and results obtained with Woo's model, it seems that the low pressure region needs a lower value of the ionization rate than the one predicted by Lupan's and Mayhan's models. This can also be extended to the high pressure region where, even Woo's model does not reach the experimental values of the corona breakdown power threshold. As it was discussed for the parallel-plate waveguide, it is also clear for the coaxial waveguide that smaller values of the ionization rate are needed to better agree with the corona breakdown measurements at high and low pressures.

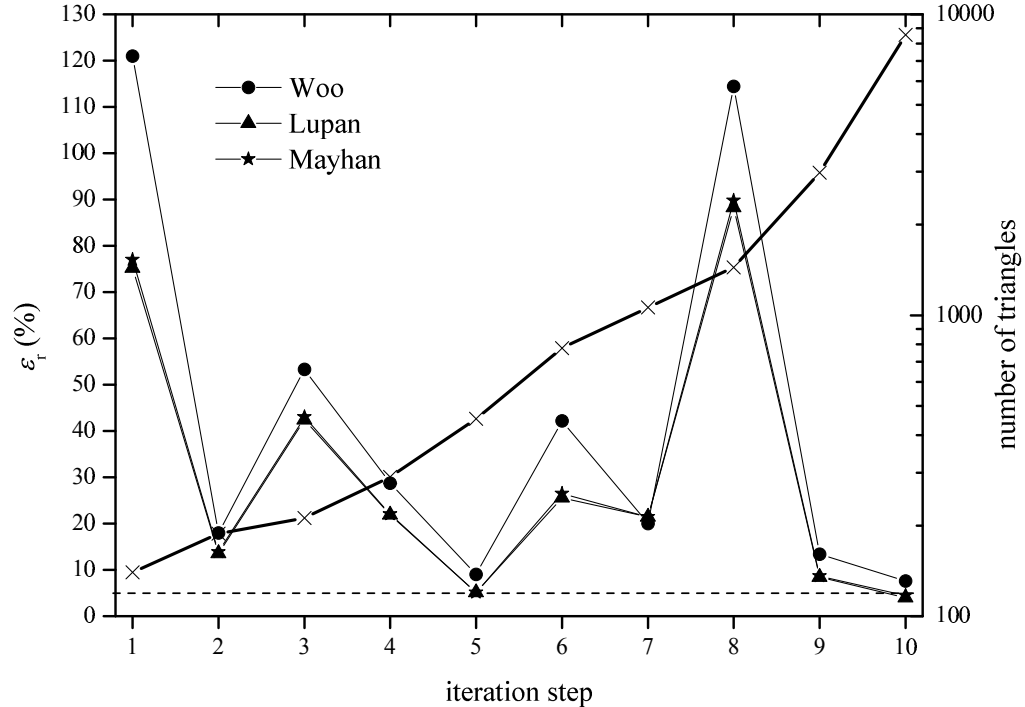
The critical pressure corresponding to the frequency used to excite the coaxial cable (3.125 GHz) should be 5 mBar according to theory expressed by (6.17). The measurements presented in [Herlin 1948b] showed that the critical pressure was lying around 4.7 mBar, near the predictions made by the transport theory of charged particles in gases. Note that the critical pressure predicted by Woo's ionization rate model is the closest to the theoretical value (see Fig. 6.19). As it was observed before, the choice of the ionization rate model has some influence on the prediction of the critical pressure obtained with the FEM, whereas the theory shows that it only depends on the collision rate. Another interesting property that the plot shows is that the critical pressure seems to depend significantly on the number of elements for Woo's model only, since the predicted value obtained with the rest of the models did not change with the mesh (see Fig. 6.19). Indeed, the ionization rate model influences the predicted critical pressure as it has been observed for the circular waveguide more remarkably. At the same time the number of elements modifies the predicted values of the critical pressure, though, apparently, only for Woo's model, what has not been explained yet.

6.5.4.3 Range of validity of parameter α

To finish the analysis of the coaxial cable, we are going to study the accuracy in the evaluation of the ionization rate to solve the corona equation by checking the amount of nodes of the mesh that exhibit a value of (6.19) outside the range of validity corresponding to the powers plotted in the Paschen curves shown in Fig. 6.18. The



(a) The electric field has been obtained **analytically**.



(b) The electric field has been obtained **numerically**.

Figure 6.17: Convergence study of the minimum corona breakdown threshold for the coaxial waveguide obtained with three different models of the ionization rate. The number of triangles used is represented by crosses.

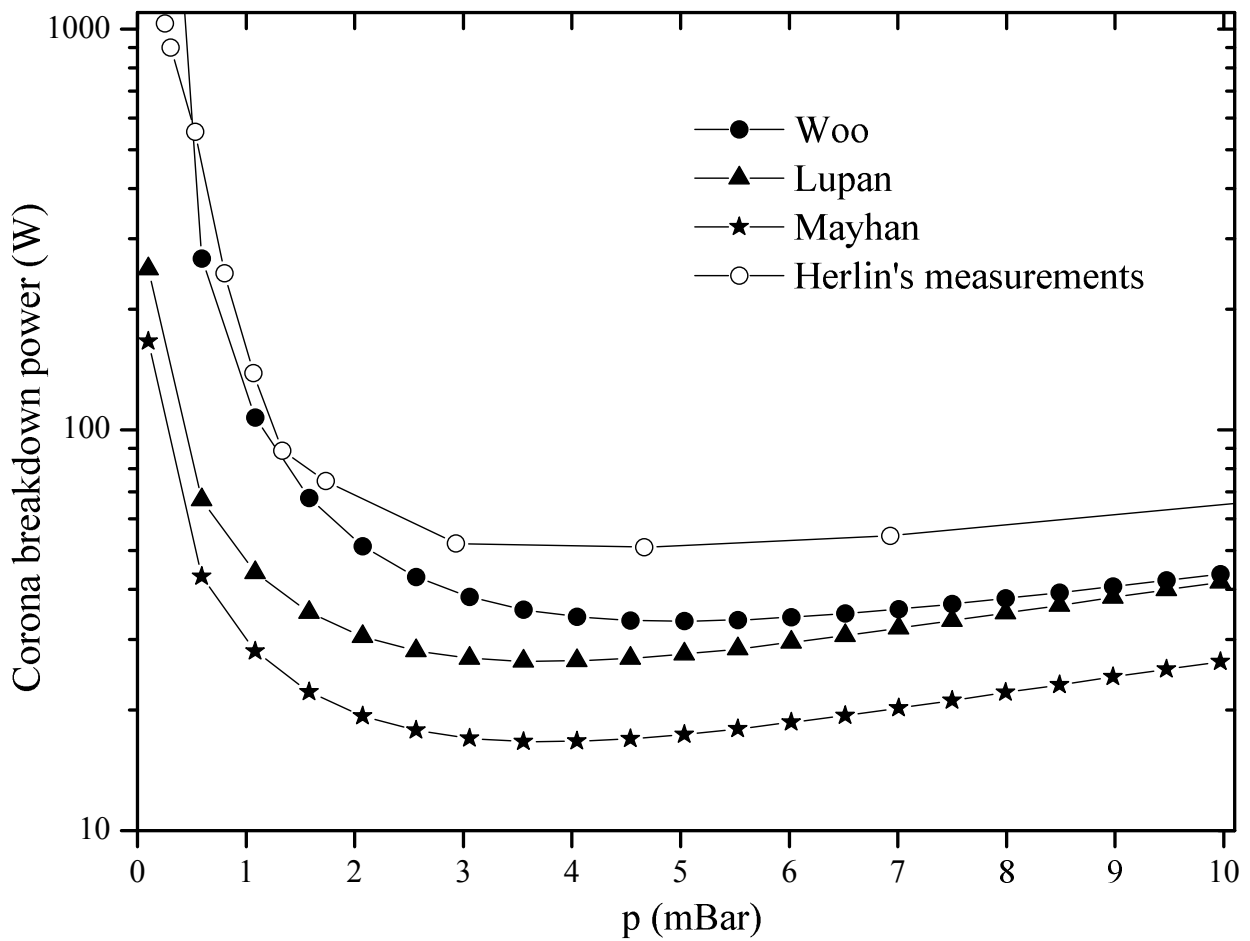


Figure 6.18: Paschen curve for the coaxial cable obtained with three different models of the ionization rate. The electric field has been obtained **analytically**.

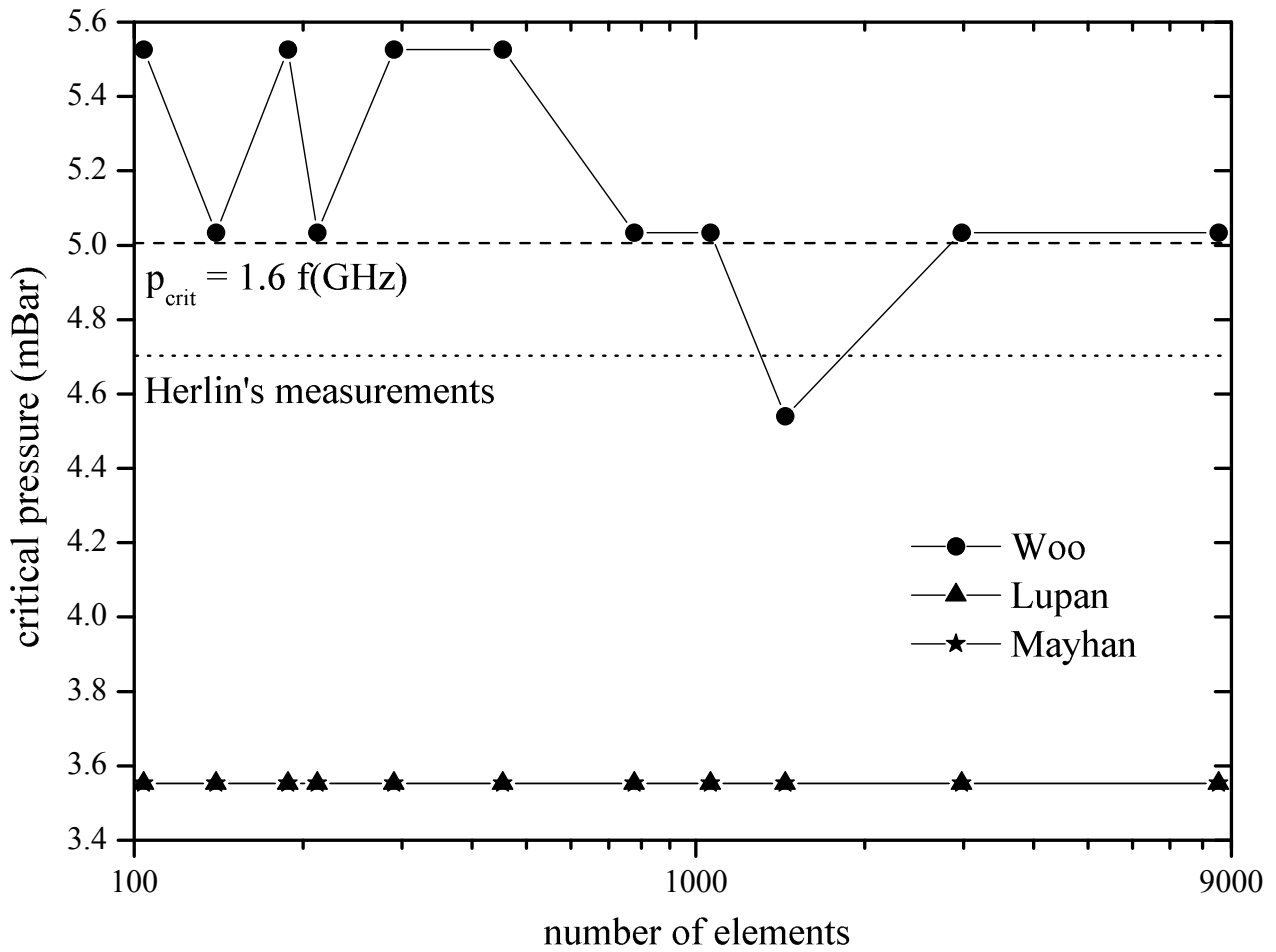


Figure 6.19: Convergence study of the critical pressure for the coaxial cable obtained with three different models of the ionization rate. The dashed line is the critical pressure predicted by (6.17) and the dotted line the measurements presented in [Herlin 1948b]. The electric field has been obtained **analytically**.

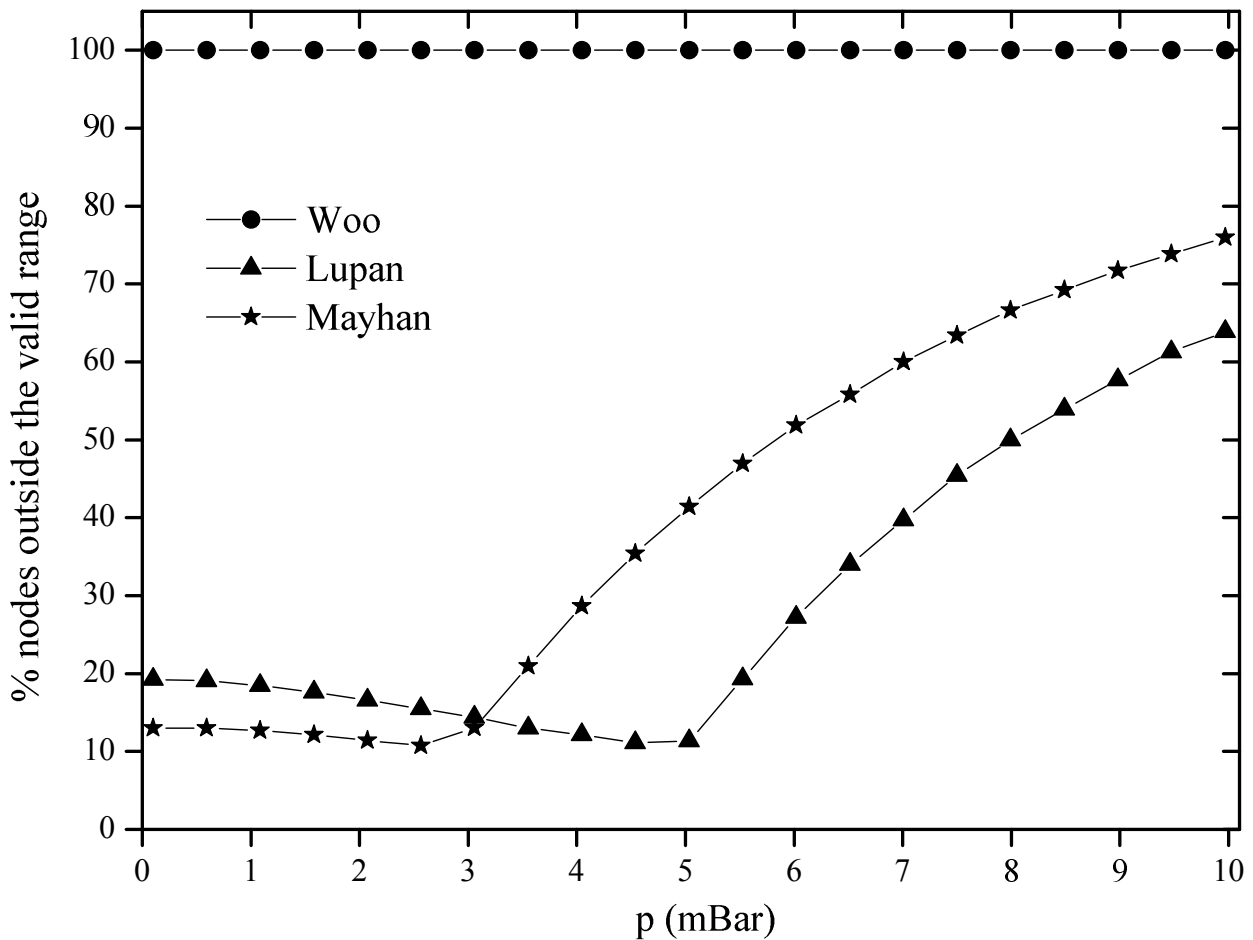


Figure 6.20: Percentage of nodes outside the range of validity for the parameter α to describe accurately the ionization rate models when the electric field of the coaxial waveguide has been obtained **analytically**.

percentage of nodes for which the parameter α lies outside the region of validity is plotted in Fig. 6.20 for the different ionization frequency models.

The high coaxial cable aspect ratio of this coaxial waveguide leads to a highly inhomogeneous electric field, what implies that few nodes of the mesh will lie within the range of validity, thus a high portion will lie either above or below it for any pressure and input power. As it was commented before, the values of (6.19) evaluated at the mesh nodes corresponding to the powers of all the points of the Paschen curve obtained with Woo's model lie above the range of validity (see Fig. 6.20). Nevertheless, the small percentage of nodes outside the range of validity shown for Lupan's and Mayhan's models in the low pressure zone suggests that the discrepancies between measurements and simulations in Fig. 6.18 are not due to the invalidity of the value of α to represent the ionization rate values. It is actually the Paschen curve obtained with Woo's model the one which lies closer to the measurements than the rest of models, at the same time that it is the only model for which every node of the mesh lies outside the range of validity according to Fig. 6.20.

6.5.4.4 Summary

Unlike for the circular waveguide, the convergence of the corona breakdown threshold obtained with the FEM-2D for the coaxial waveguide did not show much difference when evaluating the electric field numerically as for the analytical field.

As it was observed in the results for the circular waveguide, Mayhan's model predicts values of the corona breakdown threshold that lie remarkably below the ones obtained with the other models. In general, the simulations showed that the currently used ionization models predict values of the corona threshold that lie below the measurements, what suggests the need of smaller values of the ionization rate to better fit the measurements. An exception to this trend is shown for the results obtained with Woo's model at low pressures. Smaller values of the ionization rate at low and high pressures could make Lupan's and Mayhan's models fit better the experimental values, as it was pointed out in the case of the parallel-plate waveguide. Smaller values of the ionization rate for Woo's model are also required in order to fit the measurements in the high pressure are of the Paschen curve. This, together with the fact that the values of α corresponding to the Paschen curve obtained with Woo's model lie above the validity range, suggest that a smaller value of the ionization frequency is requested for α bigger than $100 \text{ [V cm}^{-1} \text{ Torr}^{-1}]$.

In the problem of the coaxial waveguide the ionization models showed to have some influence on the predicted critical pressure obtained by the numerical solution of the corona equation. Nevertheless, the discrepancies between the results obtained with the different ionization rate models and the one predicted by the theory in (6.17) are much smaller than in the case of the circular waveguide. The main difference between both structures is the working frequency, although other factors like the inhomogeneity of the electric field profile may be the reason of the smaller discrepancies. The influence of the critical pressure predicted by Woo's ionization rate model on the mesh has been also observed in the coaxial waveguide like for the circular one, however, no reason has been found to explain why it does not occur the same for the other ionization frequency models.

The Paschen curve obtained with Woo's model predicted values of the corona threshold close to the measurements in the low pressure regions while all the mesh nodes exhibited values of α outside its region of validity. Therefore, the influence of the values of α at the mesh nodes lying outside the range of validity in the solution of the corona equation (6.16) is not enough to explain the discrepancies between simulations and measurements. New ionization rate models are, therefore, required to predict correctly the experimental values of the corona breakdown power threshold.

6.5.5 Corona discharge in a rectangular cavity

The analysis of the corona discharge for two rectangular cavities is done in this section with the three ionization rate models. The results obtained have been compared with the simulations and measurements shown in [Rasch 2009]. In order to study the corona breakdown power threshold, a 3D Galerkin in-house FEM code has been developed using the GetFEM libraries [Renard 2010]. The solution of the corona equation has been carried out importing the analytical values of the electric field corresponding to the fundamental mode of a rectangular cavity (TE_{110}) or (TE_{011}) with a resonant frequency of $f = 8.85 \text{ GHz}$ into the FEM software.

The dimensions of the considered rectangular cavities are given in Table 6.1 where the geometry of the cavity has been drawn in Fig. 6.21.

The magnitude of the electric field within a rectangular cavity excited by the fundamental mode reads

$$\text{TE}_{110} \rightarrow \mathbf{E} = E_0 \sin\left(\frac{\pi x}{a}\right) \sin\left(\frac{\pi y}{b}\right) \hat{z}, \quad (6.39)$$

Table 6.1: Dimensions of the rectangular cavities.

Label	a (cm)	b (cm)	L (cm)	Mode
Cavity 1	2.286	2.492	1.016	TE ₁₁₀
Cavity 2	0.9525	2.32	1.47	TE ₀₁₁

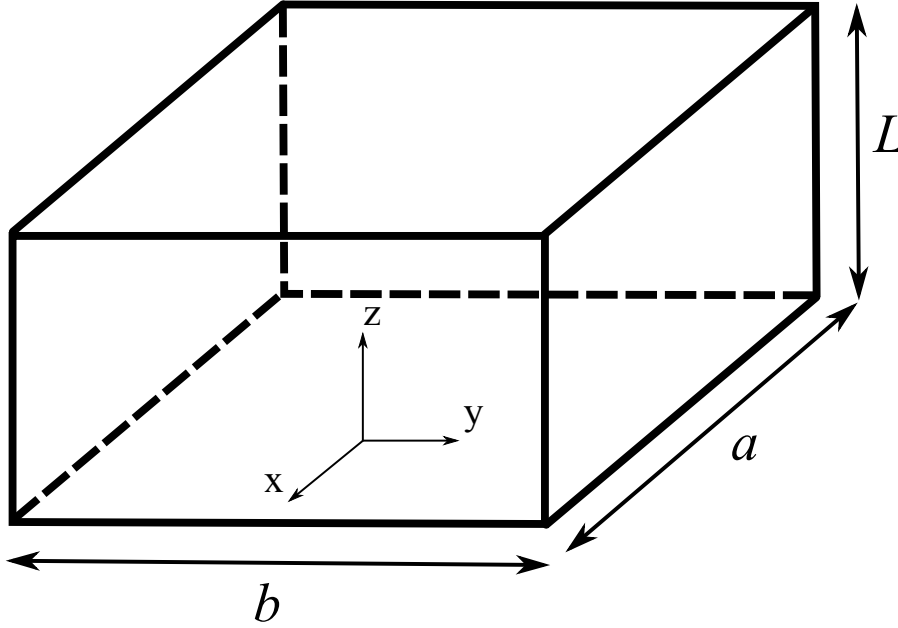


Figure 6.21: Sketch of the rectangular cavity.

for the first cavity and

$$\text{TE}_{011} \rightarrow \mathbf{E} = E_0 \sin\left(\frac{\pi y}{b}\right) \sin\left(\frac{\pi z}{L}\right) \hat{x}, \quad (6.40)$$

for the second one, where E_0 is the maximum value of the electric field in the center of the cavities.

Since the walls of the device have been assumed to be perfectly conducting, it is not possible to calculate the input power that would trigger the corona discharge onset. As no losses apply at the boundaries of the cavity for this ideal case, the constant insertion of energy within the cavity by a power source would imply a never-ending growth of the electromagnetic energy. Instead, the total energy stored for a given E_0 can be used to study the convergence of the solution of the corona equation. The electromagnetic energy stored within a rectangular cavity is expressed as [Pozar 1998b]:

$$W_{em} = \frac{\epsilon abL}{8} E_0^2, \quad (6.41)$$

where ϵ is the relative permittivity of the medium inside the cavity, in our case, air.

The convergence study of the solution of the corona equation has been done showing the total energy stored in the second rectangular cavity associated to the electric field breakdown vs. pressure for one of the ionization rate models augmenting the number of tetrahedra used. The plot in Fig. 6.22 shows that the convergence in

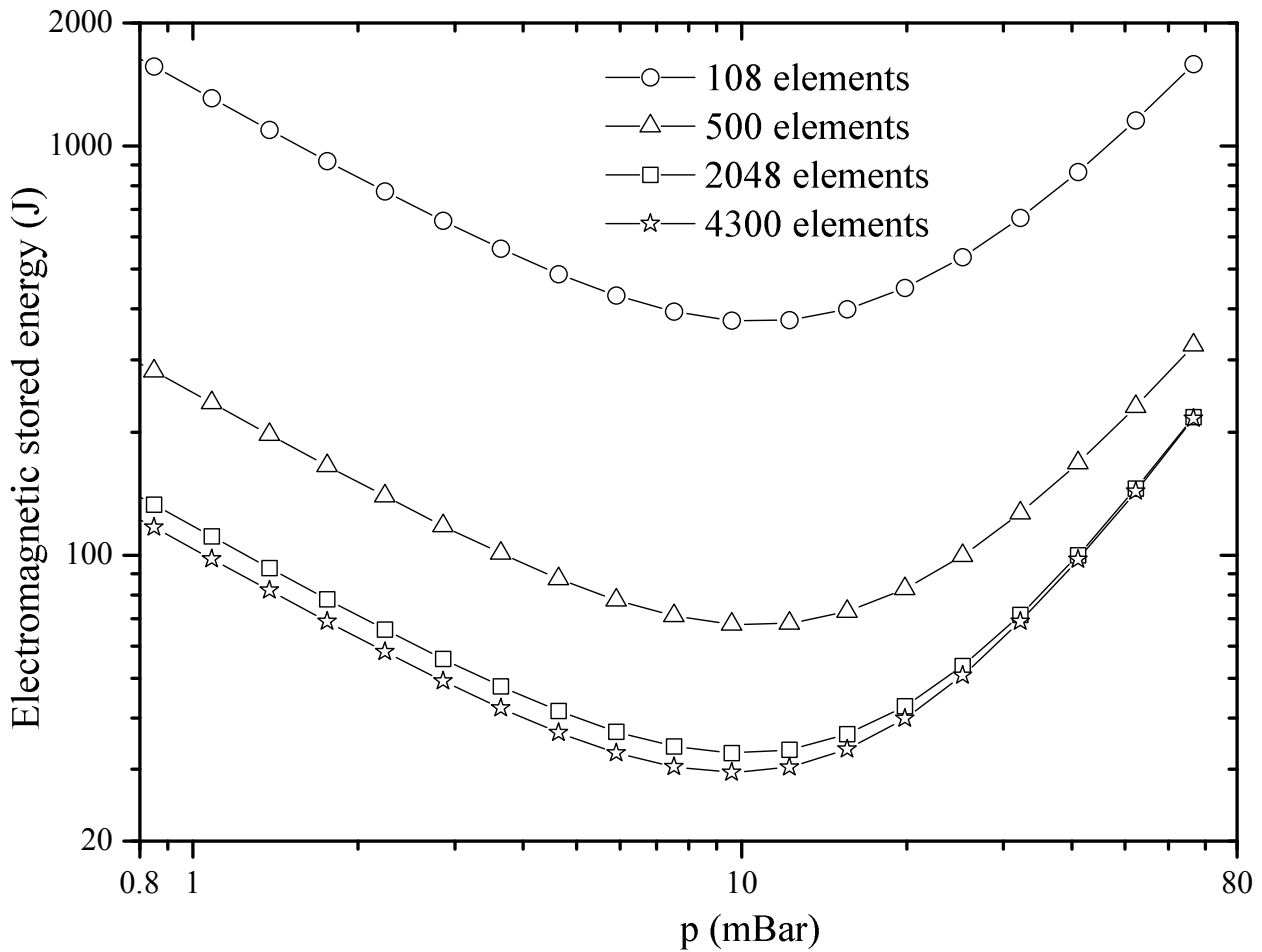


Figure 6.22: Convergence study of the corona breakdown threshold for the second cavity analyzed with Lupan's model.

this case is much smoother than in the previous examples where the minimum breakdown power threshold of the Paschen curve varied quite abruptly as the number of elements increased. This shows that the rectilinear devices present a smoother convergence than the curvilinear ones, which entails a more stable solution of the corona equation for the rectangular cavity with the FEM. The convergence can be clearly established for this structure when using 4300 elements.

Regarding the critical pressure, note in Fig. 6.22 how it lies around 10 mBar as the number of elements increases, what shows a better agreement with the theory than in the case of the circular waveguide. According to (6.17) the critical pressure must lie around 14 mBar, what yields a noticeable discrepancy, though smaller than for the circular waveguide.

In Fig. 6.23 the solution of the corona equation for the first cavity calculated with the different ionization rate models using 4000 elements is represented together with the results exhibited in [Rasch 2009], showing a very good agreement between the different models. The vertical axis shows the maximum value of the effective electric field over pressure within the cavity that induces the microwave gas breakdown. The horizontal axis

shows the pressure in Torr multiplied by the length of the cavity, L , over π . The area where the maximum value of the effective electric field over pressure lies within the range of validity of the ionization rate models as mentioned above, is found between the two horizontal dashed lines drawn in Fig. 6.23. Although the values of the maximum effective electric field over pressure lie within the range of validity for most of the area of the plot, it must be mentioned that there are nodes of the mesh for which the values of the parameter α do not stay within it because the intensity of the electric field is smaller. Let us remind that the plot shows the maximum effective electric field over pressure inside the cavity. Therefore, the solution of the corona equation is found using some values of the electric field for which the ionization rate is not accurately described by the used models.

The percentage of nodes that lie outside the range of validity of the parameter α for the solution of the corona equation in the case of the first cavity are represented in Fig. 6.24. It can be seen that the minimum percentage of non-valid nodes to represent the ionization frequency is placed at the low pressure region, what corresponds to the case when the parameter α , presented in Fig. 6.23, is close to the maximum of the valid range. This occurs because the value of the electric field at any node of the mesh is lower than the one represented in Fig. 6.23, which corresponds to the maximum one inside the rectangular cavity. Thus, when the maximum value of the electric field yields the maximum value of α within the valid range, the amount of nodes within the range of validity is maximal.

The fact that the electric field evaluated at most of the nodes do not accurately represent the ionization rate does not seem to affect much the results comparing our predictions with the results and measurements shown by Rasch. In this example the electric fields evaluated at nodes that yield values of α outside the range of validity result in points below the lower limit of the validity range.

The corona breakdown threshold of the second cavity has been simulated using 4300 elements, and the results are shown in Fig. 6.25 for the three ionization rate models together with the predictions obtained by Rasch. In this case, it can be noticed again the satisfactorily good agreement between the results obtained with the different ionization rate models. Note how the trend of the plot obtained with Woo's model changes at low pressures where the parameter α is outside the range of validity, showing a trend that predicts an increase of the corona threshold above the one predicted with Mayhan's model. This can be expected by recalling that the values of the ionization rate presented by Woo's model are lower than the ones of the other models outside the valid range of α , as it is shown in Fig. 6.4. Therefore, as the ionization frequency is lower, the intensity of the electric field must increase to enhance the electron gain and provoke the corona discharge.

In the second cavity the percentage of nodes outside the range of validity of the parameter α is more or less the same as in the first cavity. In any case, the analysis done for these two rectangular cavities show the best agreement between the different models and the reference among the cases studied before, what reflects the fact that the withstanding corona capability of structures with a smooth electric field profile whose corona breakdown threshold lie within the range of validity of the parameter α for most of the points within the structure can be satisfactorily analyzed with the ionization rate models presented here.

6.5.6 Corona discharge of a monopole antenna

The occurrence of corona discharge for open structures is an important issue for devices like slot or monopole antennas in CW operation as well as for pulsed signals [Chown 1959, Scharfman 1960, Fante 1965a, Fante 1965b, Clavier 1966, Fante 1968, Fante 1969, Fante 1970, Fu 2008]. The presence of the discharge affects the VSWR, the pulse shape of the signal, it modifies the radiation pattern and decreases the radiated power of the antenna, provoking the blackout of the communication system of the air- or the space-craft if the distortion of these

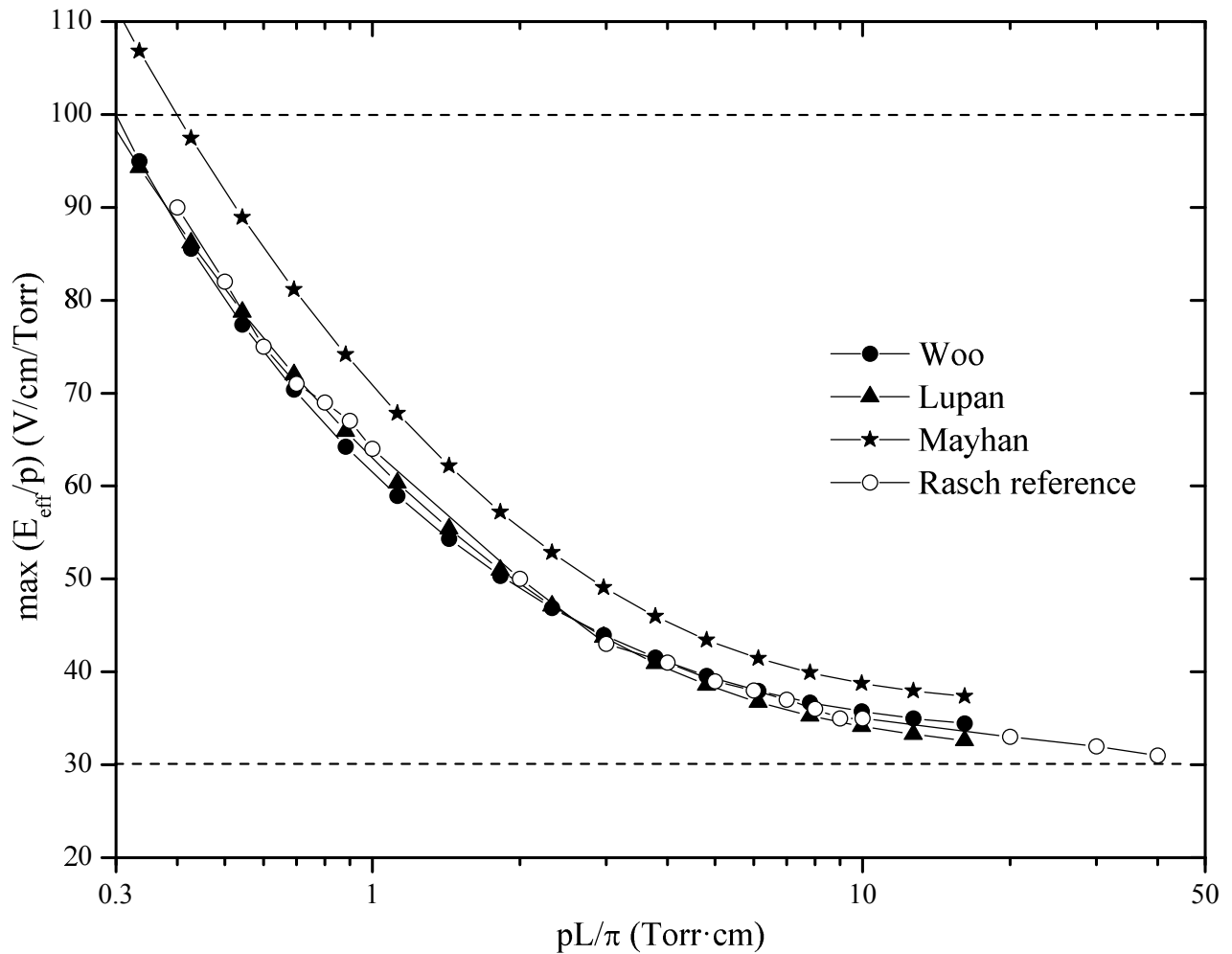


Figure 6.23: Corona electric field breakdown threshold of the first cavity together with the simulations presented in [Rasch 2009]. The dashed lines delimit the range of values of α where the ionization rate models are valid.

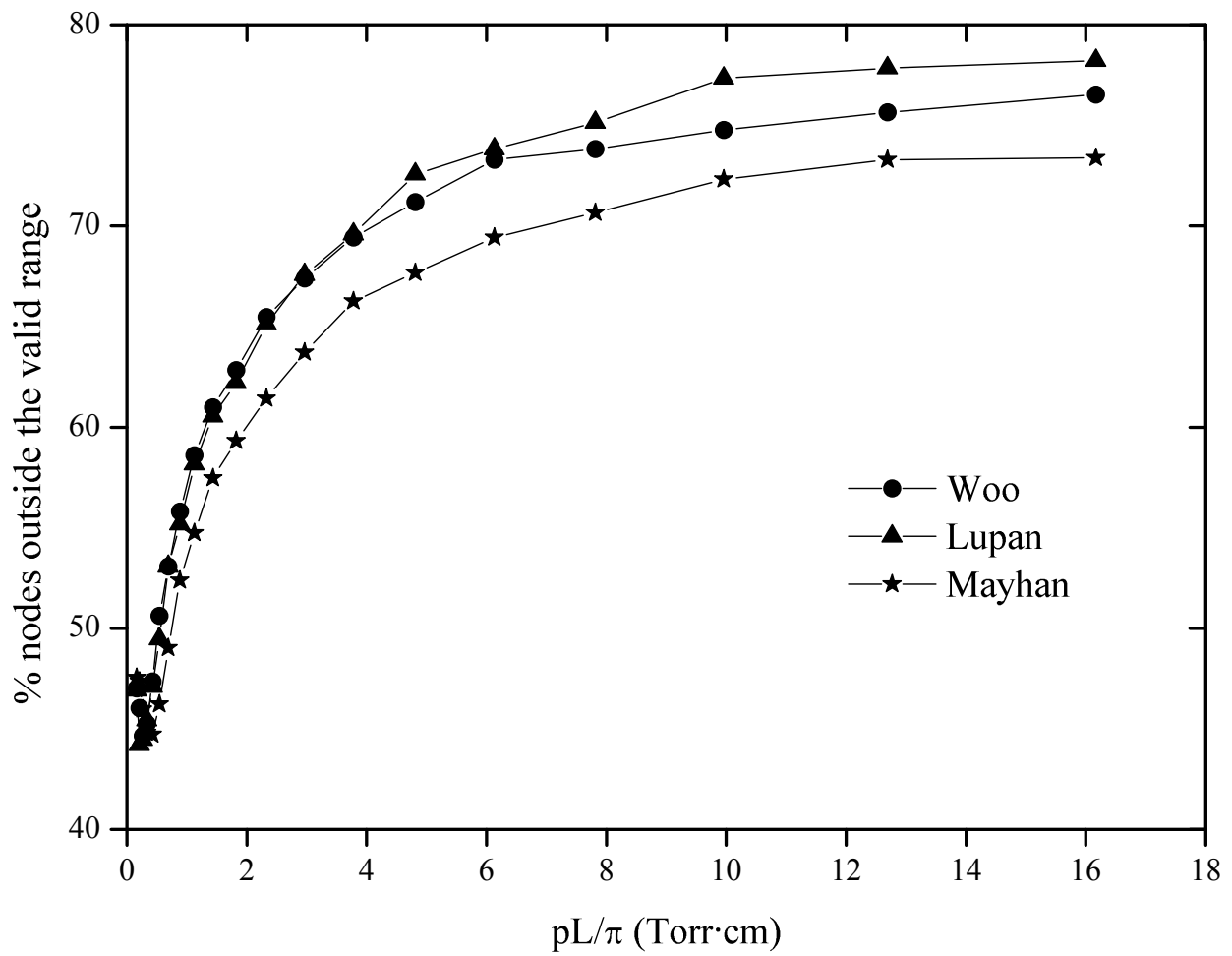


Figure 6.24: Percentage of nodes outside the range of validity of the parameter α for the first cavity presented in [Rasch 2009].

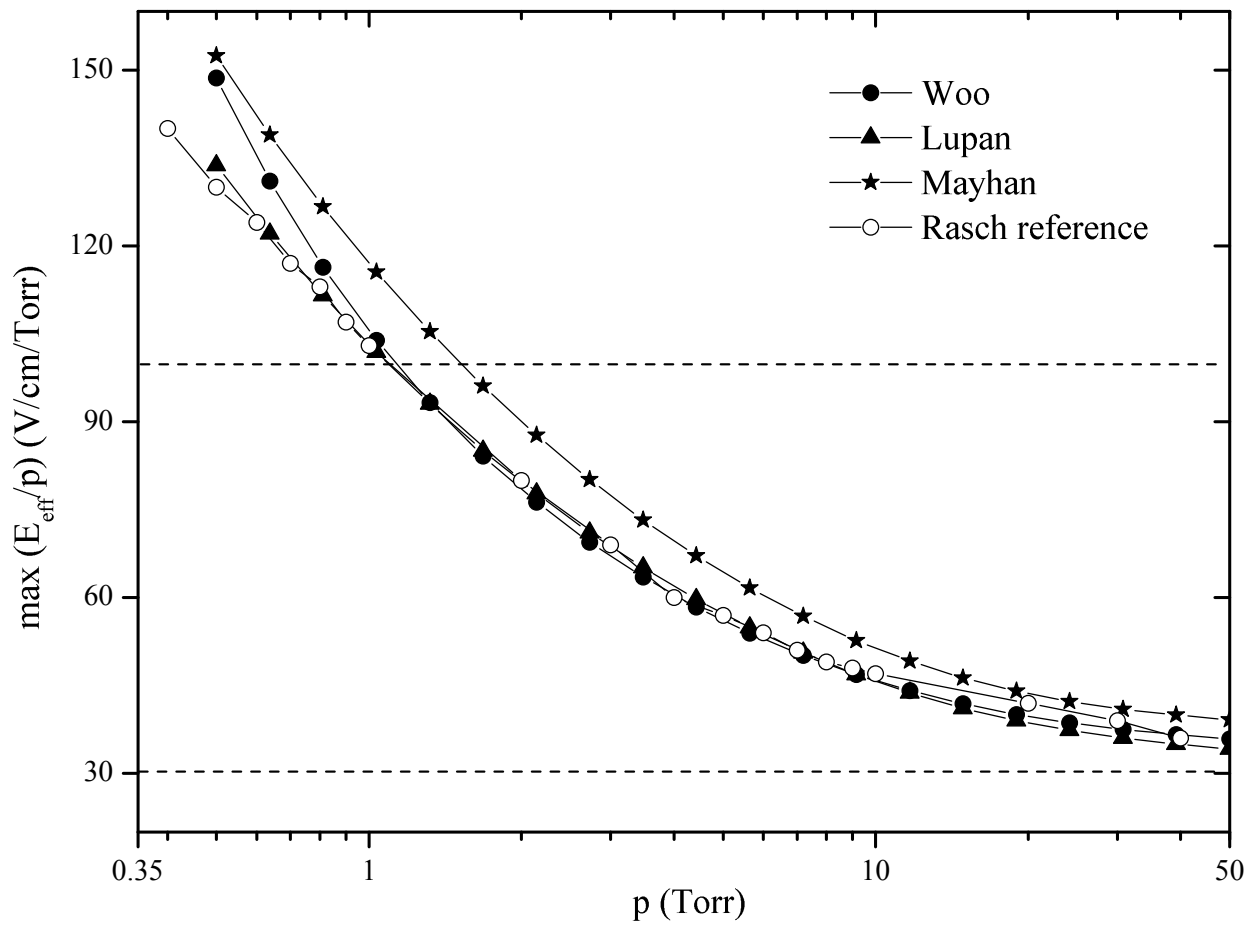


Figure 6.25: Corona electric field breakdown threshold of the second cavity together with the simulations presented in [Rasch 2009]. The dashed lines delimit the range of values of α where the ionization rate models are valid.

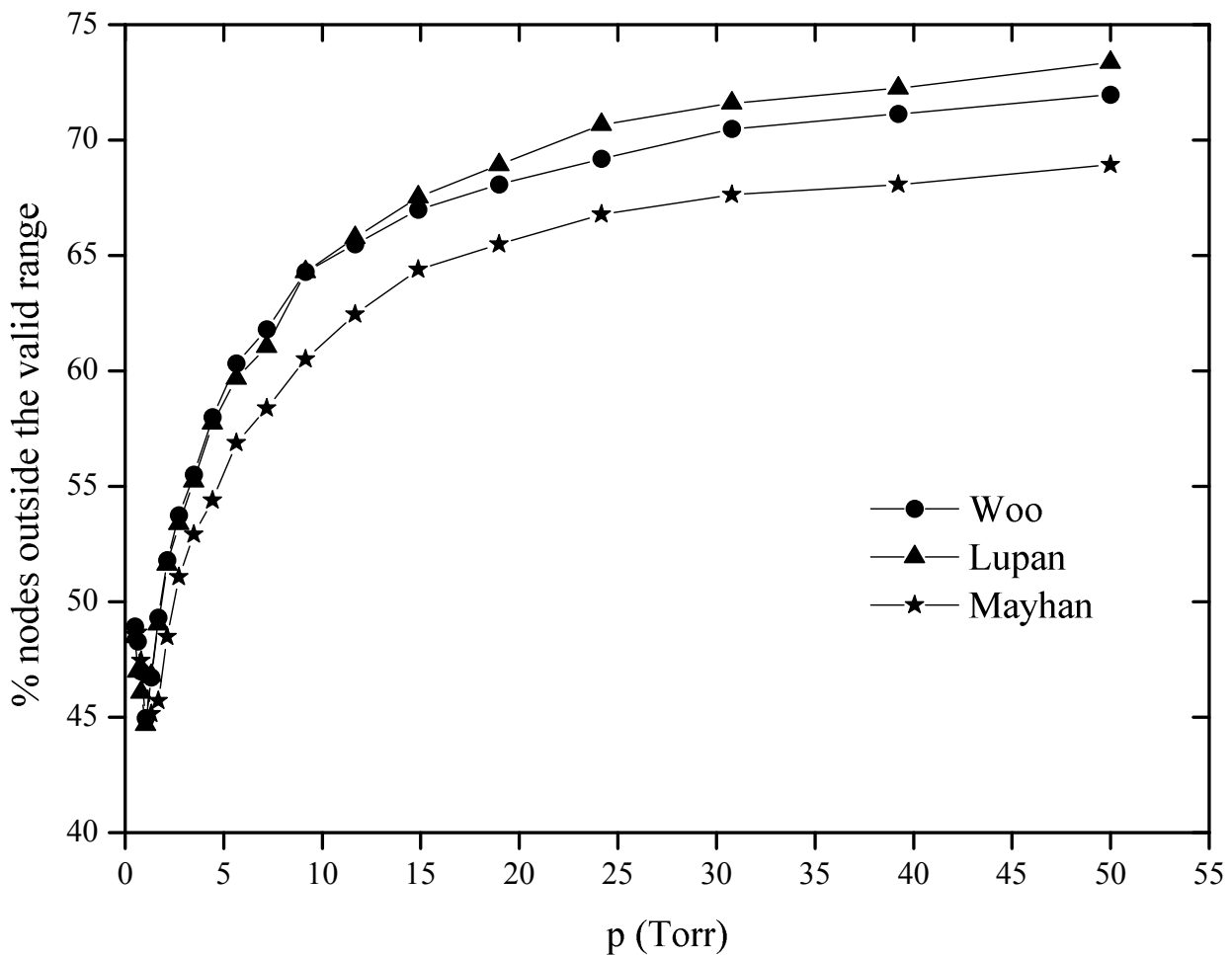


Figure 6.26: Percentage of nodes outside the range of validity of the parameter α for the second cavity presented in [Rasch 2009].

parameters is too severe with respect to the normal functioning of the microwave device.

An example of analysis of the corona discharge for open structures is going to be presented in this section, where the corona withstanding capabilities of a monopole antenna are studied. The open space problem has been approximated by a vertical rod placed in the center of the side of an air-filled box with perfect conductor walls, which encloses the solution domain of the corona equation. The space defined by the metallic box surrounding the monopole has been meshed with tetrahedra and the Dirichlet boundary conditions have been applied on the walls as in the cavity case. The analytical electric field has been evaluated at the nodes of the mesh and imported into the 3D FEM software as input for the ionization rate. This is a good approximation of the real situation when the size of the box is big enough, since the electron population density is negligible far from the source in a realistic scenario when the corona discharge occurs. Furthermore, it has been concluded by other authors that when the electric field is strongly inhomogeneous, the near field is the main responsible of the corona breakdown threshold by the high ionization within a relatively small region near the microwave source and the subsequent outward diffusion of the electrons [Jordan 2006].

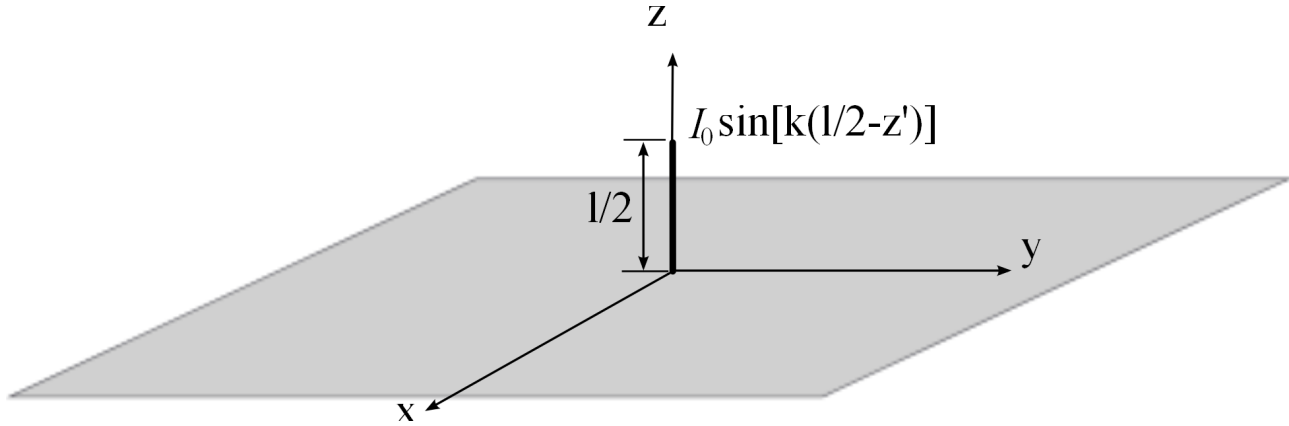


Figure 6.27: Sketch of the monopole antenna of length $l/2$ on a grounded perfect electric conductor.

The simulations of the Paschen curve obtained with the three ionization rate models have been compared with the measurements presented in [Scharfman 1960], where the experimental values of the corona breakdown power threshold of a monopole antenna placed on a grounded perfect electric conductor are presented. The radius of the monopole is $r = 1.5875$ mm, the height $h \equiv l/2 = 0.3$ m, the exciting frequency $f = 240$ MHz and $k = 2\pi f/c$ is the wave-number of the signal. The sketch of the problem is shown in Fig. 6.27, where a harmonic signal driven by a current generator excites the monopole with a current amplitude I_0 , as it can be seen in the drawing.

Applying the image theory, a grounded monopole antenna can be considered as a dipole antenna of double length of that one of a monopole, as depicted in Fig. 6.28a. As the thickness of the monopole antenna satisfies $r < \lambda/200$, the electric field of the monopole can be found analytically at any point of the space, and the components of the electric field are given by [Balanis 1997a]:

$$E_\rho = j \frac{\eta I_0}{4\pi\rho} \left[\left(z - \frac{l}{2} \right) \frac{e^{-jkR_1}}{R_1} + \left(z + \frac{l}{2} \right) \frac{e^{-jkR_2}}{R_2} \right] \quad (6.42a)$$

$$E_z = -j \frac{\eta I_0}{4\pi} \left[\frac{e^{-jkR_1}}{R_1} + \frac{e^{-jkR_2}}{R_2} - 2 \cos\left(\frac{kl}{2}\right) \frac{e^{jkr}}{r} \right] \quad (6.42b)$$

where η is the free-space impedance, and the following variables have been used:

$$r = \sqrt{\rho^2 + z^2}, \quad (6.43a)$$

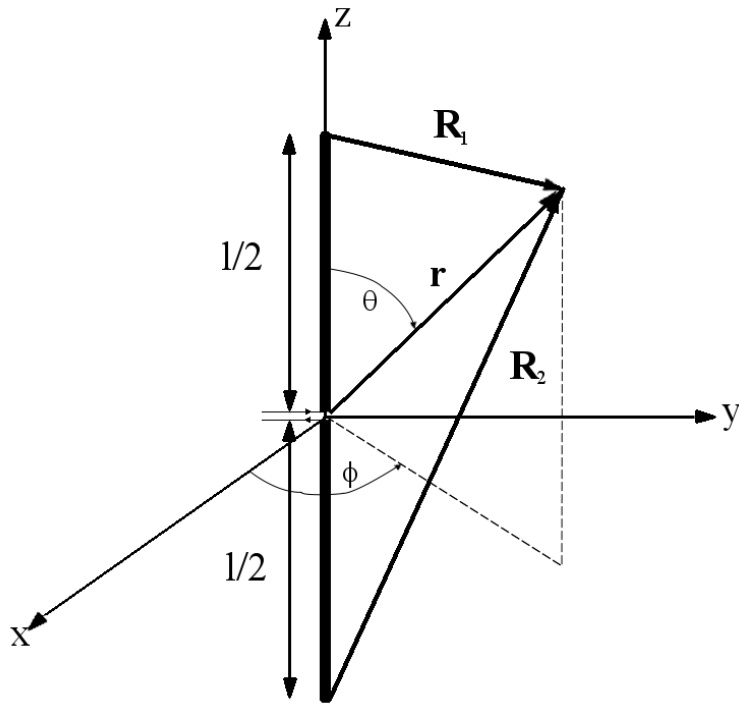
$$R_1 = \sqrt{\rho^2 + \left(z - \frac{l}{2} \right)^2}, \quad (6.43b)$$

$$R_2 = \sqrt{\rho^2 + \left(z + \frac{l}{2} \right)^2}, \quad (6.43c)$$

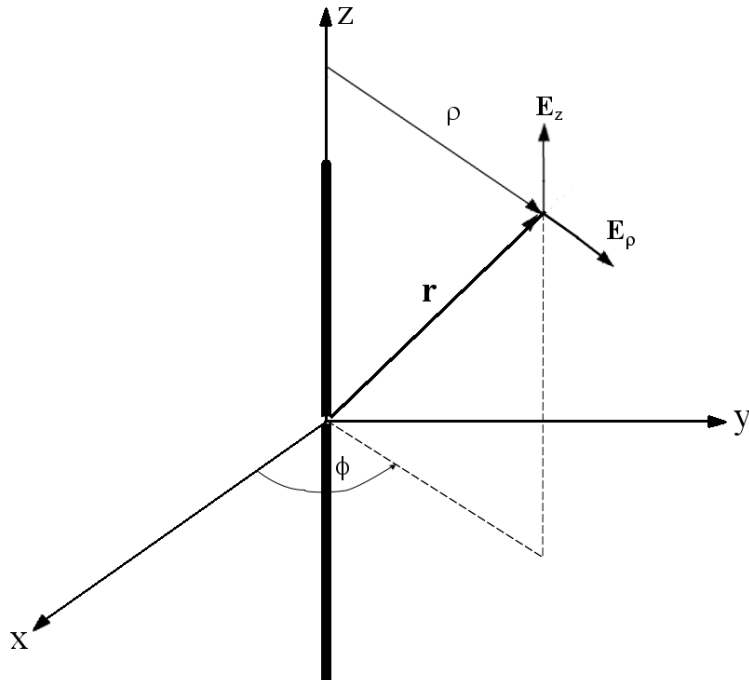
which are depicted in Figs. 6.28a and 6.28b.

The relation between the current amplitude I_0 and the input power of the generator is $P_{in} \approx 32.47|I_0|^2$ for this particular case, as it is calculated in Appendix B. The value of E_{rms} is calculated as

$$E_{rms} = \sqrt{\frac{|E_\rho|^2 + |E_z|^2}{2}}.$$



(a) Dipole antenna as equivalent to a grounded monopole antenna.



(b) Cylindrical coordinates system defined in order to describe the electric field radiated by the antenna.

Figure 6.28: Sketch of the equivalent problem to describe the electromagnetic field of a monopole antenna.

We use the rms values of the electric field evaluated at the nodes of the mesh to solve the corona equation and plot the Paschen curve of the monopole antenna. In Fig. 6.29 the rms value of the electric field is represented on a cross section of a squared cavity of 1 m side-length, where the monopole antenna is enclosed. Note how the electric field profile becomes quite homogeneous near the walls of the cavity. It must be mentioned that the simulations have been done for a cavity of 2 m side-length to guarantee the suitability of the approximation to the open space problem. Furthermore, the simulations have been done with a much finer mesh close to the rod in order to accurately describe the near-field profile of the monopole when solving the corona equation. In Fig. 6.30 an example of the mesh profile on a cross section of a 2 m side-length box is shown around the monopole when using 1259 elements. Note how the mesh is quite fine near the surface of the monopole.

The simulations of the Paschen curve have been done meshing a 2 m side-length squared box surrounding the monopole with 3779 tetrahedra, for which the convergence was attained. The results of the simulations obtained with the three ionization rate models are shown in Fig. 6.31 together with the experimental measurements of Scharfman. In this case we can see that all the ionization rate models predict the same corona breakdown threshold at high pressures, where the microwave discharge is mainly controlled by the attachment rate. Therefore, as the value of the different ionization rates becomes less important as the attachment frequency increases with the pressure, there are not many differences in the results at the high pressure region since the expression of the attachment rate (6.21) is the same for all the models. The experimental values of the corona breakdown power threshold lie, however, far below the predictions obtained with Woo's model. Lupan's and Mayhan's models predict values of the corona breakdown threshold that lie closer to the experimental results.

A possible reason to explain the discrepancies between simulations and results is also that the value of the attachment rate is overestimated, since the simulations predict higher input powers than the experimental results to trigger the discharge. Indeed, if the attachment rate is higher than in the reality, the loss of electrons is overestimated and a more intense electric field is needed to increase the gain of the electron population density by ionization, resulting in an overestimated input power needed to induce the breakdown. On the other hand, a too low ionization frequency may lead to values of the corona breakdown power threshold higher than in the reality, as it occurs with Woo's ionization rate model.

However, the discrepancies between the measurements and the simulations obtained with Mayhan's and Lupan's models are quite reduced at low pressures, and the tendency of the Paschen curve obtained with Woo's model seems to agree better with the experimental measurements at the low pressure region, too. As it was described in the analysis of the circular waveguide, recalling the theory of the corona discharge at very low pressures, it is expected that under these conditions the corona threshold does not depend on the ionization frequency model.

The first source of error that can be remarked in the analysis of the corona breakdown for this problem is due to the mesh of the problem. In fact, the profile of the electric field corresponds to an infinitely thin monopole antenna but the mesh was made around a rod of finite radius. Therefore, the values of the electric field predicted by (6.42) cannot be adequately described for a thick monopole because the maximum electric field on the surface of the rod, which defines the corona withstanding capabilities of the antenna [Jordan 2006], will be smaller than in the reality at $\rho = 0, (0 \leq z \leq l/2)$ for an infinitely thin antenna. Therefore, the actual electric field of a thick monopole evaluated on its surface will be smaller compared to the infinitely thin antenna evaluated at the position of the surface of the thick rod. Then, the approximation that has been done represents the solution of an intermediate problem between the ideal infinitely thin monopole antenna and the actual thick one. Indeed, the experiments show that the corona breakdown power threshold grows as the radius of the monopole augments [Scharfman 1960], since the maximum electric field decreases as the radius of the rod grows. It is thus natural expecting that the simulations obtained using the electric field of an infinitely thin

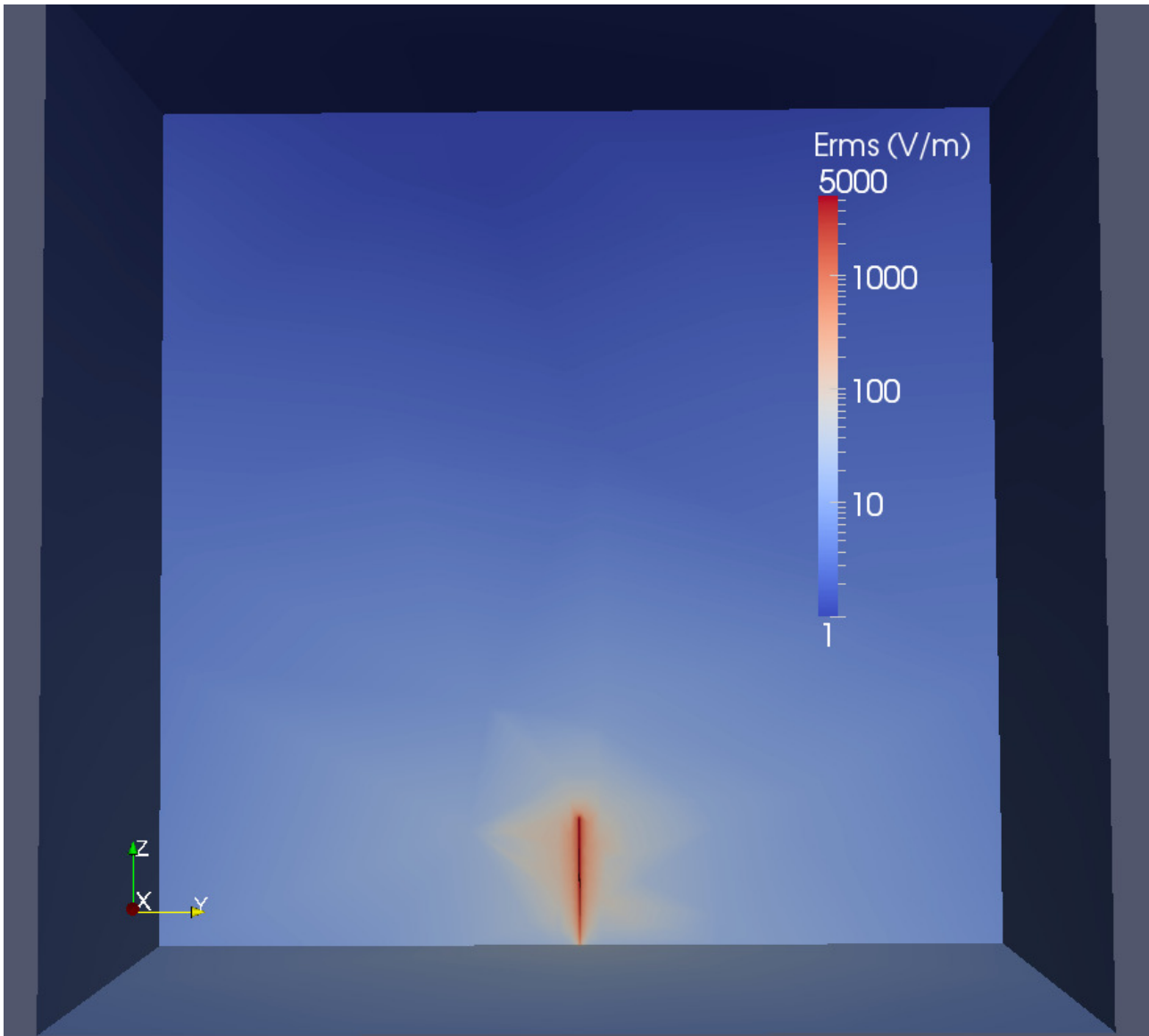


Figure 6.29: Profile of the rms electric field provided by the monopole antenna for 1 W input power. The monopole antenna has been placed within a squared cavity of 1 m side-length.

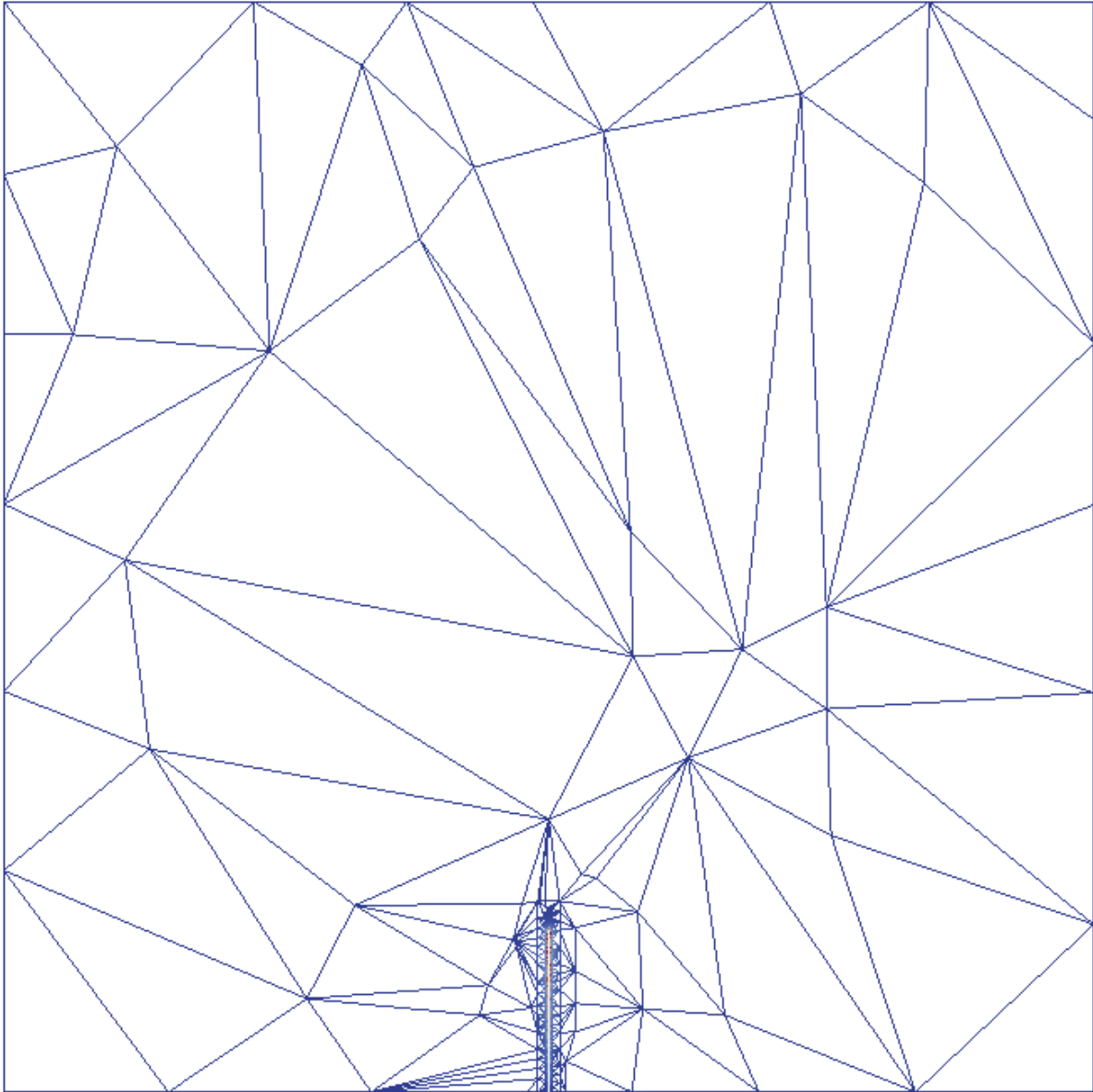


Figure 6.30: Example of the cross-section of the mesh made within a squared box 2 m side-length enclosing the monopole antenna with 1259 elements.

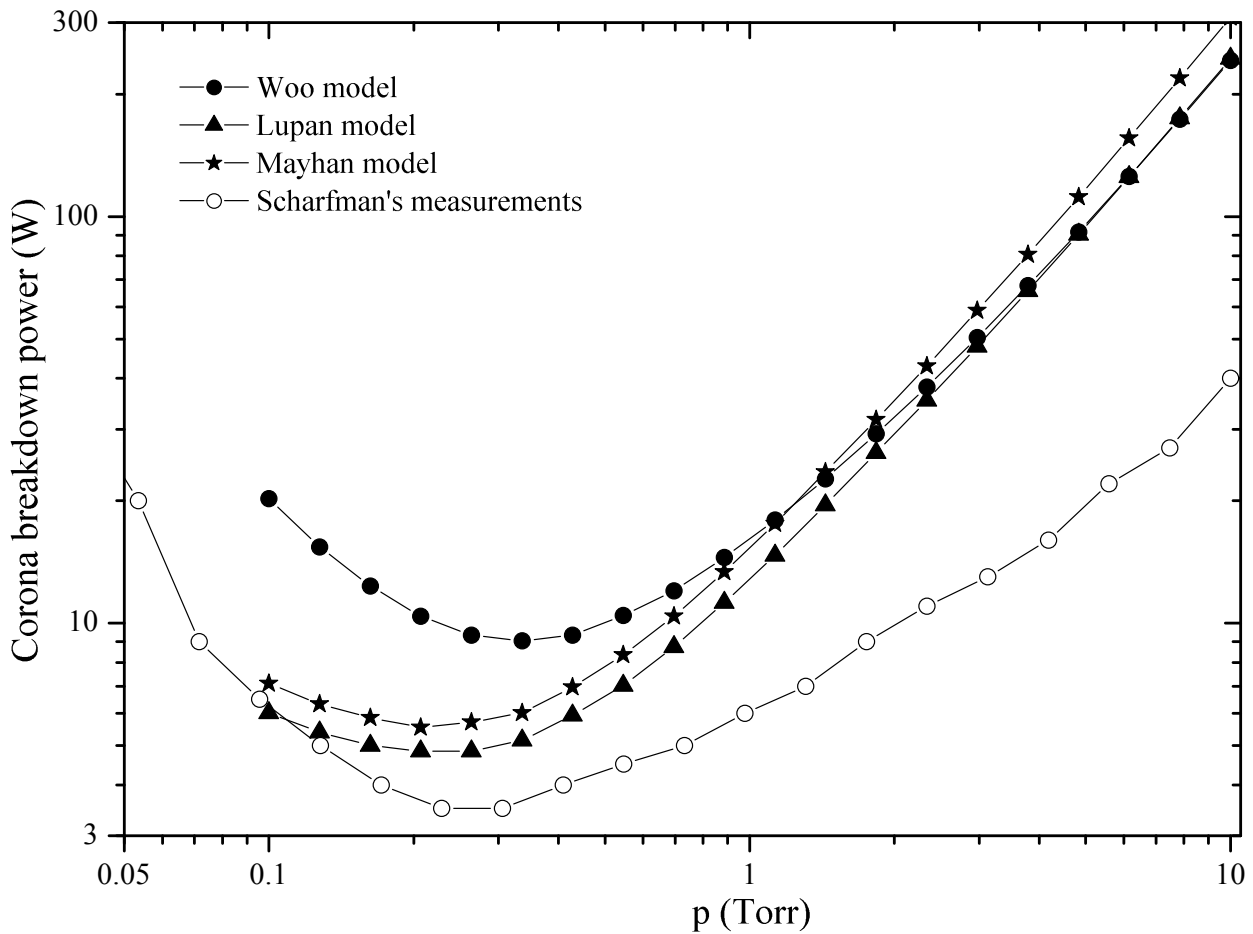


Figure 6.31: The Paschen curve of the monopole antenna obtained with the three ionization rate models presented together with the measurements shown in [Scharfman 1960].

monopole antenna meshing as if there was a thick one lie above the experimental measurements, as shown in Fig. 6.31.

On the other hand, we know that there are many nodes for which the parameter α evaluated at the corresponding power breakdown threshold lie outside the range of validity to suitably define the value of the ionization rate (see Fig. 6.32). This source of error could be considered to contribute to the inaccuracy of the numerical calculation of the corona breakdown power threshold, however, all the models exhibit similar percentages of non-valid nodes whereas their predicted Paschen curves differ noticeably. Furthermore, it has already concluded from the previous examples that the profile of nodes whose parameter α lies outside the range of validity does not have much influence on the solution of the corona equation. It is rather the maximum electric field which determines the critical corona breakdown power threshold.

In order to quantitatively estimate the error in the Paschen curve induced by an inaccurate value of the ionization rate, the plot of the corona breakdown threshold vs. pressure has been plotted in Fig. 6.33 for Woo's ionization rate model modifying the ionization frequency by $\pm 20\%$. This is the relative error that the author of this model claims to exist between both extremes of the valid range of α where this model is supposed to be

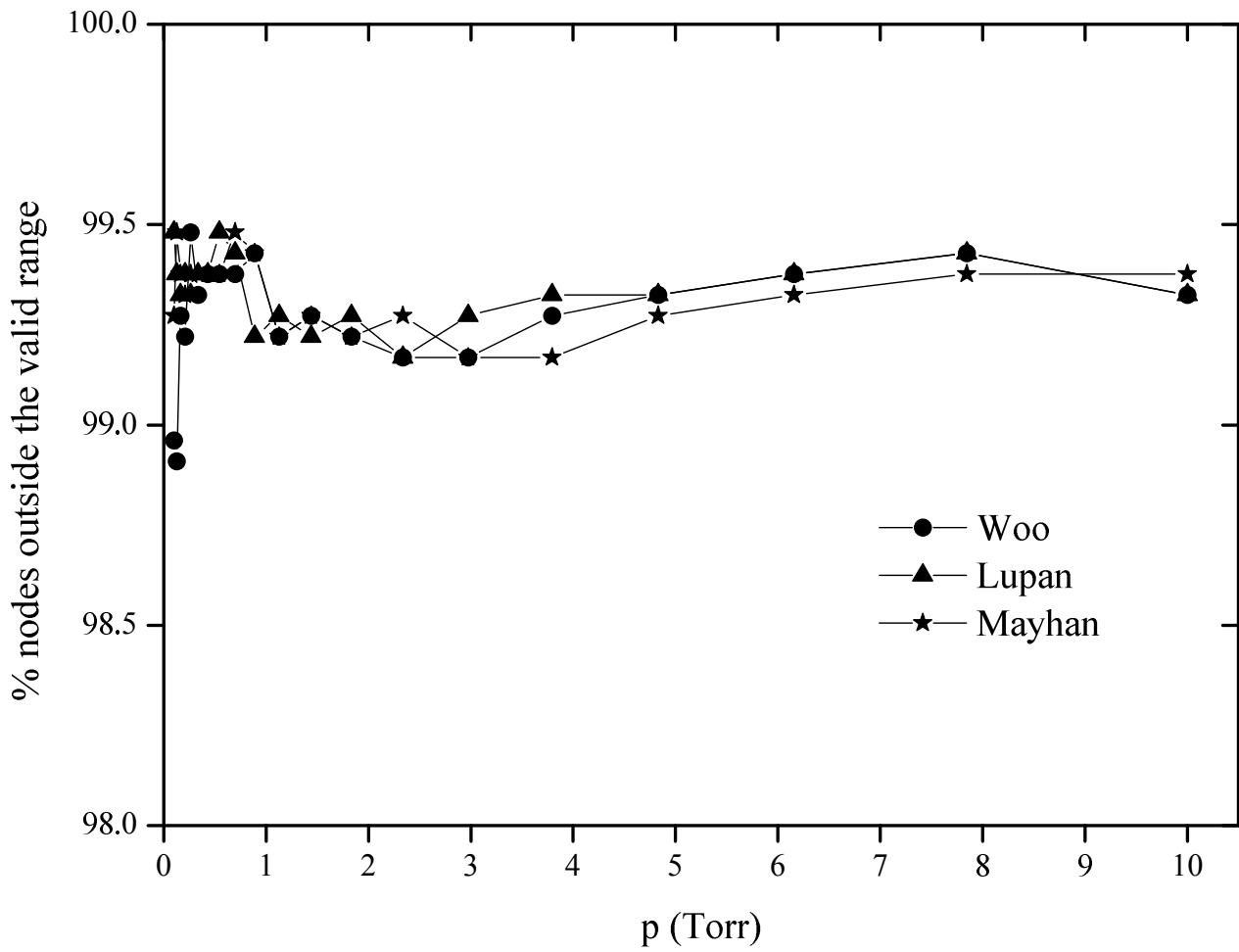


Figure 6.32: Percentage of nodes outside the range of validity of the parameter α to accurately represent the ionization rate of the models presented.

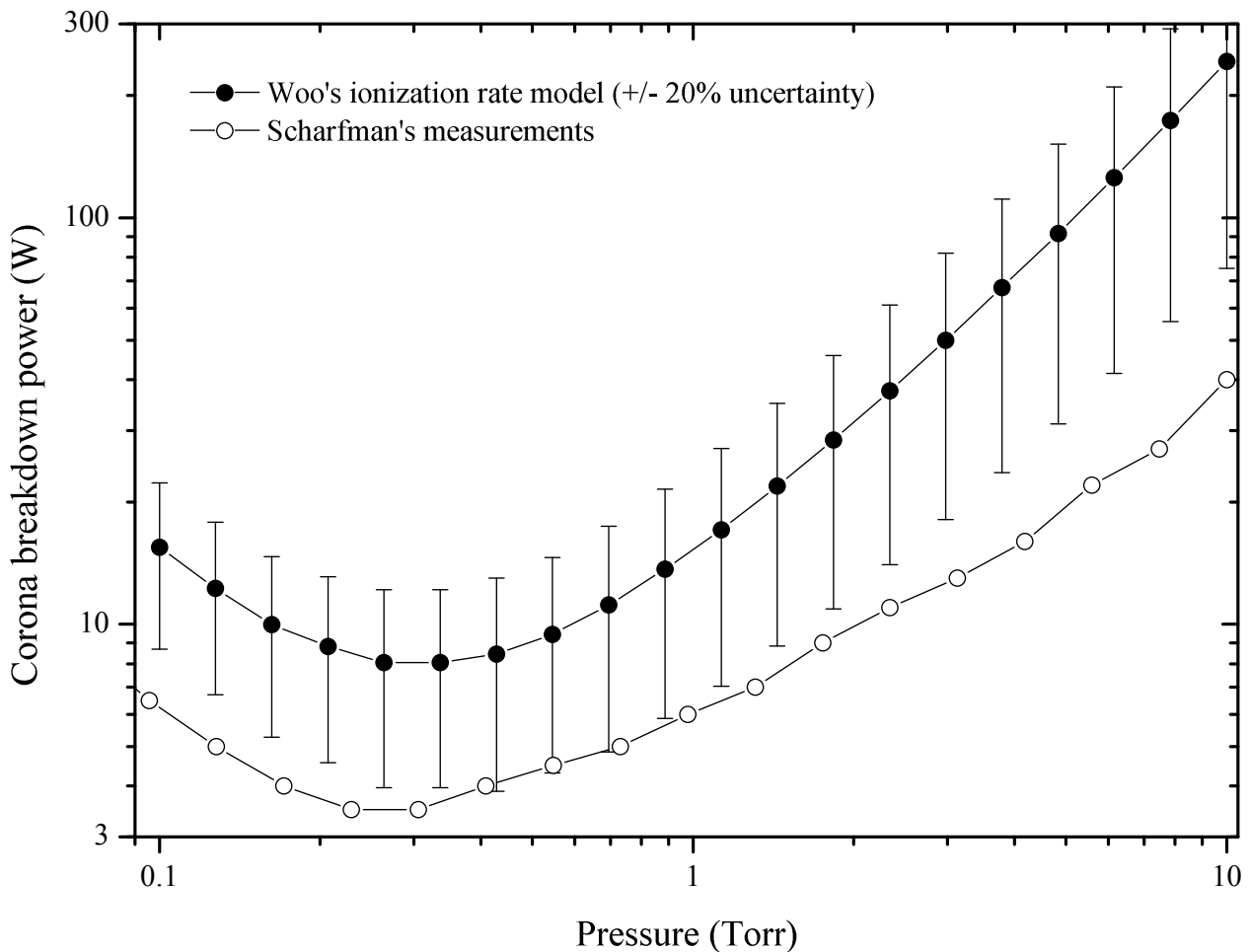


Figure 6.33: The Paschen curve obtained with Woo's model for the ionization rate modified by $\pm 20\%$.

accurate enough [Woo 1984]. It can be clearly seen that the Paschen curve obtained with only 0.2 times a higher value of the ionization rate shows a corona breakdown threshold that approaches remarkably the experimental results. As it is shown in Fig. 6.4, the ionization frequency of Woo's model outside the range of validity is smaller than for the other two, this is the reason why the consideration of an ionization rate 20% higher predicts a Paschen curve that lies close to the one obtained with the other models of ionization.

The plot shows that a value of the ionization rate modified by 20% can lead to differences in predicted corona breakdown threshold above +3dB. For instance, at the high pressure region of Fig. 6.33, the two last points of the curve show that the breakdown power threshold can vary from around 60 W to almost 200 W and from around 75 W to around 230 W, respectively. Taking into account the fact that $\pm 20\%$ is the relative error of the ionization rate for Woo's model within the range of validity, the error in the value of the ionization frequency outside the range of validity is expected to be larger. Therefore, the prediction of the Paschen curve with an accurate model of the ionization frequency should be able to retrieve the experimental results of the corona breakdown threshold obtained by Scharfman for the monopole antenna.

To finish the study of the microwave gas breakdown for the monopole antenna the maximum effective electric field corresponding to the corona breakdown power threshold evaluated at the surface of the monopole is calculated. The results are compared with the experimental results shown in [Scharfman 1960] and plotted in Fig. 6.34 vs. the pressure (Torr) times the radius of the antenna (cm). The experimental data, represented by circles in the plot, correspond to the average of the corona breakdown threshold obtained for many monopoles of different dimensions collected by the author. His goal was to find a scaling law applicable to any monopole antenna regardless its height and radius. And it seems that the scaling law that he found is satisfactorily represented by the results obtained in our simulations with Woo's ionization rate model at any pressure. Therefore, although the Paschen curve obtained with Woo's model of ionization differs from the experimental measurements noticeably, the average corona breakdown threshold obtained for many monopole antennas seems to be better described by Woo's model of ionization. In any case the other models of ionization do not differ much from the experimental values mostly at the high pressure region, or for thick monopoles.

Nevertheless, it has been observed experimentally that the corona breakdown power threshold is subject to a source of fluctuations [Mitani 1957, Jordan 2006], which could be due to the presence of impurities in the gas, changes in the humidity conditions, contamination, etc. and lead to a spread in the experimental values of the microwave gas discharge threshold that requests a statistical post-processing of the data.

6.6 Summary

The analysis of the corona breakdown threshold has been studied by solving the corona equation at different pressures using the FEM for three different ionization rate models found in the literature. The Paschen curve predicted by the three models have been plotted for different devices and there have been found some discrepancies between the different predictions. The results obtained with Woo's and Lupan's models for the coaxial cable and the circular waveguide were similar to measurements and simulations obtained by another method, respectively. Mayhan's model always predicted the lowest corona breakdown power threshold.

It seems, then, that Mayhan's model exhibits a value of the ionization frequency that is too small to suitably describe the corona discharge. The results presented by Woo's model exhibited the highest breakdown power threshold in every example, as it is natural since it defines the lowest ionization rate in most of the domain of the parameter α . In any case Woo's model predicted quite accurately the experimental corona threshold, except at high pressures, where a slightly higher ionization frequency would be required to better fit the measurements.

The simulations of the corona withstanding capabilities made for the coaxial and the circular waveguides have been done with the analytical values and the numerical calculation of the electric field. The convergence of the critical corona threshold when the electric field was analytical was attained using less elements than for the numerical approximations of the electric field.

A result that could not be explained was the remarkable discrepancy between the predicted critical pressure obtained by the simulations for the circular cavity at $f = 10$ GHz with any ionization rate model, and the theoretical value predicted by (6.17). Moreover, the discrepancy extends as well to the critical pressure predicted by [Tomala 2005], which was quite close to the results obtained with our simulations and far from the value predicted by the transport theory of electrons in gases.

For the three-dimensional cases the simulations done for the two rectangular cavities showed satisfactory agreement between the corona breakdown threshold predicted by the different ionization models when the values of the effective electric field over pressure did not exceed much the top of the range of validity of α . It seems that the withstanding corona capability of structures with smooth electric field profiles whose corona

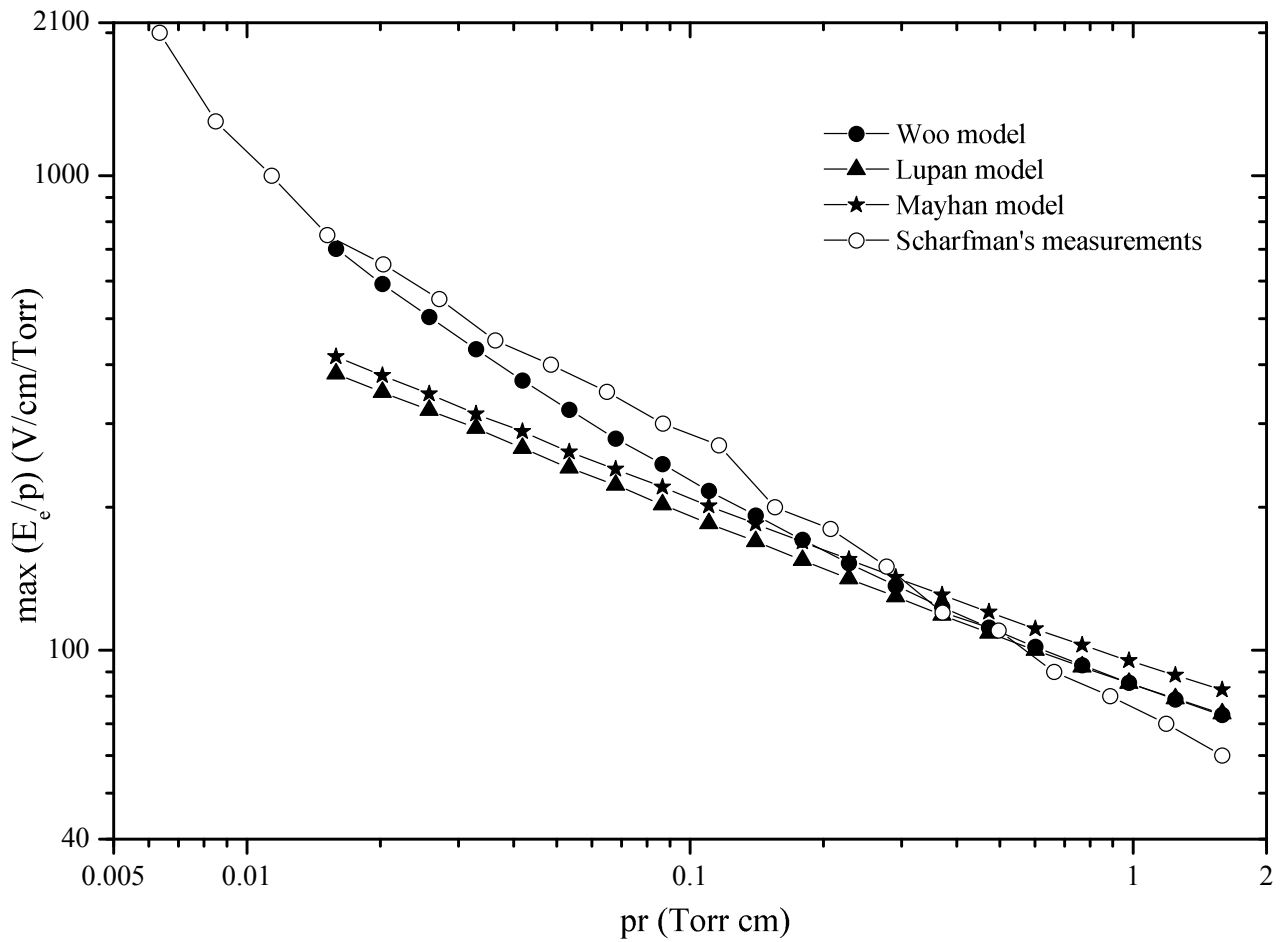


Figure 6.34: The maximum value of the effective electric field over pressure plotted vs. pr where r is the monopole radius.

breakdown electric field threshold lies within the range of validity of the parameter α , can be satisfactorily analyzed with the ionization rate models presented here. However, the constraints in the specifications of the microwave devices used for space applications do not necessarily fulfill those conditions, what obliges us to search a more general ionization rate model capable to suitably prognosticate the corona breakdown threshold of the device under more general conditions. Nevertheless, a small deviation in the corona electric field breakdown entails a larger inaccuracy in the calculation of the corona power breakdown threshold, since the power is proportional to the square of the electric field, and the relative error propagates by a factor of two.

For the antenna monopole it must be remarked that open-structure problems can also be satisfactorily analyzed by solving the equivalent problem of enclosing the microwave device within a sufficiently big perfect electric conductor box, as long as the size is big enough as to suitably represent the diffusion of the electrons. A fine mesh near the electromagnetic source is also needed so that the maximum electric field of the structure, responsible of the maximum ionization frequency, is suitably represented, and the corona breakdown threshold accurately calculated. However, the convenience of modeling a finite thickness monopole with the electric field expressions of an infinitely thin one was questioned at high pressures, since the maximum electric field of a thin monopole is higher than the one of a thick monopole antenna. Therefore, the predictions of the corona breakdown power threshold obtained when modeling the problem with a thick monopole lie naturally above the experimental measurements since the maximum electric field is lower than what would correspond to a real thin monopole. The influence of the accurate value of the ionization and attachment rates was also analyzed, showing the importance of a universal expression for these parameters, essential in the calculation of the Paschen curve. Nevertheless, the scaling law of the corona withstanding capabilities proposed by Scharfman was verified by comparing the results obtained in our simulations with the measurements performed by the author, showing especially a satisfactory agreement with the predictions obtained with Woo's model.

Finally, it is worthwhile to mention the future possibility of analyzing the corona discharge for structures with dielectrics using the FEM to solve the corona equation. Although the corona discharge has not been studied here for structures with dielectrics, it may be interesting to analyze devices like the parallel-plate waveguide with a dielectric slab placed on one of the conductors. This study may result important for design purposes if the corona withstanding capabilities of such a device enhances its functioning, increasing its working power without the risk of corona breakdown. To the best of our knowledge this case has not been studied in literature because the diffusion problem within a dielectric for the corona discharge still remains an open problem for microwave frequencies. Perhaps in the future the physics of the problem can be described and solved applying the numerical technique shown in this chapter.

The convergence analysis will be recalled when designing microwave devices of circular or coaxial geometry as it is the case for the new coaxial connector presented in Chapter 7. The implemented FEM tool will also be used for the optimization of the corona breakdown withstanding capabilities of the new connector studying the different ionization models.

Power Sub-miniature connector

Contents

7.1 Motivation	161
7.1.1 Coaxial connector parameters	162
7.1.2 Coaxial connector series	162
7.1.3 Space applications	164
7.2 Guidelines	166
7.2.1 Multipactor guidelines	166
7.2.2 Corona guidelines	168
7.2.3 Outgassing and venting	170
7.3 PSM design	171
7.4 High power analysis	172
7.4.1 Multipactor analysis	172
7.4.2 Corona analysis	173
7.5 Test results	173
7.5.1 Low power performance	176
7.5.2 High power performance	176
7.5.3 Multipactor tests	176
7.5.4 Corona tests	178
7.6 Discrepancies	181
7.7 Summary	182

7.1 Motivation

Microwave coaxial connectors are essential in the radio spectrum, since they are often used to connect two units such as the antenna to a transmission line, a receiver or a transmitter. The mechanical stability, the excellent electromagnetic shielding and the good thermal handling capabilities, make coaxial connectors the best candidates for connecting different microwave devices within the payload of satellites for high power applications. On the other hand, printed circuit technology is omnipresent in the RF front-ends of modern communication systems. Their small size and low weight make them very attractive for space applications. In the recent years, printed circuits have therefore also conquered the space market. A common way to feed these circuits is the use of coaxial cables and coaxial connectors. With the advent of Solid State Power Amplifiers (SSPAs), printed circuits became also attractive for the output stages of high-power transmitters on board of

satellites. Formerly, this task was reserved to much heavier Traveling Wave Tubes Amplifiers (TWTAs), and therefore, standard waveguide technology had to be used in this part of the system.

Coaxial cable connectors, often called RF connectors, are in widespread use. Wherever radio frequency or RF connections need to be made there is the possibility of using coaxial connectors. Where signals reach frequencies above a few million Hertz, these coaxial connectors need to be used. The need for their use arises because it is necessary to transfer radio frequency energy from one place to another using a transmission line. The most convenient and hence, the most commonly used form of transmission line, is the coaxial cable, which consists of two concentric conductors, the inner and the outer conductors, being the latter often called screen. Between these two conductors there is an insulating dielectric. There is a variety of connectors that are used for RF applications. Impedance, frequency range, power handling, physical size and a number of other parameters, including cost, will determine the best type for a given application.

7.1.1 Coaxial connector parameters

To properly select a coaxial connector one must firstly know the frequency of operation, characteristic impedance, insertion loss and power handling capability. Other considerations are the application, environmental considerations, mechanical dimensions and durability, finish and cost. The impedance of coaxial connectors is very important to prevent VSWR mismatches. All RF coaxial connectors are designed to have low VSWR (typically 1.1:1 or better) and very low insertion loss (<0.05 typical and 0.1 dB maximum) over a large bandwidth with a minimum of variations. Power handling is a function of the diameter of the dielectric, the thermal properties of the dielectric material used internally, and the size of the center pin. As with transmission lines, the higher the frequency, the higher the VSWR mismatch and insertion loss and the lower the power handling capability of the connector. Before selecting a connector, it is important to know the application and whether it will be used once or inserted numerous times, or whether it is going to be used outside and need to be weatherproof. The mechanical dimensions are also important and are a function of the connector series. The finish and plating are also important. Most connectors use some form of nickel plating, but some of the more expensive types are silver or gold plated. Finally, connector interfaces may be threaded, bayonet, snap-on or push-on. Furthermore, the optimum connector is not always possible so tradeoffs are often necessary.

7.1.2 Coaxial connector series

Coaxial connectors are usually referred to by series designations. Fortunately, although there are thousands of different coaxial connectors on the market, there are only about a dozen or so groupings or series designations. Each has its own important characteristics, and the most popular RF coaxial connector series are N, BNC, TNC, SMA, SMB, SMC, UHF and 7-16 DIN.

7.1.2.1 N-TYPE

The N-type connector is a high performance RF coaxial connector used in many RF applications. This coaxial connector was designed by Paul Neill of Bell Laboratories, and it gained its name from the first letter of his surname. This RF connector has a threaded coupling interface to ensure that it mates correctly. It is available in either 50 Ohm or 75 Ohm versions. These two versions have subtle mechanical differences which do not allow the two types to mate. The connector is able to withstand relatively high powers compared to the BNC or TNC connectors. The standard versions are specified for operation up to 11 GHz, although precision versions are available for operation up to 18 GHz. The N-type coaxial connector is used for many radio frequency

applications including broadcast and communications equipment, since its power handling capability is good enough as to be used for medium power transmitters, however it is also used for many receivers and general RF applications.

7.1.2.2 BNC

The BNC coax connector is widely used in applications being used on most oscilloscopes and many other laboratory instruments. The BNC connector is also largely used when RF connections need to be made. The BNC connector has a bayonet fixing to prevent accidental disconnection while being easy to disconnect when necessary. This RF connector was developed in the late 1940s and it gains its name from a combination of the fact that it has a bayonet fixing and from the names of the designers, the letters BNC standing for Bayonet Neill Concelman. In fact the BNC connector is essentially a miniature version of the C connector which was a bayonet version of the N-type connector. Electrically the BNC coax cable connector is designed to present a constant impedance and it is most common in its 50 Ohm version, although 75 Ohm ones can be also obtained. It is recommended for operation at frequencies up to 4 GHz, and it can be used up to 10 GHz provided the special top quality versions specified to that frequency.

7.1.2.3 TNC

The TNC connector is very similar to the BNC connector. The main difference is that it has a screw fitting instead of the bayonet one. The TNC connector was developed originally to overcome problems during vibration. As the bayonet fixing moved slightly there were small changes to the resistance of the connections and this introduced noise. To solve the problem a screw fixing was used and the TNC coax cable connector gains its name from the words Threaded Neill Concelman. Like the BNC connector, the TNC connector has constant impedance, and in view of the threaded connection, its frequency limit can be extended. Most TNC connectors are specified to 11 GHz, and some may be able to operate to 18 GHz.

7.1.2.4 SMA

This sub-miniature RF coaxial cable connector takes its name from the words Sub-Miniature A connector. It finds many applications for providing connectivity for RF assemblies within equipments. It is often used for providing RF connectivity between boards, and many microwave components including filters, attenuators, mixers and oscillators use SMA connectors. The connectors have a threaded outer coupling interface that has a hexagonal shape, allowing it to be tightened with a spanner. Special torque spanners are available to enable them to be tightened to the correct tightness, allowing a good connection to be made without over-tightening them. The SMA connector was originally designed in the 1960s for use with 141 semi-rigid coax cable. Here the center of the coaxial cable forms the center pin for the connection, removing the necessity for a transition between the coaxial center conductor and a special connector center pin. However, its use extended to other flexible cables and connectors with center pins were introduced. SMA connectors are regularly used for frequencies well into the microwave region, and some versions may be used at frequencies up to 26.5 GHz. For flexible cables, the frequency limit is normally determined by the cable and not by the connector.

7.1.2.5 SMB

The SMB connector derives its name as it is termed a Sub-Miniature B connector. It was developed as a result of the need for a connector that was able to connect and disconnect swiftly. It does not require nuts to be tightened when two connectors are mated. Instead the connectors are brought together and they snap fit together. Additionally, the connector utilizes an inner contact and overlapping dielectric insulator structures to ensure a good connectivity and a constant impedance. SMB coaxial connectors perform well under moderate vibration only and the 50 Ohm versions are often specified to 4 GHz. 75 Ohm versions of the SMB coaxial connector are also available, but they are often not specified for the same frequencies, often only up to 2 GHz. SMB coaxial connectors are not as widely used as their SMA counterparts. They are used for inter-board or assembly connections within equipment, although they are not widely used for purchased microwave assemblies in view of their inferior performance.

7.1.2.6 SMC

A third SM type connector is not surprisingly the Sub Miniature C or SMC coaxial cable connector. It is similar to the SMB connector, but it uses a threaded coupling interface rather than the snap-on connection. This provides a far superior interface for the connection and as a result, SMC coaxial cable connectors are normally specified to operate at frequencies up to 10 GHz. SMC coaxial cable connectors provide a good combination of small size and good performance. They may also be used in environments where vibration is anticipated. In view of their performance they find applications in microwave equipment, although they are normally not used for military applications where SMA connectors tend to be preferred.

7.1.2.7 UHF

The UHF connector, also sometimes known as the Amphenol coaxial connector was designed in the 1930s by a designer of the Amphenol company for use in the radio industry. These coaxial connectors have a threaded coupling, and this prevents them from being removed accidentally. It also enables them to be tightened sufficiently to ensure a good low resistance connection to be made between the two halves. The drawback of the UHF is that it has a non-constant impedance, what limits their use to frequencies of up to 300 MHz. However, despite this disadvantage, UHF connectors are cheap and suitable for many applications, provided that the frequencies do not rise. In view of their non-constant impedance, these connectors are now rarely used for many professional applications, being generally limited to Citizen's Band (CB), amateur radio and some video and public address systems.

7.1.2.8 7-16 DIN

7-16 DIN connectors were only recently developed in Europe. Hence the part number represents the size in millimetres and DIN specifications. This connector series was primarily designed for high power applications where low intermodulation is important, such as locations where multiple high power transmitters and antennas are placed (like cellular poles). It is much more expensive than most other connector types.

7.1.3 Space applications

Concerning power handling, when power levels exceed 10 W in space applications one is forced to use the heavy and bulky TNC connectors. Thus, TNC connectors are usually utilized in payloads for space applications,

substituting the much lighter Sub-miniature-A (SMA) connectors, when the RF power is above a few Watts. SMA connectors are only used in low level power applications. However, in the middle power range, there is no suitable connector with the right balance between power handling, mass and size. In this case, the RF designer has to make a conservative decision by using TNC connectors instead of SMA to handle the power delivered by the amplifiers. The larger size of the TNC connectors implies an unnecessary over-sizing of other components, which, together with the higher mass of the TNC connector, results in a relatively high mass of the equipment and RF harness. The existence of a lighter connector with, at least, the same power withstanding capability as the one of TNC connectors would decrease significantly the monetary and environmental cost of many space missions ensuring the functioning of the microwave devices onboard satellites.

For this, the design of a new coaxial connector was developed within the framework of the ESA project: “High power SMA connectors” AO/1-5363/07/NL/GLC, where EPFL, Technische Universität Darmstadt (TUD) and the company Huber+Suhner collaborated together to optimize the mechanical, as well as the thermodynamic and the electromagnetic properties of a new coaxial connector. The project was aimed at the development of a new family of high power SMA connectors for space use capable to withstand power levels up to 50W CW to match the levels delivered by the new generation of SSPAs on board of future telecommunication payloads. The envisioned frequencies were within the L-, C- and Ku- bands, and the connector had to be able to handle, at least, 50W CW and 200W at 2% duty cycle to cover multi-carrier effects.

The activity was also intended to realize a connector with a mass reduction of around 40% compared to the standard TNC connector with an overall size equivalent to the standard SMA. The plan was targeted to any space mission and particularly to GEO mobile missions due to the large amount of these connectors used in their payloads. The new SMA-like connector is named Power Sub-miniature (PSM), which was designed manufactured and tested successfully according to the requested specifications established in the Statement of Work (SoW) along the project. The requested high power features of the connector are summarized in Table 7.1, though security margins are always applied for space applications. Thus, the corona and multipactor breakdown tests under continuous wave signals will be made applying an input power 3 dB above the values specified in the SoW, and a security margin of +6 dB will be applied when testing the multipactor withstanding capabilities of the PSM for pulsed signals.

In this chapter the concept and design of the newly developed high power PSM connector will be presented, experimental tests shown and comparison with other available space grade connectors will be done. The PSM connector has the size and the mass of the standard SMA connector but in terms of power handling comes close to or even exceeds the performance of TNC connectors, as it will be shown later. To achieve the ambitious goals of the project, first suitable theories of corona discharge, multipactor and thermal heating in coaxial structures had to be established or adapted from known similar problems. Second, the power limiting effects in SMA connectors like the internal air gap and all the thermal issues had to be identified and eliminated by appropriate changes of the connector design. Third, suitable materials for the individual parts and the manufacturing process of the new high power PSM connectors must be analyzed and selected.

In order to show the design guidelines followed during the project to end up with the PSM, let us firstly study the standard SMA connector. In Fig. 7.1 the cross-section of a mated standard SMA connector is shown with its main dimensions. The dark parts of the plot represent the metal, usually copper, and the white zones the dielectric, usually PTFE (Polytetrafluoroethylene or Teflon) or FEP (Fluorinated Ethylene Propylene). The red rectangle encloses the gap between the inner and the outer conductors produced by the unavoidable mechanical tolerances in the male-female interface. The inherent manufacturing process makes the appearance of gaps where the electrons coming from the outer space can enter into and, driven by the microwave field, collide with the walls of the devices releasing secondary electrons (see Section 2.2). It is therefore crucial for

Table 7.1: High power requirements specified at the SoW

Type	Band	f (GHz)	Operating power (W)
<i>Corona (CW)</i>	L-band	1	40
	C-band	4	30
	Ku-band	10	30
<i>Multipactor (CW)</i>	L-band	1	50
	C-band	4	50
	Ku-band	10	50
<i>Multipactor (Pulsed, 2% duty cycle)</i>	L-band	1	200
	C-band	4	180
	Ku-band	10	120

space applications a good coating on the metallic parts of the connectors, not only to increase the electrical conductivity, but to reduce the secondary emission as well.

It is an experimental fact that the electron secondary emission of rough surfaces is smaller than the one of flat surfaces [Vaughan 1989]. As the secondary electrons are emitted in all directions, they can be easily reabsorbed by the metal when the surface is rough, since they have more probabilities to collide against the peaks of the rough surface at low energies, binding to the metal lattice again. Nevertheless, it is also known that the electrical conductivity is low when the surface is not well polished. Thus, in space technology the non-negligible electron secondary emission is a trade-off to an acceptable electrical conductivity. Few tenths of microns gold or silver layer are usually enough to increase the first cross-over point of the electrodes (see Section 2.2) and exhibit an acceptable electrical conductivity within the Gigahertz frequency-bands, as presented above.

7.2 Guidelines

In order to design a coaxial connector with better high power withstanding capabilities than the standard SMA, let us study the multipactor and corona breakdown power thresholds for this connector to see the improvement that might be done. To do so we are going to analyze the multipactor and corona breakdown separately and follow the guidelines proposed in the ESA documentation [ECSS 2000, ECSS 2003].

7.2.1 Multipactor guidelines

As it was shown in Section 2.6 the multipactor susceptibility chart exhibits a minimum breakdown voltage around $fd = 0.6$ GHz mm when the initial velocity of the electrons is $v_0 = 1$ eV or around $fd = 1$ GHz mm when $v_0 = 5$ eV (see Fig. 2.15). Since the initial velocity distribution of the secondary electrons shows a small thermal spread around its maximum, typically located around 3 eV, we can consider that the multipactor breakdown voltage threshold of a parallel-plate waveguide is placed between those values of the frequency-gap product.

The same can be concluded for the coaxial electrodes according to the similarity principle [Woo 1967], which shows that the boundaries of the multipactor susceptibility chart modify their position for other geometries than the parallel-plates, but exhibiting the same features. Therefore, as it has been experimentally

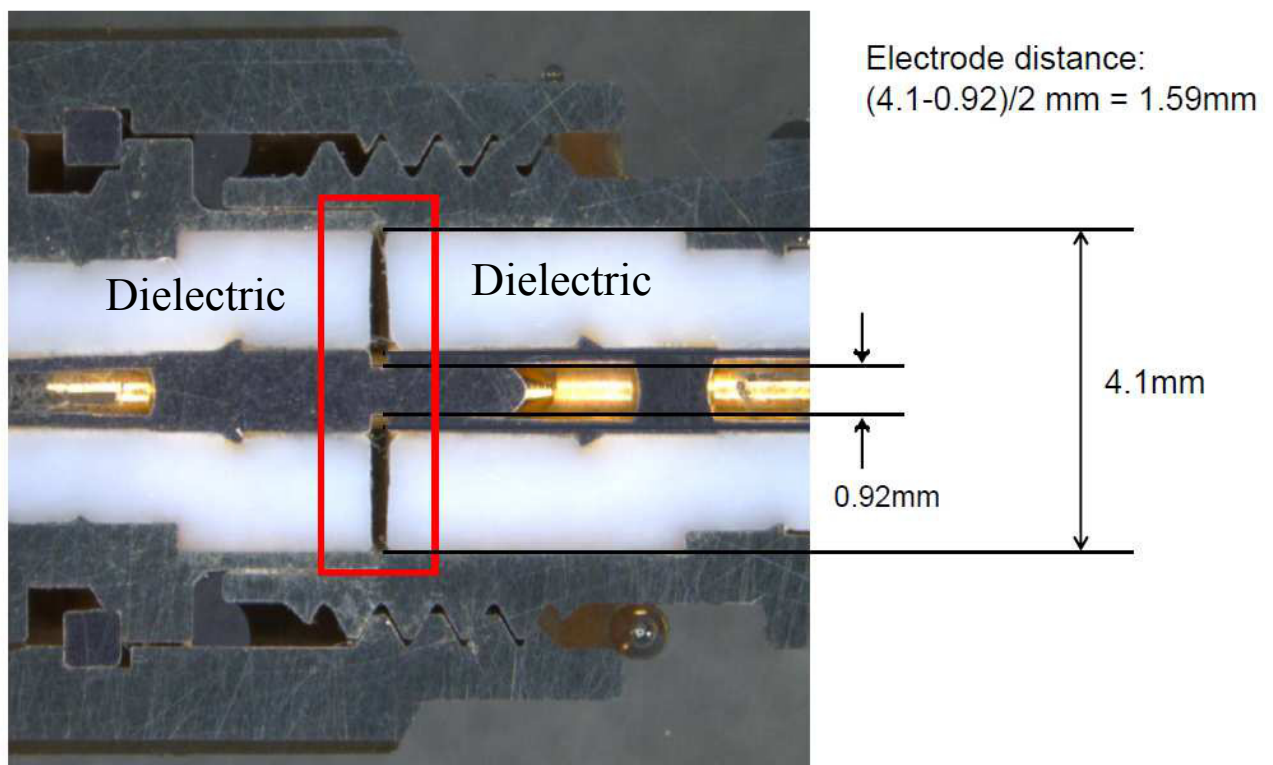


Figure 7.1: Cross-section of a standard SMA connector. Courtesy of H+S AG

confirmed, the multipactor susceptibility chart of the coaxial waveguide presents a minimum breakdown voltage threshold around similar values of the frequency-gap product (see Fig. 7.2). In this plot the measured multipactor breakdown voltage extracted from [Woo 1968] is shown for different coaxial cable aspect ratio. The minimum of the multipactor chart lies around the above-mentioned values of the frequency-gap product for all the cases.

Therefore, it is clear that, in order to increase the multipactor breakdown power threshold of the coaxial connector, the height of the gap between inner and outer conductor must change so that the fd product moves away from the minimum of the multipactor chart. The gap height can thus be either increased or reduced to ensure that the fd product lies far from 1 GHz mm. The augmentation of the gap height is the approach followed by the TNC concept, but it implies a dramatic increase of the connector size and weight, so it is discarded for the purposes of the project. Another possibility is the choice of the right dimensions such that the gap distance is small enough so that the frequency-gap product for the highest working frequency lies far on the left from the values for which the multipactor chart predicts the minimum breakdown voltage threshold.

This concept was identified as a staircase approach, which made the main gap between the inner and outer conductors evolve as sketched in Fig. 7.3. The figure shows the part of the coaxial connector equivalent to the top half of the SMA presented in Fig. 7.1. The dotted region represents the dielectric and the dashed areas the inner and outer electrodes of the coaxial connector. The advantage of this approach is twofold: on the one hand the tiny space between the dielectrics within the oblique gap makes the resonance between the motion of the electron and the microwave signal difficult at low voltages (see Section 2.2); on the other hand, the gap is bounded by PTFE, and the first cross-over point of this material is usually higher than the one of Silver or Gold. At the same time, the conclusions that have been reached in Chapter 2 concerning the analysis of the parallel-plate are feasible to be applied for the oblique gap since the electric field is quite uniform in this region. Therefore, as the value of the frequency-gap product lies on the left of the minimum multipactor chart, this approach guarantees a higher multipactor breakdown voltage threshold than for the standard SMA.

7.2.2 Corona guidelines

Regarding the gas discharge or corona breakdown, the guidelines followed to enhance the corona withstanding capabilities of the coaxial connector are:

- Avoiding sharp edges or peaks within the connector, which could lead to very intense electric fields and, subsequently, to dramatically high ionization rates.
- Trying to decrease the maximum electric field as much as possible by reducing the dimensions of the inner conductor, making its value compatible with the rest of the requirements of the connector (impedance).
- Reducing the volume of the gaps as much as possible to increase the diffusion loss and the corona breakdown power threshold.

The first point defines the need of good electrical contact between all the parts of the connector to avoid internal mismatches and the presence of stationary waves which could locally enhance the electric field strength, reducing the corona breakdown power threshold. On the other hand, the presence of sharp corners must be prevented so that the surface charge density does not induce too intense electric fields. Another way to decrease the maximum electric field within a coaxial structure is enlarging the diameter of the inner conductor, what

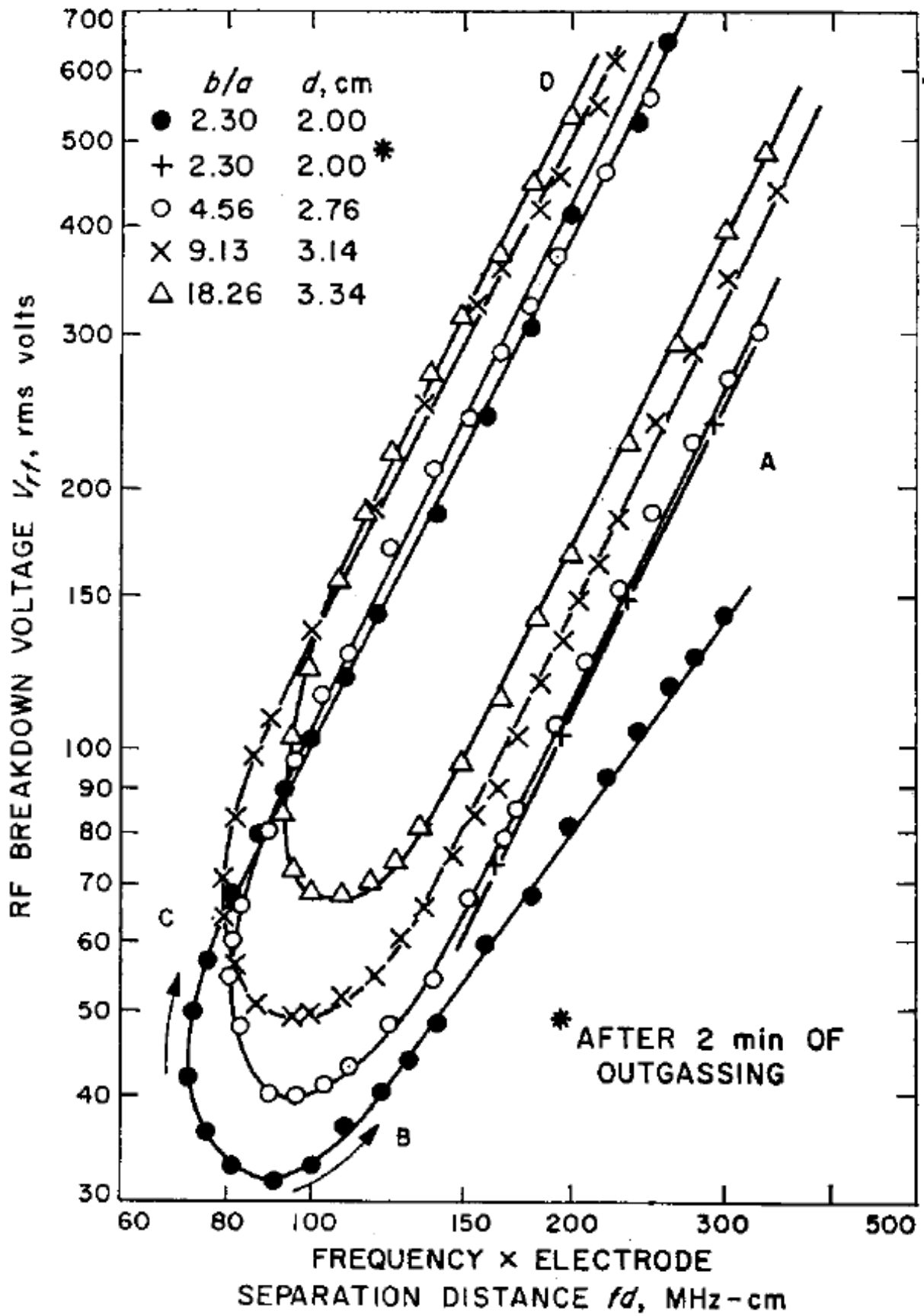


Figure 7.2: Experimental multipactor susceptibility chart for coaxial geometries. Extracted from [Woo 1968].

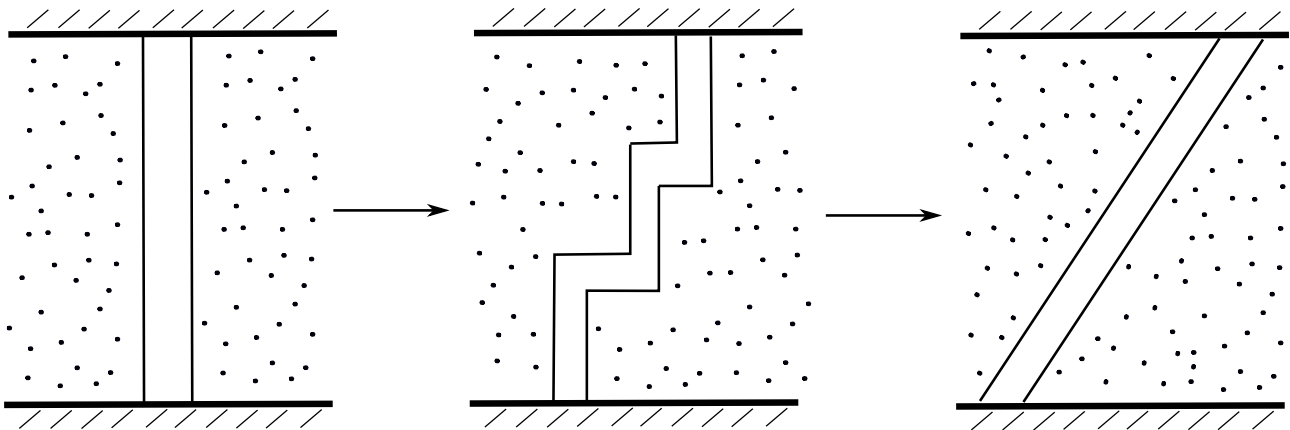


Figure 7.3: Sketch of the staircase approach concept till arriving to the oblique gap.

decreases the maximum electric field of the coaxial connector [Marcuvitz 1951]. Nevertheless, in order to keep the impedance of the connector when increasing the inner conductor, the diameter of the outer electrode must also be increased, what implies that the cut-off frequency of the higher mode decreases, limiting the maximum working frequency of the coaxial connector. Therefore, again the dimensions of the inner and outer electrodes were chosen to balance the maximum field strength, and subsequently, the ohmic losses, against the maximum working frequency of the coaxial connector, which should be, at least, the same as the one of the standard SMA.

The third guideline is intended to increase the diffusion loss since the diffusion current increases as the volume decreases. Indeed, let us imagine a gas filling the space between two flat electrodes of a parallel-plate waveguide. As it was described in Section 6.2, the electron population at the electrodes is null, therefore, if the space between the plates is smaller, the gradient of the electron density must be larger to satisfy the boundary conditions, with the subsequent increase of the diffusion current (see (6.12)). As the diffusion loss becomes more important, the electric field must become more intense to induce a higher ionization rate that compensates the diffusion and produces the gas breakdown [Brown 1951].

7.2.3 Outgassing and venting

The outgassing is a natural effect that occurs when the environmental pressure diminishes, enabling the gases or any possible contaminant attached to the surface of any material to escape to the environment. The outgassing can be enhanced by a local temperature rise, increasing the local pressure and the risk of corona breakdown. If a good venting of the on-board satellite microwave device is not guaranteed, corona breakdown may appear, whose power threshold is always lower than the one of the high-vacuum multipactor breakdown, [Woode 1989], for which the device has been designed to work correctly.

Therefore, besides the proposed approach for the gap in the male-female interface, the standard [ECSS 2003] describes that a crucial point in the design of components for space applications is a good venting to ensure that the pressure within the device falls below $1.5 \cdot 10^{-3}$ Pa before RF power is applied under orbit conditions. It has been observed experimentally that the fulfillment of this requirement discards the possibility of the corona onset [Woode 1989].

Therefore, like every microwave device used for space applications, the gaps produced in the manufacturing process of the coaxial connector must be adequately connected to the outer space environment through venting holes to ensure that there is no remaining gas within the components which might trigger a low power

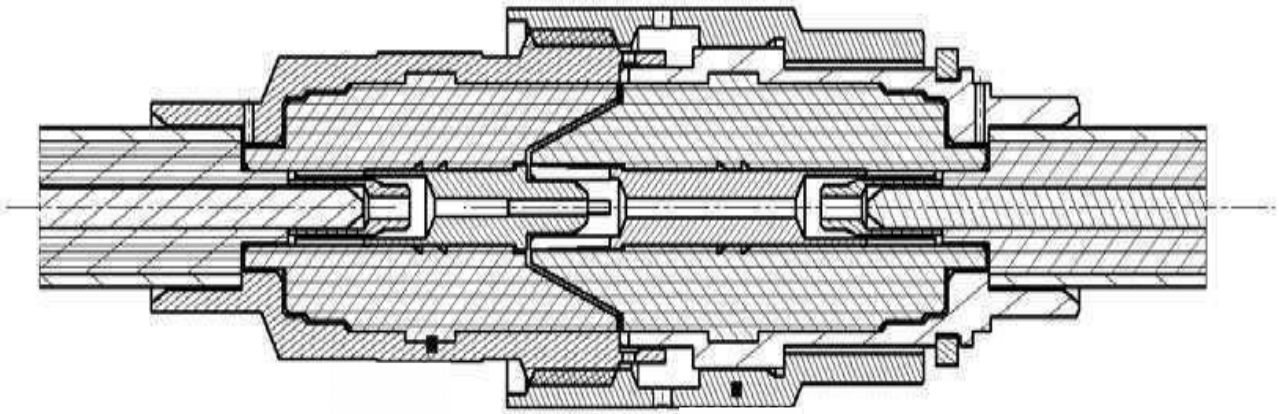


Figure 7.4: Sketch of the final design of the PSM connector. Courtesy of H+S AG.

corona breakdown, much more harmful than the multipactor discharge. The venting holes are usually placed on the nut of the connector at the male-female interface and at the cable entries. In order to avoid any electromagnetic interference with other devices on the satellite payload through the venting holes, the diameter of the latter must be small enough so that no coupling of the electromagnetic energy to the other components is guaranteed. On the other hand, it is known that the smaller the hole diameter, the smaller the venting conductance [ECSS 2003], what makes slower the gas evacuation of the possible outgassing contaminants. Again, the design of the PSM implied the choice of a venting hole diameter which resulted in the compromise between high pumping conductance and low electromagnetic radiation.

7.3 PSM design

The cross section of the final design of the PSM connector together with the cable-entry interface is outlined in Fig. 7.4, where the oblique gap can be observed in the plug-jack connection. In order to reduce the weight of the connector the inner conductor is hollow, and the venting channels have been designed to evacuate the residual gas through the venting holes at the nut of the PSM. The design has been made in such a way that the expansion due to a possible increase of temperature closes the gaps produced in the cable entry. This makes the connector mechanically more stable and reduces the risk of the appearance of gaps that could induce either corona or multipactor breakdown.

The reduction of the mass of the PSM with respect to the standard TNC is around 50%, the PSM exhibiting better high power capabilities concerning corona and multipactor discharges.

Table 7.2: Predicted multipactor breakdown power threshold of the PSM obtained with MEST for CW signals.

f (GHz)	Breakdown power (W)
1	477
4	477
10	3351

7.4 High power analysis

Following the guidelines proposed in Chapter 5 of [ECSS 2003], firstly, the calculation of the electric field within the gaps of the coaxial connector was done. The electromagnetic fields of the proposed design were calculated with HFSS. Once the electric field within the gaps of the coaxial structure was calculated, the line integral of the electric field along the gap was defined as the gap voltage, analogously to the voltage of a parallel-plate waveguide. Regarding the corona discharge, the electric field found by HFSS across the geometry defined by the gaps of the structure has been exported to the in-house FEM-2D code and the breakdown power threshold calculated. The azimuthal symmetry of the connector has been used to reduce the simulation size, considering only one quarter of the PSM.

7.4.1 Multipactor analysis

The predicted multipactor breakdown voltage of the gap was calculated inserting the length of the gap and the corresponding frequency in the software Multipactor Electron Simulation Tool (MEST) [de Lara 2006]. MEST is a software that calculates the motion of the electron within a parallel-plate waveguide and simulates the electron population growth by using the SEY model presented in [Furman 2003]. Regarding the SEY properties, as MEST can only simulate homogeneous boundaries, the gaps, whose bottom and top side were made of different materials, were analyzed considering the material with the lowest first cross-over point (see Section 2.2). This approach was followed in order to avoid the over-estimation of the breakdown threshold and optimize the design of the connector. Once the multipactor breakdown voltage was found, the breakdown power was calculated taking into account that the gap voltage found by HFSS corresponds to 1 W rms input power. Thus, the predicted multipactor breakdown power threshold was calculated with the formula:

$$P_B = \left(\frac{V_{MEST}}{V_{HFSS}} \right)^2. \quad (7.1)$$

This procedure was done for each gap formed within the connector structure, calculating the gap voltage and the multipactor power threshold. The gap that exhibited the lowest multipactor breakdown power defined the most critical gap and the multipactor breakdown power threshold of the whole structure.

The results are summarized in Table 7.2, where the multipactor threshold was found for the gaps existing in the cable-entry. This shows that the multipactor power threshold of the male-female part of the connector is higher than for the cable-connector interface. Indeed, the multipactor withstanding capabilities of the cable-entry limited the maximum working power of the PSM connector.

Table 7.3: Predicted minimum (critical) corona breakdown threshold of the PSM for CW signals.

f (GHz)	<i>Minimum breakdown power (W)</i>		
	Woo	Lupan	Mayhan
1	112	19	12
4	238	110	72
10	512	347	231

7.4.2 Corona analysis

Regarding the study of the corona withstanding capabilities of the PSM, once the electric field along the structure of the connector was found with HFSS, the FEM-2D code imported the values of the electric field. By finding the minimum input power that results in the solution of the eigenvalue problem (6.16) for each pressure, the Paschen curve was found. The simulations were done taking advantage of the azimuthal symmetry only meshing one quarter of the connector. The convergence analysis of the solution of the corona equation with the 2D FEM code for Woo's ionization model is shown in Fig. 7.5, where the last step corresponds to 7422 triangles, before reaching the memory limit of the computer. The convergence study was done by calculating the relative distance between the minimum corona breakdown threshold of the Paschen curve obtained with different number of triangles as demonstrated in Section 6.5.2.1. As it has been remarked in that section, the convergence followed basically the same behavior regardless the ionization rate model, thus the fact that the convergence has been reached for Woo's model guarantees that the same applies for the rest of the models.

The corona equation was solved with the 2D FEM code for each ionization model using 7422 elements. As it was observed in Section 6.3.4 for any microwave device, Mayhan's model predicted values of the corona breakdown power threshold for the PSM much lower than the rest of the ionization models. Taking into consideration the three ionization models presented in Section 6.3 for design purposes, the Paschen curves obtained with the models predicting the highest and the lowest corona breakdown power threshold have been plotted. The results are shown in Fig. 7.6 for each frequency specified in the SoW, where the space enclosed by the difference between both curves has been marked with different colors for each frequency.

The predicted values of the minimum corona breakdown power threshold of the Paschen curve (critical corona threshold) obtained with each model presented in Section 6.3 for the three working frequencies are shown in Table 7.3. According to this, the predicted critical corona threshold of the PSM ranges from 12 W to 112 W at 1 GHz. The predicted critical corona threshold at higher frequencies lies above the requirements of the project (40 W according to Table 7.1) in the worst case, since Mayhan's model predicts a corona breakdown power of 72 W at 4 GHz and a much higher threshold at 11 GHz. This constitutes an input power above the requirements of the project (see Table 7.1), thus the lowest frequency fixes the limiting input power without the risk of corona discharge to occur.

7.5 Test results

The low power results are extracted from the assessment report of the PSM [Mattes 2011] and the high power test results are extracted from the final report of the test campaign of the PSM done in the ESA-VSC consortium in Valencia (Spain) [Esteve 2011].

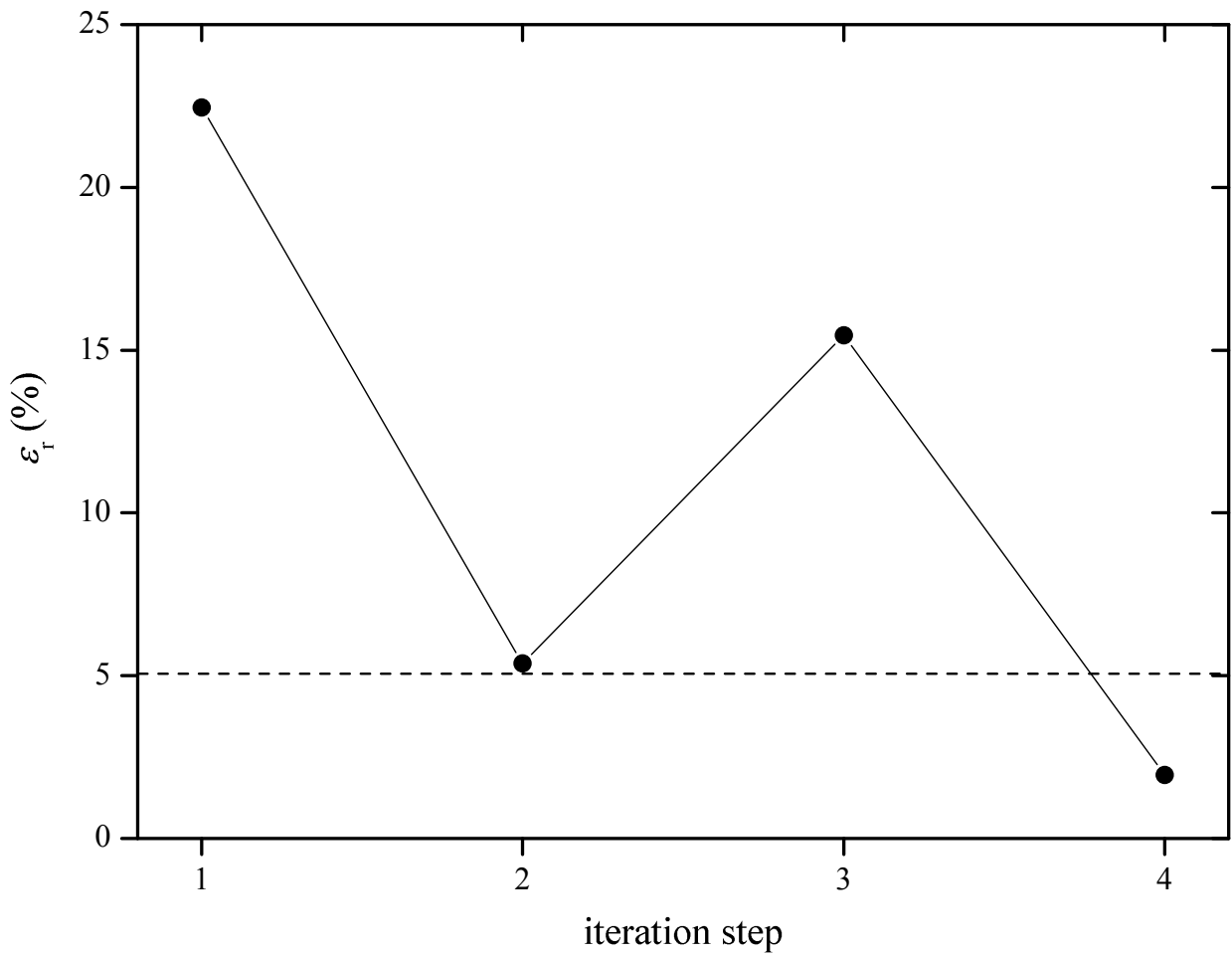


Figure 7.5: Convergence study of the Paschen curve of the PSM connector found by calculating the average of the corona breakdown threshold obtained with the three ionization rate models presented in Chapter 6.

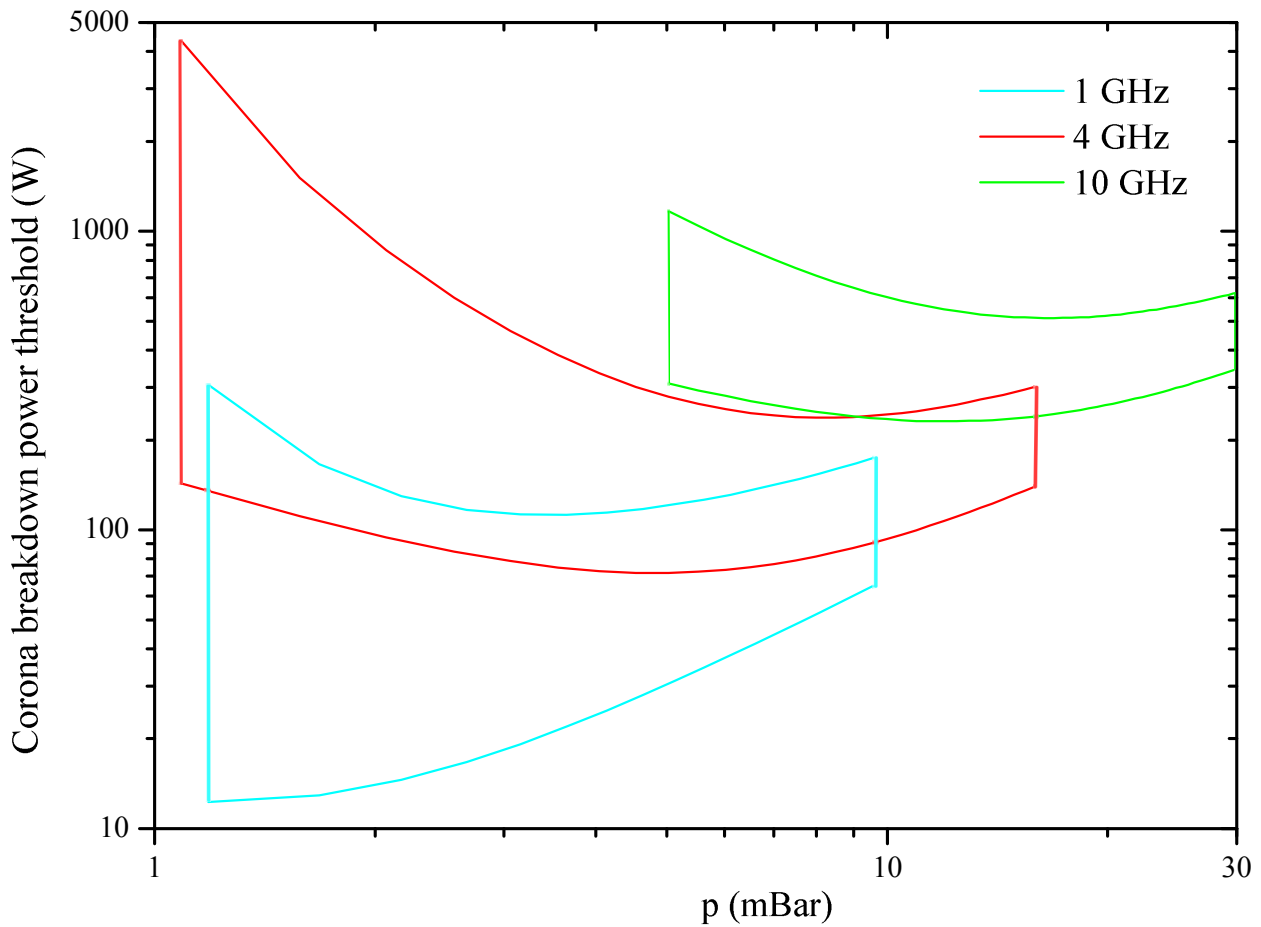


Figure 7.6: Paschen curve of the PSM connector obtained with Woo's and Mayhan's ionization rate models presented in Chapter 6 for three frequencies. The results of Woo's and Mayhan's models predict the highest and the lowest values of the corona breakdown power threshold, respectively.

7.5.1 Low power performance

The measurement of the S-parameters of the new connector have been done for a 1 m long cable connected to the PSM and are shown in Fig. 7.7, where the measurements of the reflection coefficient, (S_{11}), have been made with a gating in such a way that only the region from the beginning of the PSM to a few centimeters inside the cable contributed to the result. The red curve in Fig. 7.7b shows the transmission coefficient, (S_{21}), of the 1 m long cable connected to the PSM and the blue curve the one of the connector together with the cable. The fact that both curves lie very close to each other indicates that the main contribution to the non-negligible values of the transmission coefficient comes from the ohmic losses produced in the cable. The results show the good performance of the PSM within the whole bandwidth, from 1 GHz to 18 GHz, the reflection coefficient lying below -20 dB within the complete frequency range.

7.5.2 High power performance

The experimental tests concerning the high power withstanding capabilities of the PSM were carried out at the joint ESA-VSC high power RF laboratory in Valencia (Spain). The detection systems used to assess the occurrence of multipactor and/or corona discharges are described in [ECSS 2003] and can be enumerated as follows:

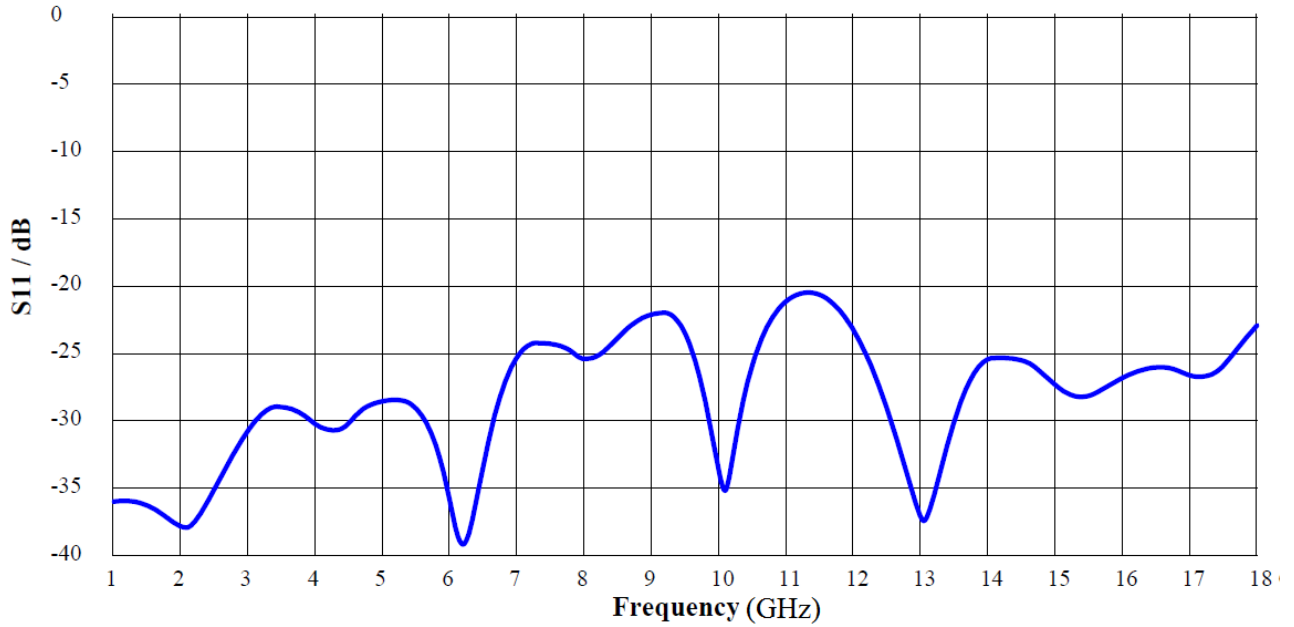
- Forward/Reverse power nulling.
- Third harmonic monitoring.
- Electron avalanche detector (electron probe).
- Optical detection.

The breakdown according to [Esteve 2011] was supposed to have taken place when the discharge was found by more than one method. This is the standard approach followed to avoid that anomalous responses of low intensity, provoked by other phenomena like thermal issues, could create confusion. This occurs because, as it was commented in Chapter 5, there is not a univocal and commonly accepted criterion yet to assess experimentally the multipactor breakdown onset.

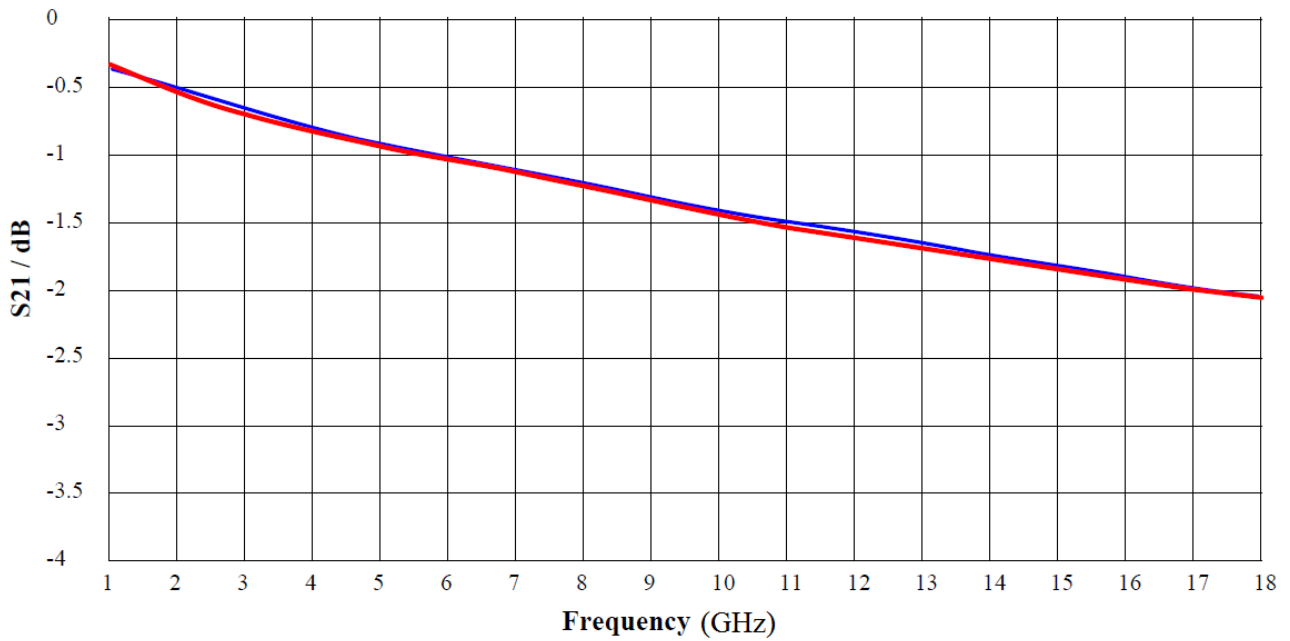
7.5.3 Multipactor tests

The multipactor tests were done for the three above-mentioned working frequencies described in the SoW of the project for CW and pulsed signals. The pulsed signal consisted of a rectangular waveform with a pulse repetition frequency (p.r.f.) of 1 kHz at 2% duty cycle (d.c.). The results of the multipactor tests carried out on the PSM are shown in the Tables 7.4 and 7.5 where the temperature has also been recorded to check the performance of the connector under thermal stress. It is known that the higher the frequency the bigger the ohmic losses and, therefore, the higher the expected temperature within the connector. As the high temperature can melt the welding points at the cable entry, the temperature is continuously tracked to check the good contact between the cable and the connector.

The multipactor tests were done increasing the input power step by step if no discharge was detected till the maximum power of the amplifiers was reached. Due to some technical issues in the workbench at 10 GHz, the test frequency chosen for the Ku-band was 11 GHz. The maximum power provided by the amplifiers at disposal at the ESA-VSC lab facilities was 1500 W at the L-band and 1200 W at the C- and Ku-bands.



(a) Return loss of the PSM.



(b) Insertion loss of the PSM.

Figure 7.7: Experimental S-parameters of the PSM connector.

It is worth to mention that the multipactor tests done at 438 MHz and 1 GHz for the pulsed signal were limited by the maximum power that the amplifiers could provide. This means that the high power performance of the PSM connector is better than what the experimental setup could detect. That is the PSM is able to withstand similar power levels as the TNC for pulsed signals at the P- and L-bands without the risk of multipactor occurrence. The same can be said about the results obtained at 4 GHz, where the maximum input power was 1200 W.

f (GHz)	T (°C)	Max. power applied (W)	Result
1	–	100	No breakdown detected
4	20	100	No breakdown detected
4	40	100	No breakdown detected
11	60	100	No breakdown detected

Table 7.4: Results of multipactor tests for the PSM with the CW signal.

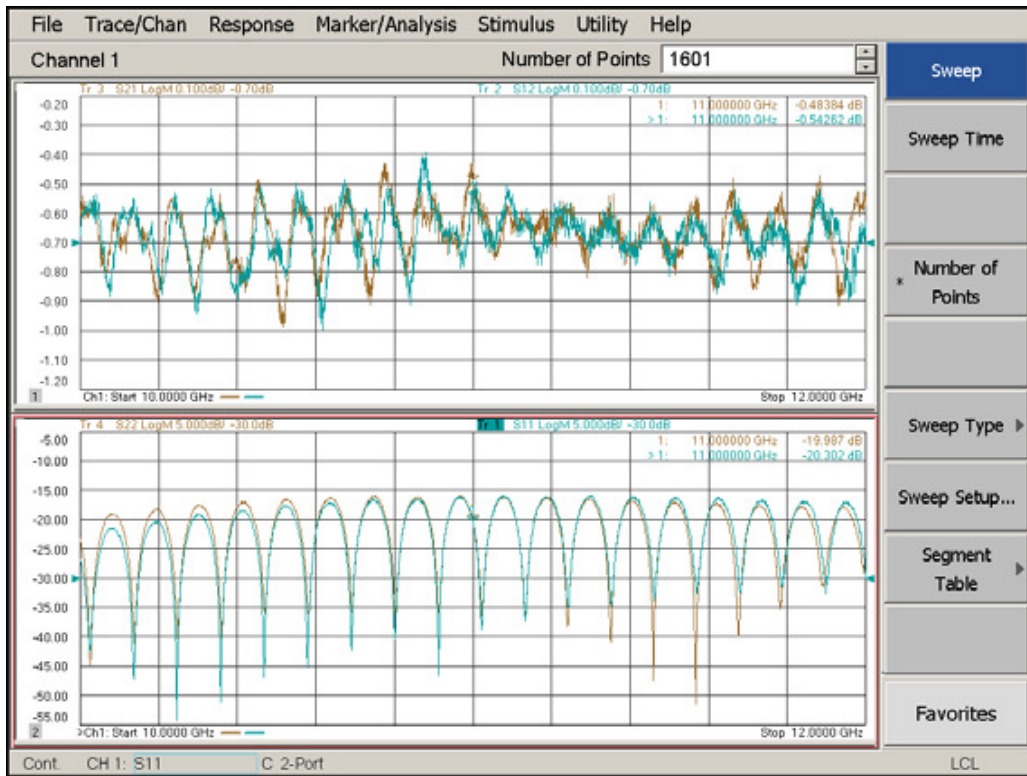
f (GHz)	T (°C)	Max. power applied (W)	Result
0.438	–	1500	No breakdown detected
1	–	1500	No breakdown detected
4	20	1200	No breakdown detected
4	40	1200	No breakdown detected
11	60	1000	Breakdown detected

Table 7.5: Results of multipactor tests for the PSM with the modulated signal (2% d.c.)

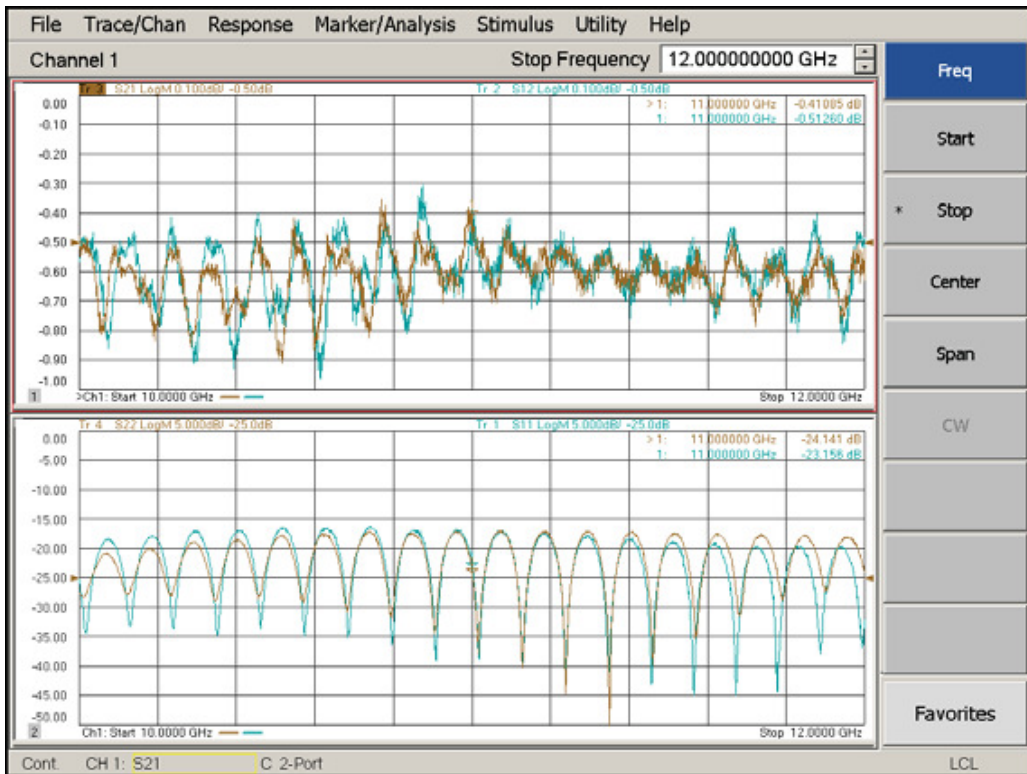
In order to check the robustness of the PSM, the S-parameters before and after the multipactor test with the CW signal at 11 GHz are shown in Fig. 7.8. The results show that no appreciable change in the S-parameters was produced in the PSM connector after being subject to 100 W during around 10 minutes with an environmental temperature of 60°C.

7.5.4 Corona tests

Due to the high cost of the working hour and the big amount of hours required to obtain experimentally the Paschen curve of the PSM, it was decided during the project to fix the input power (3dB higher than the one specified in the SoW as security margin) and check whether the PSM could withstand that power without breakdown detection. The results are summarized in Fig. 7.9, where the black bars show the predicted critical corona breakdown power threshold obtained with Woo's model and the white bars the one obtained with Mayhan's model. The gray bars show the input power fixed during the corona tests during which the pressure was swept from 10^{-5} mBar to the atmospheric pressure. There was no discharge detection in any corona test, what shows that the PSM could withstand more than 80 W at 1 GHz and more than 60 W at 4 and 11 GHz, which are the values represented by the gray bars in Fig. 7.9.



(a) S-parameters of the PSM before the Ku-band multipactor test.



(b) S-parameters of the PSM after the Ku-band multipactor test.

Figure 7.8: Experimental S-parameters of the PSM connector during the Ku-band multipactor test performed to 100 W CW during 10 minutes. The frequency ranges from 10 GHz to 12 GHz.

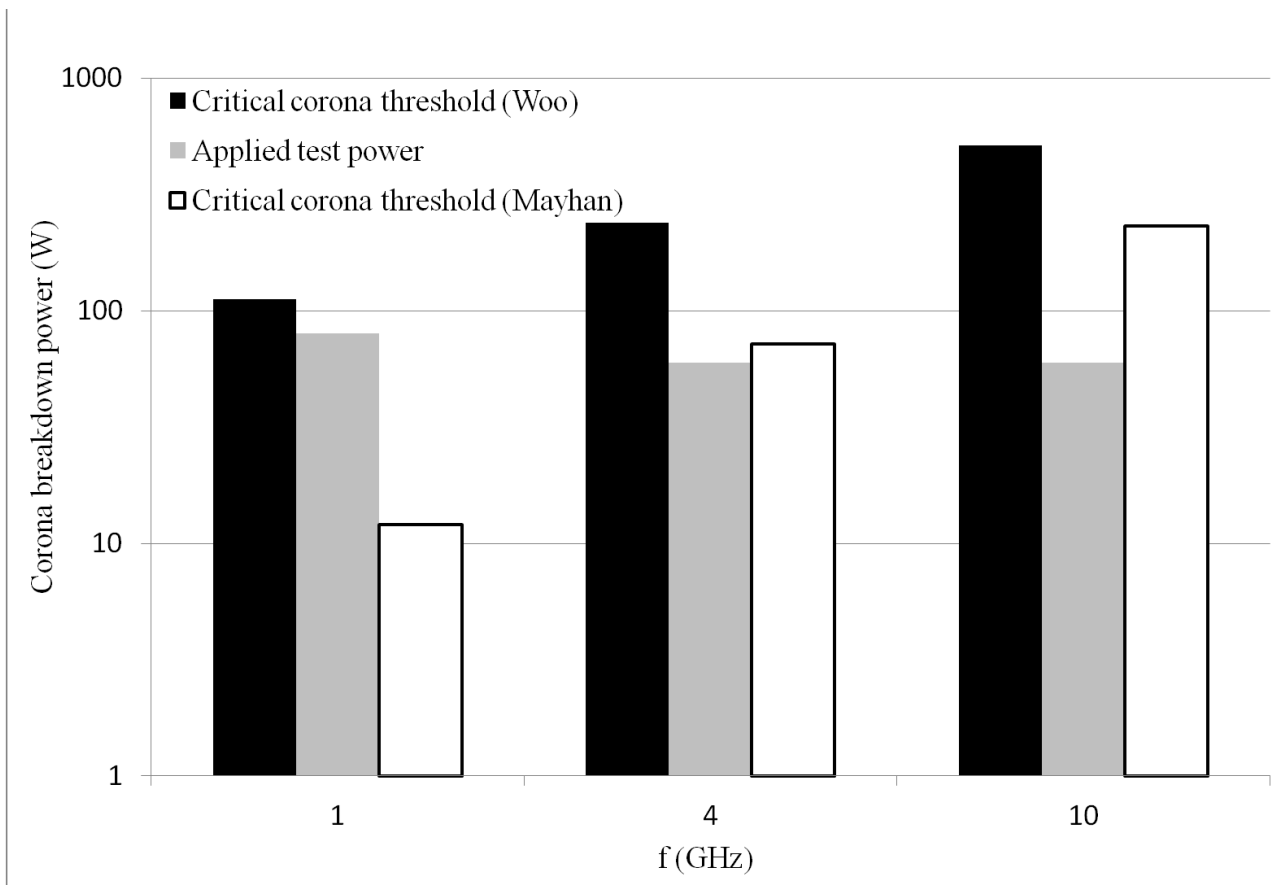


Figure 7.9: Results of the corona test. The gray bars represent the input power fixed during the experimental tests and the black and white bars represent the critical corona breakdown power threshold predicted by Woo's and Mayhan's models, respectively.

7.6 Discrepancies

The results of the multipactor tests exhibited some discrepancies with the predictions (cf. Tables 7.2, 7.4 and Fig. 7.5). The reasons that could explain these discrepancies are the following:

- The predictions of the multipactor threshold were obtained assuming that the electric field within the gaps of the connector was uniform, like the one of an infinite parallel-plate waveguide. Neither the coaxial geometry profile nor the fringing field effects at the edges of the gaps were taken into account in the simulations. Both effects are supposed to increase, in general, the breakdown threshold with respect to the parallel-plate geometry.
- The simulations of the multipactor threshold were done assuming a homogeneous boundary, i.e., a single material, since no simulation tool for non-homogeneous gaps was available at the time of the project. In order not to overestimate the multipactor threshold the material with the lowest first cross-over point was utilized in the design process.
- It has been observed experimentally the dependence of the SEY parameters on the temperature, like the decrease of the maximum SEY or the change in the value of the first cross-over point [Woode 1989, Hilleret 2003, Kobayashi 2003, Stacey 2009]. Nevertheless, this temperature dependency has not been taken into account during the design process, that is, in the simulations, since there is no model available to evaluate it.
- Changes of the structure of the PTFE due to the thermal expansions decreasing the gap widths or even closing them completely plus the uncertainty in the dimensions due to the mechanical tolerances.

The effect of taking into account the coaxial electric field profile within the gaps is not expected to contribute much to the explanation that justifies the discrepancies of more than 3 dB between simulations and measurements, because the gaps are quite small and the deviation from the uniform field is negligible.

On the other hand, as the critical gap of the PSM was made of gold and Teflon, and the first cross-over point of the SEY curve of PTFE is higher than the one of gold, the experimental multipactor threshold is expected to be higher than the one obtained in the simulations with gold. The simulations using Teflon predicted a multipactor threshold at 1 and 4 GHz around 1300 W, what results in a noticeable increase of the breakdown power threshold.

Nevertheless, the temperature rise due to the ohmic losses in the cable is expected to contribute the most to explain the differences between the experimental and the predicted multipactor threshold. As it has been commented before, the multipactor tests were run at 40°C and 60°C at 4 and 11 GHz, respectively, what implies an expansion of the dielectric within the PSM that closes some gaps, as it was decided during the design process. This could have made that the critical gaps for which the simulations predicted a multipactor threshold of 477W were closed and the multipactor threshold of the PSM must be associated to another gap. The multipactor threshold predicted for any other gap was higher, thus this could explain why the experimental multipactor threshold at 4 and 11 GHz was higher than the ones obtained in the simulations.

On the other hand, as it has been observed experimentally, a big heating induces a decrease of the first cross-over point and a change in the SEY parameters of the materials that entails a reduction of the multipactor threshold predicted at 11 GHz. The measured breakdown power at 60°C was 1000 W at that frequency (see Table 7.5) instead of the predicted 3351 W at 10 GHz. The ohmic losses at that frequency are so important that

a local increase of the temperature could entail a gas discharge by the appearance of outgassing contaminants and the subsequent pressure rise [Woode 1989].

Concerning the corona tests, the results show that Woo's and Mayhan's models predict both values of the critical corona breakdown threshold above the fixed input power, except at 1 GHz, where Mayhan's model predicted a corona discharge at 12 W. The measurements showed that there was no corona discharge for 80 W at 1 GHz CW, what is a challenge for such a small connector. On the other hand, the PSM did not show any sign of corona breakdown for 60 W at 4 and 11 GHz, exhibiting a very good high power performance.

7.7 Summary

The measured high power characteristics of the PSM cable assemblies are excellent. The design in terms of high power transmission is close to the physical limit of the chosen small geometry of connector and cable. The measurements showed a very good performance regarding multipactor capabilities in P-band (438MHz) as well as in L-band (1124 MHz), being able to withstand at least up to 1500 Watts input power, for a pulsed signal of 2% duty-cycle, without showing any trace of multipactor discharge. This implies an improvement of 50% compared to other powerful connectors such as TNC. Concerning corona breakdown, the PSM was able to withstand more than 80 Watts without showing any sign of glowing or noticeably discharge, what constitutes a challenge for coaxial connectors at these input powers.

As it has already been pointed out, the origin of the discrepancies between simulations and measurements may be due to the limitation of the simulation tools and to the temperature rise provoked in the cable, what induces an important thermal stress on the connector at high frequencies and powers. On the other hand, the appearance of mechanical tolerances may noticeably modify the predicted multipactor breakdown power threshold by a small change on the assumed size of the gap. The thermal expansion due to the temperature rise may also increase the dimensions of some gaps and modify the multipactor breakdown power threshold of the connector. Indeed, the experiments showed that the only power limitation of the PSM lies in the temperature stress that the cable, and consequently the connector, can withstand.

The success in the design of the PSM according to the requirements specified in Table 7.1 is depicted in Fig. 7.10 where the validation of the high power tests have been represented by a green case. Note that the maximum power that the PSM can withstand exceeds by far the specifications requested in the SoW of the project at low frequencies. The maximum input power that the connector can withstand at high frequencies is determined by the high temperatures reached due to the ohmic losses. Compared to the SMA connector the PSM is able to withstand much higher input powers exhibiting no corona and multipactor breakdown but at power levels comparable to the working limits of the TNC connector with lower mass.

Type	f (GHz)	Requirements (W)	Test	Comments
Corona (CW)	1	80		
	4	60		
	10	60		Test done @ 11 GHz
Multipactor (CW)	1	100		
	4	100		
	10	100		Test done @ 11 GHz
Multipactor (Pulsed, 2% d.c.)	1	800		No breakdown for 1500 W
	4	720		No breakdown for 1200 W
	10	480		Test done @ 11 GHz

 = Successful

Figure 7.10: Summary of the results obtained during the high power tests applied on the PSM connector.

Outlook and future work

The development of a rigorous multipactor criterion is essential to avoid high cost test campaigns for the design of microwave components for space applications. The results obtained in this thesis can help in the future success of this task. The development of an analytical model to predict the maximum surface charge density in the multipactor steady-state, together with the study of the radiated power spectrum of a multipactor discharge within a parallel-plate intend to bring new insights towards the development of such a criterion. Nevertheless, the analysis of this discharge should be extended to other waveguides and more realistic scenarios.

For instance, the study of multipactor saturation considering more than one electron sheet could serve to model the thermal spread of the secondary electrons resulting in a distribution of their initial velocity, moving beyond Sombrin's model. The influence of the magnetic field on the levels of the saturation charge for a parallel-plate waveguide can also be analyzed, as well as the presence of a DC field as it occurs for parallel-plate waveguides with dielectrics can be taken into consideration.

On the other hand, the saturation analysis must be extended to more realistic scenarios like rectangular waveguides with a large width-to-height ratio, where the parallel-plate approximation could help to estimate the surface charge density in the multipactor steady-state by finding the analytical motion of the electron cloud.

The analysis of multipactor saturation for a coaxial waveguide can also be studied under Sombrin's model, representing the electron cloud by a cylindrical sheet of charge concentric to the inner conductor of the waveguide. The analytical motion of the electron sheet at very high frequencies and large coaxial cable aspect ratio has been developed by [Udiljak 2007], and the study of the saturation under the same conditions may bring new analytical formulas to predict the surface charge density of saturation for coaxial waveguides. The analysis of more than one electron sheet to model the thermal spread of the secondary electron for coaxial geometries can also be studied in this case.

Therefore, the equations of motion of the electrons taking into account space charge effects, and considering more than one electron sheet for rectangular and coaxial waveguides must be developed. By knowing the equations of motion of the electron cloud, the radiated power spectrum of a multipactor discharge following the same approach as in this thesis can be extended to these devices.

On the other hand, the study of saturation has been developed for the true secondary electrons, but the influence of the backscattered and the reflected electrons on the saturation must be considered as well in order to extend the analysis of multipactor steady-state to a more realistic scenario.

The theoretical radiated power spectrum extended to rectangular and coaxial geometries taking into account the space charge effect must be compared with the experimental measurements in a test campaign to be validated. This will be useful to find or, in any case, to get closer to an unambiguous multipactor onset assessment criterion.

Furthermore, the study of the radiated power spectrum for more general geometries, as it occurs in particle accelerators, request the development of numerical techniques to find the motion of the electron cloud produced within the particle beam pipe. The Fourier transform of the multipactor current produced can be calculated to find the radiated power spectrum of a multipactor discharge. The analysis of both the power spectrum and the

influence of an external field on the dynamics of the electron cloud can be used to reduce or even suppress the electron cloud build-up in particle accelerators, like in the LHC.

Concerning corona breakdown, a more rigorous analysis of the ionization rate models must be done including the development of a more general model, able to predict the values of the corona breakdown threshold lying closer to the measurements. This new and more general ionization model should be able to predict accurately the ionization rate for bigger values of the effective electric field-to-pressure ratio than shown for the models described in this thesis.

Concerning the PSM connector, it must pass the space qualification campaign to validate its functioning within the harsh space weather. The proposition of a space mission with the PSM to validate its performance by testing simple properties, like, for instance, the response of the S-parameters in the real space weather, has been outlined within the framework of the Space Center at EPFL.

Returning limit analysis

A.1 Returning limit equation

Neglecting for the moment the restriction (2.22) for the acceleration, we can use the equations of motion and the definitions of variables v_ω and V_ω to rewrite the system of equations (2.22) as follows:

$$\left\{ \begin{array}{l} V_\omega(\phi_R - \alpha_R) + \cos \phi_R - \cos \alpha_R + (\phi_R - \alpha_R) \sin \alpha_R = 0 \\ V_\omega + \sin \alpha_R - \sin \phi_R = 0 \end{array} \right. \quad \begin{array}{l} \text{(A.1a)} \\ \text{(A.1b)} \end{array}$$

Eq. (A.1b) shows that it is impossible to find the requested solution to the system of equations for $V_\omega > 2$, since the quantity $|\sin \alpha_R - \sin \phi_R|$ can be 2 at the most. Furthermore, the velocity of the electron cannot be lower than zero for values of V_ω larger than 2, therefore, we can conclude that the electron never impacts against the initial plate when $V_\omega > 2$.

Besides the positive acceleration at impact time, we will impose the condition $\phi_R - \alpha_R > 0$ in order to guarantee that the launch phase precedes the impact phase, ensuring a physically meaningful solution. As the acceleration is proportional to $-\cos \phi_R$ (see (2.1)) the first condition, (A.1a), implies that the phase of the RF field when reaching the birth plate, ϕ_R , must lie between $\pi/2$ and $3\pi/2$ to guarantee that the acceleration is positive.

Isolating V_ω in (A.1b) as $V_\omega = \sin \phi_R - \sin \alpha_R$ and substituting it into (A.1a) we can rewrite (A.1a) as follows:

$$(\phi_R - \alpha_R) \sin \phi_R + \cos \phi_R - \cos \alpha_R = 0.$$

We define $\Psi \equiv \phi_R - \alpha_R$ and rewrite the system of equations as follows

$$\left\{ \begin{array}{l} \Psi \sin \phi_R + \cos \phi_R - \cos \alpha_R = 0 \\ V_\omega + \sin \alpha_R = \sin \phi_R \end{array} \right. \quad \begin{array}{l} \text{(A.2a)} \\ \text{(A.2b)} \end{array}$$

Using (A.2b) in (A.2a) we can write

$$\Psi(V_\omega + \sin \alpha_R) \pm \sqrt{1 - (\sin \alpha_R + V_\omega)^2} - \cos \alpha_R = 0, \quad \text{(A.3)}$$

where the sign of the square root provides the sign to the cosine of the impact phase. Therefore, as it has been discussed above, the sign must be negative. Hence, the physically meaningful solution leads us to write Ψ as a function of α_R in the following form:

$$\Psi(\alpha_R) = \frac{\cos \alpha_R + \sqrt{1 - (\sin \alpha_R + V_\omega)^2}}{(\sin \alpha_R + V_\omega)}. \quad \text{(A.4)}$$

The impact phase can be expressed as $\phi_R = \Psi(\alpha_R) + \alpha_R$, and we can substitute (A.4) into (A.2b) to find α_R as the solution of the following equation:

$$V_\omega + \sin \alpha_R = \sin (\Psi(\alpha_R) + \alpha_R) \quad (\text{A.5})$$

what results in the equation

$$V_\omega + \sin \alpha_R - \sin \left\{ \alpha_R + \frac{\cos \alpha_R + \sqrt{1 - (\sin \alpha_R + V_\omega)^2}}{\sin \alpha_R + V_\omega} \right\} = 0. \quad (\text{A.6})$$

The launch phase provoking the returning to the initial plate with zero velocity is given by the solution of (A.6), however, this equation has an infinite amount of roots as long as $V_\omega < 1$, with the peculiarity that the distance between roots decreases as $\sin \alpha_R \rightarrow -V_\omega$. This is easy to understand if we remark that a small change in the value of the denominator of the argument of the sine function in the last term of the LHS of (A.6) induces a big change as the denominator tends to zero. It must be remarked that in case that $V_\omega \neq 0$, the accumulation of the roots is produced around two values of α_R , corresponding to both branches of the arcsine function, otherwise all the roots gather around $\alpha_R = 0$.

The physical meaning of the infinite amount of roots comes from the fact that the solution of (A.1) defines all the phases for which the electron reaches the bottom plate with zero velocity ignoring the possibility that the theoretical trajectory of the electron may imply a previous impact against the initial plate (see Fig. A.1). Only the first launch phase, $\alpha_R^{(1)}$, provides the requested solution, since only for this launch phase the electron impacts against the initial plate with zero velocity for the first time after being launched. The other solutions for the initial phase lead to impacts against the initial plate with zero velocity after colliding with the initial plate previously, what it is not of our interest.

In order to find the roots of (A.6) let us firstly study the case for $V_\omega = 0$ for the sake of clarity.

A.1.1 Zero initial velocity

For zero initial velocity the variable V_ω is also null and the solution of the returning limit becomes quite simple, in this case the function $\Psi(\alpha_R)$ is written as

$$\Psi(\alpha_R) = \frac{\cos \alpha_R + |\cos \alpha_R|}{\sin \alpha_R} \quad (\text{A.7})$$

1. For $\alpha_R \in \left[\frac{\pi}{2}, \frac{3\pi}{2} \right]$ the solution of (A.6) is the trivial one: $\Psi_R = 0 \rightarrow \phi_R = \alpha_R$, since $\cos \alpha_R = -|\cos \alpha_R|$ within this interval.

2. For $\alpha_R \in \left[\frac{-\pi}{2}, \frac{\pi}{2} \right]$ the returning limit is found by solving

$$\sin \alpha_R - \sin \left\{ \alpha_R + \frac{2}{\tan \alpha_R} \right\} = 0. \quad (\text{A.8})$$

Taking into account the condition (2.22c) at the impact time and (2.1), it can be concluded that the impact phase must lie within the second branch of the arcsine function. As the argument of the sine function of the second term of the LHS of (A.8) corresponds to ϕ_R , the solution of (A.8) can be written as follows

$$(2k + 1)\frac{\pi}{2} - \alpha_R^{(k)} - \cot \alpha_R^{(k)} = 0. \quad (\text{A.9})$$

The maximum value of $\alpha_R^{(k)}$ as solution of (A.9) within the defined range is found for $k = 0$ with $\alpha_R^{(0)} = \frac{\pi}{2}$, what implies $\Psi_R = 0 \rightarrow \phi_R^{(0)} = \alpha_R^{(0)}$.

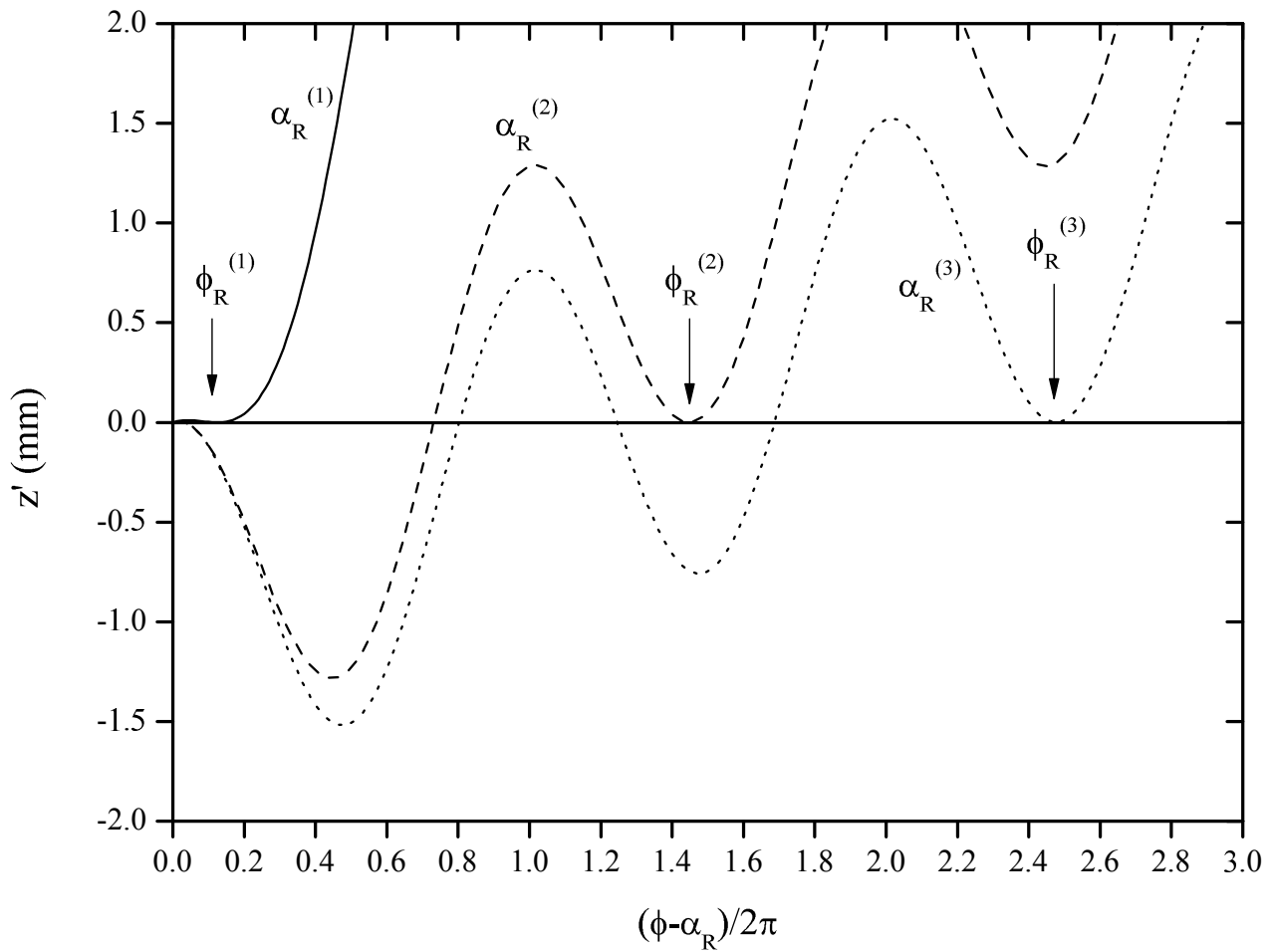


Figure A.1: Example of returning for several solutions of (A.6) for $fd = 1 \text{ GHz} \cdot \text{mm}$, $v_0 = 1 \text{ eV}$ and $V_{RF} = 212 \text{ V}$. The values of the launch phases are $\alpha_R^{(1)} = 1.048 \text{ rad}$, $\alpha_R^{(2)} = 0.117 \text{ rad}$ and $\alpha_R^{(3)} = 0.0281 \text{ rad}$.

A.1.2 Non-zero initial velocity

For non-zero initial velocities $V_\omega > 0$ holds, and the solution of the returning limit is more difficult to deal with. First of all, we have to delimit the root search to the domain where the physically meaningful roots are located and this has not been found yet. The condition of positive acceleration at the moment of impact against the initial plate has already been applied in the choice of the branch of ϕ_R , but the conditions to guarantee $\Psi(\alpha_R) > 0$ have still to be studied. Nevertheless, the conditions that guarantee the solution of Ψ_R to be real-valued must be analyzed first, and this is described by the conditions:

- If $\alpha_R \in \left[-\frac{\pi}{2}, \frac{\pi}{2}\right] \rightarrow \alpha_R < \arcsin(1 - V_\omega)$
- If $\alpha_R \in \left[\frac{\pi}{2}, \frac{3\pi}{2}\right] \rightarrow \alpha_R > \pi - \arcsin(1 - V_\omega)$

In order to ensure that the impact phase is bigger than the launch phase we have to study (A.6) for different cases:

1) If $(\sin \alpha_R + V_\omega) > 0$, the following must be satisfied

$$\cos \alpha_R + \sqrt{1 - (\sin \alpha_R + V_\omega)^2} > 0. \quad (\text{A.10})$$

1a) If $\alpha_R \in \left[-\frac{\pi}{2}, \frac{\pi}{2}\right]$ this implies that $\cos \alpha_R > 0$, therefore, (A.10) is always satisfied as long as the launch phase is bounded by the condition

$$\alpha_R > -\arcsin V_\omega. \quad (\text{A.11})$$

1b) If $\alpha_R \in \left[\frac{\pi}{2}, \frac{3\pi}{2}\right]$ this implies that $\cos \alpha_R < 0$ and, therefore, it must hold

$$-|\cos \alpha_R| + \sqrt{1 - (\sin \alpha_R + V_\omega)^2} > 0$$

equivalent to

$$\alpha_R > \pi + \arcsin\left(\frac{V_\omega}{2}\right) \quad (\text{A.12})$$

as long as

$$\alpha_R < \pi + \arcsin V_\omega. \quad (\text{A.13})$$

2) If $(\sin \alpha_R + V_\omega) < 0$, the following must be satisfied:

$$\cos \alpha_R + \sqrt{1 - (\sin \alpha_R + V_\omega)^2} < 0. \quad (\text{A.14})$$

2a) If $\alpha_R \in \left[-\frac{\pi}{2}, \frac{\pi}{2}\right]$ this implies that $\cos \alpha_R > 0$, therefore, (A.14) can never be satisfied.

2b) If $\alpha_R \in \left[\frac{\pi}{2}, \frac{3\pi}{2}\right]$ this implies that $\cos \alpha_R < 0$ and, therefore, it must hold

$$-|\cos \alpha_R| + \sqrt{1 - (\sin \alpha_R + V_\omega)^2} < 0$$

equivalent to

$$\alpha_R < \pi + \arcsin\left(\frac{V_\omega}{2}\right).$$

Nevertheless, this condition is contradictory with the initial hypothesis of

$$\pi + \arcsin V_\omega < \alpha_R < \frac{3\pi}{2}.$$

Thus, no solution can be found for $(\sin \alpha_R + V_\omega) < 0$.

After this analysis we can define the boundaries of the domain of the launch phase that provokes the return of the electron to the initial plate as function of the variable V_ω . The conditions (A.12) and (A.13) define the domain of validity for the second branch of α_R , but only one of the boundaries for the first branch has been limited by (A.11). The second limit for the first branch comes from the condition that the argument of the square root function in (A.10) must be positive, imposing that $\alpha_R < \arcsin(1 - V_\omega)$. The boundaries are thus, defined by:

$$\left\{ \begin{array}{l} \arcsin(1 - V_\omega) > \alpha_R > -\arcsin V_\omega \\ \pi + \arcsin V_\omega > \alpha_R > \pi + \arcsin\left(\frac{V_\omega}{2}\right) \end{array} \right\} \quad (\text{A.15})$$

$$(\text{A.16})$$

All these conditions together provide the plot shown in Fig. A.2 where the domain of validity to find the returning launch phase is represented in gray.

The solution of (A.6) can be calculated taking into account that $\sin \alpha_R + V_\omega = \sin \phi_R$, and as ϕ_R must be located within the second branch of the arcsine function, (A.6) can be rewritten as

$$(2k + 1)\pi - \arcsin(\sin \alpha_R + V_\omega) = \alpha_R + \frac{\cos \alpha_R + \sqrt{1 - (\sin \alpha_R + V_\omega)^2}}{(\sin \alpha_R + V_\omega)}. \quad (\text{A.17})$$

The first branch solution for α_R is calculated by finding the root of (A.17) for $k = 0$ within the interval defined by the first branch of the arcsine function. Analogously the second branch solution is evaluated by finding the root of the same equation for $k = 1$. It can be shown that there is a maximum value of V_ω above which the value of α_R predicted by the solution of (A.17) at any branch is not real-valued.

We can write V_ω as function of α_R and ϕ_R from (A.17) as follows:

$$V_\omega = \frac{\cos \alpha_R - (\phi_R - \alpha_R) \sin \alpha_R + |\cos \phi_R|}{\phi_R - \alpha_R}. \quad (\text{A.18})$$

The plot of V_ω as function of α_R for different values of ϕ_R is depicted in Fig. A.3 together with the domain of definition of the solution analyzed before. The maximum value of V_ω for which the solution is real-valued is found numerically around $V_\omega \approx 1.26$. Therefore, we should add another limitation to the value of V_ω in order to guarantee the existence of the returning limit, more restrictive than the first one defined in the beginning of the appendix:

The electron never impacts against the initial plate when $\frac{v_0 m_e \omega d}{e V_{RF}} \gtrsim 1.26$.

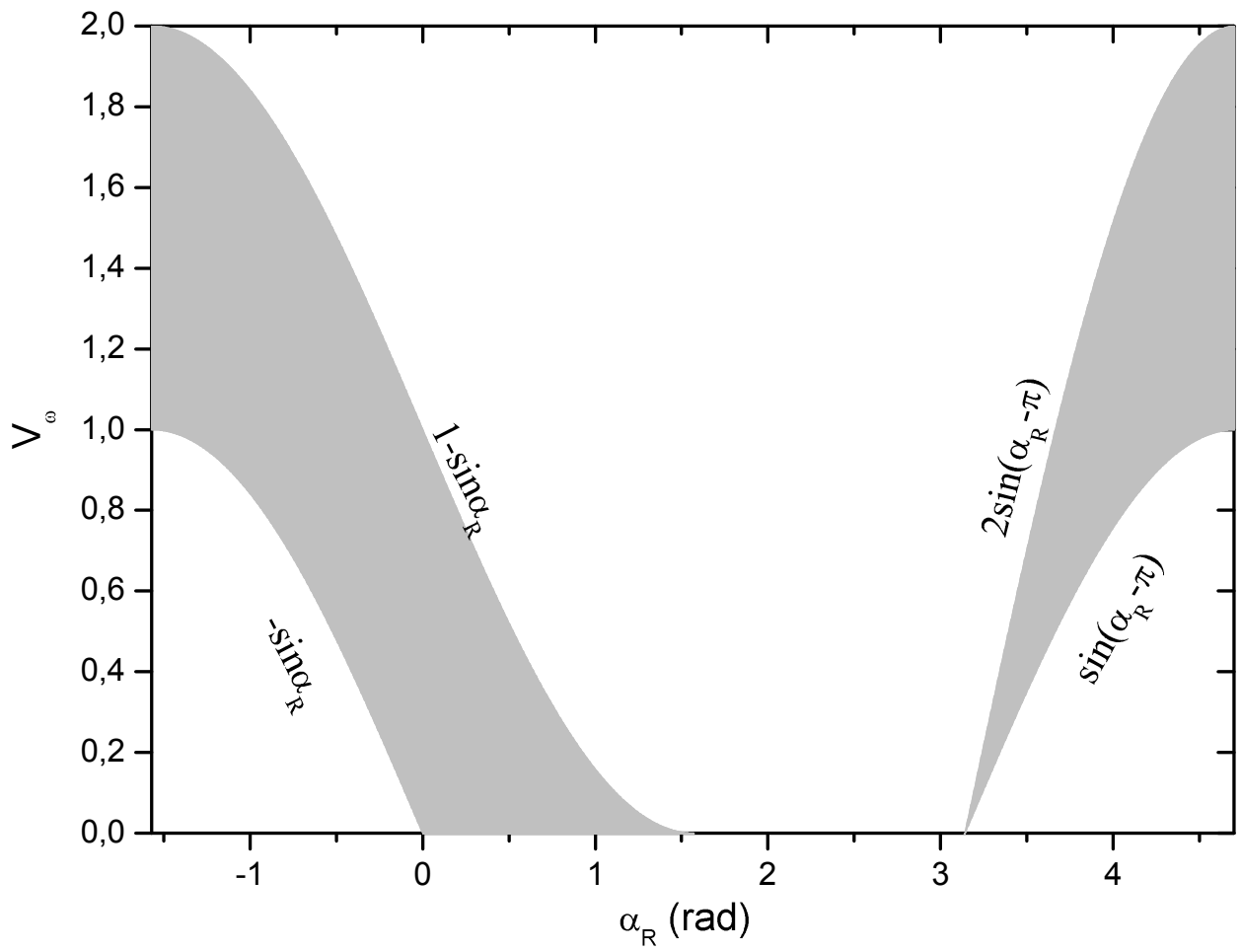


Figure A.2: Domain of validity for the returning limit condition.

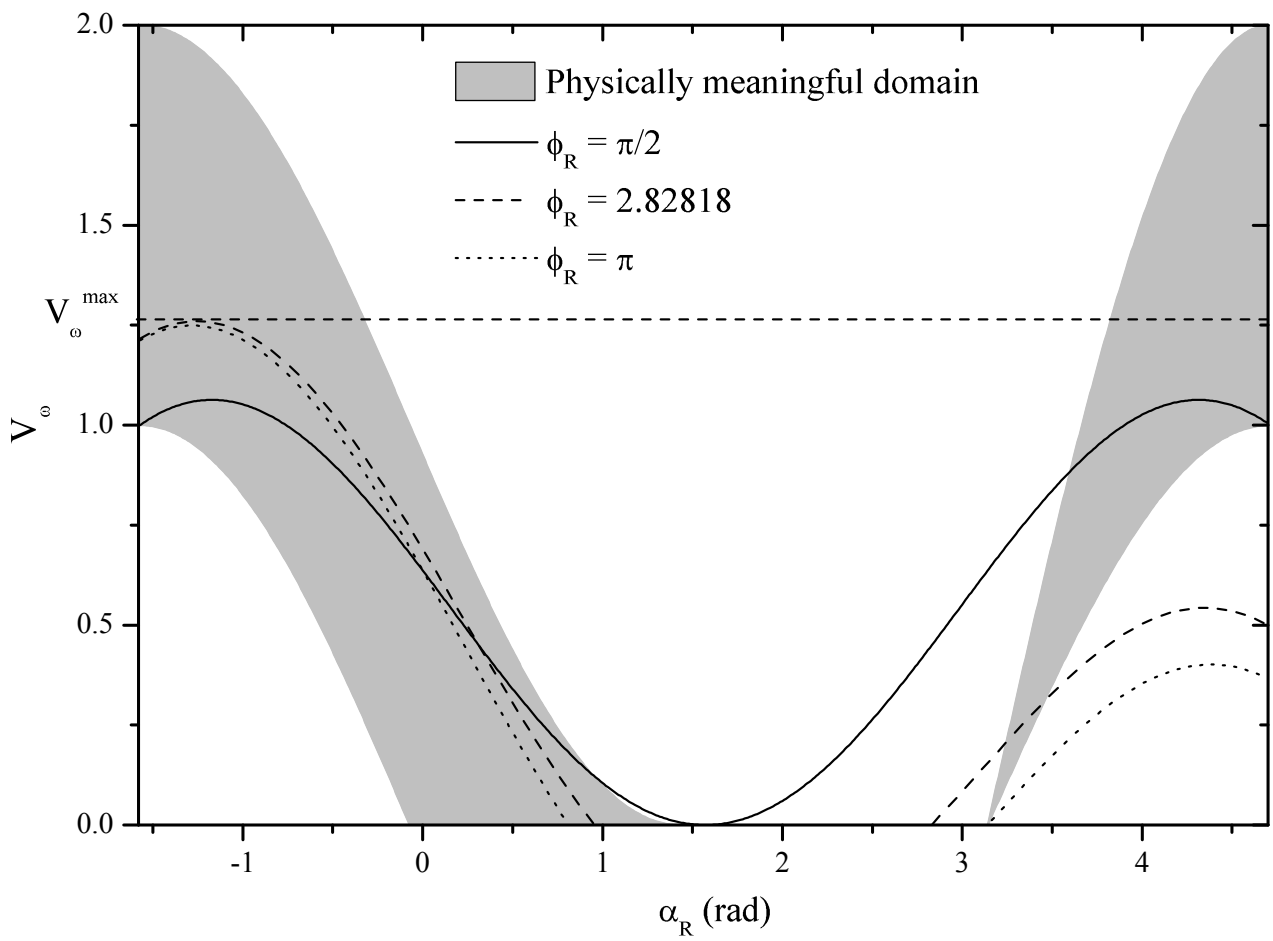


Figure A.3: Search of the maximum value of V_ω for which (A.17) presents a real-valued solution.

Input power of a monopole antenna

The relation between the current amplitude of a current generator feeding an infinitely thin monopole antenna placed on a grounded perfect electric conductor is found by calculating the impedance of the antenna. The current distribution of the monopole antenna above a grounded metal is the same as the one of a dipole antenna, which reads [Balanis 1997b]

$$\mathbf{I}(x' = 0, y' = 0, z') = \begin{cases} I_0 \sin \left[k \left(\frac{l}{2} - z' \right) \right] \hat{\mathbf{z}}, & (0 \leq z' \leq l/2) \\ I_0 \sin \left[k \left(\frac{l}{2} + z' \right) \right] \hat{\mathbf{z}}, & (-l/2 \leq z' \leq 0), \end{cases} \quad (\text{B.1a})$$

$$(\text{B.1b})$$

where the geometry of the problem can be seen in Fig. 6.28a.

The input power of the antenna fed by the current generator is

$$P_{in} = \frac{1}{2} \text{Re} [Z] |I_0|^2, \quad (\text{B.2})$$

where Z is the impedance of the antenna seen from the generator. Thus, we must find the real part of the impedance of the infinitely thin monopole antenna, which is not analytical, and depends on the frequency and the height of the rod. The real part of the impedance of the antenna seen from the generator can be expressed as [Balanis 1997a]

$$R_{in} = \frac{R_r(kl)}{\sin^2(kl/2)}, \quad (\text{B.3})$$

where R_r is a function of the wavenumber times the length of the equivalent dipole (twice the height of the monopole). This function is expressed as

$$R_r(kl) = \frac{\eta}{2\pi} \left\{ C + \ln(kl) - C_i(kl) + \frac{1}{2} \sin(kl) [S_i(2kl) - 2S_i(kl)] \right. \\ \left. + \frac{1}{2} \cos(kl) [C + \ln(kl/2) + C_i(2kl) - 2C_i(kl)] \right\} \quad (\text{B.4})$$

where $C \approx 0.5772$ is the Euler-Mascheroni constant. The functions $C_i(x)$ and $S_i(x)$ are the cosine and sine integral functions, respectively, defined as follows:

$$C_i(x) = \int_{\infty}^x \frac{\cos y}{y} dy \\ S_i(x) = \int_0^x \frac{\sin y}{y} dy.$$

Table B.1: Reference values of the cosine and sine integral functions.

x	$C_i(x)$	$S_i(x)$
3.0	0.11963	1.84865
3.1	0.08699	1.85166
6.0	-0.06806	1.42469
6.1	-0.05198	1.42087

Table B.2: Interpolated values of the cosine and sine integral functions.

x	$C_i(x)$	$S_i(x)$
3.016	0.1144	1.849
6.032	-0.0629	1.4235

Taking into account that $kl = 2\pi fl/c$, and in the case that we are studying, $f = 240$ MHz, $l = 0.48\lambda$ and $\lambda \approx 1.25$ m, the value of the limits of integration are $x_1 \equiv kl \approx 3.016$ and $x_2 \equiv 2kl \approx 6.032$. The evaluation of the cosine and sine integral functions for the requested values of x has been done by interpolating linearly between the closest points extracted from [Balanis 1997c] and shown in Table B.1. The resulting values of the functions found by interpolation are shown in Table B.2.

Therefore, substituting the values of all the parameters requested in Eqs. B.3 and B.4 for the considered monopole antenna, the input power can be expressed as

$$P_{in} \approx 32.47 |I_0|^2. \quad (\text{B.6})$$

Equations of motion of multipactor with space charge effects

In this appendix the equation of motion of the electron cloud, modeled like an infinitely thin sheet of charge, is going to be found within a parallel-plate waveguide driven by the microwave field of the fundamental mode, TEM-mode. By using the electric field within the space between the plates, $\mathbf{E}_{\text{total}}$, given by (5.3), the Lorentz force applied on a single electron of the sheet, neglecting the magnetic field, $\mathbf{F}_T = -e\mathbf{E}_{\text{total}}$, can be calculated as follows:

$$\mathbf{F}_T = \left\{ \frac{-eV_{RF}}{d} \cos \omega t + \frac{e^2 \sigma (z'(t)/d - 1/2)}{\epsilon_0} \right\} \hat{z}. \quad (\text{C.1})$$

Therefore, the acceleration that the electron is subject to can be expressed as

$$\frac{d^2 z'(t)}{dt^2} = \frac{-eV_{RF}}{m_e d} \cos \omega t + \frac{e^2 \sigma (z'(t)/d - 1/2)}{m_e \epsilon_0}, \quad (\text{C.2})$$

which can be rewritten as follows:

$$\frac{d^2 z'(t)}{dt^2} = a \cos \omega t + b z'(t) + c, \quad (\text{C.3})$$

where the following quantities have been defined

$$\left\{ \begin{array}{l} a = \frac{-eV_{RF}}{m_e d} \\ b = \frac{e^2 \sigma}{m_e \epsilon_0 d} \\ c = \frac{-e^2 \sigma}{2m_e \epsilon_0} \end{array} \right. \quad (\text{C.4a})$$

$$\left\{ \begin{array}{l} b = \frac{e^2 \sigma}{m_e \epsilon_0 d} \end{array} \right. \quad (\text{C.4b})$$

$$\left\{ \begin{array}{l} c = \frac{-e^2 \sigma}{2m_e \epsilon_0} \end{array} \right. \quad (\text{C.4c})$$

In order to find the general solution of the differential equation we split the solution into the homogeneous and the particular parts:

$$\left\{ \begin{array}{l} \frac{d^2 z'_h(t)}{dt^2} - b z'_h(t) = 0 \\ \frac{d^2 z'_p(t)}{dt^2} - b z'_p(t) = a \cos \omega t + c \end{array} \right. \quad (\text{C.5a})$$

$$\left\{ \begin{array}{l} \frac{d^2 z'_p(t)}{dt^2} - b z'_p(t) = a \cos \omega t + c \end{array} \right. \quad (\text{C.5b})$$

such that the position of the electron is given by $z'(t) = z'_h(t) + z'_p(t)$.

In order to find the homogeneous solution, the Ansatz $z'_h(t) = Ae^{\lambda t} + Be^{-\lambda t}$ is proposed and inserted into (C.5a), resulting in

$$\lambda^2 - b = 0 \rightarrow \lambda = \pm \sqrt{b}. \quad (\text{C.6})$$

Therefore, the homogeneous solution is given by

$$z'_h(t) = Ae^{\sqrt{b}t} + Be^{-\sqrt{b}t}. \quad (\text{C.7})$$

Analogously, the particular solution is found by proposing the Ansatz $z'_p(t) = C \cos \omega t + D$. Inserting the proposed solution into (C.5b) we obtain

$$-C\omega^2 \cos \omega t - b(C \cos \omega t + D) = a \cos \omega t + c. \quad (\text{C.8})$$

In order to find the coefficients of the particular solution we can set the same number of equations as linearly independent functions exist in the equation above. This leads to a system of equations whose solution reads

$$\begin{cases} C = -\frac{a}{b + \omega^2} \\ D = -\frac{c}{b}. \end{cases} \quad (\text{C.9a})$$

$$\quad (\text{C.9b})$$

Therefore, the particular solution can be expressed as

$$z'_p(t) = -\left(\frac{a}{b + \omega^2} \cos \omega t + \frac{c}{b}\right). \quad (\text{C.10})$$

Bringing together (C.7) and (C.10) we obtain the position of a single electron belonging to the sheet of charge moving within the space between the plates as follows:

$$z'(t) = \left(Ae^{\sqrt{b}t} + Be^{-\sqrt{b}t}\right) - \left(\frac{a \cos \omega t}{b + \omega^2} + \frac{c}{b}\right). \quad (\text{C.11})$$

In order to find the coefficients A and B the initial conditions must be applied, thus we need to calculate the velocity of the electron, $\dot{z}'(t)$, which can be written

$$\dot{z}'(t) = \sqrt{b} \left(Ae^{\sqrt{b}t} - Be^{-\sqrt{b}t}\right) + \frac{a \sin \omega t}{b + \omega^2}. \quad (\text{C.12})$$

Let us assume that the electron leaves the plate placed at z'_0 with velocity v_0 at the instant t_1 . Thus, the coefficients will be found from the following system of equations:

$$\begin{cases} \left(Ae^{\sqrt{b}t_1} + Be^{-\sqrt{b}t_1}\right) - \left(\frac{a \cos \omega t_1}{b + \omega^2} + \frac{c}{b}\right) = z'_0 \\ \sqrt{b} \left(Ae^{\sqrt{b}t_1} - Be^{-\sqrt{b}t_1}\right) + \frac{a \sin \omega t_1}{b + \omega^2} = v_0. \end{cases} \quad (\text{C.13a})$$

$$\quad (\text{C.13b})$$

If we multiply (C.13a) by \sqrt{b} and we add it to (C.13b) we obtain the coefficient A :

$$A = \left\{ z'_0 + \frac{v_0}{\sqrt{b}} + \left(\frac{a \cos \omega t_1}{b + \omega^2} + \frac{c}{b}\right) - \frac{a \sin \omega t_1}{\sqrt{b}(b + \omega^2)} \right\} \frac{e^{-\sqrt{b}t_1}}{2}. \quad (\text{C.14})$$

If we multiply (C.13a) by \sqrt{b} and we subtract (C.13b) the coefficient B is found:

$$B = \left\{ z'_0 - \frac{v_0}{\sqrt{b}} + \left(\frac{a \cos \omega t_1}{b + \omega^2} + \frac{c}{b}\right) + \frac{a \sin \omega t_1}{\sqrt{b}(b + \omega^2)} \right\} \frac{e^{\sqrt{b}t_1}}{2}. \quad (\text{C.15})$$

If we substitute the coefficients A and B of (C.14) and (C.15), respectively, into (C.11) we obtain:

$$z'(t) = \left(z'_0 + \frac{a \cos \omega t_1}{b + \omega^2} + \frac{c}{b} \right) \cosh \left[\sqrt{b}(t - t_1) \right] + \left(v_0 - \frac{a \sin \omega t_1}{b + \omega^2} \right) \frac{\sinh \left[\sqrt{b}(t - t_1) \right]}{\sqrt{b}} - \left(\frac{a \cos \omega t}{b + \omega^2} + \frac{c}{b} \right). \quad (\text{C.16})$$

Analogously, we can rewrite (C.12) as:

$$\dot{z}(t) = \left(v_0 - \frac{a \sin \omega t_1}{b + \omega^2} \right) \cosh \left[\sqrt{b}(t - t_1) \right] + \sqrt{b} \left(z'_0 + \frac{a \cos \omega t_1}{b + \omega^2} + \frac{c}{b} \right) \sinh \left[\sqrt{b}(t - t_1) \right] + \frac{a \sin \omega t}{b + \omega^2}. \quad (\text{C.17})$$

By inserting the coefficients provided by (C.4) into (C.16) and (C.17), it is easy to arrive to the equations of motion expressed by (5.4) and (5.5).

Bibliography

- [Abe 2006] T. Abe, T. Kageyama, K. Akai, K. Ebihara, H. Sakai and Y. Takeuchi. *Multipactoring zone map of an rf input coupler and its application to high beam current storage rings*. Phys. Rev. ST - Accel. Beams, vol. 9, page 062002, 2006.
- [Abramowitz 1970] M. Abramowitz and I. A. Stegun. Handbook of mathematical functions. Dover publications, 1970.
- [Akishev 1999] Yu. S. Akishev, M. E. Grushin, A. A. Deryugin, A. P. Napartovich, M. V. Pankin and N. I. Trushkin. *Self-oscillations of a positive corona in nitrogen*. J. Phys. D: Appl. Phys., vol. 32, pages 2399–2409, 1999.
- [Anderson 1986] D. Anderson, M. Lisak and T. Lewin. *Self-consistent structure of an Ionization wave produced by microwave breakdown in atmospheric air*. Phys. Fluids, vol. 29, pages 446–449, 1986.
- [Ang 1998] L. K. Ang, Y. Y. Lau, R. A. Kishek and R. M. Gilgenbach. *Power deposited on a dielectric by multipactor*. IEEE Trans. Plasma Sci., vol. 26, page 290, 1998.
- [Arndt 2004] F. Arndt. *Fast CAD and optimization of waveguide components and aperture antennas by hybrid MM/FE/MoM/FD methods - State-of-the-art and recent advances*. IEEE Trans. Microw. Theory. Tech., vol. 52, no. 1, 2004.
- [Asvestas 2006] J. S. Asvestas. *Radiation of a Coaxial Line Into a Half-Space*. IEEE Trans. Antennas Propag., vol. 54, no. 6, 2006.
- [Balanis 1989] Constantine A. Balanis. Advanced engineering electromagnetics. John Wiley and Sons Inc., 1989.
- [Balanis 1997a] Constantine A. Balanis. Antenna theory. Analysis and Design. 2nd Edition, Chapter 8, pages 405–410. John Wiley and Sons Inc., 1997.
- [Balanis 1997b] Constantine A. Balanis. Antenna theory. Analysis and Design. 2nd Edition, Chapter 4, page 151. John Wiley and Sons Inc., 1997.
- [Balanis 1997c] Constantine A. Balanis. Antenna theory. Analysis and Design. 2nd Edition, Chapter Appendix III, pages 889–892. John Wiley and Sons Inc., 1997.
- [Bauer 1964] H. Bauer. *Tables of zeros of cross product Bessel functions*. Math. Comp., vol. 18, no. 85, 1964.
- [Bauer 1988] H. F. Bauer. *Mass transport in flow of sources*. Heat and mass transfer, vol. 23, no. 1, 1988.
- [Bell 1970] A. T. Bell. *Spatial Distribution of Electron Density and Electric Field Strength in a High-Frequency Discharge*. I&EC Fundamentals, vol. 9, pages 160–164, 1970.
- [Blyakhman 2000] L. G. Blyakhman, M. A. Gorshkova and V. E. Nechaev. *Saturation of a one-sided multipactor in crossed fields*. Radiophys. and Quantum Electronics, vol. 43, page 904, 2000.

- [Boyer 1969] T. H. Boyer. *Concerning the zeros of some functions related to Bessel functions*. J. Math. Phys., vol. 10, no. 9, 1969.
- [Bridge 1962] J. F. Bridge and S. W. Angrist. *An extended table of roots of $J'_n(x)Y'_n(\beta x) - J'_n(\beta x)Y'_n(x) = 0$* . Math. Comp., vol. 16, no. 78, 1962.
- [Brown 1951] S. C. Brown. *High-Frequency Gas-Discharge Breakdown*. Proc. I.R.E., pages 1493–1501, 1951.
- [Buyanova 2006] Maria Buyanova. *Multipactor Discharge: Theoretical Analysis and Numerical Simulations*. PhD thesis, Chalmers University of Technology, 2006.
- [Buyanova 2010] M. Buyanova, V. E. Semenov, D. Anderson, M. Lisak and J. Puech. *Influence of secondary emission yield on the saturation properties of multipactor discharges between two parallel metal plates*. Phys. Plasmas, vol. 17, page 043504, 2010.
- [Capolino 2005] F. Capolino, D. R. Wilton and W. A. Johnson. *Efficient computation of the 2-D Green's function for 1-D periodic structures using the Ewald method*. IEEE Trans. Antennas Propag., vol. 53, pages 2977–2984, 2005.
- [Chanin 1962] L. M. Chanin, A. V. Pleps and M. A. Biondi. *Measurements of the Attachment of Low-Energy Electrons to Oxygen Molecules*. Phys. Rev., vol. 128, pages 219–230, 1962.
- [Chatterton 1965] P. A. Chatterton and J. D. Craggs. *Attachment coefficient measurements in carbon dioxide, carbon monoxide, air and helium-oxygen mixtures*. Proc. Phys. Soc., vol. 85, pages 355–362, 1965.
- [Chown 1959] J. B. Chown, W. E. Scharfman and T. Morita. *Voltage Breakdown Characteristics of Microwave Antennas*. Proc. I.R.E., pages 1331–1337, 1959.
- [Cimino 2004] R. Cimino, I. R. Collins, M. A. Furman, M. Pivi, F. Ruggiero, G. Rumolo and F. Zimmermann. *Can Low-Energy Electrons Affect High-Energy Physics Accelerators?* Phys. Rev. Lett., vol. 93, no. 1, page 014801, 2004.
- [Clavier 1966] P. A. Clavier and L. Webb. *Electromagnetic Breakdown of Air*. J. Appl. Phys., vol. 37, pages 742–744, 1966.
- [Cochran 1966a] J. A. Cochran. *The analyticity of cross-product Bessel function zeros*. Proc. Camb. Phil. Soc., vol. 62, 1966.
- [Cochran 1966b] J. A. Cochran. *The asymptotic nature of zeros of cross-product Bessel functions*. Quart. Journ. Mech. and Appl. Math., vol. 19, 1966.
- [Coves 2008] A. Coves, G. Torregrosa-Penalva, C. P. Vicente, B. Gimeno and V. E. Boria. *Multipactor Discharges in Parallel-Plate Dielectric-Loaded Waveguides Including Space-Charge Effects*. IEEE Trans. Electron Devices, vol. 55, no. 9, page 2505, 2008.
- [de la Rubia 2005] V. de la Rubia and J. Zapata. *An Efficient Method for Determining TE and TM modes in Closed Waveguides Made up of N Cylindrical Conductors*. IEEE Trans. Microw. Theory Tech., vol. 53, no. 2, 2005.

- [de Lara 2006] J. de Lara, F. Pérez, M. Alfonseca, L. Galán, I. Montero, E. Román and D. Raboso. *Multipactor prediction for on-board spacecraft RF equipment with the MEST software tool*. IEEE Trans. Plasma Sci., vol. 34, no. 2, page 476, 2006.
- [Dekker 1957] A.J. Dekker. Solid state physics, Chapter 17. Prentice Hall, 1957.
- [Druyvesteyn 1940] M. J. Druyvesteyn and F. M. Penning. *The Mechanism of Electrical Discharges in Gases of Low Pressure*. Rev. Mod. Phys., vol. 12, pages 87–176, 1940.
- [Dutton 1963] J. Dutton, F. M. Harris and F. Llewellyn Jones. *The determination of Attachment and Ionization Coefficients in Air*. Proc. Phys. Soc., vol. 81, pages 52–64, 1963.
- [Dwight 1948] H. B. Dwight. *Table of roots for natural frequencies in coaxial type cavities*. J. Math. Phys., vol. 27, 1948.
- [ECSS 2000] ECSS editor. Space engineering. Space environment., 2000.
- [ECSS 2003] ECSS editor. Space engineering. Multipaction design and test., 2003.
- [Esteve 2011] L. Esteve, D. Smacchia, O. Monerris, M. Reglero and M. Taroncher. *Test Report: PIM, Power Handling and Multipactor Tests on three samples of PSM cable assembly designed and manufactured by Huber+Suhner AG (Switzerland)*. Technical report, ESA, 2011.
- [Ewald 1921] P. P. Ewald. *Die berechnung optischer und elektrostatischer gitterpotentiale*. Annalen der Physik, vol. 64, page 253, 1921.
- [Fante 1965a] R. L. Fante. *Mathematical Analysis of Microwave Breakdown in Flowing Gases*. IEEE Trans. Antenna Propagat., pages 781–788, 1965.
- [Fante 1965b] R. L. Fante. *Note on Nonlinear Microwave Breakdown*. IEEE Trans. Antenna Propagat., pages 984–985, 1965.
- [Fante 1968] R. L. Fante and J. T. Mayhan. *Bounds on the Electric Field Outside a Radiating System*. IEEE Trans. Antenna Propagat., vol. 16, pages 712–717, 1968.
- [Fante 1969] R. L. Fante and J. T. Mayhan. *Microwave Breakdown Predictions for a Rectangular Aperture Antenna*. J. Appl. Phys., vol. 40, pages 4750–4752, 1969.
- [Fante 1970] R. L. Fante and J. T. Mayhan. *Bounds on the Electric Field Outside a Radiating System-II*. IEEE Trans. Antenna Propagat., vol. 18, pages 64–68, 1970.
- [Farnsworth 1934] P. T. Farnsworth. *Television by electron image scanning*. J. Franklin Inst., vol. 218, pages 411–444, 1934.
- [Fowler 1928] R. H. Fowler and L. Nordheim. *Electron Emission in Intense Electric Fields*. Proc. Royal Society London, vol. 119, pages 173–181, 1928.
- [Fu 2008] H. Fu, Y. Xie and J. Zhang. *Analysis of Corona Discharge Interference on Antennas on Composite Airplanes*. IEEE Trans. Electromagn. Compat., vol. 50, pages 822–827, 2008.

- [Furman 2003] M. A. Furman and M. T. F. Pivi. *Simulation of Secondary Electron Emission Based on a Phenomenological Probabilistic Model*. Phys. Rev. ST Accel. Beams, vol. 5, no. 12, 2003.
- [G. Valerio 2007] P. Burghignoli G. Valerio P. Baccarelli and A. Galli. *Comparative Analysis of Acceleration Techniques for 2-D and 3-D Green Functions in Periodic Structures Along One and Two Directions*. IEEE Trans. Antennas Propag., vol. 55, pages 1630–1643, 2007.
- [Gilardini 1992] Aldo L. Gilardini. *New breakdown modes of the multipactor discharge*. J. Appl. Phys., vol. 71, pages 4629–4631, 1992.
- [Gimeno 1996] B. Gimeno and M. Guglielmi. *Multimode equivalent network representation for junctions between coaxial and circular waveguides*. Int. J. Microw. Millimet.-Wave Comput.-Aided Eng., vol. 7, no. 2, 1996.
- [Gimeno 1997] B. Gimeno and M. Guglielmi. *Full Wave Network Representation for Rectangular, Circular and Elliptical to Elliptical Waveguide Junctions*. IEEE Trans. Microw. Theory Tech., vol. 45, no. 3, 1997.
- [Gimeno 2009] B. Gimeno, E. Sorolla, S. Anza, C. P. Vicente, J. Gil, A. M. Pérez, V. E. Boria, F. J. Pérez-Soler, F. Quesada, A. Álvarez and D. Raboso. *Multipactor radiation analysis within a waveguide region based on a frequency-domain representation of the dynamics of charged particles*. Phys. Rev. E, vol. 79, page 046604, 2009.
- [Gopinath 1998] V. P. Gopinath, J. P. Verboncoeur and C. K. Birdsall. *Multipactor electron discharge physics using an improved secondary emission model*. Phys. Plasmas, vol. 5, no. 5, page 1535, 1998.
- [Gorshkova 1999] M. A. Gorshkova and V. E. Nechaev. *Saturation of a one-sided multipactor in a decelerating electrostatic field*. Radiophys. Quantum Electronics, vol. 42, page 967, 1999.
- [Gould 1956] L. Gould and L. W. Roberts. *Breakdown of Air at Microwave Frequencies*. J. Appl. Phys., vol. 27, pages 1162–1170, 1956.
- [Gray 1895] A. Gray and G. B. Mathews. *A treatise on bessel functions and their applications to physics*. London MacMillan, 1895.
- [Griffiths 1999] D. J. Griffiths. *Introduction to electrodynamics*, pages 102–103. Prentice Hall, 1999.
- [Gusarova 2009] M. A. Gusarova, V. I. Kaminsky, L. V. Kravchuk, S. V. Kutsaev, M. V. Lalayan, N. P. Sobenin and S. G. Tarasov. *Multipacting simulation in accelerating RF structures*. Nucl Instrum Methods A, vol. 599, pages 100–105, 2009.
- [Gutton 1928] C. Gutton and H. Gutton. *Sur la décharge électrique en haute fréquence*. Compt. Rend., vol. 186, pages 303–305, 1928.
- [Hanson 2002] G. W. Hanson and A. B. Yakovlev. *Operator theory for electromagnetics*. Springer-Verlag, 2002.
- [Harkay 2003] K. Harkay. *Electron Cloud Observations*. In 30th Advanced ICFA Beam Dynamics Workshop on High Luminosity e+e- Collisions, 2003.

- [Harrison 1953] M. A. Harrison and R. Geballe. *Simultaneous Measurement of Ionization and Attachment Coefficients*. Phys. Rev., vol. 91, pages 1–7, 1953.
- [Hatch 1954] A. J. Hatch and H. B. Williams. *The Secondary Electron Resonance Mechanism of Low-Pressure High-Frequency Gas Breakdown*. J. Appl. Phys., vol. 25, no. 4, page 417, 1954.
- [Hatch 1958] A. J. Hatch and H. B. Williams. *Multipacting modes of High-Frequency Gaseous Breakdown*. Phys. Rev., vol. 112, pages 681–685, 1958.
- [Herlin 1948a] M. A. Herlin and S. C. Brown. *Breakdown of a Gas at Microwave Frequencies*. Phys. Rev., vol. 74, pages 291–296, 1948.
- [Herlin 1948b] M. A. Herlin and S. C. Brown. *Electrical Breakdown of a Gas between Coaxial Cylinders at Microwave Frequencies*. Phys. Rev., vol. 74, pages 910–913, 1948.
- [Höhn 1997] F. Höhn, W. Jacob, R. Beckmann and R. Wilhelm. *The transition of a multipactor to a low-pressure gas discharge*. Phys. Plasmas, vol. 4, page 940, 1997.
- [Hilleret 2003] N. Hilleret, C. Scheuerlein and M. Taborelli. *The secondary-electron yield of air-exposed metal surfaces*. Appl. Phys. A, vol. 76, pages 1085–1091, 2003.
- [IEEE 2012] IEEE editor. Spectrum 2.12, February 2012.
- [Izawa 1995] M. Izawa, Y. Sato and T. Toyomasu. *The Vertical Instability in a Positron Bunched Beam*. Phys. Rev. Lett., vol. 74, pages 5044–5047, 1995.
- [Jones 1953] F. L. Jones. *Electrical Discharges*. Rep. Prog. Phys., vol. 16, pages 216–264, 1953.
- [Jordan 2006] U. Jordan, D. Anderson, L. Lapierre, M. Lisak, T. Olsson, J. Puech, V. E. Semenov, J. Sombrin and Rafal Tomala. *On the Effective Diffusion Length for Microwave Breakdown*. IEEE Trans. Plasma Sci., vol. 34, pages 421–430, 2006.
- [Kelly 1960] D. Kelly and H. Margenau. *High-Frequency Breakdown of Air*. J. Appl. Phys., vol. 31, pages 1617–1620, 1960.
- [Kennard 1938] E. H. Kennard. Kinetic theory of gases, page 188. McGraw-Hill Book Co., Inc., 1938.
- [Kishek 1995] R. A. Kishek and Y. Y. Lau. *Interaction of Multipactor Discharge and RF Circuit*. Phys. Rev. Lett., vol. 75, no. 6, page 1218, 1995.
- [Kishek 1996] R. A. Kishek and Y. Y. Lau. *A novel phase focusing in multipactor discharge*. Phys. Plasmas, vol. 3, no. 5, page 1481, 1996.
- [Kishek 1997] R. A. Kishek, Y. Y. Lau and D. Chernin. *Steady-state multipactor and dependence on material properties*. Phys. Plasmas, vol. 4, page 863, 1997.
- [Kishek 2012] R. A. Kishek. *Ping-Pong Modes: A New Form of Multipactor*. Phys. Rev. Lett., vol. 108, page 035003, 2012.
- [Kline 1948] M. Kline. *Some Bessel equations and their application to guide and cavity theory*. J. Math. Phys., vol. 27, 1948.

- [Kobayashi 2003] Shinichi Kobayashi and Yoshio Saito. *Secondary Electron Emission (SEE) Measurements on Materials under Stress (Preliminary measurements of SEE under high temperature condition)*. Technical report, High Energy Accelerator Research Organization (KEK), 2003.
- [Koss 2004] R. Koss, P. Crespo-Valero and J. R. Mosig. *Precise computation of coaxial waveguide eigenvalues based on interlacing properties*. Conference Proceedings of JINA'04, 2004.
- [Kravchuk 1999] L. V. Kravchuk, G. V. Romanov, S. G. Tarasov and V. V. Paramonov. *The computer code for investigation of the multipactor discharge in rf cavities*. In Proc. Particle Accelerator Conference, New York, 1999, 1999.
- [Kryazhev 2002] A. Kryazhev, M. Buyanova, V. Semenov, D. Anderson, M. Lisak, J. Puech, L. Lapierre and J. Sombrin. *Hybrid resonant modes of two-sided multipactor and transition to the polyphase regime*. Phys. Plasmas, vol. 9, pages 4736–4734, 2002.
- [Kuffel 2004] E. Kuffel, W. S. Zaengl and J. Kuffel. *High voltage engineering fundamentals*. Butterworth-Heinemann, 2004.
- [Kustepeli 2000] A. Kustepeli and A. Q. Martin. *On the splitting parameter in the Ewald method*. IEEE Microwave and Guided Wave Letters, vol. 10, pages 168–170, 2000.
- [Laslett 1962] L. J. Laslett and W. Lewish. *Evaluation of the zeros of cross-product Bessel functions*. Math. Comp., vol. 16, pages 226–232, 1962.
- [Lee 1996] J. H. Lee, H. J. Eom and K. H. Jun. *Reflection of a Coaxial Line Radiating Into a Parallel Plate*. IEEE Microwave and Guided Wave Letters, vol. 6, no. 3, 1996.
- [Light 1969] G. C. Light. *High-Temperature-Air Microwave Breakdown*. J. Appl. Phys., vol. 40, pages 1715–1720, 1969.
- [Lorentz 1909] H. A. Lorentz. *The theory of electrons*. B. G. Teubner, 1909.
- [Lupan 1978a] Yu. A. Lupan and A. A. Krasutskii. *Pulsed RF Breakdown of Air at an Inductive Diaphragm in a Waveguide*. Izvestiya VUZ, Radiofizika, vol. 21, pages 572–581, 1978.
- [Lupan 1978b] Yu. A. Lupan, A. A. Krasutskii and S. V. Zakrevskii. *Microwave breakdown field in air*. Zh. Tekh. Fiz., vol. 48, pages 572–581, 1978.
- [Lyapunov 1992] A. M. Lyapunov. *The general problem of the stability of motion*. CRC Press, 1992.
- [Lyneis 1977] C. M. Lyneis, H. A. Schwettman and J. P. Turneaure. *Elimination of electron multipacting in superconducting structures for electron accelerators*. Appl. Phys. Lett., vol. 31, no. 8, 1977.
- [MacDonald 1949] A. D. MacDonald and S. C. Brown. *High Frequency Gas Discharge Breakdown in Helium*. Phys. Rev., vol. 75, pages 411–418, 1949.
- [MacDonald 1959] A. D. MacDonald. *High-Frequency Breakdown in Air at High Altitudes*. Proc. I.R.E., pages 436–441, 1959.

- [MacDonald 1963] A. D. MacDonald, D. U. Gaskell and H. N. Gitterman. *Microwave Breakdown in Air, Oxygen and Nitrogen*. Phys. Rev., vol. 150, pages 1841–1850, 1963.
- [MacDonald 1966] A. D. MacDonald. *Microwave breakdown in gases*. John Wiley and Sons Inc., 1966.
- [Marcuvitz 1951] N. Marcuvitz. *Waveguide handbook*. McGraw-Hill Book Company, Inc., 1951.
- [Margenau 1946] H. Margenau. *Conduction and Dispersion of Ionized Gases at High Frequencies*. Phys. Rev., vol. 69, pages 508–513, 1946.
- [Mattes 2011] M. Mattes, E. Sorolla, H. Hartnagel and H. Karstensen. *Technical Note TN-CCN4-Assessment Report*. Technical report, H+SEPFLTUD, 2011.
- [Mayhan 1969] J. T. Mayhan and R. L. Fante. *A Variational Formulation Specifying the Breakdown Criteria for Plasmas Subjected to Spatially Nonuniform Electric Fields*. J. Appl. Phys., vol. 40, pages 449–453, 1969.
- [Mayhan 1971] J. T. Mayhan, R. L. Fante, R. O'Keefe, R. Elkin, J. Klugerman and J. Yos. *Comparison of Various Microwave Breakdown Prediction Models*. J. Appl. Phys., vol. 42, pages 5362–5369, 1971.
- [McMahon 1894] J. McMahon. *On the Roots of the Bessel and certain Related Functions*. The Annals of Mathematics, vol. 9, no. 1/6, 1894.
- [Mitani 1957] K. Mitani and H. Kubo. *Randomness of Microwave Gas Breakdown Voltage*. J. Phys. Soc. Japan, vol. 12, pages 437–438, 1957.
- [Mosig 1981] J. R. Mosig, J. C. E. Besson, M. Gex-Fabry and F. E. Gardiol. *Reflection of an open-ended coaxial line and application to nondestructive measurement of materials*. IEEE Trans. Instrum. Meas., vol. 30, 1981.
- [Nagesh 2005] S. K. Nagesh, D. Revannasiddiah and S. V. K. Shastry. *Investigation of multipactor breakdown in communication satellite microwave co-axial systems*. Pramana Journal of Physics, vol. 64, no. 1, pages 95–110, 2005.
- [Ney 1987] M. M. Ney, S. R. Valluri, W. Yuw, G. I. Costache and W. J. R. Hofer. *A Study of Electric-Field Breakdown in E-Plane Lines at Centimeter and Millimeter Wavelengths*. IEEE Trans. Microw. Th. Tech., vol. 35, pages 502–509, 1987.
- [Nielsen 1937] R. A. Nielsen and N. E. Bradbury. *Electron and Negative Ion Mobilities in Oxygen, Air, Nitrous Oxide and Ammonia*. Phys. Rev, vol. 51, pages 69–75, 1937.
- [Noh 1999] Y. C. Noh and H. J. Eom. *Radiation from a Flanged Coaxial Line into a Dielectric Slab*. IEEE Trans. Microw. Theory Tech., vol. 47, no. 11, 1999.
- [Ohmi 1995] K. Ohmi. *Beam-Photoelectron Interactions in Positron Storage Rings*. Phys. Rev. Lett., vol. 75, pages 1526–1529, 1995.
- [Ohmi 2000] K. Ohmi and F. Zimmermann. *Head-Tail Instability Caused by Electron Clouds in Positron Storage Rings*. Phys. Rev. Lett., vol. 85, pages 3821–3824, 2000.

- [Olçer 1968] N. Y. Olçer. *On a heat flow problem in a hollow circular cylinder*. Proc. Camb. Phil. Soc., vol. 64, 1968.
- [Panariello 2001] G. Panariello, L. Verolino and G. Vitolo. *Efficient and Accurate Full-Wave Analysis of the Open-Ended Coaxial Cable*. IEEE Trans. Microw. Th. Tech., vol. 49, no. 7, 2001.
- [Panofsky 1955] Wolfgang K. H. Panofsky and Melba Philips. *Classical electricity and magnetism*. Addison-Wesley Publishing Company, Inc., 1955.
- [Park 1998] Myun-Joo Park and Sangwook Nam. *Rapid summation of the Green's function for the rectangular waveguide*. IEEE Microw. Th. Tech., vol. 46, pages 2164–2166, 1998.
- [Paschen 1889] F. Paschen. *Über die zum Funkenübergang in Luft, Wasserstoff und Kohlensäure bei verschiedenen Drucken erforderliche Potentialdifferenz*. Annalen der Physik, vol. 273, 1889.
- [Petrusenko 2001] I. V. Petrusenko. *High-order approximation of wave propagation constants in uniformly curved waveguide*. IEE Proc.-Microw. Antennas Propag., vol. 148, no. 5, 2001.
- [Polycarpou 2006] A. C. Polycarpou. *Introduction to the finite element method in electromagnetics*. Morgan and Claypool, 2006.
- [Pojar 1998a] David M. Pozar. *Microwave engineering*, 2nd ed., Chapter 3, pages 135–136. John Wiley and Sons Inc., 1998.
- [Pojar 1998b] David M. Pozar. *Microwave engineering*, 2nd ed., Chapter 6, pages 315–316. John Wiley and Sons Inc., 1998.
- [Press 1992] W. H. Press, S. A. Teukolsky, W. T. Vetterling and B. P. Flannery. *Numerical recipes in fortran 77 (the art of scientific computing)*, volume 1. Cambridge University Press, 2nd édition, 1992.
- [Raizer 1991] Yuri P. Raizer. *Gas discharge physics*, Chapter 2, page 13. Springer-Verlag, 1991.
- [Rasch 2009] J. Rasch, D. Anderson, M. Lisak, V. E. Semenov and J. Puech. *Microwave Corona Breakdown in a Gas-filled Rectangular Resonator Cavity*. J. Phys. D: Appl. Phys., vol. 42, page 055210, 2009.
- [Renard 2010] Y. Renard and J. Pommier. *GetFEM++*, 2010.
- [Riyopoulos 1995] S. Riyopoulos, D. Chernin and D. Dialetis. *Theory of electron multipactor in crossed fields*. Phys. Plasmas, vol. 2, no. 8, page 3194, 1995.
- [Riyopoulos 1997] S. Riyopoulos. *Multipactor saturation due to space-charge-induced debunching*. Phys. Plasmas, vol. 4, no. 5, page 1448, 1997.
- [Rose 1957] D. J. Rose and S. C. Brown. *Microwave Gas Discharge Breakdown in Air, Nitrogen and Oxygen*. J. Appl. Phys., vol. 28, pages 561–563, 1957.
- [Ruiz-Cruz 2004] J. A. Ruiz-Cruz and J. M. Rebollar. *Eigenmodes of waveguides using a boundary contour mode-matching method with an FFT scheme*. Int. J. RF Microw. C E, vol. 15, no. 3, 2004.

- [Rummolo 2001] G. Rummolo, F. Ruggiero and F. Zimmermann. *Simulation of the electron-cloud build up and its consequences on heat load, beam stability, and diagnostics*. Phys. Rev. ST - Accel. Beams, vol. 4, page 012801, 2001.
- [Ryan 1915] H. J. Ryan and R. G. Marx. *Sustained Radio Frequency High Voltage Discharges*. Proc. I.R.E., vol. 3, pages 349–365, 1915.
- [Ryzko 1965] H. Ryzko. *Drift velocity of electrons and ions in dry and humid air and in water vapour*. Proc. Phys. Soc., vol. 85, page 1283, 1965.
- [Salchev 1973] L. Z. Salchev and V. B. Popov. *Determination of the zeros of a cross-product Bessel function*. Proc. Camb. Phil. Soc., vol. 74, 1973.
- [Sanders 1932] F. H. Sanders. *The Value of the Townsend Coefficient for Ionization by Collision at Large Plate Distances and Near Atmospheric Pressure*. Phys. Rev., vol. 41, pages 667–677, 1932.
- [Scharfman 1960] W. E. Scharfman and T. Morita. *Voltage Breakdown of Antennas at High Altitude*. Proc. I.R.E., vol. 8, pages 104–114, 1960.
- [Schreiber 2002] E. Schreiber and H. J. Fitting. *Monte Carlo simulation of secondary electron emission from the insulator SiO_2* . Journal of Electron Spectroscopy and Related Phenomena, vol. 124, pages 25–37, 2002.
- [Segura 1998] J. Segura. *A global Newton method for the zeros of cylinder functions*. Num. Alg., vol. 18, 1998.
- [Semenov 2001] V. Semenov, A. Kryazhev, D. Anderson and M. Lisak. *Multipactor suppression in amplitude modulated radio frequency fields*. Phys. Plasmas, vol. 8, pages 5034–5039, 2001.
- [Semenov 2005] V. Semenov, V. Nechaev, E. Rakova, N. Zharova, D. Anderson, M. Lisak and J. Puech. *Multiphase regimes of single-surface multipactor*. Phys. Plasmas, vol. 12, page 073508, 2005.
- [Semenov 2007] V. E. Semenov, E. I. Rakova, D. Anderson, M. Lisak and J. Puech. *Multipactor in rectangular waveguides*. Phys. Plasmas, vol. 14, no. 3, page 033501, 2007.
- [Shemelin 1986] V. D. Shemelin. *Existence zones for multipactor discharge*. Zh. Tekh. Fiz., vol. 56, pages 1730–1736, 1986.
- [Sombrin 1983] J. Sombrin. *Effect Multipactor*. Technical report No. 83/DRT/TIT/HY/119/T, CNES, 1983.
- [Somersalo 1998] E. Somersalo, P. Ylä-Oijala, D. Proch and J. Sarvas. *Computational methods for analyzing electron multipacting in RF structures*. Proc. 1995 Particle Accelerator Conference, vol. 59, 1998.
- [Sorolla 2008] E. Sorolla, S. Anza, B. Gimeno, A. M. Pérez, C. P. Vicente, J. Gil, F. J. Pérez-Soler, F. D. Quesada, A. Álvarez and V. E. Boria. *An Analytical Model to Evaluate the Radiated Power Spectrum of a Multipactor Discharge in a Parallel-Plate Region*. IEEE Trans. Electron Devices, vol. 55, no. 8, page 2252, 2008.
- [Sorolla 2011] E. Sorolla and M. Mattes. *Globally convergent algorithm to find the zeros of the cross-product of Bessel functions*. In International Conference on Electromagnetics in Advanced Applications, 2011.

- [Sorolla 2012] E. Sorolla, J. R. Mosig and M. Mattes. *Algorithm to calculate a large number of roots of the cross-product of Bessel functions*. IEEE Trans. Antennas Propag., 2012. (Submitted).
- [Stacey 2009] A. Stacey, S. Prawer, S. Rubanov, R. Ahkvlediani, Sh. Michaelson and A. Hoffman. *The effect of temperature on the secondary electron emission yield from single crystal and polycrystalline diamond surfaces*. Applied Physics Letters, vol. 95, page 262109, 2009.
- [Stakgold 1979] I. Stakgold. *Green's functions and boundary value problems*, Chapter 3. John Wiley & Sons, 1979.
- [Stratton 1941] J. A. Stratton. *Electromagnetic theory*. McGraw-Hill, 1941.
- [Tai 1983] C. T. Tai. *Dyadic Green's Functions for a Coaxial Line*. IEEE Trans. Antennas Propag., vol. 31, pages 355–358, 1983.
- [Tao 2008] T. Tao, L. Cheng, Y. Dan and L. Jun. *Simulation of the Attenuation and Refraction of High Power Microwave Breakdown in the Atmosphere*. In ICMMT2008, 2008.
- [Tomala 2005] R. Tomala, U. Jordan, D. Anderson and M. Lisak. *Microwave Breakdown of the TE₁₁ mode in a Circular Waveguide*. J. Phys. D: Appl. Phys., vol. 38, pages 2378–2381, 2005.
- [Truell 1943] R. Truell. *Concerning the Roots of $J'_\nu(x)N'_\nu(qx) - J'_\nu(qx)N'_\nu(x) = 0$* . J. Appl. Phys., vol. 14, 1943.
- [Udiljak 2003] R. Udiljak, D. Anderson, P. Ingvarson, U. Jordan, U. Jostell, L. Lapierre, G. Li, M. Lisak, J. Puech and J. Sombrin. *New Method for Detection of Multipaction*. IEEE Trans. Plasma Sci., vol. 31, no. 3, page 396, 2003.
- [Udiljak 2007] Richard Udiljak. *Multipactor in Low Pressure Gas and in Nonuniform RF Field Structures*. PhD thesis, Chalmers University of Technology, Göteborg, Sweden, 2007.
- [Vaughan 1988] J. R. M. Vaughan. *Multipactor*. IEEE Trans. Electron Devices, vol. 35, no. 7, page 1172, 1988.
- [Vaughan 1989] J. R. M. Vaughan. *A New Formula for Secondary Emission Yield*. IEEE Trans. Electron Devices, vol. 36, no. 9, page 1963, 1989.
- [Vicente 2005] C. P. Vicente, M. Mattes, D. Wolk, H. L. Hartnagel, J. R. Mosig and D. Raboso. *FEST 3D – A simulation tool for multipaction procedure*. In Proceedings of the 5th International Workshop on Multipactor, RF and DC Corona and Passive Intermodulation in Space RF Hardware, 2005.
- [Woo 1967] R. Woo and A. Ishimaru. *A Similarity Principle for Multipacting Discharges*. J. Appl. Phys., vol. 38, pages 5240–5244, 1967.
- [Woo 1968] R. Woo. *Multipacting Discharges between Coaxial Electrodes*. J. Appl. Phys., vol. 39, pages 1528–1533, 1968.
- [Woo 1984] W. Woo and J. S. DeGroot. *Microwave absorption and plasma heating due to microwave breakdown in the atmosphere*. Phys. Fluids, vol. 27, pages 475–487, 1984.

-
- [Woode 1989] A. Woode and J. Petit. *Diagnostic Investigations into the multipactor Effect, susceptibility zone measurements and parameters affecting a discharge*. Technical report, ESA-ESTEC, 1989.
- [Woode 1990] A. Woode and J. Petit. *Investigations into Multipactor Breakdown in Satellite Microwave Payloads*. ESA Journal, vol. 14, 1990.
- [Yung 1984] E. K. Yung, C. Eng and C. M. Butler. *Coaxial-line driven monopole on an electrically thick conducting cylinder over a ground plane*. IEE Proceedings, vol. 131, no. 1, 1984.

List of Publications

Journal papers

- E. Sorolla, J. R. Mosig and M. Mattes, “Algorithm to calculate a large number of roots of the cross-product of Bessel functions”, *IEEE Transactions on Antennas and Propagation*, under revision.
- E. Sorolla and M. Mattes, “Multipactor saturation in parallel-plate waveguides”, *Physics of Plasmas*, vol. **19**, p. 072304, 2012.
- D. Navarro-Tapia, E. Sorolla, P. Otero-Roth and M. Mattes, “Coupling matrix synthesis of dissipative microwave filters”, *IET Microwaves, Antennas and Propagation*, vol. **5**, No. 8, pp. 895-900, 2011.
- E. Sorolla and M. Mattes, “Corona Discharge in Microwave Devices: A Comparison of Ionization Rate Models”, *IEEE Microwave Review*, vol. **16**, No. 1, pp. 41-46, 2010.
- T. Pinheiro-Ortega, J. Monge, S. Marini, J. Sanz, E. Sorolla et al., “Microwave Corona Breakdown Prediction in Arbitrarily-Shaped Waveguide Based Filter”, *IEEE Microwave and Wireless Components Letters*, vol. **20**, No. 4, pp. 214-216, 2010.
- B. Gimeno, E. Sorolla, S. Anza, C. Vicente and J. Gil et al., “Multipactor radiation analysis within a waveguide region based on a frequency-domain representation of the dynamics of charged particles”, *Physical Review E*, vol. **79**, No. 4, p. 046604, 2009.
- E. Sorolla, S. Anza, B. Gimeno, A. M. Perez, C. Vicente et al., “An Analytical Model to Evaluate the Radiated Power Spectrum of a Multipactor Discharge in a Parallel-Plate Region”, *IEEE Transactions on Electron Devices*, vol. **55**, No. 8, pp. 2252-2258, 2008.

Conference papers

- E. Sorolla, I. Koufogiannis and M. Mattes, “Corona breakdown in open structures: A comparison of several ionization rate models”, *6th European Conference on Antennas and Propagation*, Prague, Czech Republic, 2012.
- E. Sorolla, I. Koufogiannis and M. Mattes, “Ionization Rates: a Comparative Study to Predict Corona Breakdown”, *MULCOPIM 2011*, Valencia, Spain, 2011.
- A. Sounas, E. Sorolla and M. Mattes, “Analysis of Multipactor Effect in Coaxial Lines”, *MULCOPIM 2011*, Valencia, Spain, 2011.
- H. Karstensen, J. Fuchs, D. Raboso, E. Sorolla, D. Schönherr et al., “Power Sub-Miniature (PSM) Connectors for Space Applications”, *MULCOPIM 2011*, Valencia, Spain, 2011.

- D. Navarro-Tapia, E. Sorolla, P. Otero and M. Mattes, “NxN Coupling Matrix Synthesis of Dissipative Microwave Filters.”, *IEEE MTT-S International Microwave Workshop Series on Millimeter Wave Integration Technologies*, Sitges, Spain, 2011.
- E. Sorolla and M. Mattes, “Globally convergent algorithm to find the zeros of the cross-product of Bessel functions”, *International Conference on Electromagnetics in Advanced Applications and Topical Conference on Antennas and Propagation in Wireless Communications*, Torino, Italy, 2011.
- F. Perez Soler, F. Quesada Pereira, A. Alvarez-Melcon, E. Sorolla and B. Gimeno, “Discussion On The Efficient Evaluation Of The Green’s Functions Of Punctual Sources Inside Infinite Parallel Plate Waveguides”, *3rd European Conference on Antennas and Propagation*, Berlin, Germany, 2009.
- H. Karstensen, J. Fuchs, R. Härrri, E. Sorolla, M. Mattes et al., “High Power SMA Connectors”, *MULCOPIM 2008*, Valencia, Spain, 2008.
- E. Sorolla, S. Anza, B. Gimeno, A. M. Perez, C. Vicente et al., “An analytical model to evaluate the radiated power spectrum of a multipactor discharge current in a parallel-plate waveguide region”, *MULCOPIM 2008*

Workshop presentations

- E. Sorolla, F. Zimmermann and M. Mattes, “Modeling Interaction of e-cloud & Microwaves”, *E-CLOUD 2012*, Biodola, Elba, Italy, 2012.

Patents

- E. Sorolla, M. Mattes, H. Karstensen, J. Fuchs, D. Schönherr, and D. Raboso, “High Power SMA”. Depositor: Huber+Suhner AG, Switzerland, pending.

Curriculum Vitae

Edén Sorolla was born on May 12, 1980 in Alicante (Spain). He received the (BSc+MSc) degree in Physics from the University of Valencia (Spain) in 2007. He obtained a fellowship from the Applied Physics and Electromagnetism department and Material Sciences Institute (University of Valencia) to study several electron sources and multipactor detection methods as well as the secondary-electron-yield properties of some materials.

In March 2008 he enrolled the PhD studies at the Laboratoire d'Electromagnétisme et Acoustique (LEMA) of the Ecole Polytechnique Fédérale de Lausanne (EPFL), where he is currently student assistant. He has been responsible for several European Space Agency (ESA) projects:

- Responsible of the multipactor and corona discharges within the framework of the project “High power SMA connector” under the ESA contract No. 20967/07/NL/GLC.
- Responsible of the multipactor and corona discharges within the framework of the project “Light-weight RF power cables with high phase stability” under the ESA contract No. AO1-5984/09/NL/GLC.

In 2009 he made a stay of nearly one month at the ESA laboratory facilities in Noordwijk (The Netherlands) to measure the multipactor and corona withstanding capabilities of the Power Sub-miniature (PSM) coaxial connector.

He has also been responsible for the Swiss National Science Foundation (SNSF) project:

- “Modeling microwave-electron interaction in the LHC beam pipe”, SNSF contract No. 200021_129661.

As a student assistant he has led the exercises in classes on Electromagnetics I and II, graded exams, and proposed and supervised student semester projects. His current research topics include nonlinear phenomena appearing in high power microwave systems (multipactor and corona effects), but he is also interested in the study of low-density plasma applications.

